

Synthesis and Investigation of Nanostructured Functional Materials for Energy-related Applications

DISSERTATION

zur Erlangung des Grades

Doktor der Naturwissenschaften (*Dr. rer. nat.*)

an der Fakultät für Mathematik,
Informatik und Naturwissenschaften

Fachbereich Chemie
Universität Hamburg

Jonas Scholz

Hamburg, Februar 2020

Die vorliegende Arbeit wurde in der Zeit von März 2016 bis Februar 2020 in der Arbeitsgruppe von JProf. Dr. Simone Mascotto am Institut für Anorganische und Angewandte Chemie der Universität Hamburg angefertigt.

1. Gutachter: JProf. Dr. Simone Mascotto
2. Gutachter: Prof. Dr. Michael Steiger

Datum der Disputation: 29.05.2020

Datum der Druckfreigabe: 29.05.2020

I. List of Publications

- Jonas Scholz, Martin Etter, Diana Haas, Andreas Meyer, Andreas Kornowski, Uta Sazama, Simone Mascotto, Pore geometry effect on the synthesis of silica supported perovskite oxides. *Journal of Colloid and Interface Science* **2017**, *504*, 346-355.
- Jonas Scholz, Buğra Kayaalp, Anika C. Juhl, Daniel Clemens, Michael Fröba, Simone Mascotto, Severe Loss of Confined Sulfur in Nanoporous Carbon for Li-S Batteries under Wetting Conditions. *ACS Energy Letters* **2018**, *3*, 387-392.
- Jonas Scholz, Alberto Garbujo, Buğra Kayaalp, Kurt Klauke, Antonella Glisenti, Simone Mascotto, Functional Nanostructured Perovskite Oxides from Radical Polymer Precursors. *Inorganic Chemistry* **2019**, *58* (23), 15942-15952.

II. Table of Contents

I.	List of Publications	I
II.	Table of Contents	II
III.	List of Abbreviations	V
1.	Abstract	1
2.	Zusammenfassung	3
3.	Introduction	6
4.	Objective of this Work	9
5.	Scientific Background	12
5.1.	Nanostructuring	12
5.1.1.	Effects of Enhanced Surface Area	13
5.1.2.	Pore Confinement Effects	15
5.1.3.	Grain Size Effect on Ionic and Charge Mobility	17
5.2.	Nanostructured Materials and their Applications	20
5.2.1.	Perovskite Oxides	20
5.2.2.	Catalytic Properties of Lanthanum-based Perovskite Oxides	25
5.2.3.	Silica	33
5.2.4.	Mesoporous Silica as Support for Perovskite Oxides	36
5.2.5.	Carbon	38
5.2.6.	Nanoporous Carbon as Li-S Battery Cathode Material	42

5.3.	Design of Nanostructured Oxide and Carbon Materials	44
5.3.1.	Design of Nanocrystalline Oxide Materials	44
5.3.2.	Design of Nanoporous Oxide and Carbon Materials	48
5.4.	Characterization of Nanostructured Carbon Materials by means of Small-Angle Scattering	55
5.4.1.	Intrinsic Contrast-Matching	57
5.4.2.	Extrinsic Contrast-Matching Technique	59
6.	Synopsis	62
6.1.	Severe Loss of Confined Sulfur in Nanoporous Carbon for Li-S Bat- teries under Wetting Conditions	62
6.2.	Pore geometry effect on the synthesis of silica supported perovskite oxides	70
6.3.	Functional Nanostructured Perovskite Oxides from Radical Polymer Precursors	82
7.	Unpublished Work	95
7.1.	Porous Perovskite Oxides	95
7.1.1.	Characterization of Ladder-like Polysilsesquioxane Templates	96
7.1.2.	Preparation of Nanoporous $\text{LaCo}_{0.8}\text{Ti}_{0.2}\text{O}_3$ using Ladder-like Polysilsesquioxanes	99
8.	Discussion	109
9.	Experimental Section	113
9.1.	Chemicals	113
9.2.	Synthesis of ladder-like Polysilsesquioxane	113
9.3.	Synthesis of $\text{LaCo}_{0.8}\text{Ti}_{0.2}\text{O}_3$ -LLPSSO Composites	114
9.4.	Sodium Hydroxide Etching	115
9.5.	Acetic Acid Etching	115
9.6.	Characterization Methods	115

10. Bibliography	118
11. Appendix	136
11.1. Supporting Information: Distribution of Sulfur in Carbon/Sulfur Nanocomposites Analyzed by Small-Angle X-ray Scattering	136
11.2. Supporting Information: Pore geometry effect on the synthesis of silica supported perovskite oxides	144
11.3. Supporting Information: Functional Nanostructured Perovskite Ox- ides from Radical Polymer Precursors	159
11.4. Preparation of Nanoporous LaCoO ₃ using Ladder-like Polysilsesqui- oxanes	174
11.5. Preparation of Nanoporous LaCo _{0.8} Ti _{0.2} O ₃ using Ladder-like Poly- silsesquioxanes	179
11.6. List of Chemicals and corresponding Safety Information	182
11.7. Posters and Presentations	187
11.7.1. Oral Presentations	187
11.7.2. Poster Presentations	187
12. Acknowledgements	188
13. Eidesstattliche Versicherung	190

III. List of Abbreviations

AA	Acrylic acid
AAM	Acrylamide
BET	Brunauer–Emmett–Teller
CA	Citric acid
CLD	Chord-length distribution
CMC	Critical micelle concentration
CMK	Carbon Mesostructured by Korea Advanced Institute of Science and Technology
CTAB	Cetyltrimethylammonium bromide
DCM	Dichloromethane
DFT	Density functional theory
DRIFT	Diffuse reflectance infrared fourier transform spectroscopy
DSC	Differential scanning calorimetry
EDX	Energy-dispersive X-ray spectroscopy
EIS	Electrochemical impedance spectroscopy
ER	Eley-Rideal
FDU	Fudan University
FWHM	Full width at half maximum
F127	Triblock copolymer PEG-PPG-PEG
GHG	Greenhouse Gases
h	Hours
IPCC	Intergovernmental Panel on Climate Change
IR spectroscopy	Infrared spectroscopy

III. List of Abbreviations

IUPAC	International Union of Pure and Applied Chemistry
KIT	Korea Advanced Institute of Science and Technology
LCO	Lanthanum cobaltite
LFO	Lanthanum ferrite
LH	Langmuir-Hinshelwood
Li-S Battery	Lithium-sulfur battery
LNO	Lanthanum nickel oxide
LLPSSO	Ladder-like polysilsesquioxane
MA	Methacrylic acid
MCM	Mobil Composition of Matter
MIEC	Mixed ionic and electronic conductivity
MS	Mass spectrometry
NLDFT	Non-linear density functional theory
MOPTMS	3-Methacryloxypropyltrimethoxysilane
NO _x	Nitrogen oxides
PEG	Poly(ethylene glycol)
PEO	Poly(ethylene oxide)
PFO	Praseodymium ferrite
PMMA	Poly(methyl methacrylate)
POSS	Polyhedral oligomeric silsesquioxanes
PPG	Poly(propylene glycol)
PPO	Poly(propylene oxide)
PS	Polystyrene
PSD	Pore-size distribution
PTMS	Phenyltrimethoxysilane
P123	Triblock copolymer PEO-PPO-PEO
P4VP	Poly(4-vinylpyridine)
SANS	Small-angle neutron scattering
SAS	Small-angle scattering
SAXS	Small-angle X-ray scattering

SBA	Santa Barbara Amorphous
SDA	Structure-directing agent
SEM	Scanning electron microscope
SLD	Scattering length density
SNG	Synthetic natural gas
SOFC	Solid oxide fuel cell
STO	Strontium titanate
TEOS	Tetraethyl orthosilicate
TG	Thermogravimetric analysis
THF	Tetrahydrofuran
TMOS	Tetramethyl orthosilicate
TPD	Temperature-programmed desorption
TPR	Temperature-programmed reduction
T ₅₀	Half-conversion temperature
VOC	Volatile organic compound
XRD	X-ray diffraction
3D	Three-dimensional
3DOM	Three-dimensional ordered micro-/mesoporous

1. Abstract

In this work, multiple nanostructured materials were prepared and their properties were investigated with respect to their potential applications. Nanostructure plays an important role in the development of functional materials for applications in the field of catalysis or energy storage due to enhanced surface and transport properties.

A new synthesis approach yielding nanocrystalline perovskite oxides was developed. Based on a polymer-complex method, different acrylate molecules (methacrylic acid, acrylic acid and acrylamide) were used both as complexing agents and monomers. Thus, homogeneous distribution of the cations was promoted, resulting in phase pure perovskite oxides. The use of acrylamide significantly improved the catalytic activity of the perovskite oxides for the oxidation of carbon monoxide compared to materials prepared via the conventional citrate route. In addition, the powders made from acrylamide were characterized by enhanced oxygen release properties. The high flexibility of the developed synthetic method with regard to solvent and type of polymerization allowed the direct transfer of this approach to a spin coating procedure for the preparation of homogeneous perovskite oxide thin films.

By expanding the synthesis, mesoporous perovskite oxides with specific surface areas of up to $90 \text{ m}^2\text{g}^{-1}$ were produced. Silica hybrid materials with a characteristic ladder-like structure were used as hard templates, which could be covalently bound to the polymer matrix due to methacrylic acid functionalities. The increase in porosity led to an increase in oxygen release indicating increased activity in CO oxidation.

As soon as the dimensions of a material are reduced to nanometer sizes, a clear change in the material properties can be observed. Therefore, several processes at nanoscale were investigated (e.g. evaporation, crystallization) in order to gain a better understanding of the influence of the nanostructure.

The use of porous silica as support for perovskite oxides is a common method to increase the specific surface area and thereby the catalytic activity of the oxides. Ordered, porous silica systems with different pore sizes and symmetries were impregnated with a precursor solution to better understand the formation of perovskite oxides in confined spaces. The conversion of the precursors to perovskite oxides and distribution of the perovskite crystallites in the pores of the porous matrices was analysed by means of TG-MS, XRD, SAXS and electron microscopy. A correlation between silica pore size, pore symmetry, and the solvent evaporation of the precursor solution was found. Evaporation, in turn, had a major impact on nucleation and crystallization. A higher curvature of the pores slowed the evaporation of the solvent and promoted crystal formation.

Furthermore, a carbon/sulfur composite, which serves as a model system for the cathode of Li-S batteries, was investigated using neutron small-angle scattering. Deuterated solvents were utilized to match the contrast of the carbon matrix, which enabled the determination of the distribution of sulfur within the nanoporous carbon matrix in dependence of the polarity of the solvents. With decreasing polarity of the solvent, an increasing loss of the sulfur from the pores was found.

These results allow direct conclusions to be drawn about the interactions between electrolyte and sulfur in a Li-S cell. The interaction with solvents, the polarity of which corresponds to the polarity of typical electrolytic agents, led to the sulfur being washed out of the mesopores, so that only the micropores remained filled. The loss of active material severely decreases Li-S cell capacity.

2. Zusammenfassung

In dieser Arbeit wurden mehrere nanostrukturierte Materialien hergestellt und ihre Eigenschaften im Hinblick auf ihre möglichen Anwendungen untersucht. Die Nanostruktur spielt eine wichtige Rolle in der Entwicklung von funktionellen Materialien für Anwendungen im Bereich der Katalyse oder der Energiespeicherung aufgrund von veränderten Oberflächen- und Transporteigenschaften.

Es wurde eine neue Synthesemethode zur Herstellung nanokristalliner Perowskitoxide entwickelt. Basierend auf einem Polymer-Komplex-Prinzip wurden unterschiedliche Acrylat-Moleküle (Methacrylsäure, Acrylsäure und Acrylamid) als Komplexbilder und gleichzeitige Polymer-Bausteine eingesetzt. Somit wurde eine homogene Verteilung der Kationen erzielt, was zur Bildung phasenreiner Perowskitoxide führte. Durch die Verwendung von Acrylamid konnte die katalytische Aktivität der Perowskitoxide für die Oxidation von Kohlenstoffmonoxid im Vergleich zur konventionellen Citrat-Route deutlich verbessert werden. Zusätzlich zeichneten sich die Pulver durch eine erhöhte Sauerstoffabgabe aus.

Die hohe Flexibilität der entwickelten Synthesemethode im Bezug auf Lösungsmittel und Art der Polymerisation ermöglichte die direkte Anwendung dieser Methode in einem *spin coating*-Verfahren zur Herstellung von homogenen Perowskitoxid-Dünnschichten.

Durch eine Erweiterung der Synthese konnten mesoporöse Perowskitoxide mit spezifischen Oberflächen von bis zu $90 \text{ m}^2\text{g}^{-1}$ hergestellt werden. Silica-Hybridmaterialien mit charakteristischer Leiterstruktur wurden als feste Template eingesetzt, die aufgrund einer Methacrylsäure-Funktionalisierung mit in die Polymer-Matrix integriert werden konnten. Die Zunahme der Porosität führte zu einer Zunahme der

Sauerstoffabgabe, was auf eine erhöhte Aktivität bei der CO-Oxidation hinweist.

Sobald die Dimensionen eines Materials auf wenige Nanometer reduziert sind, ist eine deutliche Veränderung der Materialeigenschaften zu beobachten. Daher wurden verschiedene Vorgänge im Nanobereich untersucht (z. B. Verdampfung, Kristallisation), um den Einfluss der Nanostruktur auf diese Prozesse besser zu verstehen. Die Verwendung von porösem Silica als Träger für Perowskitoxide ist eine bevorzugte Methode um die spezifische Oberfläche und dadurch die katalytische Aktivität der Oxide zu erhöhen. Zum besseren Verständnis der Bildung der Perowskitoxide in beschränkten Räumen wurden geordnete, poröse Silicasysteme mit unterschiedlichen Porengrößen und -symmetrien mit einer Vorläuferlösung imprägniert. Die Umsetzung der Vorläufer zu Perowskitoxiden und Verteilung der Perowskitkristallite in den Poren der porösen Matrizen wurde mittels TG-MS, XRD, SAXS und elektronenmikroskopischer Methoden verfolgt. Es konnte eine Abhängigkeit zwischen der Porengröße und -symmetrie und dem Verdampfungsverhalten des Lösungsmittels der Vorläuferlösung festgestellt werden. Das Verdampfen wiederum hatte einen großen Einfluss auf die Kristallisationsprozesse. Eine höhere Krümmung der Poren führte zu einem langsameren Verdampfen des Lösungsmittels und begünstigte die Kristallbildung.

Des Weiteren wurde ein Kohlenstoff/Schwefel-Komposit, das als Modellsystem für die Kathode eines Li-S Akkus dient, mittels Neutronen-Kleinwinkelstreuung untersucht. Durch die Verwendung einer Kontrastmittelanpassung mit Hilfe von deuterierten Lösungsmitteln konnte die Verteilung des Schwefels innerhalb der nanoporösen Kohlenstoff-Matrix in Abhängigkeit von der Polarität dieser Lösungsmittel ermittelt werden. Mit abnehmender Polarität des Lösungsmittels wurde ein zunehmender Verlust des Schwefels aus den Poren festgestellt.

Diese Ergebnisse lassen direkte Rückschlüsse auf die Wechselwirkungen zwischen Elektrolytlösung und Schwefel in einer Li-S-Zelle zu. Die Wechselwirkungen mit Lösungsmitteln, deren Polarität der Polarität von typischen Elektrolytmitteln entspricht,

fürte zu einem Auswaschen des Schwefels aus den Mesoporen, sodass nur die Mikroporen besetzt blieben. Der Verlust an aktivem Material verringert die Li-S-Zellkapazität deutlich.

3. Introduction

Industrial and technological progress in recent decades has been accompanied by a constantly increasing global energy demand. Despite significant downsides, this energy is primarily generated from fossil fuels. Diminishing resources of coal, oil and natural gas lead to increasing market prices and new challenges in recovery and processing of primary energy sources.^[1,2] More concerning, however, is the emission of polluting gases (CO, CO₂, NO_x, H₂O, hydrocarbons) as a result of the combustion of fossil fuels in the fields of energy production and transportation. According to the Synthesis Report of the IPCC in 2014,^[3] energy-related greenhouse gas (GHG) release accounts for two-thirds of global emission. As a result, unprecedented warming of the land and the ocean, extreme weather, ocean acidification and rising sea levels have been observed. Nevertheless, fossil fuels remain the predominant energy source. Global GHG levels continue to rise (Figure 3.1a) and all assessed emission scenarios indicate a sustained temperature increase.^[3,4]

Thus, an immediate transition from fossil fuel consumption to clean and renewable energy sources is inevitable. Present concentrations of polluting gases should be reduced by means of capture or conversion. In addition, carbon-neutral solutions for the generation of energy such as photovoltaics and wind turbines need to be utilized extensively. By 2018, merely 4% of the world energy was generated from renewables (Figure 3.1b). The annual growth rate of renewable energy production, therefore, requires substantial increase. In order to achieve this goal, a substantial progress in energy production, emission reduction, transportation, conversion, storage, and distribution technologies must take place.^[2,4,5]

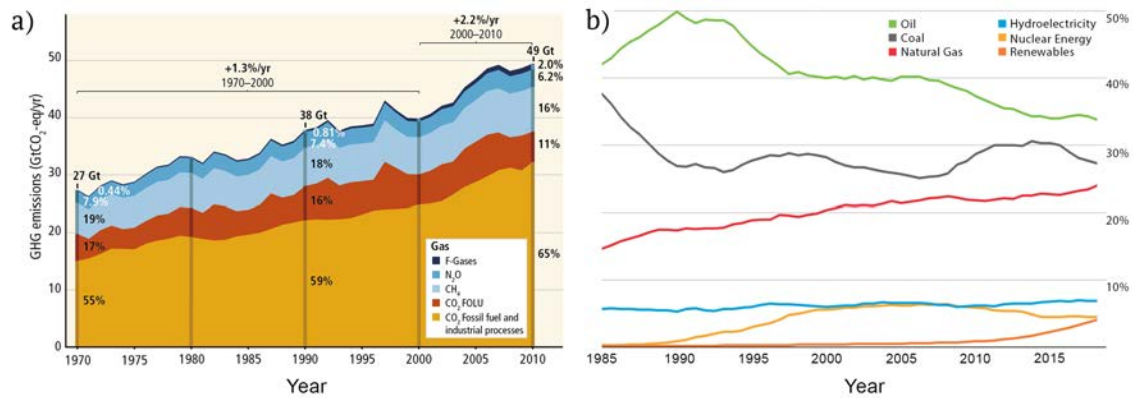


Figure 3.1.: (a) Global anthropogenic GHG emissions by gases between 1970 and 2010.^[3]
 (b) Shares of global primary energy consumption by fuel.^[6]

One approach to lower the concentration of harmful greenhouse gases is the transformation into less harmful species or even usable compounds by means of catalytic conversion, e.g. oxidation of carbon monoxide to carbon dioxide or methanation of carbon dioxide. While noble metals present the most potent catalytically active material class, their high cost and limited availability necessitate reliable alternatives. Among those, the group of perovskite oxides, which combine facile synthesis, low cost, high stability and functional variability, show great promise.^[7–10] With regard to new energy sources, renewable energies (wind turbines, solar energy) present a viable alternative to fuel-based sources. However, those sources are often dependent on the time of day and/or weather conditions. Therefore, development of new or improved energy storage utilities, e.g. batteries, are necessary to provide electricity independent of availability fluctuations. Furthermore, the topic of energy storage is of high importance concerning electromobility. Replacing internal combustion engines with zero/controlled emission vehicles, is a crucial step in reducing GHG emission. However, for electrically powered vehicles to reach long distances in between charging, batteries that combine high capacity and minimal weight and volume are desired. Even though Li-ion batteries have become the preferred choice for battery systems, the capacity limit of 300 mAh g⁻¹ requires alternative storage

3. Introduction

systems.^[1,11]

In principle, Lithium-sulfur batteries present an ideal candidate due to high theoretical specific capacity of 1675 mAh g^{-1} and abundance of sulfur. Its greatest disadvantage, the insulating nature of sulfur, can be overcome by incorporating sulfur into a conducting carbon matrix.

Both perovskite oxides for the purpose of catalysis and carbon-sulfur composites as cathode materials for Li-S batteries need to be improved to become competitive alternative technologies. Thus, systematic investigations into the nanostructuring of these materials enable further tailoring of the functional properties of the respective materials with the aim to achieve the desired performance. Suitable synthesis strategies and ensuing material properties will be presented in detail in this work.

4. Objective of this Work

The design of high-performance materials for energy-related applications, e.g. energy storage,^[11] catalytic conversion,^[12] is an intricate task as it requires the optimization of their synthesis procedures and chemical compositions. However, in many fields, chemical composition and synthesis parameters have been extensively investigated and little progress with respect to functional properties is expected any more.^[12,13]

A promising approach to further improve these material properties, however, is the modification of the structural features. Particularly, nanostructuring can be utilized to expand those functional properties as the nanostructure corresponds directly to the functional material properties. The presence of structural features in the nanometer range (pores, crystallites) originates enhanced surface areas and an increased interface-to-volume ratio. As a consequence, different textural and functional properties are observed, which include high storage capacities,^[14] enhanced ionic and/or electronic conductivity,^[14,15] increased catalytic active sites^[16] and shortened diffusion pathways.^[17,18]

The aim of this work was the development of perovskite oxides with improved functional properties by tuning of the nanostructure. In addition, confinement effects in nanostructured host-guest systems were investigated. In this regard, three different aspects were assessed separately.

Firstly, the improvement of functional properties had to be addressed by developing a suitable synthesis route to modify the nanostructure. Both nanocrystallinity and nanoporosity were emphasized in this approach. Lanthanum-based perovskite oxides present suitable model systems for the investigation of nanosize effects as

4. Objective of this Work

they display decent activity for several catalytic model reactions. Moreover, the perovskite structure can accommodate a wide variety of structural defects and compositional variation, e.g. cationic substitution.^[8,19]

The synthesis approach was based on a polymer-complex method. A correlation between different synthesis parameters and catalytic activity by means of CO oxidation was investigated. An emphasis was placed on the assessment of surface characteristics and functional properties of the nanocrystalline products. In addition, the enhancement of the accessible surface area was addressed through integration of hard templates into the novel preparation method.

The second aspect comprises the investigation of nanostructural phenomena. With respect to the tailoring of functional properties of materials, precise understanding of the processes taking place at the nanoscale is a necessity. Processes such as evaporation and crystallization proceed differently under nanoconfinement.^[20] Mesoporous silica materials with varying pore geometry provide suitable pores for the investigation of these phenomena. Reiterating the role of perovskite oxides, their bulk mechanisms are well understood.^[21] Changed crystallization behaviour in dependence of nanosized constraints, however, can provide valuable information for the understanding of confinement effects.

Insights into nanosized processes are also important within the context of nanocomposites such as C/S-composites for cathode materials in Li-S batteries. Interactions between the host and guest species and a surrounding liquid electrolyte play a pivotal role in the processes taking place in a battery cell.^[11,22-24] However, those interactions are difficult to assess by conventional characterization methods. Transmission electron microscopy and nitrogen physisorption are not suitable as both techniques require the presence of a high vacuum, which prohibits the use of volatile electrolyte liquids. While small-angle X-ray scattering already presents a well-established tool for the investigation of binary nanocomposites, the presence of three different phases makes the reliable interpretation of the data difficult.^[25] Accordingly, the third aspect constituted the establishment of a characterization

method that enabled a direct and comprehensive investigation of a three-phase system comprising carbon, sulfur and a liquid. Ordered nanoporous carbon CMK-8 was chosen as a model system as it comprises both micro- and well-ordered mesopores.^[26] Thus, this method translates readily to different microporous and mesoporous carbon systems. Matching of the scattering-length density of the carbon matrix by incorporating deuterated solvents is exploited in the context of small-angle neutron scattering to obtain a readily analyzed binary system.^[27,28] Thus, by using solvents, the properties such as polarity of which compared to commercially available electrolytes, this method allowed for direct assessment of the interactions between sulfur and electrolyte liquids within a nanoporous matrix.

5. Scientific Background

5.1. Nanostructuring

Nanostructured materials are defined by their textural and morphological characteristics at the nanometer scale. Compared to bulk materials, nanostructured solids (e.g. thin films, superlattices, nanoparticles) display special properties.^[21,29] These properties include immense surface areas of up to several thousand square meters per gram as observed in nanoporous carbon.^[30] With respect to lithium-ion batteries, nanometer-sized electrode structures enable short diffusion lengths for Li^+ ions and fast diffusion rates of the charge carriers along the many grain boundaries.^[17] In this context, nanocomposites can be also utilized to enhance electrochemical storage properties.^[18,31] Furthermore, a considerable melting point depression under nanoconfinement can be observed for several solids such as ice and different organic molecules. The melting point of nano-sized gold particles was even decreased by several hundred degrees centigrade.^[20,32]

This list of nanoscale phenomena is in no way complete. Many more examples, in which nanostructuring alters the material properties significantly, are known. This list is rather meant as a short overview to convey the impact of nanostructuring. The distinct characteristics of nanostructured materials can be ascribed to *nanometer size effects*. Enhancement of the specific surface area of a solid for example leads to an increased surface-to-volume ratio. This can be either achieved by creating nanosized pores inside of bulk material or by reducing the size of a solid in one or more dimensions.^[33]

Furthermore, at nanoscaled dimensions, the interfacial properties are altered due

to very short distances between respective interfaces and material properties are changed. As depicted in Figure 5.1, this effect implies a change of the chemical potential, μ , because an additional contribution from surface free energy needs to be taken into account.^[17,18] Accordingly, the chemical potential at the nanoscale is defined as:

$$\mu_{nano}(r) = \mu_{bulk}(r = \infty) + 2(\gamma/r)V \quad (5.1)$$

where $\mu_{nano}(r)$ and $\mu_{bulk}(r = \infty)$ describe the chemical potential of nanosized and bulk material, respectively, r refers to the effective grain radius, γ represents the effective surface tension, and V is the molar volume.^[17]

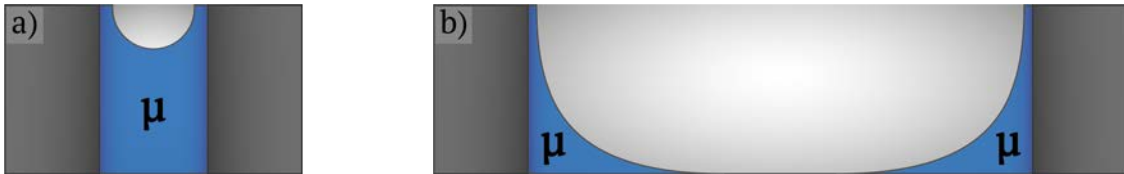


Figure 5.1.: Schematic illustration of the chemical potential, μ , in the context of nanostructured (a) and of bulk material (b). Adapted from Maier *et al.*^[18]

Size effects can be used to selectively tailor material properties. In the following sections, a detailed description of confinement effects, grain size effects, and benefits of an enhanced specific surface area of different nanostructured materials will be given. Additionally, an emphasis will be placed on the corresponding properties with regard to energy-relevant applications.

5.1.1. Effects of Enhanced Surface Area

In this section, nanosize effects with respect to an increased surface-to-volume ratio will be discussed. In the fields of catalysis and sensing, for example, the surface represents the reaction site, i.e. the place of direct interaction between catalyst and

reactant. A higher accessible surface area provides an increased amount of active sites. Thus, the surface area significantly affects the overall functional properties of a material.^[34,35]

Different methods can be used to enhance the accessible surface area. One approach is to reduce the particle size in one or more dimensions to the nanometer scale. Accordingly, thin films (one confined dimension), nanorods (two confined dimensions), or nanoparticles (three confined dimensions) can be prepared. Another type of nanostructuring refers to the generation of nanometer sized pores inside a rigid material. The addition of void space to a solid leads to a sizeable increase in specific surface area.

With respect to porosity, pores within a solid matrix (e.g. carbon, silica, metal oxide) can be categorized according to IUPAC^[36] depending on their size:

- **micropores** describe pore widths below 2 nm
- **mesopores** refer to pore widths between 2 and 50 nm
- **macropores** comprise pore widths surpassing 50 nm

Pores below a size of 100 nm are often summarized as nanopores.

Microporous materials usually exhibit very high specific surface areas of several thousand m^2g^{-1} . However, small pore sizes severely limit mass transport through the porous matrix and larger reactants are prevented from reaching the reaction site. Mesopores, in turn, combine high specific surface areas and excellent transport properties. Accordingly, solids based on mesoporous materials have been of interest for many catalytic applications.^[17,37,38]

Additional benefits of highly porous solids include reduced density and high accessible pore volume (i.e. high loading capacity). These characteristics make them suitable materials for the incorporation of guest species, e.g. for energy storage corresponding to Li-S batteries.^[11] Moreover, the possibility of finely tuning the pore properties (e.g. size, curvature) of nanoporous materials enables a distinct investigation of host-guest systems at the nano scale.

5.1.2. Pore Confinement Effects

Given the various characteristics of pores (topology, size and surface polarity), confinement effects can occur when incorporating guest species into nano-sized pores as the nucleation and crystallization behaviour changes drastically depending on the host morphology.^[39,40]

Before addressing the principles of crystallization within nanometer sized constraints, a classical description of crystallization processes will be provided. The crystal formation of a material depends on its surface free energy and volume free energy. The destabilizing surface free energy, ΔG_A , which is always positive, depends on the interface between the forming nucleus and a surrounding medium. The volume free energy, ΔG_V , is a result of the interatomic bonding energies and is always negative and stabilizing. When the volume free energy surpasses the surface free energy at the critical radius, nucleation and subsequent crystal growth occur (Figure 5.2a).

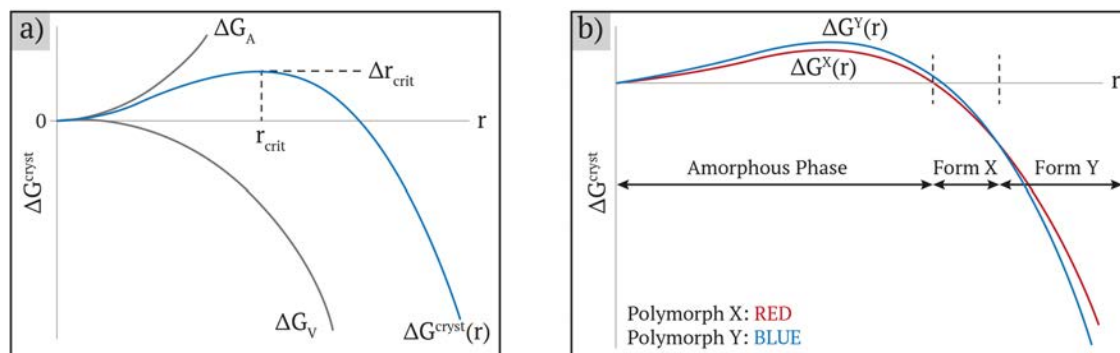


Figure 5.2.: (a) Illustration of the profiles of surface free energy, ΔG_A , and volume free energy, ΔG_V , of a growing crystal nucleus as a function of crystal radius, r . (b) Schematic representation of the free energy profiles of two competing nuclei corresponding to different polymorphs.^[20]

Generally, nucleation is considered a kinetically controlled process. At nanometer

dimensions, however, the dimensions correspond approximately to the critical nucleus size. Accordingly, kinetics and thermodynamics intersect. As a consequence, different phases are thermodynamically stable at corresponding values of free energy (Figure 5.2b). The free energy can be adjusted accordingly by confining the growing nuclei.^[20,41]

Thus, the pore size gives direct control over the crystal growth behaviour and polymorph stability of a material.^[40,42,43] This pore size-dependence has been demonstrated by Ha *et al.*^[44,45] for the crystallization of different organic molecules within the constraints of nanoscaled pores of various size.

Aside from the pore size, the pore shape represents another crucial factor in the crystallization processes of a material. Diao *et al.*^[40] investigated the crystallization behaviour of aspirin in pores of varying angularity, i.e. spherical, hexagonal and cubic. Crystallization was favoured in hexagonally shaped pores. The hexagonal structure provided more angles, which acted as nucleation sites. This finding coincides with simulation-based results of Page and Sear^[46] who reported that nucleation is favoured in wedges as opposed to a flat surface. In that regard, the nucleation rate directly correlated with the angular fit of the crystal lattice into the wedge. The ideal angle is specific for each crystal structure.

The chemical composition of the matrix has a small influence on the crystallization behaviour as well. The surface chemistry of the pore walls plays a role as attractive and repulsive interactions with the crystallizing species are able to direct crystal orientation.^[39,43,47]

In summary, pore properties (size, shape and surface composition) of the porous host can be adjusted to directly control the nucleation kinetics of the crystallizing molecule. Since the pore constraints dictate the growth of nuclei, orientational order and polymorph can be tailored accordingly.^[40,48]

Nanostructuring can also be used to limit diffusion within a host-guest system. By confining a solid guest species in a narrow pore (i.e. micropore), the diffusion of the guest species is slowed down considerably. Accordingly, confinement can be

used as a tool to entrap the guest species inside of a porous host.^[18,49–51]

This aspect of confinement also needs to be considered with regard to evaporation of a guest species. The evaporation temperature and evaporation rate of a liquid confined in a nanosized pore is strongly dependent on pore size or rather the size of the pore neck. With respect to confined solutions, the crystallization kinetics correspond to the evaporation behaviour of the solvent as supersaturation of the solution is a determining factor.^[44,52]

5.1.3. Grain Size Effect on Ionic and Charge Mobility

One of the most important features of a mixed conductor is the material surface or interface as it represents catalytic reaction sites. However, only the external surface of a material is accessible to reactants. Nevertheless, interior interfaces play an equally important role for the development of functional properties such as oxygen mobility.^[19]

With regard to crystalline materials such as perovskite oxides, the interface of a grain presents an area of structural deviation from the bulk. This boundary can constitute the transition zone between two crystallites with different orientation or form the interface between two different phases (Figure 5.3a). Either way, atomic disorder exists at the interface, which leads to ion and electron redistribution. As a result, a defective crystal structure is obtained in the interface region, which originates deviations from electro-neutrality and stoichiometry.^[53–55]

In nanosized crystals, approximately one of ten atoms sits at the surface or interface. Considering the fact that solids generally consist of agglomerated crystallites, a change from micro- to nanosized crystallites constitutes an exponential increase in grain boundaries (Figure 5.3b). Thus, reduced grain size directly translates to a considerably more defective material.^[14,53]

Klie *et al.*^[56] addressed the defect chemistry of grain boundaries of various nanocrystalline perovskite oxides. They confirmed that crystallite interfaces exhibit domains of atomic disorder. Correspondingly, an increased amount of oxygen vacancies was

observed at the grain boundaries.

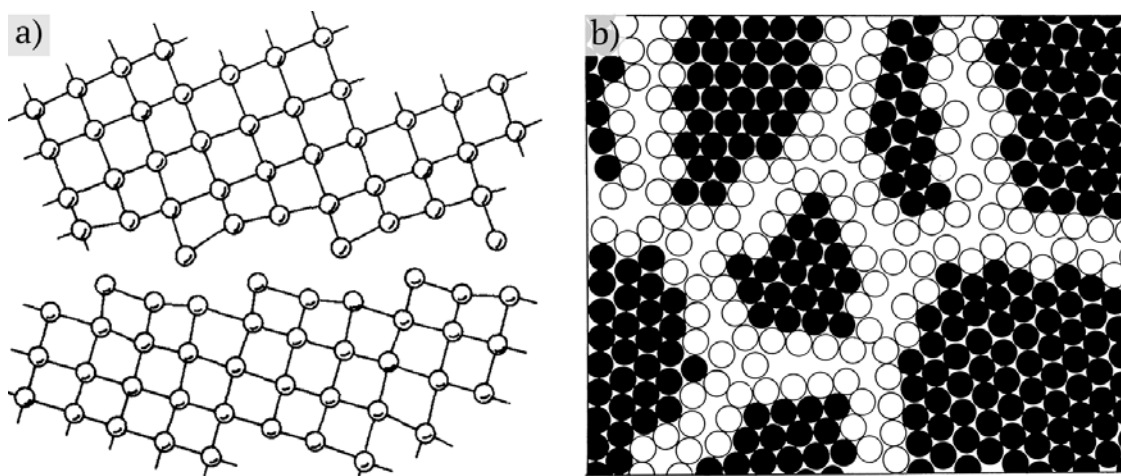


Figure 5.3.: (a) Atomic structure of a grain boundary between two crystallites with different orientation.^[57] (b) Two-dimensional model of a nanostructured material. The atoms in the centers of the crystals are depicted in black, interface atoms are displayed in white.^[55]

With respect to perovskite oxides, a high density of defects such as oxygen vacancies is desirable in catalytic applications. Oxygen ion vacancies contribute to the ionic charge transport through the lattice and facilitate the exchange between atmospheric oxygen and lattice oxygen. Thus, they are essential for catalytic reactions and other applications relying on oxygen transport.^[58–61] The aspects of defect chemistry will be emphasized in the section 'Nanostructured Materials and their Applications'.

Furthermore, different transport phenomena were observed that correlate to the crystallite size. Royer *et al.*^[15] reported a dependence between the grain size of LaCoO_3 and the diffusion of oxygen along the grain boundaries. Reduction of the crystallite sizes lead to shorter diffusion lengths within the material. Thus, oxygen-mobility and therefore activity at low temperatures was enhanced.^[19,53,62]

In addition, the defect chemistry at the grain boundaries promotes the formation

of a space charge layer adjacent to the interface. If the dimensions of the space charge layers exceed the spacing of the interfaces, i.e. for small crystallite sizes, the layers overlap. Accordingly, the material is charged throughout.^[14,54] The grain-size dependent overlap was reported for several nanocrystalline perovskite oxides^[19,56,63] and altered transport properties were observed. However, depending on the charge of the space-charge zone, conductivity was either enhanced or impeded compared to bulk material.^[18]

Ghasdi and Alamdari^[62] investigated the influence of the crystallite size on the sensing performance of LaCoO_3 for CO in air by preparing samples of different crystallite sizes (11 nm, 20 nm, 1000 nm). The specific surface area was kept constant for all samples. According to Figure 5.4, the response ratio increased as the crystallite size decreased. The response corresponds to the mobility of oxygen inside the material. Correspondingly, the amount of desorbed oxygen, determined by O_2 -TPD measurements, rose inversely proportional to the crystallite size, demonstrating improved response ratios for nanocrystalline metal oxide.

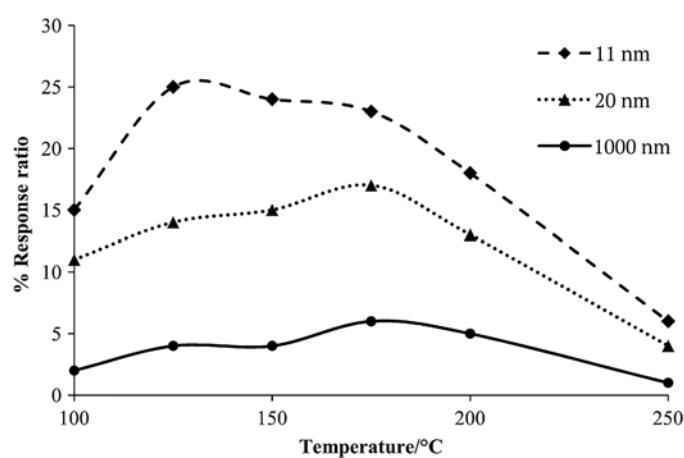


Figure 5.4.: Response ratio of LaCoO_3 with a crystallite size of 11 nm, 20 nm and 1000 nm for 100 ppm CO in air as a function of temperature. Adapted from Ghasdi *et al.*^[62]

5.2. Nanostructured Materials and their Applications

In the following section, an overview over different nanostructured materials will be given. However, compositional contributions to the material properties will be briefly addressed as well. Perovskite oxides will be discussed with regard to both grain size effects and enhanced surface area. In the context of ordered mesoporous carbon and silica materials, the focus will be placed on pore confinement phenomena.

5.2.1. Perovskite Oxides

The compound class of *perovskites oxides* comprises metal oxides of the general formula ABO_3 . The A position is occupied by a large cation, usually a rare earth or alkaline earth element, which is coordinated by twelve O^{2-} ions. The smaller cations, mainly transition metal elements, are usually found in the B position surrounded by corner-sharing octahedrons formed of O^{2-} ions (Figure 5.5). Various cations can be combined as long as their combined oxidation state equals six. As a consequence, more than 90% of metallic elements of the periodic table can form a perovskite oxide structure.^[7,9,21,64]

The compositional diversity of the perovskite oxides results in an extraordinarily wide range of properties, i.a. mixed ion-electron conductivity^[9,65], high stability under oxidizing conditions^[66] and reversible oxygen release from the structure^[9] and is the reason why they have been given the name 'inorganic chameleon'.^[67] Among the list of possible cation combinations, some specific compositions were found to exhibit very intriguing properties, e.g. high catalytic activity of $LaCoO_3$ for the oxidation of carbon monoxide.^[7,8,68] These systems were extensively investigated and comprehensive information about characteristic properties was obtained. Thus, those perovskite oxides present ideal systems for comparison with regard to structure-property relationships.^[69] This enables a more detailed understanding

when modifying material properties, e.g. formation of nanostructure.

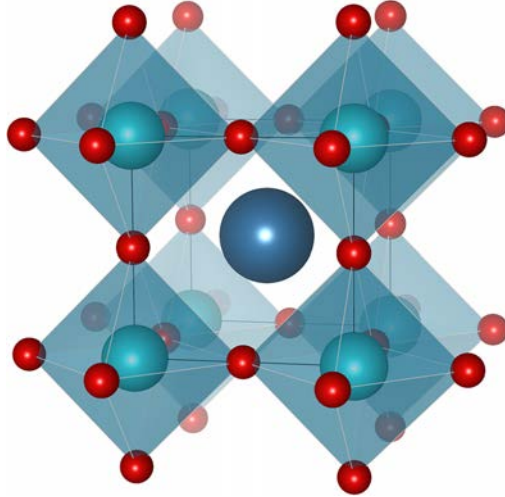


Figure 5.5.: Crystal structure of the ideal perovskite oxide.^[70,71]

At first glance, solids from the class of perovskite oxides do not appear to represent typical nanostructured materials. Traditional synthesis methods originate dense ceramic materials that exhibit low specific surface areas, which rarely exceed values of $1 \text{ m}^2\text{g}^{-1}$, and exhibit large grain sizes in the micrometer range.^[7,67,72–75] However, novel synthesis procedures, the details of which will be discussed in the section 'Design of Nanostructured Oxide and Carbon Materials', enabled the preparation of perovskite oxides with nanostructural features. Crystallite sizes in the nanometer range and enhanced specific surface areas were obtained.

The ideal perovskite structure has a cubic unit cell, crystallizes in the space group $\text{Pm}\bar{3}\text{m}$ and is represented by SrTiO_3 at room temperature. However, considering the multitude of cationic compositions, deviation from the ideal perovskite arrangement occurs frequently while the material maintains its structural integrity. This tolerance regarding structural variability is a significant and unique attribute of the perovskite structure. In order to correlate the structural geometry of a composi-

tion to the ionic radii of the cations, Goldschmidt proposed a tolerance factor t in 1926^[76] described as

$$t = \frac{(r_A + r_O)}{\sqrt{2}(r_B + r_O)} \quad (5.2)$$

with r_A and r_B being the radii of the respective cations and r_O representing the anionic radius.

Stable perovskite compounds are found in the range of $0.71 < t < 1.10$. A tolerance factor of $t=1$ represents the idealized cubic perovskite structure. Nevertheless, a cubic structure is found for values between 0.9 and 1.0. For higher and lower t values, perovskites with distorted lattice geometry are obtained. Lowering of the symmetry by this distortion results in orthorhombic, rhombohedral, hexagonal, tetragonal, monoclinic or triclinic systems. Within the scope of distorted phases, variation of the cationic sizes as well as defect perovskites with cationic or oxygen vacancies can be observed.^[21,77,78]

Furthermore, the chemical and physical properties of this compound class can be finely tuned by substitution of some or all of the A- or B-site cations with cations of equal or different valency. A general formula of $A_{1-x}A'_x B_{1-y}B'_y O_{3\pm\delta}$ is therefore better suited to account for resulting oxygen excess or deficiency.^[7,9,21,68,77]

Defect Chemistry of Perovskite Oxides

One of the integral qualities of perovskite oxides is the high tolerance for structural defects. The irregularities within the lattice are easily accommodated in the perovskite structure and play an essential role in many of their applications. Within the context of nanocrystalline perovskite oxides, an enhanced interface contribution results in a high defect density of the overall solid.^[21,55]

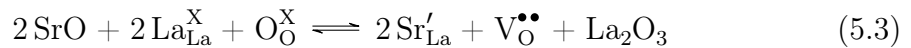
While intrinsic defects occur naturally in all crystals, extrinsic defects can be incorporated deliberately by doping. The kind and amount of those extrinsic de-

fects can be controlled in order to improve catalytic activity and electrochemical properties.^[58,78,79]

In the perovskite oxide lattice, zero-dimensional point-defects are most relevant, comprising electronic defects, oxygen ionic defects and cationic defects. Electronic defects, which occur to a certain degree in any crystal, either refer to excess electrons or electron holes in the lattice structure. The excess of electron defects can be raised by donor doping, i.e. substituting cations of higher valency than the initial cations. Thus, additional electrons are provided as majority charge carriers resulting in n-type conductivity. The use of acceptor dopants, in turn, constitutes a p-type conductor. Lower-valent dopant cations introduce freely moving electron holes, which behave like electrons with a positive charge and increased effective mass.

Electronic charge carriers are crucial to the catalytic performance of ABO_3 . They enable charge-transfer during the surface reaction and are indispensable for the distribution of oxygen vacancies through the bulk material by means of ambipolar diffusion.^[59,61,78,79]

Oxygen vacancies are often formed as a consequence of aliovalent cation substitution with acceptor dopants, i.e. replacement of a cation for a cation with lower valency. A prominent example is the partial replacement of La^{3+} by Sr^{2+} . This substitution at the A-site is displayed in Figure 5.6. The resulting charge difference requires compensation by creating an oxygen vacancy (eq 5.3, Figure 5.6b). Alternatively, electro-neutrality can be achieved by oxidation of the B-site cation, which in turn improves the redox properties (eq 5.4, Figure 5.6c).^[9,58,59,61,78]



5. Scientific Background

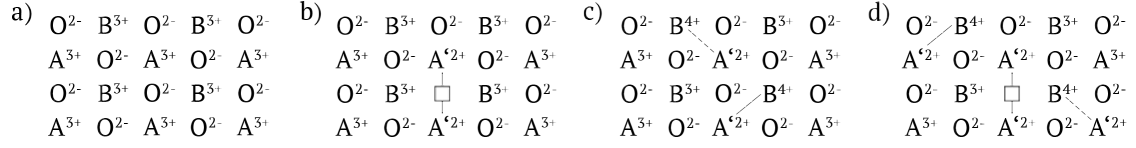


Figure 5.6.: Charge compensation in a defect $\text{A}_{1-x}^{3+}\text{A}_x^{2+}\text{BO}_{3-\delta}$ structure by formation of oxygen vacancies (b), change of the oxidation state of the B cation (c), or simultaneous occurrence of both phenomena (d). An ideal ABO_3 structure is displayed as a comparison (a). Adapted from Zhu *et al.*^[68]

As mentioned in Section 5.1.3, the importance of oxygen ion vacancies for oxygen transport within the perovskite oxide cannot be overstated. The presence of these anionic vacancies strongly influence the exchange rate between atmospheric and lattice oxygen. In addition, the incorporation of atmospheric oxygen into the vacancies results in the formation of electronic holes. Thus, the mixed conductivity (ionic and electronic) increases corresponding to the amount of oxygen vacancies depending on n- or p-type conductivity.^[58–60]

Moreover, cationic deficiencies are known to enhance ionic transport properties. Studies on different perovskite oxides^[80–82] have shown that Schottky disorder is energetically favoured over Frenkel defects. Accordingly, the introduction of cationic vacancies results in additional oxygen vacancies to maintain charge neutrality within the lattice. A-site cation deficiencies are energetically favoured compared to defects at the B-site.^[78,83,84]

The location of these point-defects within the solid were investigated by Read *et al.*^[58] They determined that the surface defect energies were lower than the defect energies in the bulk crystal. This implies that dopants and oxygen vacancies segregate to the surfaces or interfaces. Thus, the catalytic and electrochemical activity of the material is enhanced.

5.2.2. Catalytic Properties of Lanthanum-based Perovskite Oxides

Commercial usage of catalysts is almost exclusively limited to noble metals (e.g. Pt, Pd, Ru) due to their high catalytic activity. Scarcity, high costs and susceptibility to catalyst poisoning, however, increase interest in exploring alternatives. Among those options, lanthanum-based perovskite oxides present a viable candidate due to their low cost, earth abundance, thermal stability, excellent redox properties, oxygen mobility and their surface acid-base character. While their excellent properties also spawn interest in other areas of applications (e.g. gas sensors,^[85] solid oxide fuel cells^[86,87]), their potential in the field of heterogeneous catalysis is promising.^[12,16,88,89]

In order to compete with noble metal catalysts, however, the specific surface area, crystallite size and crystal structure of utilized perovskite oxides require optimization. Hence, a suitable synthesis of these materials for catalytic applications originates highly crystalline materials exhibiting large accessible surface area, i.e. enhanced interface contribution. Additionally, the prepared material requires high ionic and electronic conductivity, which can be further improved, e.g. by acceptor doping.^[8,21,58,88]

The main role of lanthanum in the A-site position is to provide stability to the perovskite structure. Its impact on catalytic properties is considered negligible. However, different activities have been reported for different rare-earth cations as they have an impact on spin and valence state of the B site cation.^[19,90–93] Moreover, when substituting with cations of alternate valence to introduce vacancies etc., doping of the A site can be a crucial factor in the catalytic activity (Section 5.2.1).^[9,58] A fundamental aspect of heterogeneous catalysis is Sabatier's principle of catalysis. It postulates that the catalytic reaction rate depends on the surface binding energies between reactant and catalyst. A highly active catalyst provides ideal interactions, i.e. the bond to the reactant is neither too strong nor too weak.^[12]

With regard to perovskite oxides, the nature of the B site cation is considered responsible for the catalytic activity. Shao-Horn *et al.*^[94] reported a correlation

5. Scientific Background

between the occupancy of the e_g orbital of the BO_6 octahedron of surface cations and the catalytic activity of different perovskite oxides for the oxygen evolution reaction. A similar e_g filling dependence was also found for other catalytic reactions, i.a. oxidation of CO.^[12,69] The e_g orbital occupancy corresponds to the strength of the adsorbate interactions. With respect to the concept of Sabatier, an occupancy value of e_g close to unity presents ideal binding conditions (Figure 5.7b).

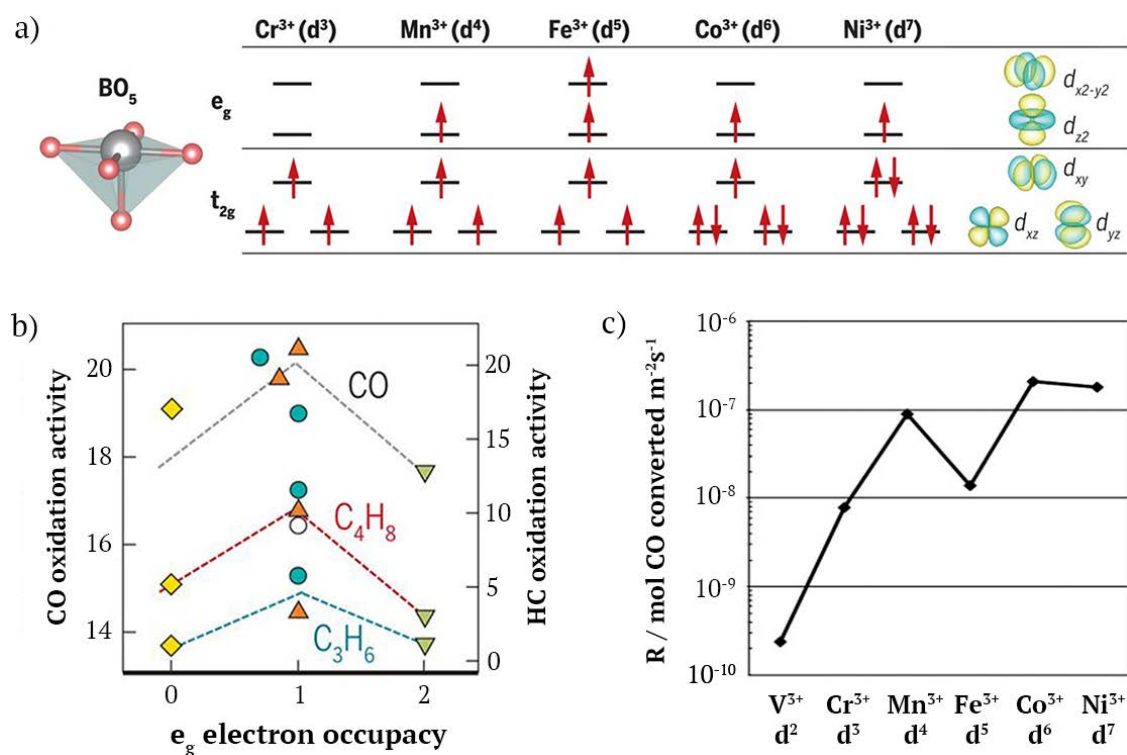


Figure 5.7.: (a) Electronic configuration of relevant metal orbitals of first-row transition metals for a superficial BO_5 configuration.^[12] (b) Correlation between e_g occupancy and catalytic activity for CO, propene (C_3H_6), and isobutylene (C_4H_8) oxidation of first-row transition metal perovskite oxides; B = Cr (yellow), Mn (orange), Fe (green), Co (turquoise), Ni (white).^[12] (c) Catalytic CO conversion rate of LaBO_3 . B represents different first-row transition metals.^[9,95]

The e_g occupancy of a perovskite oxide can be easily adjusted, e.g. by partial substitution of the cationic composition^[94] or by reduction of the particle size.^[96] Thus, the e_g filling enables direct control over material properties.^[12]

Another factor in the catalytic activity of the material is the redox stability of the respective B site cations as it has a strong impact on the oxygen exchange properties.^[9,95] In that context, Mueller *et al.*^[97] discovered that participation of superficial oxygen is an integral part of the redox reaction. Thus, the B-O₆ octahedron should be considered a redox-active entity. High 'instability' of that entity facilitates change in the oxidation state. Accordingly, reversible addition and removal of oxygen can easily take place during catalytic reactions.

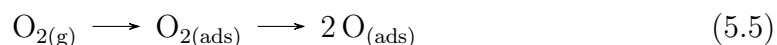
Among the B-site cations in Figure 5.7c, Co³⁺ is most easily oxidized. In addition, the e_g occupancy equals unity (Figure 5.7a). Accordingly, LaCoO₃ and solid solutions thereof represent potent systems for different catalytic applications.^[8,59]

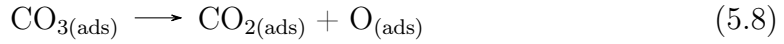
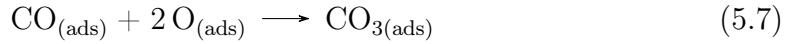
In the following subsection, the principles of CO oxidation will be introduced. This low-temperature catalytic process essentially takes place at the surface and therefore demonstrates the impact of the surface chemistry. In this context, the influence of nanocrystallinity will be detailed. Subsequently, the impact of an increased surface-to-volume ratio will be demonstrated for several catalytic reactions.

CO oxidation reaction

The conversion of CO, emitted with automotive exhaust gases, into less harmful CO₂ with the assistance of a catalyst is an indispensable prerequisite for the reduction of hazardous gases.^[8,12]

At low temperatures, the oxidation of CO favours a suprafacial mechanism according to Tascon *et al.*^[98] The catalyst provides surficial adsorption sites of adequate symmetry and electronic properties to facilitate bonding of the reactant molecules. Lattice oxygen is not involved in this process.^[8,98]





Molecular oxygen is adsorbed on the metal surface (denoted as *ads* for adsorbed), followed by dissociation into the reactive oxygen species. The adsorption of CO at surficial O²⁻ sites generates a labile species that further reacts with adsorbed oxygen to form a bidentate carbonate. Transformation into a less stable monodentate leads to decomposition into CO_{2(ads)} and O_(ads) before desorption of CO₂ occurs. The final step, the decomposition of carbonate to gaseous CO₂, is considered the rate-determining step.^[7,8,98]

This process combines an Eley-Rideal (ER) and a Langmuir-Hinshelwood (LH) mechanism. According to the ER mechanism, only one reactant is adsorbed on the local surface before the reaction takes place (Figure 5.8). In contrast, during the process described by LH, both reactants are adsorbed on the surface before they react.^[99] The coexistence of the ER and the LH mechanism was proven by Zhang-Steenwinkel *et al.*^[100] by utilizing step response analysis with the use of labelled and unlabelled oxygen.

Accordingly, several authors described a strong correlation between catalytic activity and surface properties. An increase in surface area is accompanied by improved catalytic activity up to a certain value.^[101-103] Enhancement of the catalytic performance can be further achieved by decrease of the crystal size,^[104] improved surface crystallinity,^[105,106] suitable morphology^[107] and synthesis method.^[7,108]

Another approach to improve the catalytic performance of a perovskite oxide is the introduction of dopants. It was observed that A-site acceptor doping significantly facilitates the cobalt reducibility. Nakamura and co-workers^[109,110] confirmed by means of oxygen isotopic exchange that the lability of both surface oxygen and bulk oxygen was increased following the substitution of A-site cations. Other substitu-

tions can also provide an increase in catalytic activity if the lattice oxygen mobility is improved.^[8,111–113] These observations indicate that at higher temperatures, lattice oxygen contributes to the oxidation reaction. Correspondingly, transition to an intrafacial mechanism according to Mars-van-Krevelen takes place (Figure 5.8c).^[114] Thus, oxygen from the bulk is consumed during the oxidation reaction. Regeneration of the catalyst then occurs through adsorption-dissociation-incorporation of oxygen from the gas phase.^[7,115] Hueso *et al.*^[116] discovered a complete shift from supra- to intrafacial reaction around 320 °C.

The complexity of the reaction and dependence on the material composition and morphology complicate the precise description of the processes taking place. Therefore, different mechanisms are proposed that can only contribute to a complete comprehension.^[7]

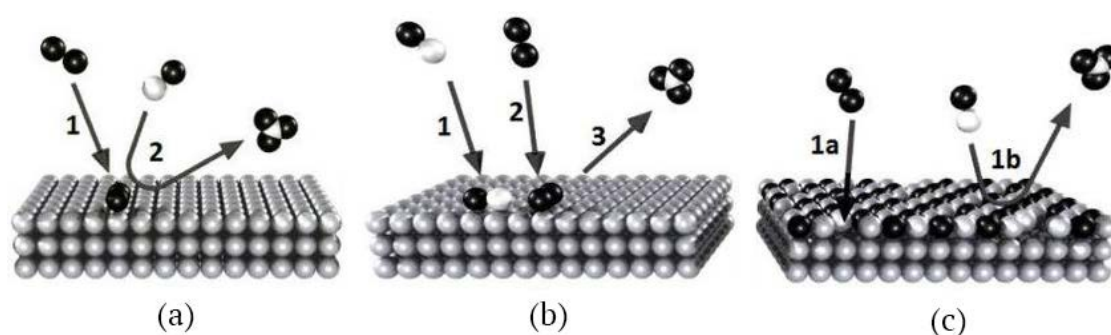


Figure 5.8.: Surface processes according to Eley-Rideal (a), Langmuir-Hinshelwood (b) and Mars-van-Krevelen (c). Adapted from Misono *et al.*^[117]

Among La-based perovskite oxides, compounds in which Co is located at the B position are most suitable as catalyst for the CO oxidation reaction (Figure 5.7c). The Lewis acidity of Co^{3+} allows for the adsorption of carbon monoxide, whereas oxygen in the form of molecular O_2 favours adsorption on Co^{2+} sites. The high redox activity of cobalt results in the coexistence of Co^{3+} and Co^{2+} and provides the necessary active sites for the CO oxidation.^[9,68,118]

Grain Size Effect on Catalytic Activity

The influence of the grain size on the catalytic activity for the oxidation of CO to CO₂ will be presented in this subsection. Seyfi *et al.*^[88] reported 50% conversion over LaCoO₃ at 280 °C. The perovskite oxide material was synthesized via a citrate method. The resulting solids exhibited a specific surface area of 5.3 m²g⁻¹ and crystallite sizes around 100 nm. Taguchi *et al.*,^[105] in turn, achieved 50% conversion as low as 124 °C. A similar synthesis approach compared to the work of Seyfi *et al.* based on the citrate method was used for the synthesis of the LaCoO₃ catalyst. However, lower calcination temperature and shorter calcination time originated a material with different textural properties. The nanostructured solid exhibited a BET surface area of 13.0 m²g⁻¹ and crystallite sizes around 20 nm. A comparison of the results of Seyfi and Taguchi demonstrates the impact of the nanostructure with regard to the catalytic performance. While differences in synthesis and surface area affect the activity of LaCoO₃, the increased interface contribution distinctly promotes the CO oxidation reaction.

This aspect is even further emphasized in the work of Taguchi and co-workers.^[105] Minimal variation of synthesis parameters reportedly lead to perovskite oxide materials with slightly different crystallite sizes in the nanometer range. A clear correlation between the grain size and the catalytic conversion of carbon monoxide over LaCoO₃ was observed (Figure 5.9). The lowest half-conversion temperature (T₅₀) was realized by the nanostructured perovskite oxide which exhibited the smallest crystallite size. As the crystallite size increased, T₅₀ increased accordingly. Textural properties such as specific surface areas and average particle sizes also varied corresponding to the synthesis conditions. However, a clear relationship between those properties and the catalytic performance was not detectable. Therefore, this study further exemplifies the correlation between nanometer size effects due to an increased interface contribution and functional properties of perovskite oxide materials.

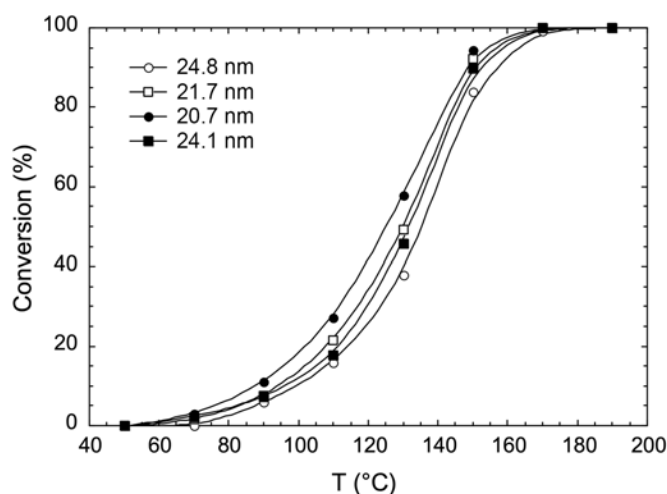


Figure 5.9.: Catalytic conversion of CO to CO₂ over nanocrystalline LaCoO₃. Adapted from Taguchi *et al.*^[105]

Effect of Enhanced Surface Area on Catalytic Activity

In the previous paragraph, the influence of the grain size of nanostructured materials on the catalytic activity of perovskite oxides was presented. A strong contribution of the crystallite interfaces was shown. In this subsection, the focus will be placed on the impact of the exterior surface, i.e. the site of heterogeneous catalysis. The presence of nanosized pores inside the material leads to a considerably enhanced accessible surface area. Accordingly, the reaction site is enlarged, which promotes catalytic activity.^[9] With respect to the pore size, mesopores are favoured as opposed to micropores. The bigger mesopores allow sufficient transport rates for the reactants.

The suitability of perovskite oxides for catalytic processes is not limited to CO oxidation. Especially cobaltites, manganites and ferrites can be utilized as catalyst in the oxidation of volatile organic compounds such as methane, reduction of NO and total oxidation of methanol.^[9]

Wang *et al.*^[119] were able to demonstrate the influence of the surface area for

the complete oxidation of methane over mesoporous LaCoO_3 . Materials with a high specific surface area of $96.7 \text{ m}^2\text{g}^{-1}$ were prepared via a nanocasting method, employing vinyl silica KIT-6 as exotemplate. Comparison of the temperature-dependant methane combustion between nanocast LCO and bulk LCO ($8.3 \text{ m}^2\text{g}^{-1}$) revealed significantly improved light-off and half-conversion temperatures in favour of the mesoporous compound (Figure 5.10). Repeated catalytic runs led to a decrease in catalytic conversion as a consequence of diminished specific surface area ($69.5 \text{ m}^2\text{g}^{-1}$) due to particle sintering. However, this fact further supports the impact of the surface area on the catalytic activity.

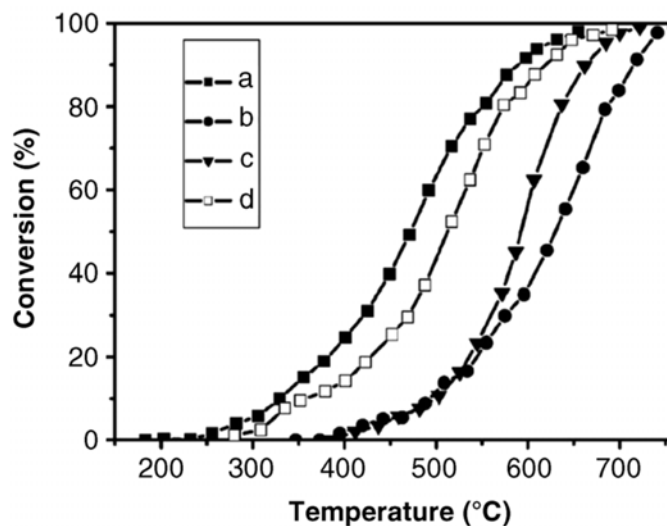


Figure 5.10.: Catalytic conversion of methane over mesoporous LCO (a), silica-LCO composite (b), bulk LCO (c) and mesoporous silica after a repeated catalytic run (d).^[9,119]

Nair *et al.*^[120] investigated the impact of the BET surface area of LaMnO_3 for the total oxidation of methanol. By means of the nanocasting technique, the reactive grinding process and the citrate method, solids with specific surface areas of 155, 40 and $15 \text{ m}^2\text{g}^{-1}$ were obtained, respectively. The catalytic activity corresponded

very well to the accessible surface area. Full conversion of methanol was achieved at 150 °C in the case of highly porous LaMnO₃. The employment of LaMnO₃ obtained via reactive grinding and in a citrate process resulted in full conversion at 185 °C and 220 °C, respectively.

Similar surface area-dependencies were also reported by de Lima and co-workers for the reduction of NO to N₂ in the presence of CO utilizing nanocast LaFeO₃ with increased specific surface area as catalyst.^[121] The improved performance of the nanocast materials display the benefits of an increased surface-to volume ratio, hence, demonstrating once more the impact of nanostructuring with respect to material properties.

5.2.3. Silica

As the transition is made from mixed metal oxides to a single metal oxide, crystalline aspects can be neglected due to the amorphous nature of silica. In general, silica is obtained through a sol-gel process, which starts from molecular precursors, usually in the form of silicon alkoxides (e.g. tetraethyl orthosilicate (TEOS)). The sol-gel process consists of several steps that are controlled by hydrolysis and condensation of the reactants. First, a stable suspension of colloidal solid particles in a liquid, a sol, is formed (Figure 5.11). Progressive polycondensation reactions of the particles lead to gelation during which a network is generated. The sol-gel transition is then followed by aging. Further condensation reactions of neighbouring silanol groups and mass transfer from thermodynamically unfavourable to favourable regions can occur during aging. This step is often accompanied by expulsion of pore liquid and the spontaneous shrinkage of the gel (syneresis). Finally, the remaining liquid is removed from the gel. Conventional drying of the gel often leads to a collapse of the network originating a densified *xerogel*. Upon supercritical drying, the network structure is maintained and an *aerogel* is obtained.^[67,122–124]

5. Scientific Background

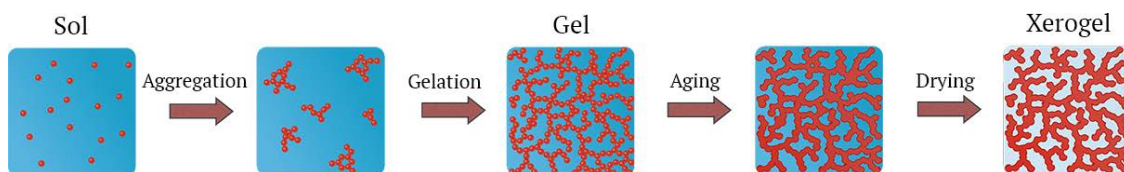


Figure 5.11.: Schematic illustration of the sol-gel process. Supercritical instead of conventional drying results in an aerogel instead of a xerogel. Adapted from Schubert *et al.*^[122,125]

The sol-gel approach offers a facile method of preparing hybrid materials, which enables the combination of beneficial properties from inorganic and organic compounds. Substitution of an alkoxy group of the precursors for an organic group that is covalently attached through a Si-C bond leads to the creation of networks containing both functionalities. The inorganic silica framework provides chemical resistance and thermal stability to the network. The organic functional groups provides versatile functional sites.^[126] Substituted alkoxides are also used for the formation of various cage-like polyhedral oligomeric silsesquioxanes (POSS)^[127–129] and ladder-like polysilsesquioxanes (LLPSSO).^[130–133] The characteristic structures are displayed in Figure 5.12. Photocurable moieties as organic functionality, e.g. methacryl groups, enable the integration of polysilsesquioxanes into an acrylate polymer. Simultaneous UV curing of acrylate monomers and methacrylate-functionalized polysilsesquioxanes results in the formation of a nanocomposite.^[130] Variation of length, rigidity, geometry of substitution and functionality of the organic side group can impact the bulk properties of the material significantly, e.g. flexibility, hydrophobicity, diffusion, stability, and make for new and improved functional materials.^[122,134,135]

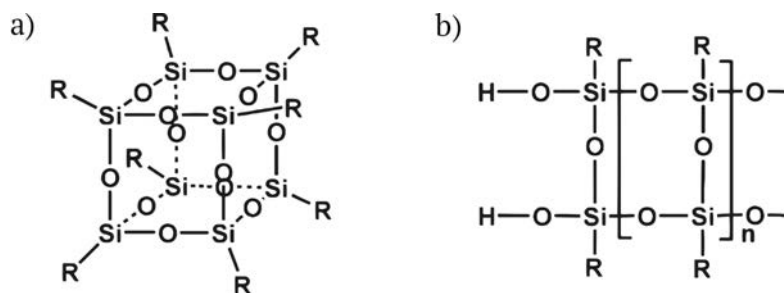


Figure 5.12.: Characteristic silsesquioxane structures of POSS (a) and LLPSSO (b). R refers to organic functionality.^[130]

Nanoporous silica is prepared by an endotemplating technique. The resulting materials display well-ordered pores of unanimous size and high specific surface areas. Depending on the syntheses conditions, different porous systems can be obtained. Some relevant representatives of ordered mesoporous silica include SBA-15, KIT-6 and FDU-12.^[136]

SBA-15 was first reported by Stucky *et al.*^[137,138] and has a two-dimensional channel-like pore system. The cylindrical pores are hexagonally-packed exhibiting $p6mm$ symmetry (Figure 5.13a). Pore sizes between 4.6 and 30 nm can be readily obtained. Additional micropores, which connect the main channels, can be observed. KIT-6 was introduced by Ryoo and co-workers.^[139] It is composed of a three-dimensional cubic pore system in the $Ia\bar{3}d$ space group. The pore system can be described by a pair of interpenetrating bicontinuous networks of channels (Figure 5.13b). Similar to SBA-15, the channels are connected through micropores. The pore size can be controlled, varying from 4 to 12 nm.

FDU-12 was developed by Zhao *et al.*^[140] and displays a pure face-centered cubic mesophase with $Fm\bar{3}m$ symmetry. The materials present a cage-like pore structure. Large pore cavities are connected by pore entries of smaller size, which are referred to as windows (Figure 5.13c). Pore sizes can be tuned in a range from 12 to 60 nm. The window sizes can be accordingly adjusted from 4 to 35 nm.

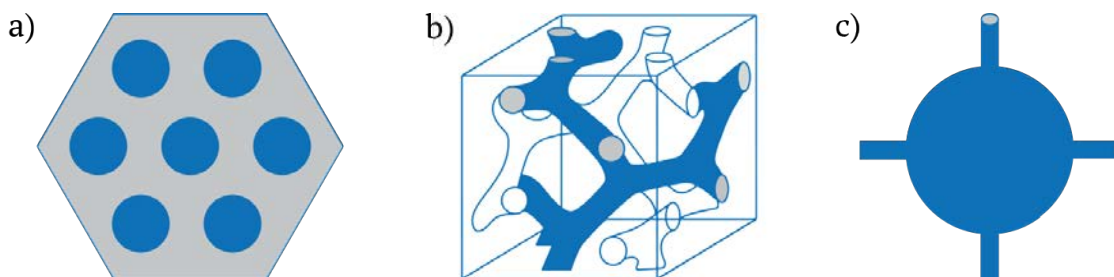


Figure 5.13.: Schematic illustration of the pore system of SBA-15 (a),^[136] KIT-6 (b),^[136] and FDU-12 (c),^[140] respectively.

In addition, mesoporous silica is widely used as a hard template for the fabrication of other porous materials (e.g. porous carbon). It can be utilized as an exotemplate for a nanocasting procedure. Thus, it plays a crucial part in the development of several nanoporous materials.^[136] The synthesis details of different templating methods will be described in the section 'Design of Nanostructured Oxide and Carbon Materials'.

5.2.4. Mesoporous Silica as Support for Perovskite Oxides

Before addressing the role of mesoporous silica as support, some aspects regarding the guest species (perovskite oxides) need to be reiterated. As mentioned before, nanoparticles or nanocrystals of perovskite oxides are beneficial for applications such as catalysis. They exhibit an increased surface-to-volume ratio compared to bulk materials and accordingly show improved catalytic activity. However, high calcination temperatures promote the growth of perovskite oxide particles.^[141,142] One approach to limit the growth relies on the use of porous hosts such as ordered mesoporous silica as support. Particles or clusters can form inside of the pores. The confines of the pore space, in turn, limit the growth of perovskite oxide particles and impede agglomeration of these particles during thermal treatment. Particle sizes that correspond to the sizes of the pores can be obtained. Accordingly, these small

crystallites exhibit high specific surface areas for enhanced catalytic activity.^[143–145] Yi *et al.*^[146] prepared LaCoO_3 by conventional citrate-method inside the pores of silica SBA-15 and compared it to bulk LCO. Exploiting the confinement effects of the pore constraints, highly crystalline LCO particles ranging from 5 to 8.5 nm were obtained within the host matrix. The bulk material constituted crystallites of 15.6 nm. As a consequence, the smaller LCO particles exhibited enhanced specific surface areas. Moreover, the functional properties of the materials were assessed according to their catalytic performance in the complete oxidation of methane. The normalized activity (with respect to the specific surface area) of bulk LCO was reported to be superior to the activity of supported LCO. Thus, the lower activity of the supported perovskite oxide material can be ascribed to differences in the structure or composition.

Nguyen and co-workers^[147] investigated the role of LaCoO_3 inside of a mesoporous silica host with regard to the catalytic oxidation of methane. While they could demonstrate an improved catalytic performance of the LCO/SiO_2 composite compared to bulk LCO, a perovskite oxide phase was only formed if the precursor loading in the silica host exceeded 30 wt%. Additional perovskite oxides crystallites formed on the exterior of the silica matrix.

Accordingly, confinement effects need to be considered with regard to this approach. Conversion and crystallization of the perovskite oxide precursors proceed differently in nanosized confined spaces compared to bulk processes. Complete understanding of the processes at the nanoscale is required to fully exploit this promising approach. Mesoporous silica represents a very suitable material for the investigation of confinement effects. It is well-investigated and the pore properties can be easily and precisely tuned through an endotemplating method. Accordingly, pore size, pore curvature and symmetry, surface modification and pore accessibility can be controlled.^[143,148] Thus, it makes them ideal model systems for the investigation of nanoconfinement effects.

5.2.5. Carbon

Before introducing nanostructured carbon materials, some general information about carbon will be provided since carbon exhibits specific properties which are also essential for certain applications of nanostructured carbon.

Carbon is considered a remarkable element due to its variety of allotropic crystal modifications. In diamond, each carbon atom is tetrahedrally surrounded by four different carbon atoms, connected by overlap of sp^3 hybrid orbitals. The high binding energy of the C-C bond renders it the hardest naturally occurring substance. Due to the absence of π -bonds, diamond crystals exhibit excellent electronic insulation.^[149,150]

Another modification constitutes graphite, which is characterized by a layer structure. Sp^2 hybridized carbon atoms form σ -bonds to three neighbouring carbon atoms in a plane (Figure 5.14a). The excess valence electrons are delocalized inside of π -orbitals and can move freely throughout the plane. Accordingly, graphite exhibits significant conductivity parallel to the sheets.^[149]

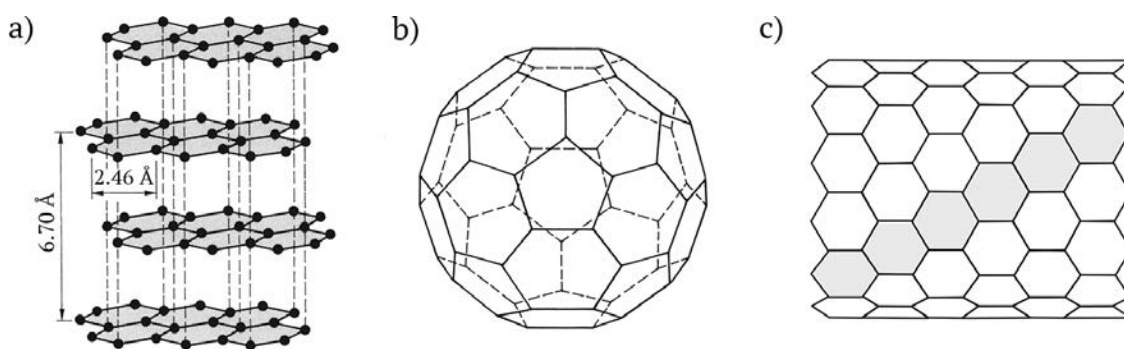


Figure 5.14.: Display of selective carbon allotropes: crystal structure of α -graphite (a), C_{60} molecule of a Buckminster fullerene (b), and zig-zag configuration of a carbon nanotube (c).^[150]

A single layer of graphite is referred to as graphene. The graphene sheets are

held together by weak van der Waals forces and π -interactions. Thus, graphite can be easily split or shifted parallel to the plane.^[149,150]

Other allotropes comprise fullerenes (Figure 5.14b) and nanotubes (Figure 5.14c), both of which are derived from a distorted graphite structure. Fullerenes present spherical cage-like molecules consisting of condensed C_5 and C_6 rings. In contrast to graphite, π -electrons are localized and therefore, fullerenes are less thermodynamically stable.^[149,150] Carbon nanotubes can be considered rolled up graphene sheets. Due to nanosize effects, they display special properties, e.g. high mechanical stability^[150] and enhanced electronic conductivity.^[151]

Aside from allotropic modifications of carbon, various graphite materials can be prepared from a wide range of carbon-containing precursors (e.g. hard woods, fruit stones, coals, phenolic resins). Graphite materials refer to substances that are at least partially composed of graphite such as synthetic graphite, pyrolytic graphite, and activated carbon.^[150,152]

The nature of the starting material plays a crucial role with regard to the development of the graphite structure. According to Franklin,^[153] those starting materials can be divided into graphitizing carbons and non-graphitizing carbons (also denoted as chars). Graphitizing carbon can be fully converted to graphite through pyrolysis at temperatures above 2000 °C. In contrast, complete graphitization is not possible in the case of non-graphitizing carbon, even at high temperatures. During pyrolysis of graphitizing carbons, planar cross-links are formed between graphite stacks of 2 to 4 graphite-like layers (Figure 5.15a). This pre-arrangement of the carbon structure facilitates the conversion of graphitizing carbon into the characteristic graphite layer structure at elevated temperatures. The formation of a dense graphite structure impedes the formation of pores.^[153–155]

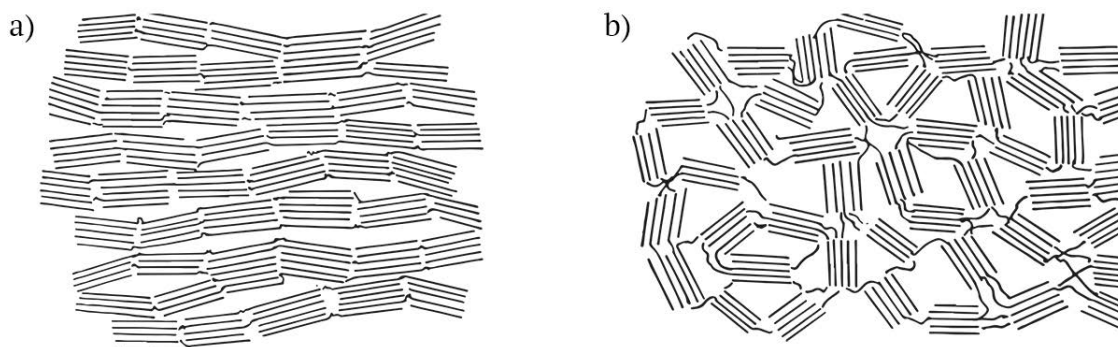


Figure 5.15.: Schematic illustration of the structure of graphitizing carbon (a) and non-graphitizing carbon (b).^[153]

With respect to non-graphitizing carbon, high oxygen content is exhibited in the starting materials. The increased presence of oxygen is assumed to promote curvature in the carbon structure, which leads to the formation of distorted graphene sheets during pyrolysis. These distorted graphene sheets form thermally stable cross-links between randomly oriented graphite-like domains as displayed in Figure 5.15b. Thus, the cross-links prevent a long-range ordering. The distances between the domains directly translate to the presence of micropores.^[150,152-154]

The nanostructure and correspondingly the properties of the final material (e.g. electric conductivity, hardness, microporosity) are strongly affected by the carbonization temperature. McDonald-Wharry and co-workers^[154] reported a temperature-dependence for the development of the carbon structure (Figure 5.16). At carbonization temperatures below 500 °C, the majority of the mass is composed of amorphous carbon. Accordingly, the material exhibits poor electric conductivity. At increased temperatures, the amorphous carbon is gradually converted into graphitic carbon. Depending on the oxygen-content, randomly oriented domains of regular and distorted graphene are formed and cross-linked. At high temperature treatment, the graphitic character is further emphasized. Accordingly, the products display a more pronounced nanostructure and strongly enhanced conductivity.^[156]

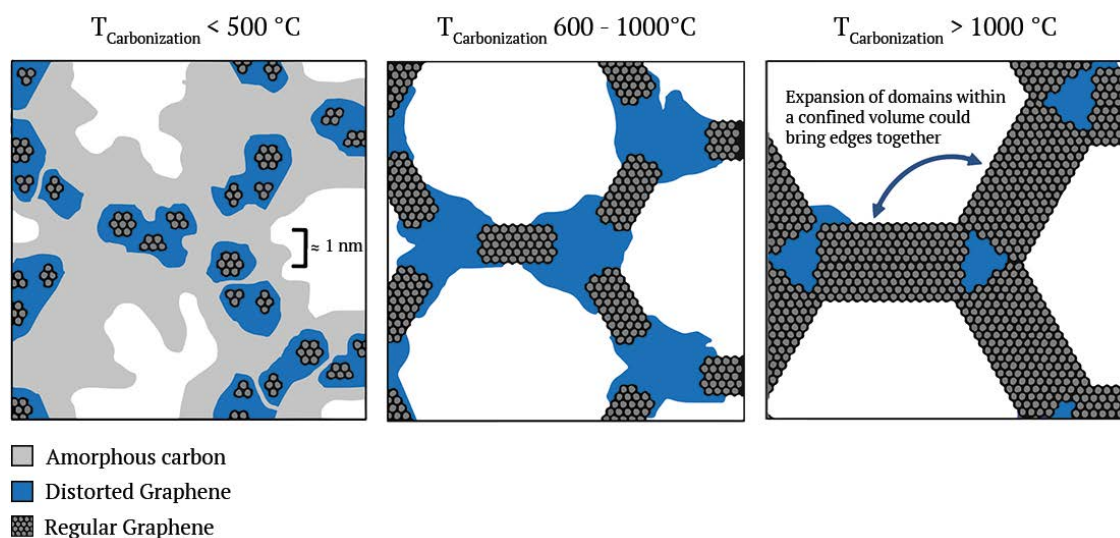


Figure 5.16.: Schematic illustration of the nanostructure of non-graphitizing carbon at different carbonization temperatures.^[154]

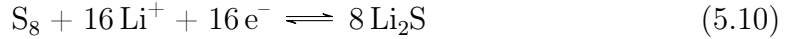
Porous carbon materials possess electric and thermal conductivity, chemical stability, low density, high storage capacity, and are widely available. Thus, they combine attributes of allotropic carbons and benefits of nanostructural properties, which makes them attractive for many advanced electrochemical applications.^[26,157,158] In many applications, the porous carbon usually acts as host for an active material, e.g. sulfur. Ordered, nanoporous carbons like CMK-8 present ideal model systems for the understanding of the processes taking place in such host-guest systems. They are usually prepared by a template-assisted synthesis method, which is emphasized in the section 'Design of Nanostructured Oxide and Carbon Materials'. The resulting carbons comprise both micro- and mesopores, which enables the simultaneous investigation of different pore ranges. Moreover, they exhibit extremely high specific surface areas and pore volumes compared to other mesoporous materials such as silica.^[26,157]

The role of these nanoporous carbons in the investigation of electrochemical processes is described in the following paragraph.

5.2.6. Nanoporous Carbon as Li-S Battery Cathode Material

Applications for nanoporous carbons include electrode materials for batteries,^[11,159] fuel cells^[160,161] and supercapacitors,^[162,163] sorbent for gas storage^[164,165] and separation processes^[166,167] and catalyst support.^[168,169] Due to its relevance to this work, the focus will be the use of nanoporous carbon as cathode materials for Li-S batteries.

The Li-S cell relies on a simple principle, introduced by Herbert and Ulam in 1962.^[170] The anode is made of Li metal, while sulfur is used at the cathode site. On discharge, dissolved lithium ions are transported through an electrolyte to the cathode, where sulfur is gradually reduced to form various polysulfides (Figure 5.17). The reversible redox reaction is described as follows:



Considering the high theoretical values for specific capacity (1675 mAh/g) and energy density (ca. 2600 Wh/kg) in addition to low cost, abundant resources and high safety, Li-S batteries deem superior options for energy storage compared to Li-ion technology.^[11,171,172] However, some major challenges prevent the Li-S cells from reaching their full potential. One of the main issues is the capacity fading due to the polysulfide shuttle. During charge and discharge processes, soluble long-chain polysulfide intermediates Li_2S_n ($3 \leq n \leq 6$) are formed and migrate to the lithium anode to be further reduced. There, either insoluble Li_2S and Li_2S_2 are formed and deposit on the anode or the intermediates are transported back to the cathode followed by reoxidation and repeated diffusion to the anode. This shuttle effect therefore leads to a progressive loss of active mass and reduces the coulombic efficiency in the charging process. Another drawback is the insulating character of sulfur and its solid discharge products. As a consequence, poor electrical connectivity within the sulfur cathode is observed resulting in an inefficient use of active material.^[11,23,160,172]

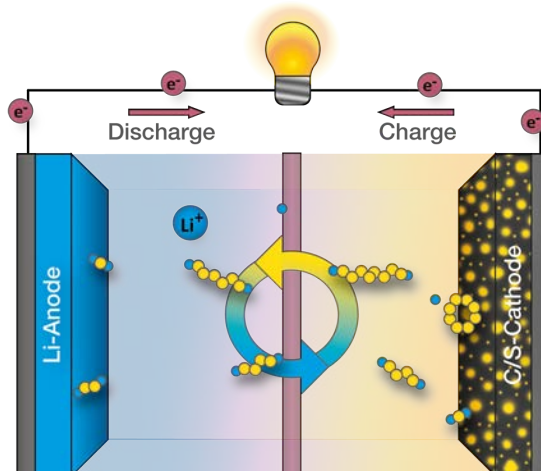


Figure 5.17.: Schematic illustration of the Li-S cell and the polysulfide shuttle.

One approach to remedy the aforementioned issues is the design of a composite cathode consisting of ordered nanoporous carbon filled with sulfur. The carbonaceous nature provides electronic conductivity, the high specific pore volume accommodates high sulfur loading and the narrow pore sizes are intended for entrapment of sulfur and its polysulfide intermediates to prevent loss of active material.^[11,171,172] Nazar *et al.*^[159] first employed CMK-3/sulfur composites as cathode material resulting in reversible capacities up to 1320 mAh/g. The ordered nanoporous carbon materials are usually obtained through exotemplating of 3DOM silica. CMK-3 is a negative replica of SBA-15, whereas KIT-6 is used as scaffold in the synthesis of CMK-8. The combination of both meso- and microporosity benefits high sulfur loadings and allows for sufficient space for lithium ion diffusion (mesopores), while polysulfides are confined within the micropore space.^[173]

However, considerable loss of active material is still observed and, by modification of the carbon host, the shuttle effect could only be limited. Thus, further research is required to improve understanding of the processes in Li-S batteries, also with regard to the interactions between the electrolyte and sulfur.^[159,171,174]

5.3. Design of Nanostructured Oxide and Carbon Materials

In the first section, several nanostructure phenomena were introduced, whereas the second section comprises different nanostructured materials and their applications. In this paragraph, different methods will be presented to design these nanostructured materials. Considering the importance of nanoporous materials for a wide array of applications (Section 5.2), various preparation techniques have been established or are being modified to improve the material properties.^[20,175]

5.3.1. Design of Nanocrystalline Oxide Materials

In the context of this work, nanocrystalline materials refer to perovskite oxides. Accordingly, this paragraph outlines methods and design principles to prepare nanocrystalline perovskite oxides.

Conventional synthesis methods (i.e. solid-state synthesis) for perovskite oxides require high reaction temperatures exceeding 1000 °C to ensure high diffusion rates between solid precursors. Insufficient diffusion originates an inhomogeneous product phase and the presence of undesirable phases in the final material. However, high reaction temperatures increase grain growth of the crystallites. According to the principles of crystallization (5.1.2), a more thermodynamically stable form is preferred at elevated temperatures. This is achieved by reducing the interface energy, i.e. decreasing the radius of curvature of the grain boundaries by increasing the size of the grain. Thus, the contribution of unfavourable surface free energy is minimized and the contribution of stabilizing volume free energy is raised.^[20,55,176] As stated in Section 5.1.3, however, an increased grain size is detrimental to the functional properties of a perovskite oxide. Correspondingly, a suitable approach for the synthesis of nanocrystalline solids at low reaction temperatures is required.

Polymer Complex Route

Soft chemistry methods like liquid phase syntheses fulfil the requirement of low reaction temperatures. Due to homogeneous mixing of the reactants at the atomic level, products with high purity and nanocrystalline structure can be obtained at low temperatures. Several authors correspondingly reported the formation of single phase perovskite oxide structures as low as 500 to 600 °C.^[177–180]

A very prominent representative of this synthesis type is the Pechini method,^[181] in which soluble precursors are added to a mixture of a carboxylic acid such as citric acid, and a polyol, e.g. ethylene glycol. The citric acid acts both as monomer and chelating agent to form complexes with the metal cations, giving this reaction type the name 'polymer complex route'. Polyesterification of the citric acid and the polyol, which acts as solvent and as bridging agent in the polymerization, results in the formation of an organic-inorganic gel (Figure 5.18). The fixation of the homogeneously distributed cations within a polymeric matrix ensures short diffusion pathways and prevents phase separation during the subsequent heat treatment.

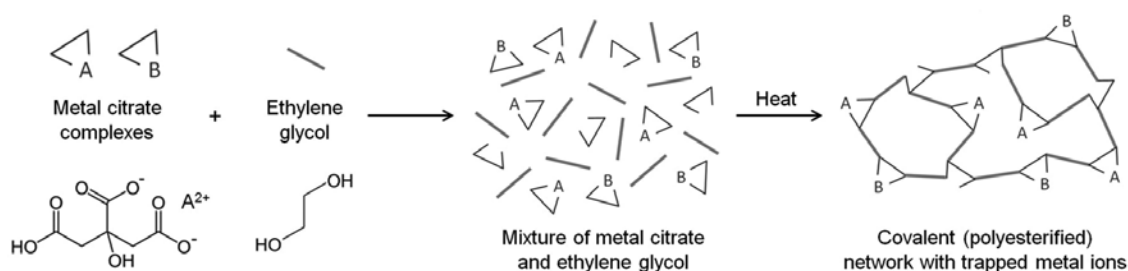


Figure 5.18.: Schematic illustration of the processes of the Pechini method.^[72]

In the final combustion step, the organic content is decomposed at elevated temperatures. As the organic compounds are thereby removed, the metal precursors transition into crystalline intermediates - carbonates are favored for A-site cations while B-site cations usually form a spinel structure as reported by Caro *et al.*^[182] Upon further heating of the mixture, a solid state reaction at the nanoscopic scale

takes place resulting in the degradation of carbonates and formation of the desired perovskite oxide material.^[67,72,183–185]

Based on this reaction principle, various modifications of the synthesis have been developed, e.g. substitution of citric acid with other mono- and di-carboxylic acids,^[186–188] addition of additives to optimize the complexing behaviour between cations and chelating agent,^[189–191] water^[184] or ethanol^[73] as a replacement for the polyol. Taguchi *et al.*^[192] presented a variation of the polymer-complex route for the preparation of LaMnO_3 , in which poly(acrylic acid) was used as complexing agent instead of citric acid. Additionally, the polymer was prepared before adding it to an aqueous metal precursor solution.

Modifications of the synthesis conditions and processes directly translate to the textural properties of the resulting product. Therefore, synthesis can become a tool to tailor the functional properties of perovskite oxides.

Taguchi *et al.*^[106] also investigated the relationship between amount of citric acid, calcination temperature and resulting nanostructure of LaCoO_3 . The amount of citric acid was varied in the range of 4 - 12 mmol. The samples were exposed to calcination temperatures between 400 and 700 °C. As displayed in Figure 5.19a, a single perovskite phase was obtained as low as 600 °C by using 5 to 11 mmol of citric acid. A citric acid content between 6 and 8 mmol also promoted crystallization at 500 °C. However, the presence of intermediate phases (La_2O_3 , Co_3O_4) was observed.

Despite variation of the amount of citric acid, similar grain sizes of approximately 12.5 nm were obtained at 600 °C. In contrast, variation of the calcination temperature constituted significant changes to the crystallite sizes. Increase of the temperatures lead to a gradual increase of the grain sizes up to 21.0 nm at 900 °C. A corresponding assessment of the functional properties by means of catalytic activity showed an enhanced conversion of CO for LaCoO_3 calcined at 600 °C.

With respect to the use of polymeric precursors such as citric acid, high organic content in the initial reaction mixture promotes the formation of carbonate phases during thermal conversion to oxides. In these cases, prolonged calcination times

at elevated temperatures or an additional acetic acid treatment are necessary to remove or reduce the presence of carbonates.^[193] The presence of these impurities in the final material can become problematic when considering (electro)catalytic applications since carrier transport in the material and oxygen exchange on the surface are hindered.^[194–197] However, the treatment can be detrimental to the functional properties of the material, i.e. grain growth due to extended high temperature treatments or alteration of the crystallinity of the perovskite oxide due to chemical instability.^[21,198] Therefore, minimal addition of organic contents limits the introduction of impurities.

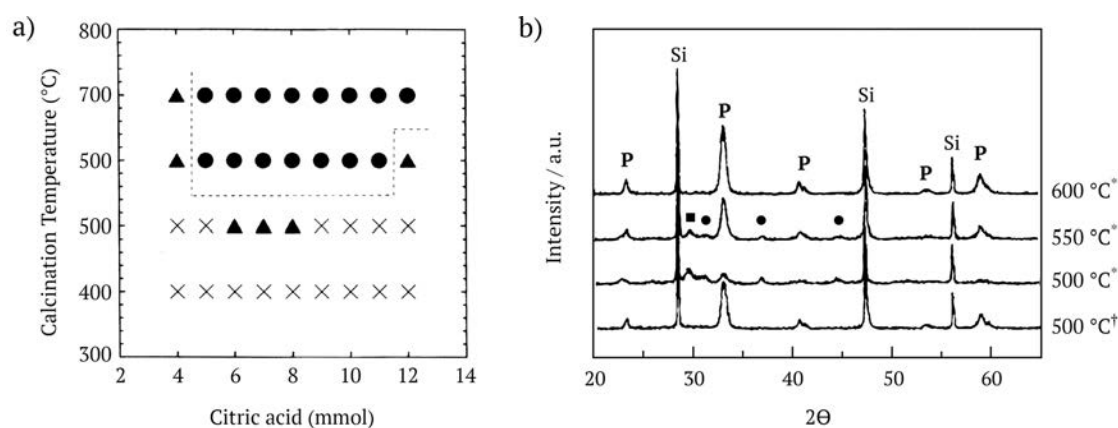


Figure 5.19.: (a) Relationship between the the crystal structure of LaCoO₃ and synthetic conditions (amount of citric acid and calcination temperature). ● refers to the formation of a single perovskite oxide phase; ▲ represents a mixture of LaCoO₃, La₂O₃, and Co₃O₄; × constitutes an amorphous product.^[106] (b) XRD patterns of LaCoO₃ calcined at 500, 550, and 600 °C, respectively. † refers to the product prepared by spray-freezing/freeze-drying, * refers to the product prepared by evaporation drying. Reflections denoted as P can be ascribed to the perovskite oxide structure; ■ refers to La₂O₃; ● represent Co₃O₄ phases; Si was used as a standard. Adapted from Lee *et al.*^[177]

While Taguchi and co-workers emphasized the effect of reactant compositions

and calcination temperatures, Lee *et al.*^[108,177] rather focussed on the processing of the reactant mixture. They were able to demonstrate the impact of the precursor-drying procedure on the (nano)structural formation of LaCoO₃. The synthesis approach was based on a citrate method and included either an evaporation-drying or a spray-freeze/freeze-drying step before calcination. The drying step strongly influenced the crystallization process. After spray-freeze/freeze-drying, a single perovskite phase was obtained as low as 500 °C. In contrast, evaporation-drying and subsequent calcination originated a pure LaCoO₃ phase only at 600 °C (Figure 5.19b). Accordingly, the solid calcined at 500 °C exhibited a higher degree of nanostructuring. Crystallite sizes of approximately 20 nm were obtained after spray-freeze/freeze-drying and calcination at 500 °C compared to grain sizes close to 100 nm after evaporation-drying and thermal treatment at 600 °C. The improved nanocrystalline properties of LaCoO₃ calcined at lower temperatures corresponded to an enhanced catalytic activity for the oxidation reaction of CO. Thus, functional properties were successfully increased.

5.3.2. Design of Nanoporous Oxide and Carbon Materials

As opposed to the synthesis of nanocrystallite materials, this section deals with the design of nanoporous perovskite oxide, silica, and carbon materials. Introduction of porosity and correspondingly, a high specific surface area, can be realized in many different ways (e.g. nonaqueous solvothermal synthesis route,^[75] self-propagating high-temperature synthesis,^[35] flame-spray pyrolysis^[199]) but often depends on the type of material. One approach to prepare porous solids is a template-assisted synthesis procedure. The template acts as a space holder during the formation of the surrounding phase. After removal of the template, the desired porous product is obtained. This enables the preparation of materials with specific structural properties.^[200,201]

Two templating methods can be distinguished: endo- and exotemplating. Endotemplating refers to the inclusion of (supra)molecular structures in the growing solid.

This method is mostly used for the synthesis of ordered mesoporous silica,^[17,202,203] various other metal oxides^[204–206] and zeolites.^[207,208] An exotemplate, in turn, presents a porous entity whose pore space is filled with target precursors. Upon conversion of the precursors into the desired material and removal of the template, a replica of the exotemplate is obtained. Ordered mesoporous carbons^[22,209–211] and mesoporous metal oxides^[212–215] are obtained via this method.^[30,200,216] Additionally, templates can also be characterized according to their chemical nature as *hard-* or *soft-templates*.^[216]

Nanoporous Silica

Nanoporous silica materials are primarily obtained through an endotemplating approach by using soft templates. Soft endotemplates comprise self-assembled agglomerates of surfactants such as long-chain alkyltrimethylammonium halides or organic block copolymers like Pluronic P123. In a liquid medium, they form ordered, mesoscaled structures, i.e. micelles, and function as structure-directing agents (SDA) for the inorganic phase.^[217] This method was first presented in 1992, when researchers from Mobil Oil Corporation developed MCM-41,^[202] a mesoporous silica material formed with the assistance of surfactant molecules.

In most conditions, the reaction mechanism follows a cooperative assembly, i.e. micellar surfactant structures and the inorganic phase form simultaneously resulting in the final composite. However, if the surfactant concentration of the medium surpasses the critical micelle concentration (CMC) prior to the addition of the silica precursor species, liquid crystals can develop (Figure 5.20).^[200]

Interactions (hydrogen or electrostatic bonds) between the organic and inorganic part are necessary to avoid macroscale phase separation. In addition, those forces facilitate the condensation of the silicon precursors around the SDA. Alkoxysilanes with the ability to undergo polycondensation reactions, such as TEOS, are usually employed as precursors.

Once a stable macromolecular network is formed around the micelles, the incorpo-

5. Scientific Background

rated SDA is removed by means of extraction or heat treatment. As a result, a porous material is obtained.^[217,218]

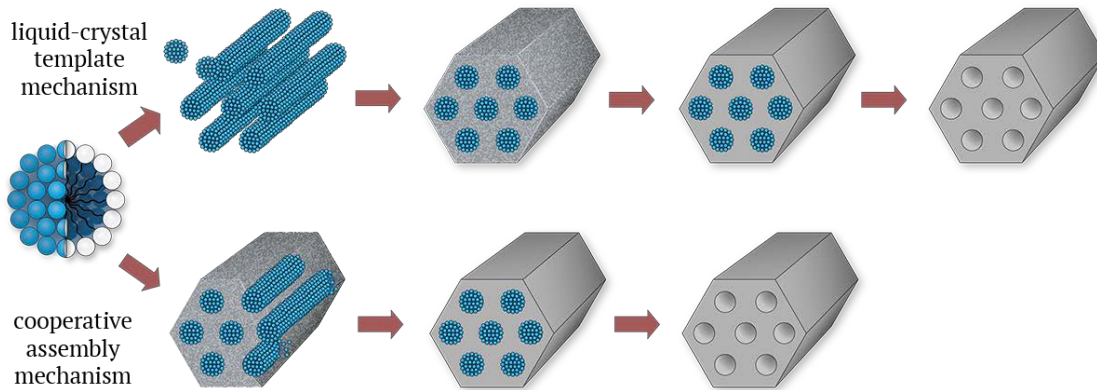


Figure 5.20.: Schematic illustration of the liquid-crystal template mechanism and the cooperative assembly mechanism.

The employment of soft matter as endotemplates gives precise control over the size of the pores while a narrow pore-size distribution is maintained. Pore sizes between 20 and 300 Å can be easily obtained. Additionally, the pore shape and symmetry can be adjusted according to the hydrophobic domains in the lyotropic phase resulting in lamellar, hexagonal or cubic structures. Both pore parameters, size and shape, depend on the concentration and properties of the SDA, the length of the hydrophobic chain/polymer blocks, the potential presence of cosurfactants, the temperature, and the pH value of the solution. This makes the mesostructure formation very sensitive to the applied reaction conditions. Moreover, this method is mostly limited to the synthesis of porous light metal oxides that are formed by means of sol/gel processes, e.g. SiO_2 , TiO_2 and Al_2O_3 .^[203,216,217,219]

Nanoporous Perovskite Oxides

The preparation of nanoporous perovskite oxides is not compatible with a soft-templating approach due to the low thermal stability of SDAs. Decomposition of the organic part often occurs prior to the formation of a stable inorganic phase and is accompanied by loss of structure.^[217–219] So far, only macroporous perovskite oxides could be obtained with the use of PMMA microspheres by Zhao *et al.*^[220] Therefore, an exotemplating approach, also referred to as nanocasting, is often used for the synthesis of nanoporous perovskite oxides. The general procedure can be described as follows: A rigid, porous host matrix, e.g. mesoporous silica, is infiltrated with metal precursors - commonly by wet impregnation methods. After conversion of the precursors into the target material at high temperatures, the exotemplate is removed by alkaline etching. As a result, a negative replica of the porous silica matrix composed of perovskite oxide is obtained (Figure 5.21).

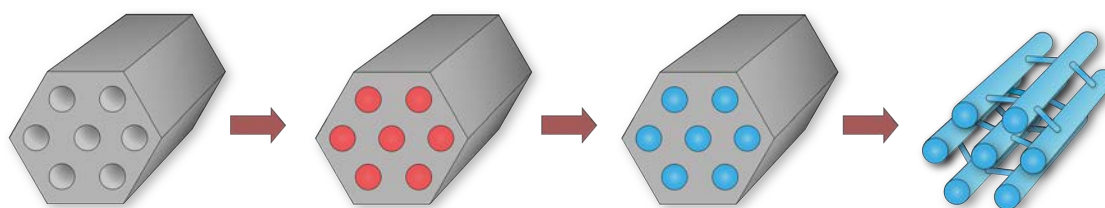


Figure 5.21.: Schematic illustration of the exotemplate approach.

Mesoporous LaFeO_3 with a specific surface area of $83.2 \text{ m}^2\text{g}^{-1}$ was prepared by Zhao *et al.*^[221] by using a SBA-15 silica matrix as a cast. Nair *et al.*^[120] employed KIT-6 as a template resulting in different La-based perovskite oxides with surface areas up to $155 \text{ m}^2\text{g}^{-1}$. However, some issues representative of the general exotemplating approach were shown in their works. The silica templates were only partially replicated. Due to incomplete filling of the porous nanocast, a rather discontinuous or disordered mesoporous solid was obtained.^[221–223] Moreover, considerable amounts up to 10% of siliceous species (e.g. rare-earth silicates) were observed in

the final solid. This poses a problem as these contaminations are detrimental to possible applications in sensing or catalysis.^[120,222,224]

Endotemplating can also be performed by inclusion of hard matter, e.g. silica templates. This can be achieved by cooperative-assembly, as reported by Kayaalp *et al.*^[179] Highly porous SrTiO₃ was prepared by addition of pre-hydrolyzed alkoxy-silane to a mixture of polymerizable chelating agent and metal precursors, subsequent conversion and removal of the siliceous phase. However, the simultaneous formation of both the silica phase and the perovskite oxide phase can lead to the presence of metal silicate phases in the final material.

As an alternative, a pre-existing silica compound can be added as an endotemplate to the initial reaction mixture to produce a nanocomposite. So far in literature, this approach has only been employed for the preparation of soft porous matter. Mesoporous organic polymers were prepared by adding nanosized silica templates to a solution of the respective monomer species.^[225,226] Due to the nature of the polymer-complex route (Section 5.3.1), in which metal cations are incorporated into an organic polymer, this approach is in theory also transferable to the preparation of mesoporous metal oxides.^[227]

Nevertheless, the addition of hard endotemplates to a reaction solution is accompanied by some challenges. Silica particles agglomerate easily, which, in turn, can lead to phase segregation from the forming polymer. Therefore, surface modifications or introduction of functional groups that interact with the emerging polymer are essential to ensure homogeneous distribution of the template. Moreover, the removal of the inorganic template requires harsh conditions due to its chemical stability. This can damage or even destroy the structure of the target material while complete removal of the siliceous species is not always attainable. Silica contaminations often remain in the final product and interfere with catalytic applications.^[227,228] Thus, an ideal synthesis approach to prepare pure, nanoporous perovskite oxide materials with high specific surface areas in a reproducible manner has not yet been reported.

Nanoporous Carbon

In the case of nanoporous carbon, the different pore regions (i.e. micro- and mesopores) can be adjusted separately.

With regard to microporosity, the carbonization temperature and the nature of the precursors determine the nanostructure of the carbon material as displayed in Section 5.2.5. However, the pore properties can be additionally tailored by activation of the carbon. Carbon activation can be best described as a process to widen existing pores and adding considerable amounts of new micropores, while also modifying the carbon surface. The activation can be initiated by removal of carbon atoms by exposure to gases (O_2 , CO_2). Alternatively, activating agents (e.g. KOH, zinc chloride, phosphoric acid) can be added to the starting mixture to prevent sintering of carbon during the carbonization.^[150,229,230]

Mesoporous carbons with monodisperse pore-size distribution and well-defined pore shape have only been successfully prepared by template-assisted approaches so far. Templates for carbons are classified according to hard or soft matter. Development of both areas has benefited from progress made in the template-based synthesis of ordered mesoporous silica (Section 5.3.2). While the general approach of endo- and exotemplating is equally applicable to carbon, some characteristics of those methods specific to carbon material will be introduced.^[26,209]

The use of soft templates for porous carbons proves to be slightly more limited compared to silica materials. Common alkyl-chain-based soft templates such as CTAB are not suited for the preparation of porous carbon as charcoal residue stemming from pyrolysis of the alkyl chain fills the space designated for the mesopores.^[26,231] A more favourable soft-templating approach relies on the employment of selected block copolymers, i.e. PS-P4VP, P123, F127. Self-assembly of the carbon precursors and formation of a mesophase requires the presence of hydrogen bonding between precursors and templates. Appropriate precursor compounds are phenolic resin monomers such as phenol and resorcinol that are converted into a respective precursor by polymerization with formaldehyde. The pore morphology of the final

5. Scientific Background

carbon material can be controlled through the volume ratio of hydrophilic to hydrophobic block of the triblock copolymer, the mixing ratio of carbon precursor to surfactant and by the carbonization conditions.^[26,230]

A different approach relies on the use of hard templates, usually ordered mesoporous silica, as a mold for carbon. Ryoo *et al.*^[232] were the first to employ MCM-48 silica hard templates to obtain ordered mesoporous carbon in a nanocasting procedure. Repeated impregnation with sucrose combined with sulfuric acid, followed by carbonization under vacuum and finalized by NaOH treatment resulted in the so-called CMK-1. However, the interpenetrating pore network was difficult to replicate.^[233] The drawbacks of MCM-48 replica lead to focussing on silica templates with different pore systems. SBA-15 was the first structure that could be completely replicated by carbon.^[158] The presence of additional micropores that connected the mesopores enabled the successful production of a hexagonally ordered mesoporous carbon replica, referred to as CMK-3 (Figure 5.22a).

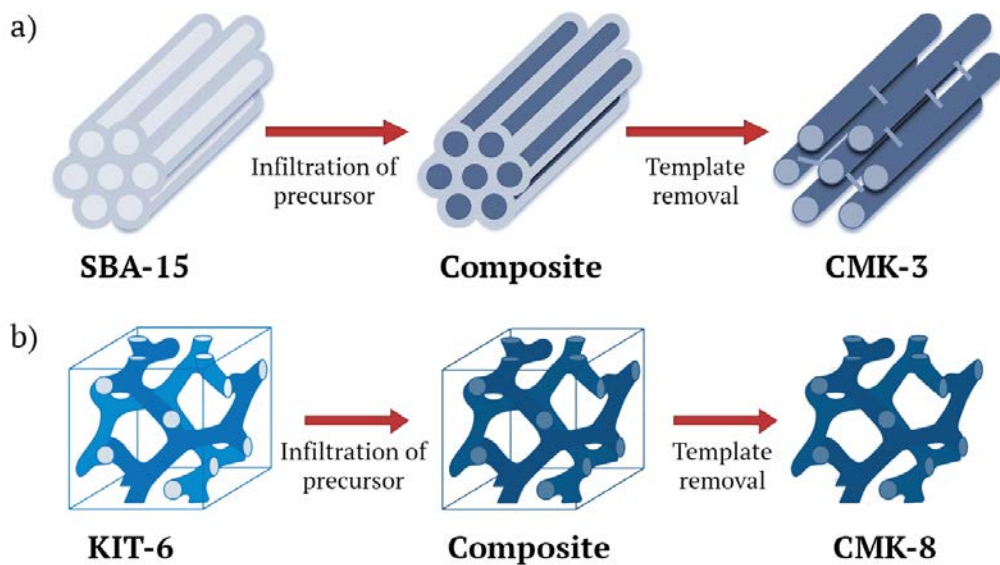


Figure 5.22.: Illustration of the nanocasting technique for the synthesis of CMK-3 (a) and CMK-8 (b) from SBA-15 and KIT-6, respectively.^[234]

Another carbon system, denoted as CMK-8, was similarly prepared by replication of KIT-6.^[139] This carbon structure with cubic Ia3d symmetry demonstrates high accessibility and a highly connected open porous network (Figure 5.22b). By tailoring of the pore characteristics of the silica template, the carbonaceous pore morphology can be controlled.

Contrary to many other ordered mesoporous solids, ordered mesoporous carbons prepared by a templating approach contain considerable amounts of micropores due to the carbonization of non-graphitizing carbon precursors, e.g. sucrose, sugar, furfuryl alcohol. Therefore, they exhibit extremely high specific surface areas and pore volumes compared to other mesoporous materials (e.g. silica), which makes them attractive for advanced electrochemical applications.^[26,157]

5.4. Characterization of Nanostructured Carbon Materials by means of Small-Angle Scattering

The detailed assessment of processes at the nanoscale requires potent characterization methods. Nitrogen physisorption is limited to the investigation of accessible pore space, whereas TEM only provides information regarding a limited sample area and relies on a potentially detrimental sample preparation and high vacuum, excluding samples containing most solvents.^[67]

A suitable tool for the characterization of nanostructured materials is small-angle scattering (SAS). It provides detailed information on structural features between 1 and 100 nm in a direct and comprehensive manner without compromising the structural and chemical integrity of the sample. Obtainable parameters comprise arrangement, size, and shape of particles or pores. In contrast to many other experimental techniques, SAS provides representative data on a large sample volume and not on a small section thereof.^[235,236] While SAS can be utilized for the investigation of various ordered and disordered materials, this section focusses on the analysis of carbon materials and composites thereof.

SAS refers to both small-angle X-ray scattering (SAXS) and small-angle neutron

scattering (SANS). The principle of SAXS is based on elastic scattering of X-rays at the electron shell. Interactions between X-rays and electrons depend purely on the electron density. In the case of SANS, neutrons are scattered elastically at the nuclei. The scattering intensity of this process depends on the scattering length density, which varies according to the atomic number and isotopes present. Correspondingly, different interaction cross sections are exhibited, which enables complementary use of SAXS and SANS techniques.^[28,235,237,238]

The scattering process in both cases is characterized by a reciprocity law. Thus, an inverse relationship between particle size and scattering angle is given. The scattering vector, q , is defined as

$$q = \frac{2\pi}{d} = \frac{4\pi}{\lambda} \sin(\theta) = [nm^{-1}] \quad (5.11)$$

with the interplanar distance d , the wavelength of the neutrons/electrons λ , and the scattering angle 2θ .^[239]

The structure of a nanomaterial such as 3DOM carbon can be described as a binary system, i.e. two phases with different scattering densities ρ_1 and ρ_2 (Figure 5.23). Both phases display a sharp distinction in scattering density at the interface, while the average scattering density of each phase is assumed to be constant. Within the context of a mesoporous carbon material, pores can be considered particles, which exhibit zero scattering density, embedded in a carbon matrix. The scattering intensity of this two-phase system, $I(q)$, is proportional to the square of the scattering density difference between both phases:^[236,237]

$$I(q) \propto (\rho_1 - \rho_2)^2 \quad (5.12)$$

Accordingly, an increased scattering density difference, i.e. higher contrast, originates enhanced intensity.

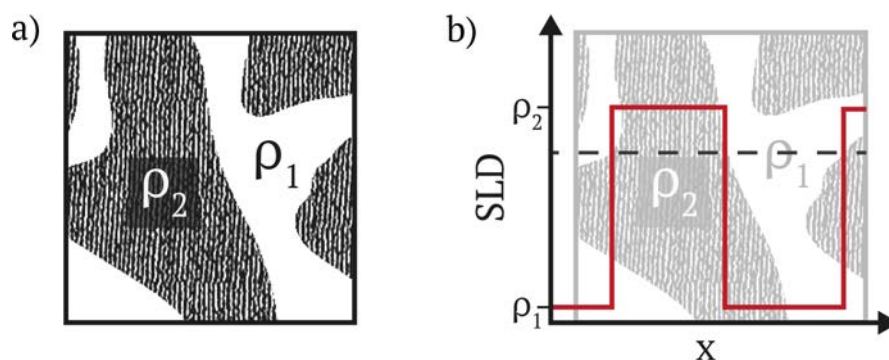


Figure 5.23.: (a) Schematic illustration of a binary system exhibiting high contrast in density. (b) Scattering density along the cross-section (dashed black line) through a binary material.^[237,239]

5.4.1. Intrinsic Contrast-Matching

Oftentimes, an ideal binary system is not provided. During the investigation of nanocomposites such as C/S host-guest systems by means of small-angle scattering, for example, three different phases need to be accounted for: the carbon matrix, impregnated sulfur and void pore space.^[25] The assessment of three- and more-phase systems, however, is less accurate since the scattering contribution of each phase cannot be distinguished precisely. Thus, structural parameters for respective phases are difficult to determine.^[237]

In the case of SAXS, the benefits of intrinsic contrast-matching can be exploited. Carbon and sulfur exhibit similar scattering densities. Hence, the contrast between these two phases is matched and they can be considered one single phase. This serves as a useful tool in the characterization of C-S nanocomposites as reported by Ji *et al.*^[159] They were able to demonstrate complete filling of a CMK-3 carbon matrix with sulfur through melt impregnation. Upon filling of the pore space, the characteristic features of CMK-3 in the SAXS pattern disappeared and the overall scattering intensity decreased due to the loss of contrast between the carbon and sulfur phase (Figure 5.24a).

5. Scientific Background

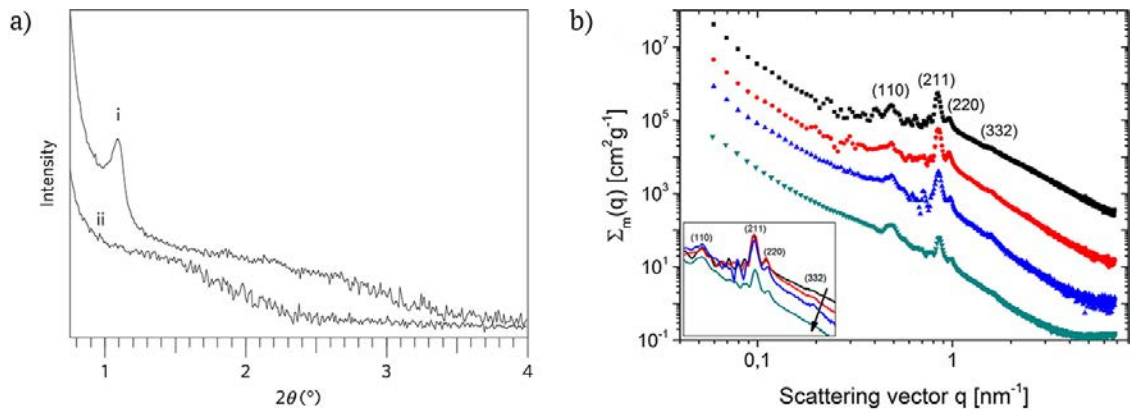


Figure 5.24.: (a) Small-angle XRD patterns of a void CMK-3 (i) and a CMK-3 C-S nanocomposite (ii).^[159] (b) Scattering curves of CMK-8 with 0, 20, 40 and 50 wt% sulfur loading. The data are normalized to the filling density and shifted upwards by a factor of 10 for clarity, except for the data referring to 50 wt% filling. The inset shows the non-shifted data magnified around the Bragg peaks.^[25]

Petzold *et al.*^[25] expanded on this concept by employing SAXS to follow the gradual filling of an ordered nanoporous carbon matrix (CMK-8) with sulfur. Accounting for the intrinsic contrast-matching between carbon and sulfur, a binary system was essentially maintained throughout the whole impregnation process. This enabled the comprehensive assessment of the impregnation behaviour of sulfur with respect to the textural properties (i.e. pore size) of the host matrix. As displayed in Figure 5.24b, at low sulfur loadings, homogeneous filling of the micropores occurs. The mesopores, in turn, are partially filled only at increased sulfur loadings as indicated by the decrease of the Bragg peaks.

5.4.2. Extrinsic Contrast-Matching Technique

The investigation of C-S nanocomposites by means of small-angle neutron scattering is a more challenging task since three phases of varying scattering length density are present. The carbon matrix, which exhibits a high scattering length density (SLD), constitutes the first phase. Sulfur, which is incorporated into nanosized pores within the carbon matrix, represents the second phase, exhibiting a lower SLD. Void pore space presents the third phase, the SLD of which is considered to be virtually zero. A schematic illustration of the cross section, x , of a three-phase material as a function of the SLD is displayed in Figure 5.25a.^[174]

The scattering contribution, $I(q)$, of each phase to the total scattering intensity of the material, $I_{total}(q)$, can be described as follows:

$$I_{total}(q) = I_{pore}(q) + I_{sulfur}(q) \quad (5.13)$$

where $I_{pore}(q)$ represents the scattering at the interface between carbon and void pores, and $I_{sulfur}(q)$ accounts for the scattering contribution of impregnated sulfur. The extrinsic contrast-matching technique presents a solution to the three-phase system. A liquid, which exhibits a scattering density similar to one of the solid phases, is added to fill the void pore space. As a result, the scattering contribution of the void pore space is masked and a quasi two-phase system is obtained (Figure 5.25b).

During SANS measurements, deuterated solvents, e.g. D_2O , d_8 -THF, d_8 -toluene, are commonly used as contrast-matching fluids. H-D substitution results in an increased scattering density that matches the density of carbon.^[27,240] Accordingly, the scattering between carbon and solvent-filled pore space, $I_{pore}(q)$, can be considered non-existent:

$$I_{pore}(q) = 0 \quad (5.14)$$

As a result, the scattering intensity of a contrast-matched C-S nanocomposite can

5. Scientific Background

be described by the following equation:

$$I_{total}(q) = I_{sulfur}(q) \quad (5.15)$$

The presence of a binary system enables a direct measurement of sulfur distribution within the carbon matrix. Thus, precious insights can be obtained regarding the distribution and loading of sulfur and interactions between the host and the guest species.

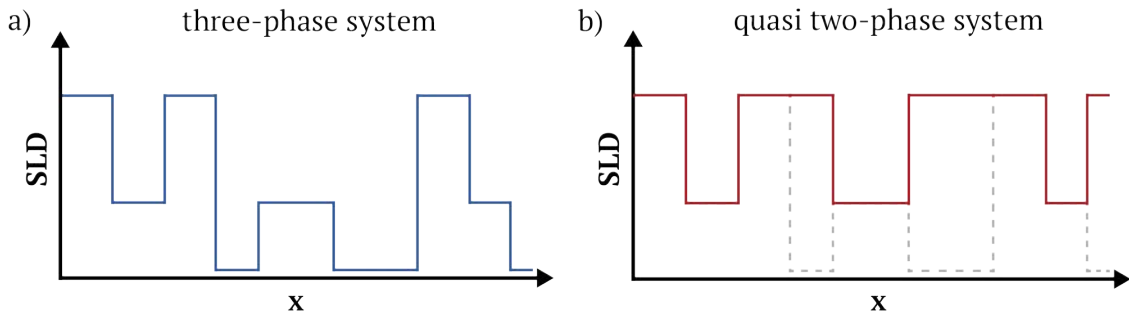


Figure 5.25.: Schematic illustration of the extrinsic contrast-matching technique. A three-phase system (a) is transformed into a quasi two-phase system (b) by filling void pore space with a contrast-matching fluid.

Risse and coworkers^[238] made use of the contrast-matching technique in the context of *operando* SANS characterization of a Li/S battery. A mixture of deuterated THF and deuterated dimethoxyethane was employed as electrolyte. The use of these contrast-matching fluids facilitated a precise analysis of the formation and dissolution process of nanoscopic Li_2S particles on the exterior surface of a microporous carbon matrix. Furthermore, the contrast-matching solvents were used to assess the wettability of the microporous carbon electrode.

The contrast-matching technique can be further utilized to account for the presence of colloidal-sized inhomogeneities within a single phase, i.e. graphitic domains in a

porous carbon material. The structural inhomogeneities (Section 5.2.5) cause fluctuations in scattering length density. Thus, an unwanted scattering contribution is observed during SANS measurements^[28,241]

$$I_{total}(q) = I_{pore}(q) + I_{fluc}(q) \quad (5.16)$$

where $I_{pore}(q)$ represents the scattering at the interface between carbon and void pores, and $I_{fluc}(q)$ describes scattering caused by density fluctuations within the carbon phase.

Filling of the pores with a contrast-matching fluid results in an extinction of the scattering contribution of $I_{pore}(q)$. Accordingly, the scattering contribution of carbon fluctuations can be isolated. This allows for the subtraction of $I_{fluc}(q)$ from either the void carbon matrix or the C-S nanocomposite in order to remove the scattering caused by inhomogeneities of the carbon phase.

6. Synopsis

6.1. Severe Loss of Confined Sulfur in Nanoporous Carbon for Li-S Batteries under Wetting Conditions

Jonas Scholz, Bugra Kayaalp, Anika C. Juhl, Daniel Clemens, Michael Fröba, and Simone Mascotto

Reproduced with permission from *ACS Energy Lett.* 2018, 3, 2, 387–392. Copyright © 2018 American Chemical Society. To access the final edited and published work see:

<https://doi.org/10.1021/acsenergylett.7b01238>

In this study, small-angle neutron scattering (SANS) measurements were performed on carbon CMK-8 at different stages of sulfur loading (i.e. void, 20 wt.% and 50 wt.%) under wetting conditions, i.e. the nanocomposite was infiltrated by D₂O, *d*-THF and *d*-toluene, respectively. The scattering length density (SLD) of the utilized liquids matched the SLD of carbon but deviated from the SLD of sulfur. Accordingly, upon filling of the void pore space with the respective fluid, a two-phase system was obtained.

This prerequisite enabled a precise assessment of the sulfur distribution within the nanoporous matrix of the potential Li-S battery cathode material. When additionally considering the properties of the different liquids, the retention of sulfur was

determined as a function of solvent polarity.

Firstly, it was confirmed that the gradual filling of the porous carbon with sulfur proceeds from the micropores to the mesopores until complete filling of CMK-8 was achieved at 50 wt.% of sulfur.

The impact of the solvent polarity was addressed separately. Lack of interaction between polar D₂O and host resulted in complete retention of sulfur inside the carbon matrix. However, as the polar character of the liquid decreased (i.e. *d*-THF), the interactions between sulfur and fluid increased and extensive removal of sulfur from the porous structure was observed. Only micropore filling was preserved. Accordingly, wetting with non-polar *d*-toluene lead to a complete leaching of sulfur from the pores.

This finding was especially concerning with regard to the possible exposure to electrolytes in the application as cathode material since common electrolyte fluids either exhibit solvent properties similar to THF or even contain THF or toluene as co-solvent.

A detrimental effect of less polar solvents on the adhesion forces of sulfur and carbon was discovered. Consequential leaching is expected to contribute a significant loss of sulfur from the cathode of Li-S batteries and to seriously affect the cell performance. To this effect, only micropores present suitable cavities for the retention of sulfur.

Severe Loss of Confined Sulfur in Nanoporous Carbon for Li–S Batteries under Wetting Conditions

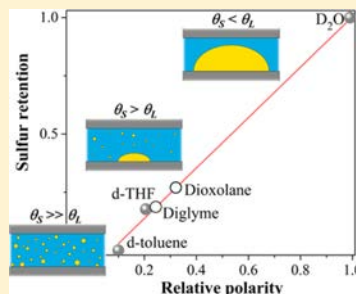
Jonas Scholz,[†] Buğra Kayaalp,[†] Anika C. Juhl,[†] Daniel Clemens,[‡] Michael Fröba,[†] and Simone Mascotto^{*,†,‡}

[†]Institut für Anorganische und Angewandte Chemie, Universität Hamburg, Martin-Luther-King-Platz 6, 20146 Hamburg, Germany

[‡]Helmholtz-Zentrum für Materialien und Energie GmbH, Hahn-Meitner-Platz 1, 14109 Berlin, Germany

 Supporting Information

ABSTRACT: One key aspect in the cathode chemistry of lithium–sulfur (Li–S) batteries is the firm contact between elemental sulfur and the conducting carbon host to ensure the occurrence of the reduction reaction. In this respect, we study the retention of sulfur in the model cathode material CMK-8 carbon loaded by 20 and 50 wt % in the presence of solvents of different nature (D₂O, *d*-THF, *d*-toluene) using small-angle neutron scattering. Exploiting the contrast matching between carbon and these liquids, the scattering of the sulfur phase is isolated and the amount and distribution of sulfur in the pores is determined in precise and direct fashion. The chord-length distribution (CLD) analysis shows that sulfur is preserved in both meso- and micropores if D₂O is used. In the case of *d*-THF, sulfur is found in the micropores only, whereas complete removal from the pore network occurs for wetting with *d*-toluene. This severe loss in the presence of solvents similar to those used in Li–S batteries (e.g., dioxolane, diglyme) is ascribed to their superior adhesion on the carbon surface and, more importantly, indicates that only a little amount of loaded sulfur is available for the electrochemical reactions.



The technological progress and the urge to reduce dependency from fossil fuels push the development of devices based on renewable energy sources, in particular, for transportation and portable applications. After more than 20 years, Li-ion batteries are slowly reaching the maximum of their performance, and novel rechargeable systems beyond Li-ion intercalation are strongly investigated as alternatives. Among these technologies, lithium–sulfur (Li–S) batteries attracted widespread interest due to their high specific capacity and low cost.¹ However, before commercialization, major problems, concerning mostly the physicochemical processes at the carbon–sulfur cathode side, still need to be solved. One of the key issues is the shuttling effect associated with soluble polysulfide species, resulting in charging inefficiency due to parasitic energy losses.^{2,3} Among different approaches, the use of nanoporous carbon (e.g., CMK-8, CMK-3) as a sulfur host revealed to be an efficient way to trap these compounds.^{4–6}

Considering the insulating properties of sulfur, the formation of polysulfides during the reduction reaction can only occur at the carbon–sulfur interface, where the electronic contact is assured. It is therefore extremely important for the battery performance that sulfur particles do not interact with the

electrolyte and maintain contact with the carbon host during cycling.

Surprisingly, despite these fundamental aspects, almost no attention is paid by the scientific community to the physicochemical processes affecting the elemental sulfur phase in the cell. One possible explanation is attributed to the very low solubility of sulfur in organic solvents,^{7,8} which would preclude the occurrence of significant interactions.

Yang's group developed an HPLC/UV analytical method for the precise determination of elemental sulfur dissolved in Li–S battery electrolytes.⁹ They showed that the solubility increases with decreasing solvent polarity and drops remarkably if additives like Li-salts are present in the solution. In a very recent work, Mulder and co-workers showed that sulfur dissolves immediately during the battery assembly and thus is always present in the electrolyte, even if in low amount (<5 wt %).¹⁰ Using custom-made cells, the authors proved that dissolved sulfur species diffuse to the carbon electrode surface

Received: December 9, 2017

Accepted: January 8, 2018

Published: January 8, 2018

and get reduced there, thus playing an active role in the whole electrochemical mechanism.

Dissolution is not the only process that can strongly influence the carbon–sulfur interface in the presence of a liquid electrolyte. Surface adhesion and wetting phenomena can also play a significant role on the properties of composite cathode materials, especially considering that sulfur is only physically impregnated onto the carbon host. In a study addressing the use of carbon–sulfur nanocomposites as adsorbents for mercury removal from natural gas, it was shown that a remarkable amount of the impregnated sulfur was removed from the host during operation.¹¹ The reason for this phenomenon was attributed to condensation of the gaseous hydrocarbons in the carbon nanopores, although no clear evidence was given.

Hence, detachment of particles of sulfur from the carbon matrix could reasonably concur with its dissolution, once wet by the liquid electrolyte. The withdrawn amount would limitedly participate in the reduction reaction of the cathode, seriously compromising the charge capacity of the Li–S cell, similarly to what has been observed in the case of polysulfide shuttling.

Precise assessment of sulfur disjoining from the nanoporous carbon surface in the presence of a liquid is a challenging task. For the characterization of material interfaces and two-phase systems at the nanoscale, small-angle scattering is considered the method of choice because it addresses structural information (e.g., surface area, domain size) in comprehensive and direct fashion.¹² We showed that small-angle scattering can be used in combination with the contrast matching technique to unravel the nanostructure of carbon–sulfur nanocomposites and porous carbon.^{13,14}

Small-angle X-ray scattering (SAXS) was previously used to investigate the sulfur distribution in carbon.¹³ Thanks to the almost complete match between the electron density of sulfur and carbon, the porous nanocomposites presented in essence a two-phase system and the filling of the host material could be precisely followed by this method. In a similar way, we used small-angle neutron scattering (SANS) in combination with gas physisorption to characterize the porous structure of a disordered microporous nongraphitic carbon.¹⁴ Deuterated *p*-xylene was used as a contrast matching fluid and progressively adsorbed in situ on the carbon surface. One main point of this analysis was the proper subtraction from the overall scattering curve of the contribution originating from the turbostratic structure of the carbonaceous material.

Herein, we use SANS to investigate the loading and distribution of sulfur in porous CMK-8 carbon, a model Li–S battery cathode material,⁴ under wetting conditions. The remaining porosity of CMK-8 loaded with 20 and 50 wt % of sulfur was filled with deuterated liquids of different polarity (D₂O, *d*-THF and *d*-toluene). Having these fluids with almost the same scattering length density (SLD) as carbon but different from that of sulfur, a two-phase system was obtained and the location of the sulfur phase in the pores could be directly investigated.

In general, the evaluation of SANS curves proceeds with the assumption of scattering bodies (e.g., pores) distributed in a homogeneous matrix. Nongraphitic carbon possesses graphitic-like lamellar stacks statistically distributed in the material, generating an inhomogeneous mass density profile.¹⁵ Hence, for a straightforward analysis of the pore structure of such

systems, the scattering contribution arising from the graphitic-like domains must be opportunely removed.

As reported previously,^{14,16} in porous carbonaceous materials, the total scattering intensity is the result of

$$I_{\text{TOT}}(q) = I_{\text{pore}}(q) + I_{\text{fl}}(q) \quad (1)$$

where $I_{\text{fl}}(q)$ is the contribution originating from the density fluctuations of the carbon texture, whereas $I_{\text{pore}}(q)$ represents the scattering between the pores and the carbon matrix. Performing contrast matching experiments with SANS, the $I_{\text{fl}}(q)$ contribution is isolated. In particular, by filling the porous network with a fluid, which has the same SLD as carbon, the contribution of the open pores will disappear and only the scattering given by the density fluctuations will remain. Therefore, by subtracting the matched curve ($I_{\text{fl}}(q)$) from the initial SANS pattern ($I_{\text{TOT}}(q)$), the signal that originated from the pores ($I_{\text{pore}}(q)$) is the only scattering measured.

In case of porous nanocomposites systems with sulfur, $I_{\text{TOT}}(q)$ will be given by

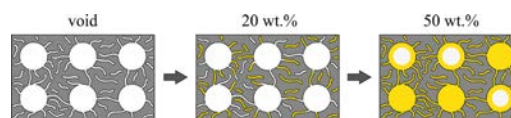
$$I_{\text{TOT}}(q) = I_{\text{pore}}(q) + I_{\text{S}}(q) + I_{\text{fl}}(q) \quad (2)$$

where $I_{\text{S}}(q)$ is the scattering of sulfur embedded in the pore matrix. This contribution is considered as resulting from a homogeneous phase, owing to the amorphous nature of impregnated sulfur.¹³ Thus, if $I_{\text{pore}}(q)$ and $I_{\text{fl}}(q)$ contributions are opportunely removed, the scattering of sulfur can be isolated and analyzed. By completely filling the pores of the material via imbibition with a fluid that has the same SLD as carbon, $I_{\text{pore}}(q)$ will cancel out and only the scattering given by sulfur and the density fluctuations will remain. Subtraction of the density fluctuation contribution ($I_{\text{fl}}(q)$) as previously assessed will result in the scattering originating solely from sulfur $I_{\text{S}}(q)$ dispersed in a homogeneous carbon matrix.

For a system of pores (or sulfur) embedded in a homogeneous material, the chord-length distribution (CLD)^{17,18} is the proper method for analysis of the scattering curve. This approach provides comprehensive structural information (average domain size, correlation length, surface area) of the system without any assumption on the form of the scattering objects. The CLD delivers a statistical description of the distances connecting phase boundaries in a pure two-phase system with sharp interface. Therefore, at large q , the curves must exhibit Porod behavior, i.e., q^{-4} dependence (see the Supporting Information for further details).

In comparison to our previous work,¹³ in which several CMK-8–sulfur compositions (20, 40, and 50 wt %) were investigated, here we focus on sulfur loadings of 20 and 50 wt %. These quantities represent precisely two different structural configurations of the nanocomposite, in which only micropores (20 wt %) and micropores plus mesopores (50 wt %) of the host are filled (Scheme 1). As the samples are from the same batch as those studied in ref 13 for microstructural and porosity

Scheme 1. Representation of the Sulfur Distribution for Loadings of 20 and 50 wt % in CMK-8 under Dry Conditions, As Discussed in Reference 13



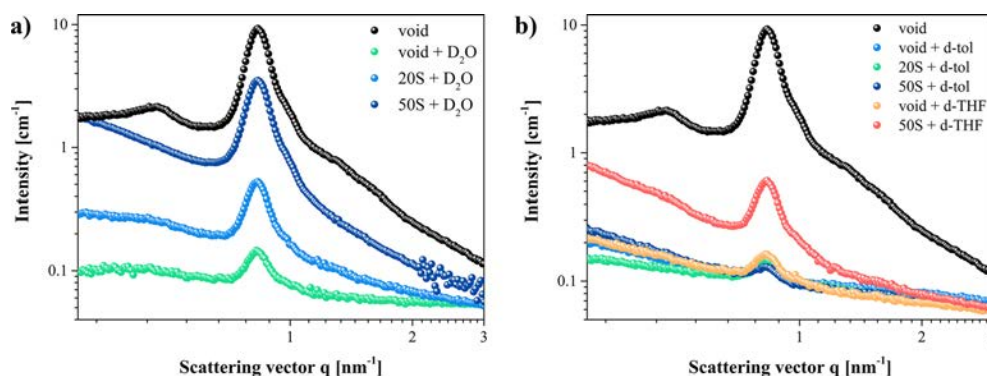


Figure 1. Small-angle neutron scattering (SANS) curves of void CMK-8 and of its sulfur nanocomposites under matching with D₂O (a) and *d*-toluene and *d*-THF (b). The scattering signal visible in the nanocomposite systems represents the sulfur confined in the carbon pores. SANS patterns were acquired with neutron wavelength (λ) $2.1 < \lambda < 7.1$ Å.

characterization, the reader is referred to that publication. The analysis of the sulfur concentration in the CMK-8 framework is additionally reported in the Supporting Information.

With respect to X-rays, the SLD of carbon ($\text{SLD} = 6 \times 10^{-6} \text{ \AA}^{-2}$) differs significantly from that of sulfur ($\text{SLD} = 1.07 \times 10^{-6} \text{ \AA}^{-2}$) for neutron radiation. Thus, the coexistence of a three-phase system made of carbon, sulfur, and a void makes the structural analysis via SANS a challenging task (Figure S1). As mentioned above, this hurdle can be overcome by filling the remaining porosity with liquids that present almost the same SLD as carbon (e.g., D₂O, *d*-THF, *d*-toluene). More importantly, if solvents with different properties are chosen, this condition offers the unique opportunity to study fluid–solid interactions at the nanoscale in direct and detailed fashion.

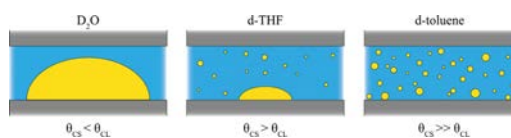
In Figure 1a, the scattering curves of CMK-8 and its sulfur composites matched with D₂O are displayed. When the pure carbon material is filled with the contrast fluid, the scattering contrast disappears. The small signal corresponding to the main peak of CMK-8 is attributed to a slight SLD mismatch.¹⁹ This result shows that the porous structure of CMK-8 gets infiltrated completely by D₂O, which is quite surprising considering the hydrophobic nature of carbon. The reason is attributed to the strong capillary forces typically occurring in micropores and small mesopores, which overcome the surface repulsion.²⁰ For the nanocomposite systems, an identical but less intense scattering pattern to the one of CMK-8 is observed. As previously shown,¹³ sulfur infiltrates the pore network homogeneously without formation of closed porosity. D₂O can therefore penetrate throughout the remaining voids and match the carbon phase. As a result, only the scattering that originated from sulfur is visible. This contribution displays the negative replica of the CMK-8 pore network due to the widespread penetration of sulfur into the micromesoporous matrix. The higher intensity of the 50 wt % curve is the result of the higher sulfur loading in the porous material.

If *d*-toluene is used as the matching fluid, a completely different scenario is observed (Figure 1b). Here, matching was achieved not only for the pure carbon matrix but also for the nanocomposites. The small signal corresponding to the CMK-8 Bragg peak is ascribed to SLD mismatch again. The absence of any sulfur scattering for both systems (20 and 50 wt %) is thus a result of a strong interaction between solvent and solid, which causes complete removal of sulfur from both the micropores

and mesopores (Scheme 1). As sulfur is soluble in toluene to an amount of approximately 5% at room temperature,⁸ only 0.01 wt % of the impregnated sulfur will be dissolved at the applied experimental conditions (see Supporting Information). Therefore, the remaining sulfur has been detached from the surface of the electrode material and formed most probably a colloidal suspension in the solvent. Besides these two cases, determined by liquids with opposite characteristics, it is worth considering an intermediate situation that also approaches the conditions at the cathode material of the Li–S cell. Standard battery solvents cannot be used as contrast fluids either for their poor availability in the deuterated form or the nonmatching SLD. In comparison, *d*-THF is a well-suited matching fluid for carbon. What is even more important, THF has properties (e.g., polarity) very close to those of solvents commonly used for Li–S battery electrolyte solutions, such as diglyme or dioxolane, and is also employed as a co-solvent.^{21–27} In Figure 1b, the SANS patterns of void CMK-8 and CMK-8 loaded with 50 wt % of sulfur under *d*-THF matching conditions are displayed. Here, the intensity of the scattering arising from the sulfur phase is between the ones observed with D₂O and *d*-toluene matching, meaning that only a fraction of the impregnated sulfur is retained in the pores while the rest is dissolved and leached. This is a plausible scenario considering that the polarity and ability to dissolve sulfur of *d*-THF are intermediate compared to those of the other two solvents.⁹

A mechanism to clarify these different solid–fluid interactions is proposed that accounts for the different surface adhesions between sulfur, the solvents, and carbon (Scheme 2). The discussion is based on the surface properties of the hydrogenated liquids due to the considerable literature data

Scheme 2. Representation of the Interactions between Sulfur and D₂O, *d*-THF, and *d*-toluene in the CMK-8 Host, with θ_{CS} and θ_{CL} Contact Angles of the Carbon–Sulfur and Carbon–Liquid Interface, Respectively



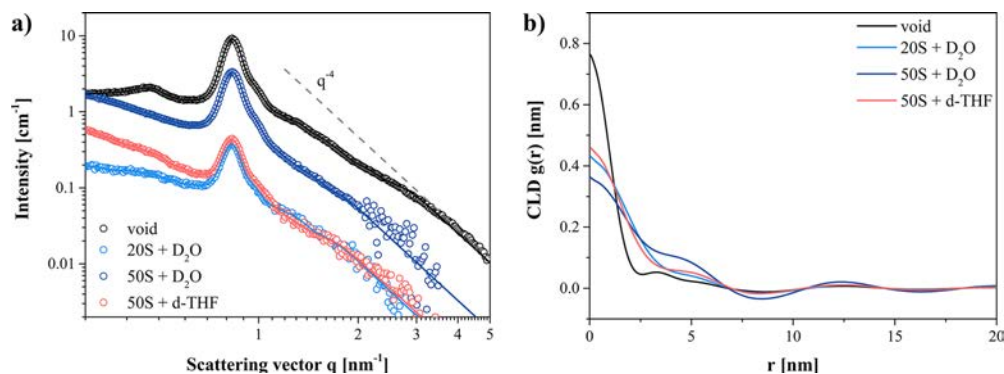


Figure 2. Pore scattering ($I_{\text{pore}}(q)$) and sulfur scattering ($I_{\text{S}}(q)$) (a) with the corresponding CLD plots (b) of void CMK-8 and of its sulfur nanocomposites using different matching fluids. The bold lines in (a) represent the fittings of the CLD analysis.

about these and the negligible differences with deuterated counterparts. According to wettability investigations, liquid sulfur deposits on both graphitic and nongraphitic carbon surfaces with a contact angle θ of approximately 50° ,²⁸ whereas water shows lower affinity ($\theta > 70^\circ$).^{29–31} Hence, the adhesion of sulfur is stronger, thus explaining the remarkable retention in the pores.

A different scenario is obtained if organic solvents are used as matching fluids. THF and toluene possess very favorable wetting on carbon than sulfur itself, showing contact angles of 12° ²⁹ and 0° ,³² respectively. Detachment from the host can thus easily occur, especially when it is considered that sulfur is only physically impregnated.²⁸ As predicted by the surface properties, we observed that withdrawal is less prominent in the case of *d*-THF and only the sulfur better anchored to the pore surface remains in the carbon structure.

Precise assessment of the sulfur location and quantification under wetting conditions are therefore of utmost importance to determine the impact of detachment. The information is gained by analysis of the scattering of pure sulfur $I_{\text{S}}(q)$, which is in turn obtained by further subtraction of $I_{\text{H}}(q)$ from the matched curves (see eq 2). Obviously, this evaluation is valid only in the case of D_2O and *d*-THF matching, for which a scattering contribution of the sulfur phase is visible. In Figure 2a, the sulfur scattering is presented for different nanocomposite systems along with the pore scattering ($I_{\text{pore}}(q)$) of void CMK-8 (obtained via eq 1 using D_2O as the matching fluid). All of the curves at high scattering vectors show the typical Porod decay as q^{-4} of pure two-phase systems.

At this stage, precise morphological description of the sulfur in the pores is realized by applying the CLD approach. The CLD plots of the sulfur curves, and by comparison of the void carbon host, are displayed in Figure 2b. Positive values of $g(0)$ are directly related to the roughness of the scattering interface. For the void system, this point is associated with the presence of micropores, whereas in the curves of the samples loaded with sulfur, it describes the sulfur in these cavities. Owing to the lower scattering contrast of the carbon–sulfur system compared to that of the carbon–void, the CLD plots cannot be fully compared. Yet, it might be reasonable to consider the void host being more angular and rougher than its sulfur replica, thus explaining the higher value of $g(0)$. The two shoulders of the CMK-8 plot at ca. 3 and 5 nm represent, respectively, the pore size and the pore walls, in very good

agreement with previous analyses.¹³ In the sulfur CLDs, these features cannot be discerned due to a lower resolution of the scattering curves, and only a shoulder, superposition of both features, is visible.

Despite this approximation, the intensity increase observed from the 20 wt % to the 50 wt % curve under D_2O matching conditions clearly shows the filling of the mesopores at this higher loading. This result is further confirmed by the considerably larger l_{p} value (Table 1), i.e., the average length

Table 1. Average Porod Length l_{p} and Porod Invariant Q of the Analyzed CMK-8 Systems, Calculated in the Range of $0.3 \leq q \leq 3 \text{ nm}^{-1}$

parameter	void	20S + D_2O	50S + D_2O	50S + <i>d</i> -THF
Q [10^7 nm^{-4}]	4.74	0.22	1.52	0.27
l_{p} [nm]	1.02	1.54	1.85	1.62

scale of the sulfur domains. This distribution of sulfur is in full agreement with that obtained with SAXS for the dry nanocomposites¹³ and summarized in Scheme 1. More importantly, this further corroborates the lack of interactions among D_2O and the infiltrated sulfur, which maintains its original place in the pores, despite the intimate fluid–solid contact.

The evident effect of strong sulfur–solvent interactions is visible in the CLD plot of the sample with 50 wt % sulfur matched with *d*-THF. The course of the graph follows the one of 20 wt %@ D_2O , indicating that mainly micropores are filled with sulfur, as also confirmed by the very similar l_{p} . Hence, sulfur gets easily leached from the mesopores but is retained in micropores, where the confinement and the interactions with the carbon matrix are stronger.

Besides spatial location, quantification of the amount of sulfur in the carbon under matching conditions is provided by the invariant Q , i.e., the integral over $q^2 I_{\text{S}}(q)$, which is proportional to the interface area produced by the confined sulfur (Table 1). For the systems in contact with D_2O , the invariant increases with the amount of impregnated sulfur as expected. However, if the high loaded sample is wetted by *d*-THF, the interface generated by sulfur is more than five times lower than that in the case of D_2O , indicating that the majority of infiltrated sulfur is removed from the carbon host. Evidently,

in the case of *d*-toluene, the absence of sulfur scattering corresponds to an interface area of zero.

With these results, a plot showing the sulfur retention as a function of liquid polarity is generated, assuming that matching with heavy water represents an ideal situation in which sulfur stays unperturbed because of lacking fluid–solid interactions (Figure 3). The progressive decrease of the guest phase follows

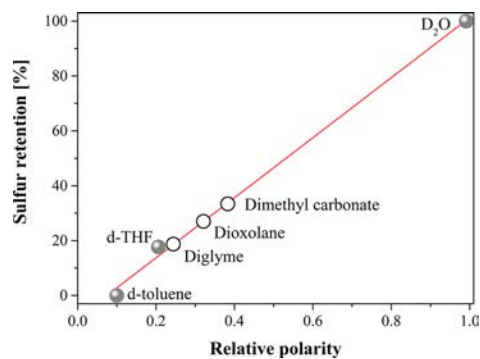


Figure 3. Variation of sulfur retention as a function of solvent polarity for D₂O, *d*-THF, and *d*-toluene. Sulfur retention values for dioxolane, diglyme, and dimethyl carbonate (void circles) were assumed to be in agreement with the linearity prediction.

the reduction of solvent polarity in a linear way. This dependency is thus exploited to envision the detachment potential of common battery solvents, e.g., diglyme, dioxolane, and dimethyl carbonate. A similar behavior for these liquids is reasonably expected as their polarity is very close to the one of THF.²² Hence, in standard battery configuration, the sulfur will be concentrated mainly in the micropores of the nanoporous carbon material where the confinement is at its most. These findings show that most of the sulfur originally impregnated is not located in proximity to the interface of the carbon electrode. Even though the reduction reaction at the cathode will still occur due to presence of dissolved sulfur species,¹⁰ the much longer diffusion pathways might severely affect the reaction kinetics. Such sulfur loss, so far unknown, can thus have detrimental consequences for the potential development of Li–S batteries and requires further clarification.

This phenomenon has strong similarity with the more renowned polysulfide shuttling because for both processes significant loss of active material occurs. This could also be the reason why many of the solutions proposed to solve the shuttling issue might be equally appropriate to hinder sulfur detachment. The most prominent example is given by the design of carbon cathode materials with enhanced microporous fraction to act as a polysulfide reservoir.^{33–35} In light of our results, sulfur not only penetrates easily into such pores but is also strongly retained in there, when it is in contact with the electrolyte solution. This explains the minimal capacity losses for these materials.³⁶ Further ways to improve the sulfur adhesion involve the strengthening of its bonding with the carbon matrix. As reported elsewhere,³⁷ doping of the carbon host with nitrogen showed high loading of sulfur and very limited capacity fading.

In summary, we assessed the interactions between solvents and sulfur confined in ordered CMK-8 nanoporous carbon

using SANS. Exploiting the contrast matching between carbon and these fluids, the scattering of the sulfur phase could be isolated and the amount and distribution of sulfur in the pores under wetting conditions determined. We showed that polarity and adhesion of the solvents on the carbon surface play a major role in the retention of the guest phase in the nanoporous network. In particular, the lack of interactions between D₂O and the nanocomposite led to a complete preservation of the sulfur in both micro- and mesopores. In the case of *d*-THF, sulfur was found only in the micropores due to stronger interactions with the host. For *d*-toluene, complete removal from the pore network occurred. As the sulfur content was too high (50 wt % with respect to the carbon mass) that only dissolution was taking place, sulfur detachment is the most accredited explanation, especially when the increasing adhesion of the solvent on the carbon surface and the weak carbon–sulfur bonding are considered. More importantly, this so far unknown phenomenon is likely to proceed also in the cathode material of Li–S cells because THF has not only similar properties to standard battery solvents (e.g., dioxolane, diglyme) but together with toluene is also used as an additive or co-solvent in these devices. This work sheds new light on the role of surface adhesion forces on the chemistry of Li–S batteries and attributes to the electrolyte wetting being one of the major causes for the sulfur loss from the cathode material. In the future, detachment of sulfur needs therefore to be better understood to disclose to what extent it contributes to the performance of Li–S cells, especially in comparison to polysulfide shuttling.

■ ASSOCIATED CONTENT

5 Supporting Information

The Supporting Information is available free of charge on the ACS Publications website at DOI: 10.1021/acseenergylett.7b01238.

Experimental details, evaluation methods of the SANS data, characterization of sulfur content in the carbon matrix, and additional SANS measurements of reference materials (PDF)

■ AUTHOR INFORMATION

Corresponding Author

*E-mail: simone.mascotto@chemie.uni-hamburg.de.

ORCID

Simone Mascotto: 0000-0002-3503-6391

Notes

The authors declare no competing financial interest.

■ ACKNOWLEDGMENTS

The Helmholtz-Zentrum Berlin is gratefully acknowledged for the allocated beamtime and the technical and financial support.

■ REFERENCES

- (1) Bruce, P. G.; Freunberger, S. A.; Hardwick, L. J.; Tarascon, J.-M. Li–O₂ and Li–S Batteries with High Energy Storage. *Nat. Mater.* **2011**, *11*, 172–172.
- (2) Mikhaylik, Y. V.; Akridge, J. R. Polysulfide Shuttle Study in the Li/S Battery System. *J. Electrochem. Soc.* **2004**, *151*, A1969–A1976.
- (3) Cui, Y.; Fu, Y. Polysulfide Transport through Separators Measured by a Linear Voltage Sweep Method. *J. Power Sources* **2015**, *286*, 557–560.

- (4) Ji, X.; Lee, K. T.; Nazar, L. F. A Highly Ordered Nanostructured Carbon–sulphur Cathode for Lithium–sulphur Batteries. *Nat. Mater.* **2009**, *8*, 500–506.
- (5) Ji, X.; Evers, S.; Black, R.; Nazar, L. F. Stabilizing Lithium–sulphur Cathodes Using Polysulphide Reservoirs. *Nat. Commun.* **2011**, *2*, 325.
- (6) Juhl, A. C.; Schneider, A.; Ufer, B.; Brezesinski, T.; Janek, J.; Fröba, M. Mesoporous Hollow Carbon Spheres for Lithium–Sulfur Batteries: Distribution of Sulfur and Electrochemical Performance. *Beilstein J. Nanotechnol.* **2016**, *7*, 1229–1240.
- (7) Sciamanna, S. F.; Lynn, S. Sulfur Solubility in Pure and Mixed Organic Solvents. *Ind. Eng. Chem. Res.* **1988**, *27*, 485–491.
- (8) Ren, Y.; Shui, H.; Peng, C.; Liu, H.; Hu, Y. Solubility of Elemental Sulfur in Pure Organic Solvents and Organic Solvent-Ionic Liquid Mixtures from 293.15 to 353.15K. *Fluid Phase Equilib.* **2011**, *312*, 31–36.
- (9) Zheng, D.; Zhang, X.; Li, C.; McKinnon, M. E.; Sadok, R. G.; Qu, D.; Yu, X.; Lee, H.-S.; Yang, X.-Q.; Qu, D. Quantitative Chromatographic Determination of Dissolved Elemental Sulfur in the Non-Aqueous Electrolyte for Lithium–Sulfur Batteries. *J. Electrochem. Soc.* **2015**, *162*, A203–A206.
- (10) Harks, P. P. R. M. L.; Robledo, C. B.; Verhallen, T. W.; Notten, P. H. L.; Mulder, F. M. The Significance of Elemental Sulfur Dissolution in Liquid Electrolyte Lithium Sulfur Batteries. *Adv. Energy Mater.* **2017**, *7*, 1601635.
- (11) Kumar Reddy, K. S.; Al Shoaibi, A.; Srinivasakannan, C. Sulfur-Leaching Facts from Sulfur-Impregnated Porous Carbons in the Mercury Removal Process. *Energy Fuels* **2015**, *29*, 4488–4491.
- (12) Smarsly, B. M.; Kaper, H.; Mascotto, S.; Weidmann, C. Charakterisierung Mesoporöser Materialien Mittels Kleinwinkelstreuung (SAXS/SANS). *Chem. Ing. Tech.* **2010**, *82*, 823–828.
- (13) Petzold, A.; Juhl, A.; Scholz, J.; Ufer, B.; Goerigk, G.; Fröba, M.; Ballauff, M.; Mascotto, S. Distribution of Sulfur in Carbon/Sulfur Nanocomposites Analyzed by Small-Angle X-Ray Scattering. *Langmuir* **2016**, *32*, 2780–2786.
- (14) Mascotto, S.; Kuzmicz, D.; Wallacher, D.; Siebenbürger, M.; Clemens, D.; Risse, S.; Yuan, J.; Antonietti, M.; Ballauff, M. Poly(ionic Liquid)-Derived Nanoporous Carbon Analyzed by Combination of Gas Physisorption and Small-Angle Neutron Scattering. *Carbon* **2015**, *82*, 425–435.
- (15) Franklin, R. E. Crystallite Growth in Graphitizing and Non-Graphitizing Carbons. *Proc. R. Soc. London, Ser. A* **1951**, *209*, 196–218.
- (16) Jafta, C. J.; Petzold, A.; Risse, S.; Clemens, D.; Wallacher, D.; Goerigk, G.; Ballauff, M. Correlating Pore Size and Shape to Local Disorder in Microporous Carbon: A Combined Small Angle Neutron and X-Ray Scattering Study. *Carbon* **2017**, *123*, 440–447.
- (17) Méring, J.; Tchoubar, D. Interprétation de La Diffusion Centrale Des Rayons X Par Les Systèmes Poreux. *J. Appl. Crystallogr.* **1968**, *1*, 153–165.
- (18) Smarsly, B.; Antonietti, M.; Wolff, T. Evaluation of the Small-Angle X-Ray Scattering of Carbons Using Parametrization Methods. *J. Chem. Phys.* **2002**, *116*, 2618.
- (19) Mascotto, S.; Wallacher, D.; Brandt, A.; Hauss, T.; Thommes, M.; Zickler, G. A.; Funari, S. S.; Timmann, A.; Smarsly, B. M. Analysis of Microporosity in Ordered Mesoporous Hierarchically Structured Silica by Combining Physisorption With in Situ Small-Angle Scattering (SAXS and SANS). *Langmuir* **2009**, *25*, 12670–12681.
- (20) Thommes, M.; Morell, J.; Cychosz, K. A.; Fröba, M. Combining Nitrogen, Argon, and Water Adsorption for Advanced Characterization of Ordered Mesoporous Carbons (CMKs) and Periodic Mesoporous Organosilicas (PMOs). *Langmuir* **2013**, *29*, 14893–14902.
- (21) Scheers, J.; Fantini, S.; Johansson, P. A Review of Electrolytes for Lithium–Sulphur Batteries. *J. Power Sources* **2014**, *255*, 204–218.
- (22) Reichardt, C. *Solvents and Solvent Effects in Organic Chemistry*; Wiley-VCH: Weinheim, Germany, 2003.
- (23) Peled, E.; Sternberg, Y.; Gorenshtein, A.; Lavi, Y. Lithium–Sulfur Battery: Evaluation of Dioxolane-Based Electrolytes. *J. Electrochem. Soc.* **1989**, *136*, 1621.
- (24) Kolosnitsyn, V. S.; Karaseva, E. V.; Seung, D. Y.; Cho, M. D. Cycling a Sulfur Electrode: Effect of Physicochemical Properties of Electrolyte Systems. *Russ. J. Electrochem.* **2003**, *39*, 1089–1093.
- (25) Zhang, C.; Yamazaki, A.; Murai, J.; Park, J. W.; Mandai, T.; Ueno, K.; Dokko, K.; Watanabe, M. Chelate Effects in Glyme/lithium Bis(trifluoromethanesulfonyl)amide Solvate Ionic Liquids, Part 2: Importance of Solvate-Structure Stability for Electrolytes of Lithium Batteries. *J. Phys. Chem. C* **2014**, *118*, 17362–17373.
- (26) Choi, J. W.; Kim, J. K.; Cheruvally, G.; Ahn, J. H.; Ahn, H. J.; Kim, K. W. Rechargeable Lithium/sulfur Battery with Suitable Mixed Liquid Electrolytes. *Electrochim. Acta* **2007**, *52*, 2075–2082.
- (27) Bieker, G.; Wellmann, J.; Kolek, M.; Jalkanen, K.; Winter, M.; Bieker, P. Influence of Cations in Lithium and Magnesium Polysulphide Solutions: Dependence of the Solvent Chemistry. *Phys. Chem. Chem. Phys.* **2017**, *19*, 11152–11162.
- (28) Kaban, I.; Nowak, R.; Bruzda, G.; Xi, L.; Sobczak, N.; Eckert, J.; Giebeler, L. Wettability and Work of Adhesion of Liquid Sulfur on Carbon Materials for Electrical Energy Storage Applications. *Carbon* **2016**, *98*, 702–707.
- (29) Mattia, D.; Bau, H. H.; Gogotsi, Y. Wetting of CVD Carbon Films by Polar and Nonpolar Liquids and Implications for Carbon Nanopipes. *Langmuir* **2006**, *22*, 1789–1794.
- (30) Raj, R.; Maroo, S. C.; Wang, E. N. Wettability of Graphene. *Nano Lett.* **2013**, *13*, 1509–1515.
- (31) Tse, J.; Adamson, A. W. Adsorption and Contact Angle Studies. *J. Colloid Interface Sci.* **1979**, *72*, 515–523.
- (32) Callaghan, I. C.; Everett, D. H.; Fletcher, A. J. P. Liquid/liquid/solid Contact Angles Measured by Interference Microscopy. *J. Chem. Soc., Faraday Trans. 1* **1983**, *79*, 2723.
- (33) Zhang, Z.; Li, Z.; Hao, F.; Wang, X.; Li, Q.; Qi, Y.; Fan, R.; Yin, L. 3D Interconnected Porous Carbon Aerogels as Sulfur Immobilizers for Sulfur Impregnation for Lithium–Sulfur Batteries with High Rate Capability and Cycling Stability. *Adv. Funct. Mater.* **2014**, *24*, 2500–2509.
- (34) Zhao, C.; Liu, L.; Zhao, H.; Krall, A.; Wen, Z.; Chen, J.; Hurley, P.; Jiang, J.; Li, Y. Sulfur-Infiltated Porous Carbon Microspheres with Controllable Multi-Modal Pore Size Distribution for High Energy Lithium–sulfur Batteries. *Nanoscale* **2014**, *6*, 882–888.
- (35) Jung, D. S.; Hwang, T. H.; Lee, J. H.; Koo, H. Y.; Shakoore, R. A.; Kahraman, R.; Jo, Y. N.; Park, M. S.; Choi, J. W. Hierarchical Porous Carbon by Ultrasonic Spray Pyrolysis Yields Stable Cycling in Lithium–Sulfur Battery. *Nano Lett.* **2014**, *14*, 4418–4425.
- (36) Hoffmann, C.; Thieme, S.; Brückner, J.; Oschatz, M.; Biemelt, T.; Mondin, G.; Althues, H.; Kaskel, S. Nanocasting Hierarchical Carbide-Derived Carbons in Nanostructured Opal Assemblies for High-Performance Cathodes in Lithium–Sulfur Batteries. *ACS Nano* **2014**, *8*, 12130–12140.
- (37) Schneider, A.; Weidmann, C.; Suchomski, C.; Sommer, H.; Janek, J.; Brezesinski, T. Ionic Liquid-Derived Nitrogen-Enriched Carbon/Sulfur Composite Cathodes with Hierarchical Microstructure—A Step Toward Durable High-Energy and High-Performance Lithium–Sulfur Batteries. *Chem. Mater.* **2015**, *27*, 1674–1683.

6.2. Pore geometry effect on the synthesis of silica supported perovskite oxides

Jonas Scholz, Martin Etter, Diana Haas, Andreas Meyer, Andreas Kornowski, Uta Sazama, and Simone Mascotto

Reproduced with permission from *J. Colloid Interface Sci.* 2017, 504, 346-355.

To access the final edited and published work see:

<https://doi.org/10.1016/j.jcis.2017.05.107>

The aforementioned publication addressed the distribution of an impregnated material (sulfur) within a nanoporous carbon matrix and emphasized how sulfur can be retained, depending on the pore size. In a similar fashion, the present work concerns itself with the synthesis procedure of a different nanocomposite, correlating pore properties of different nanoporous silica matrices with the impregnation behaviour of perovskite precursor solutions.

A systematical study was conducted on silica-supported perovskite oxides to shed light on the intricacies of the infiltration and conversion processes. Understanding of those processes is crucial for the successful formation of silica-supported metal oxide nanoparticles with the aim of improving the functional properties of the oxide by enhancing its specific surface area. In this regard, the degradation and evaporation behaviour of different perovskite precursor solutions (LCO, LFO, PFO) depending on the pore geometry of different mesoporous silicas were assessed. The influence of the pore curvature was investigated by comparing KIT-6 ($Ia\bar{3}d$), SBA-15 ($p6mm$) and KIT-5 ($Fm\bar{3}m$) while maintaining a fixed pore size of 7.5 nm. Conversely, a constant symmetry ($Fm\bar{3}m$) was kept to determine the impact of the pore size. Accordingly FDU-5, FDU-12 and L-FDU-12 with pore sizes of 7.5, 12 and 17 nm were prepared, respectively.

A clear correlation between pore properties, conversion behaviour and corresponding location and microstructure of the impregnated perovskites showed. TEM-

images and X-ray diffractograms indicated that a high pore curvature, i.e. spherical KIT-5, promotes the crystallization process of the perovskite oxide. Nanocomposites of gyroidal structure KIT-6, in contrast, did not exhibit the presence of a crystal phase. This occurrence is in accordance with TG-MS analyses of the conversion step. The pore accessibility and pore curvature of KIT-6 facilitated fast degradation and evaporation of the precursors. As a result, isolated nanoparticles were rapidly formed, preventing nucleation and particle growth. Thus, generation of quasi-amorphous particles was observed.

Even though a filling of the pores was achieved during the impregnation step, the subsequent calcination resulted in a release of perovskite precursors from the pores to form crystallites on the outside of the silica matrices. Nevertheless, partial filling of the host was achieved.

Moreover, by means of TG-MS, confinement effects were confirmed for the degradation of the precursors. Conversion took place much faster and at lower temperatures for nanocomposite materials compared to bulk environment.

New information was provided regarding the influence of the pore constraints on the crystallization behaviour of different perovskite oxides. Strongly depending on the pore size and curvature of the silica matrix, the degradation behaviour of the respective precursors played a crucial role in distribution and crystallinity of the mixed metal oxides.



Contents lists available at ScienceDirect

Journal of Colloid and Interface Science

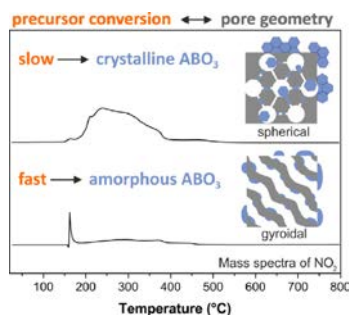
journal homepage: www.elsevier.com/locate/jcis

Regular Article

Pore geometry effect on the synthesis of silica supported perovskite oxides

Jonas Scholz^a, Martin Etter^b, Diana Haas^b, Andreas Meyer^c, Andreas Kornowski^c, Uta Szama^a, Simone Mascotto^{a,*}^aInstitut für Anorganische und Angewandte Chemie, Universität Hamburg, Martin-Luther-King Platz 6, D-20146 Hamburg, Germany^bDeutsches Elektronen-Synchrotron (DESY), Notkestraße 85, D-22607 Hamburg, Germany^cInstitut für Physikalische Chemie, Universität Hamburg, Grindelallee 117, D-20146 Hamburg, Germany

GRAPHICAL ABSTRACT



ARTICLE INFO

Article history:

Received 11 April 2017

Revised 26 May 2017

Accepted 26 May 2017

Available online 29 May 2017

Keywords:

Confinement

Heterogeneous catalysis

Perovskite

Nanocasting

Ink-bottle pores

ABSTRACT

The formation of perovskite oxide nanoparticles supported on ordered mesoporous silica with different pore geometry is here presented. Systematic study was performed varying both pore shape (gyroidal, cylindrical, spherical) and size (7.5, 12, 17 nm) of the hosts. LaFeO₃, PrFeO₃ and LaCoO₃ were chosen as target guest structures. The distribution of the oxide nanoparticles on silica was comprehensively assessed using a multi-technique approach. It could be shown that the pore geometry plays a determining role in the conversion of the infiltrated metal nitrates to metal oxide. In particular, slow degradation kinetic was observed in highly curved pores, which fostered nucleation and crystallization of the guest species. In spherical pore systems the enhancement of pore size caused a remarkable delay of the decomposition of the metal salts, but at the same time improved the homogeneous distribution of the oxide particles in the matrix.

© 2017 Elsevier Inc. All rights reserved.

1. Introduction

Infiltration of mesoporous solids has been progressively used in the last years as emerging strategy for the synthesis of novel func-

tional materials [1]. The manifold combinations between type of host, guest and process parameters create a huge toolbox for the design of nanostructured systems with numerous technological applications in hydrogen storage [2,3], lithium batteries [4,5], sensing [6,7], heterogeneous catalysis [8–10] and biomedicine [11,12].

Historically, ordered mesoporous silica have been extensively used as matrices for hosting nanostructured metal oxides. The

* Corresponding author.

E-mail address: simone.mascotto@chemie.uni-hamburg.de (S. Mascotto).<http://dx.doi.org/10.1016/j.jcis.2017.05.107>

0021-9797/© 2017 Elsevier Inc. All rights reserved.

systems which can be obtained are either supported metal oxide nanoparticles or mesoporous metal oxides, obtained by replication of the host via the nanocasting process [13]. In both cases, the synthesis procedure is characterized by the numerous steps involved, among which the most decisive is the conversion of the metal oxide precursors inside the silica pore network. Various process parameters have shown to regulate this transition, which strongly influences the structure and morphology of the final materials. The decomposition rate of the nitrate salts and its effect on the properties of the supported metal oxides particles was investigated by de Jong and coworkers depending on the drying and calcination treatment [10,14]. The use of inert gases (Ar) and nitric oxide-containing atmospheres lowered the evolution of water and nitrogen oxide with respect to the treatments in air, leading to more homogeneous distribution and growth of the supported metal oxide particles. Stucky et al. investigated the role of the container in the nanocasting synthesis of mesoporous metal oxides [15]. Narrow quasi-sealed vessels lowered the escape rate of the gaseous byproducts, enabling a homogeneous wetting of the porous network. Thus, large liquid-like precursor domains could be formed and efficiently crystallize inside the pore space. Conversely, in large open dishes amorphous isolated nanoparticles originated owing to the rapid gas evolution. Hence, if the geometry of the macroscopic container has such a remarkable effect, it can be postulated that size and shape of the nanoscopic container, namely the porous silica host, might also affect the formation of supported metal oxide nanoparticles.

The active role of porous matrices on the phase change behavior of confined species is largely known in the literature. Among others, the Ward group profusely investigated crystallization of organic molecules in nanoporous matrices ranging from controlled pore glass [16], polymer monoliths [17] and anodic alumina [18]. The close relationship between crystal growth and the morphology of the hosts increased the understanding of nucleation, size-dependent polymorphism and thermotropic behavior of nanoscale crystals [19,20].

However, the occurrence of an active role of the pore geometry during a chemical reaction such as the conversion of metal nitrates to metal oxides still needs to be demonstrated. So far the host-guest relations were considered to be of minor significance, and the focus laid more on the functional properties of the final material itself [21]. Moreover, the silica host systems chosen were either topologically too similar [22] or too different [23] to draw solid conclusions on any pore morphology effect.

Herein, we present a first study on the formation of perovskite oxide nanoparticles in ordered mesoporous silica depending on the pore geometry. Two series of hosts were prepared using self-assembly strategies [24]: the first with fixed pore size (7.5 nm) and increasing pore curvature (gyroidal → cylindrical → spherical) [25]; the second with spherical pore shape and increasing pore size (from 7.5 nm to 17 nm). Because of the growing interest in the use of perovskite oxides as non-platinum group metal (non-PGM) catalytic materials [26,27], LaFeO₃ (LFO), PrFeO₃ (PFO) and LaCoO₃ (LCO) were chosen as target guest systems. We could show that the pore curvature controls the escape rate of water and other gaseous byproducts (e.g. CO, NO) during the calcination process. In particular, early and slow water evolution, observed in curved cavities, allowed the formation of large liquid-like precursor domains, which could later nucleate and crystallize. Metal oxide nanoparticles grew both inside and outside the pore space. The pore size difference in spherical ink-bottle pore systems affected significantly both degradation and mass transport of the impregnated precursors. In particular, analyses of the particle distribution revealed, that the connecting pores get preferentially filled over the larger cages, hindering homogeneous impregnation of the host matrices. Finally, for given host matrices, different crystallization behavior

was observed for the three supported perovskites, originated by the different conversion rates of the infiltrated nitrate precursors.

2. Experimental

Chemicals: Lanthanum nitrate hexahydrate (99.9%, Alfa Aesar), iron nitrate nonahydrate (99%, Merck), cobalt nitrate hexahydrate (97.7%, Alfa Aesar), praseodymium nitrate hexahydrate (99.9%, Strem Chemicals), Tetraethoxyorthosilicate (TEOS, 98%, Alfa Aesar), ethylene glycol (99%, Alfa Aesar), potassium chloride (98.5%, Acros Organics), hydrochloric acid (37%, VWR), methanol (99.8%, Acros), Pluronic F127 (Sigma Aldrich), Pluronic P123 (Sigma Aldrich), mesitylene (98%, Merck) and butanol (100%, Merck) were used as received without further purifications.

Synthesis of the porous silica hosts

SBA-15: According to Ref. [28], Pluronic P123 (12.00 g) was dissolved in a mixture of H₂O (360 g) and 37% HCl (42.9 g). After dissolution of the polymer TEOS (24.0 g) was added. The reaction mixture was stirred for 24 h at 35 °C and subsequently kept again for 24 h at 80 °C under static conditions. After filtration, the powder was calcined in air at 550 °C for 5 h in order to remove the organic template.

KIT-6: According to Ref. [29], Pluronic P123 (12.00 g) was dissolved in a mixture of H₂O (434 g) and 37% HCl (23.6 g). The solution was stirred for 1 h at 35 °C before and after the addition of butanol (12.0 g). Subsequently TEOS (25.8 g) was added. The reaction mixture was stirred for 24 h at 35 °C and then kept at 80 °C for other 24 h under static conditions. After filtration, the powder was calcined in air at 550 °C for 5 h in order to remove the organic template.

KIT-5: Following the approach of Kleitz et al. [30] Pluronic F127 (5.00 g) was dissolved in a mixture of H₂O (240 g) and 37% HCl (10.5 g). After the addition of TEOS (24.0 g) the solution was heated to 45 °C and stirred for 24 h. Subsequently, the reaction mixture was kept at 100 °C again for 24 h under static conditions. Following the filtration of the resulting powder, the product was calcined in air at 550 °C for 5 h in order to remove the template.

FDU-12: According to Ref. [31] the triblock copolymer Pluronic F127 (3.0 g) and KCl (7.5 g) were dissolved in 2 M HCl (180 mL). After the addition of mesitylene (6.6 g), the reaction mixture was stirred for 24 h at room temperature. Subsequently, TEOS (12.3 g) was added and the solution was stirred another 24 h at room temperature. Afterwards, the reaction mixture was kept at 100 °C for one day under static conditions. Following the filtration of the resulting powder, the product was calcined in air at 550 °C for 5 h in order to remove the template.

L-FDU-12: The material was prepared following the approach of Yu et al. [32]. Pluronic F127 (3.0 g) and KCl (7.5 g) were dissolved in 2 M HCl (180 mL). Following the addition of mesitylene (6.6 g), the solution was stirred at room temperature for 24 h in a capped container. Subsequently, TEOS (12.3 g) was added and the reaction mixture stirred at room temperature for one day. Finally, after hydrothermal treatment in an autoclave at 100 °C for 72 h the product was filtered and calcined in air at 550 °C for 5 h.

Synthesis of bulk perovskite oxides: According to Ref. [33] 1.25 mmol of the metal nitrate salts were dissolved in ethylene glycol (1.5 mL) and stirred for 30 min at 60 °C. After cooling down to room temperature, methanol (1.0 mL) was added to decrease the viscosity followed by stirring for 60 min. After calcination at 650 °C for 5 h at a heating rate of 1 °C/min the corresponding perovskite oxide could be obtained.

Synthesis of the perovskite-silica nanocomposites: The porous silica hosts were infiltrated through the incipient wetness method [34] in a large open vessel as indicated in Ref. [15]. Prior to the impregnation procedure, the silica hosts were dried at

90 °C for 48 h to remove potential water residue. Subsequently, the silica powder was soaked one time with an amount of precursor solution corresponding to the total pore volume of the matrix. In order to ensure uniform distribution of the salts in the pores, to the starting solution 10% vol. of methanol was added. The mixture was stirred for 24 h at room temperature before being dried at 90 °C for 24 h. Afterwards, the infiltrated powder was calcined under air at 650 °C for 5 h to promote the conversion of the precursors to oxides.

X-ray diffraction: Laboratory X-ray diffraction measurements were carried out with an X'Pert Pro diffractometer (PANalytical Corp.) with 0.15406 nm Ni-filtered Cu-K α radiation in Bragg-Brentano geometry, operating at 45 kV and 40 mA, step size 0.0130°, step time 74 s per step. Synchrotron X-ray diffraction measurements were performed at beamline P07 at the DESY/PETRAIII synchrotron at a wavelength of $\lambda = 0.01746$ nm in transmission mode. Powder diffraction patterns were collected using a Perkin Elmer XRD 1621 area detector. The collected two-dimensional images were integrated to one-dimensional powder diffraction patterns using pyFAI [35]. Rietveld refinements of the perovskite phases were done with the Bruker TOPAS v4.2 software. The volume-weighted mean crystallite size of a phase was determined from the Scherrer equation using an internal macro of TOPAS. The mean crystallite size was subsequently calculated from the volume-weighted mean crystallite size using an empirical equation [36].

Nitrogen physisorption: The nitrogen sorption isotherms were obtained at 77 K using a Quadrasorb SI-MP by Quantachrome. Outgassing was performed with a Masterprep Degasser (Quantachrome Corp.) at 120 °C for 10 h. Specific surface areas were determined with the Brunauer–Emmett–Teller (BET) method [37] at $p/p_0 = 0.07–0.3$. Pore size distribution was determined with the NLDFT method [38] applying the cylindrical or spherical pore models from the adsorption branch depending on the host considered.

Electron microscopy: Transmission electron microscopy (TEM) and scanning transmission electron microscopy (STEM) measurements were carried out on a JEOL JEM 2200 FS at 200 kV equipped with two CEOS Cs correctors (CETCOR, CESCOR), EDS system JED-2300 T, a Gatan 4 K UltraScan 1000 camera and a HAADF (high angle annular dark field) detector. The sample was crushed into a fine powder, which was suspended in toluene and dropped on a carbon coated 400 mesh TEM grid. The excess of solvent was removed with a filter paper and by drying the grid under air.

Small-angle X-ray scattering: The SAXS measurements were conducted with an Incoatec™ X-ray source I μ S with Quazar Montel optics. The focal spot size diameter at sample was 700 μ m at a wavelength of 0.154 nm. Evacuated flight tube with variable distance between sample and detector 0.1 (WAXS) - 1.6 m (SAXS). Maximum resolution (d-spacing) = 120 nm. A CCD-Detector Rayonix™ SX165 was employed for detection. The regular measurement time per sample accounted for 20 min. SPEC (ver. 5.32) by Certified Scientific Software, Cambridge, MA, USA was employed as control software. The analysis and fitting of the SAXS data was performed by using Scatter (ver. 2.5) [39,40] by Stephan Förster, University of Bayreuth and Lian Apostol, ESRF, Grenoble.

Thermogravimetric analysis: Thermal characterization was carried out using a NETZSCH STA 449F3 coupled over a capillary with Aeolos QMS403C (TG–MS) setting a 10 °C min⁻¹ heating rate in an Ar/O₂ stream (volume ratio 80/20).

²⁹Si-NMR spectroscopy: ²⁹Si cross polarization magic angle spinning nuclear magnetic resonance (CPMAS NMR) experiments were performed at an operating frequency of 79.52 MHz on a Bruker Avancell 400 spectrometer equipped with a 4 mm double resonance probe. ¹H 90° pulse length of 4.4 μ s, contact time of 2 ms, and recycle delay of 5 s were used. All the measurements

were performed at room temperature and with the MAS frequency of 5 kHz. Continuous wave decoupling was used during the acquisition. 16 000 transients were acquired for all the samples and the spectra were plotted in a calibrated intensity scale, taking into account the analyzed sample mass.

3. Result and discussion

3.1. Porous silica hosts

The metal oxide formation in mesoporous silica was investigated as a function of the geometry of the pore surface via variation of pore shape and size. Two series of hosts were prepared using well-known block copolymer templating strategies [24]: the first one with fixed pore size (7.5 nm) and pore shape with increasing curvature (gyroidal \rightarrow cylindrical \rightarrow spherical) [25] i.e. KIT-6, SBA-15, KIT-5 materials. The second series had fixed pore shape (spherical with *Fm3m* structure) but increasing pore size (from 7.5 to 17 nm), i.e. KIT-5, FDU-12 and L-FDU-12 hosts. The synthesis of mesoporous silica with defined and highly controlled pore properties is an essential prerequisite for this study. The topology characterization of the materials was performed combining nitrogen physisorption, small-angle X-ray scattering (SAXS) and transmission electron microscopy (TEM). All the methods are in very well agreement and prove the synthesis of highly ordered materials comparable to the literature standards (Table 1, Fig. S1–S3). Particular care was given to the assessment of the pore size because it is the most critical parameter, which affects pore ordering. Thus, despite the use of NLDFT models of gas physisorption and TEM micrographs, SAXS analysis was carried out, adopting well-known evaluation approaches [39,41]. In Fig. 1 the pore size distributions obtained by gas physisorption are displayed. The systems with different pore shape present narrow distributions centered at 7.5 \pm 0.5 nm, whereas in the materials with spherical pore the size increases from 7.5 to 12 to 17 nm. These latter three silica possess a second mesopore population of ca. 3 nm, which represents the pores connecting the larger spherical ones. These have worm-like shape and are generated by the templating action of the large PEO-block of the F127 template [31,32]. For L-FDU-12 the wider size of the small mesopores is ascribed to the longer hydrothermal step during the synthesis. Aside from the morphology of the constraining medium, also the chemistry of the pore surface can play a relevant role on the process of metal oxide formation in mesopores. In the case of silica hosts, the amount of free silanol groups has shown to have a prominent effect on the crystallization of metal oxides [42]. With this respect, we investigated the chemical environment of the Si atoms via solid state ²⁹Si CP-MAS NMR (Fig. S4). The intensity of the geminal silanol (Q²), single silanol (Q³) and fully condensed silica (Q⁴) signals were found constant in all the hosts, thus excluding any particular influence of the surface chemistry on the metal oxide formation process.

3.2. Perovskite-silica nanocomposites

Perovskite-silica nanocomposites were obtained via conversion of the infiltrated metal salt precursor solution. The microstructural differences of the synthesized materials were firstly studied via X-ray diffraction (XRD). In Fig. 2a it can be clearly seen that for all three oxide systems pure perovskite phases could be obtained as bulk.

As soon as the metal salts were converted under confinement, different situations are observed depending on the host type. Let us first consider the case of matrices with same pore size but heterogeneous shape (Fig. 2b–d). In the gyroidal cavities of KIT-6

Table 1

Porous parameters of the void silica hosts: Surface area (S_{BET}), total pore volume (V_p), lattice parameter (a), mesopore size obtained by SAXS (Φ_{SAXS}), nitrogen physisorption (Φ_{phys}) and TEM (Φ_{TEM}) and pore wall thickness (Φ_{wall}) calculated from $\Phi_{\text{wall}} = a - \Phi_{\text{SAXS}}$ for SBA-15, from $\Phi_{\text{wall}} = a/2 - \Phi_{\text{phys}}$ for KIT-6 and from $\Phi_{\text{wall}} = a/\sqrt{2} - \Phi_{\text{SAXS}}$ for ink-bottle pore systems. The pore size via SAXS could not be determined for KIT-6 due to lack of physical models which simulate the gyroidal form factor of the pores. The values in brackets represent the average size of the intrawall pores of the ink-bottle pore systems.

Sample	S_{BET} [m^2/g]	V_p [cm^3/g]	a [nm]	Φ_{wall} [nm]	Φ_{SAXS} [nm]	Φ_{phys} [nm]	Φ_{TEM} [nm]
KIT-6	829.0	1.09	22.0	3.7	–	7.2 ± 0.9	7.3
SBA-15	863.7	1.09	10.7	3.3	7.42 ± 0.11	7.6 ± 1.1	7.4
KIT-5	820.4	0.58	18.5	3.8	9.32 ± 0.17	8.0 ± 1.1 (2.5 nm)	8.7
FDU-12	532.0	0.51	24.9	3.4	14.2 ± 0.12	12.4 ± 1.0 (2.5 nm)	12.4
L-FDU-12	740.8	0.80	30.0	4.2	17.0 ± 0.13	16.7 ± 1.4 (3.5 nm)	16.6

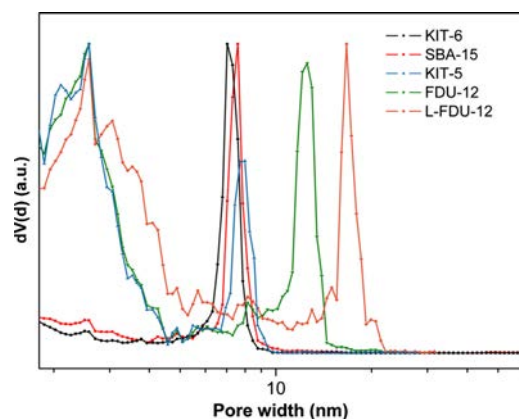


Fig. 1. Normalized pore size distribution in semilogarithmic scale of the host materials from the nitrogen physisorption isotherms calculated using the NLDFT method from the adsorption branch of the isotherm assuming either cylindrical (KIT-6 and SBA-15) or spherical (KIT-5, FDU-12 and L-FDU-12) pore morphology.

the amorphous contribution of the silica matrix superpose with the broad reflections of the perovskite lattice indicating the presence of guest structures with partial long-range order. In SBA-15 the crystallinity depends strongly by the kind of impregnated oxide. The remarkable difference between the two homologue crystal structures PFO and LFO may suggest that this effect is more related to the degradation of the single nitrate precursors than determined by the crystal structure. Such differences disappear in the ink-bottle pore host KIT-5, where all the oxides have the same low degree of crystallinity. The increase of the spherical pores size up to 12 nm (FDU-12) enhances significantly the microstructural order of the guests (Fig. 2e). However, further pore enlargement (L-FDU-12, Fig. 2f) leads back to materials with only partial long-range order. Unlike SBA-15, within the single ink-bottle pore systems all the perovskites showed the same structural properties. Hence, the crystallinity changes observed in the face-centered cubic pore structure are strongly determined by the pore size.

Deeper understanding of the microstructural differences in the highly crystalline materials was achieved by Rietveld refinement analyses (Table S1). All the investigated systems have identical lattice parameters, meaning that the structure of the oxides is not distorted or under strain. However, the smaller grain size in the nanocomposites than in the bulk shows that crystal growth might have occurred also in the pore space

3.3. Distribution of the perovskite species in the silica hosts

Unlike XRD, morphological analysis techniques such as gas physisorption, small-angle X-ray scattering, TEM and STEM,

enabled to precisely assess the spatial distribution of the metal oxide species on the siliceous matrices, thanks to their high complementary character (Scheme 1).

The location of the particles within the pore space can be indirectly determined by the accessibility of gas molecules using nitrogen physisorption. As indicated by the lower adsorbed gas volume of the nanocomposite materials (Fig. S2), all metal oxides could penetrate in the porous hosts. The decrease in adsorption capacity with respect to the void hosts is quite remarkable. This phenomenon can be explained both by the weight increase of the materials and by the heterogeneous distribution of the nanoparticles in the pore network, which generates significant amount of close porosity, inaccessible to the nitrogen flow. In KIT-6 systems the lower relative pressure of the hysteresis closure point shows lowering of the mean pore size (Fig. S2a and PSD Fig. S5), as a result of the accumulation of oxide species on the pore surface. Moreover, the analysis of the desorption branch in SBA-15 isotherms can tell in what extent the pores are filled with metal oxide species (Fig. 3a) [43]. PFO and LCO nanocomposites empty via cavitation, whereas LFO shows a mixed voiding behavior. In agreement with literature reports [44,45], it may be suggested that LFO distributes in small isolated domains, whereas PFO and LCO form larger nanoparticles, which massively block the pore space, forcing the gas to exit from very small apertures. These findings correlate very well with XRD results of Fig. 2. Further agreement is noted in the isotherms of FDU-12 systems and LCO@FDU-12 (Fig. 3b, Fig. S2e). Here, the steep increase in the final part of the adsorption step is typical of interparticle space, most probably formed by aggregation of crystalline domains grown outer the pores. In the case of the ink-bottle pore systems, the size of the connecting pores controls the outcomes of gas physisorption analysis. For KIT-5 and FDU-12 the small pore openings (Fig. 1) are significantly blocked by the metal oxide species and the observed isotherms mostly refer to the not infiltrated regions, completely accessible to the gas flow. Clear evidence of this effect is given by the pore size distribution plots of the nanocomposites (Fig. 3c, Fig. S5). The dimension of the spherical cavities remains unchanged, while the volume of the small mesopores is sensibly reduced. The larger size (4.5 nm) of the connecting pores in L-FDU-12 hosts favors the gas accessibility, thus enabling the inspection of the cage-like cavities. Lower pore widths are observed, especially for the LCO sample, evidencing the successful impregnation of the spherical pores and the formation of nanoparticles inside the voids (Fig. 3c). For the sake of completeness it should be pointed out that in all hosts also micropores are present, as usual in block copolymer templated silica. According to the literature, partial filling of these voids is likely to occur [46,47]. However, this contribution can be considered almost constant in all hosts and does not depend by pore geometry, thus playing a minor role in the interpretation of the data.

Electron microscopy offers a valuable opportunity to get clear evidence of the microstructure and topological properties of the silica based nanocomposites [48,49]. With respect to the ink-bottle pore systems, all materials present filling of the connecting

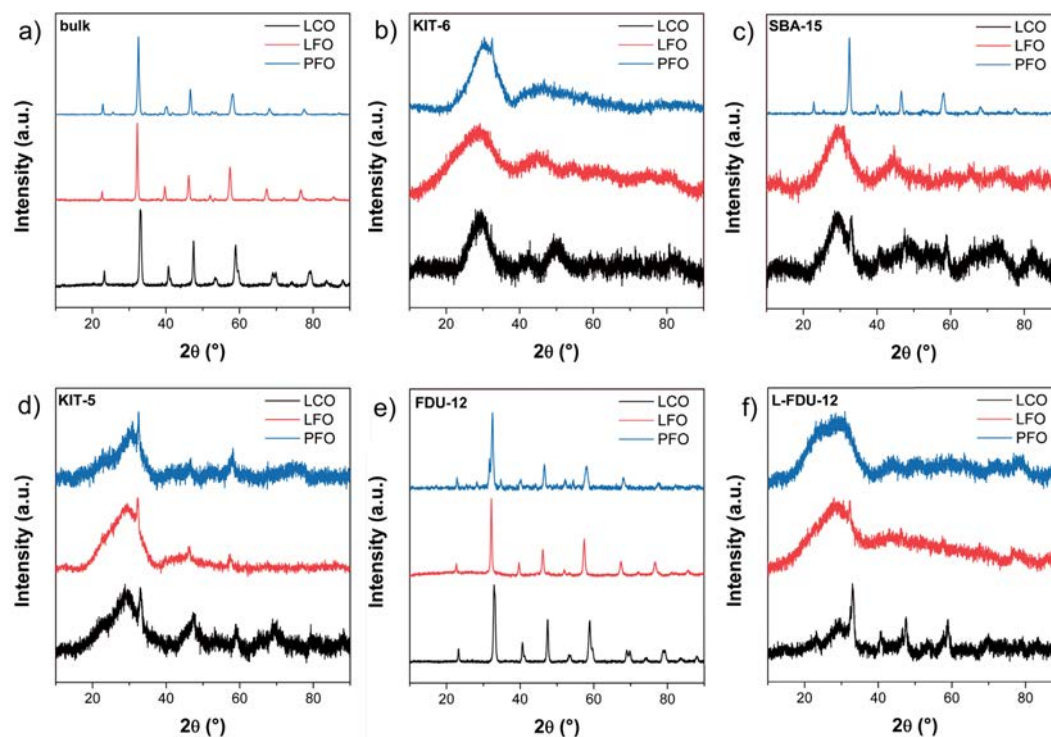
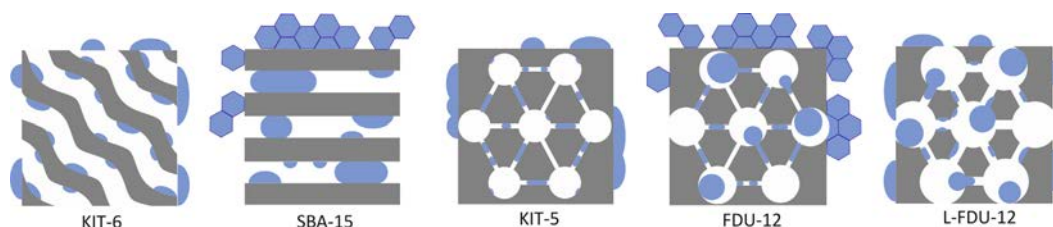


Fig. 2. XRD patterns of the bulk (a) and supported (b–f) LaCoO_3 (LCO, black), LaFeO_3 (LFO, red) and PrFeO_3 (PFO, blue). The broad patterns in b–f, originated by the superposition of silica and perovskite microstructure, indicate the low crystallinity of the materials. In FDU-12 along with PrFeO_3 also the $\text{Pr}_3\text{Fe}_5\text{O}_{12}$ phase was found via Rietveld analysis. (For interpretation of the references to colour in this figure legend, the reader is referred to the web version of this article.)



Scheme 1. Representation of PrFeO_3 distribution in the different host matrices. Depending on the pore geometry conditions either small isolated (KIT-6, KIT-5) or large particles (SBA-15, FDU-12) can be found. Crystalline material, observed mostly outside the pores, was formed only in presence of large confined oxide domains. For the sake of clarity the micropores are not depicted. The illustrations show an idealized scenario with higher pore filling than observed.

pores as shown by the brighter regions and dots at the pore walls of the HAADF S-TEM scans (Fig. 4). In FDU-12 systems it is clearly shown, that nanoparticles grew inside the pore space (brighter dots in Fig. 4a,b). In cylindrical pore systems large PFO domains can be observed in the channels of SBA-15 (Fig. 4c), confirming the findings of the physisorption analysis. All systems with crystalline perovskite phase (Fig. 2) evidence remarkable formation of crystalline nanoparticles outside the pore space (Fig. 4d), the size of which is in quite good agreement with the Rietveld analyses results (see Table S1). As EDX spectroscopy analyses showed (Fig. S6), the hosts were all homogeneously infiltrated with the guest species, with filling grade of ca. 5% (Table S2) [46]. Hence,

particle formation on the silica grain might be due to release of perovskite precursor from the pores during the calcination process (see below).

Small-angle X-ray scattering is a further suitable method for the characterization of the metal oxide nanoparticles distribution, because it addresses quantitative morphological and structural information on nanoporous systems (e.g., surface area, pore size, and pore structure) in comprehensive and direct fashion [50,51]. In the case of metal oxide nanocomposites the electron density of the guest nanoparticles is usually higher than the porous silica matrix. The analysis of such three phase systems (silica, particles and voids) is still possible using physical models and several

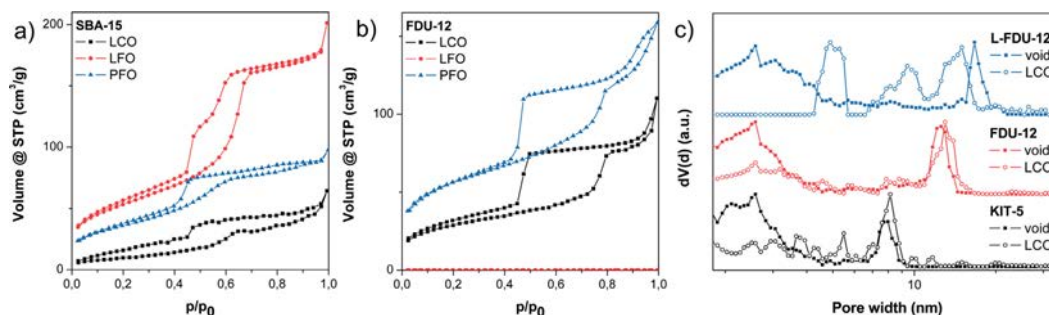


Fig. 3. Physiosorption isotherms of the SBA-15 (a) and FDU-12 nanocomposites (b). Pore size distribution of the LaCoO_3 -supported silica with ink-bottle pore geometry (c).

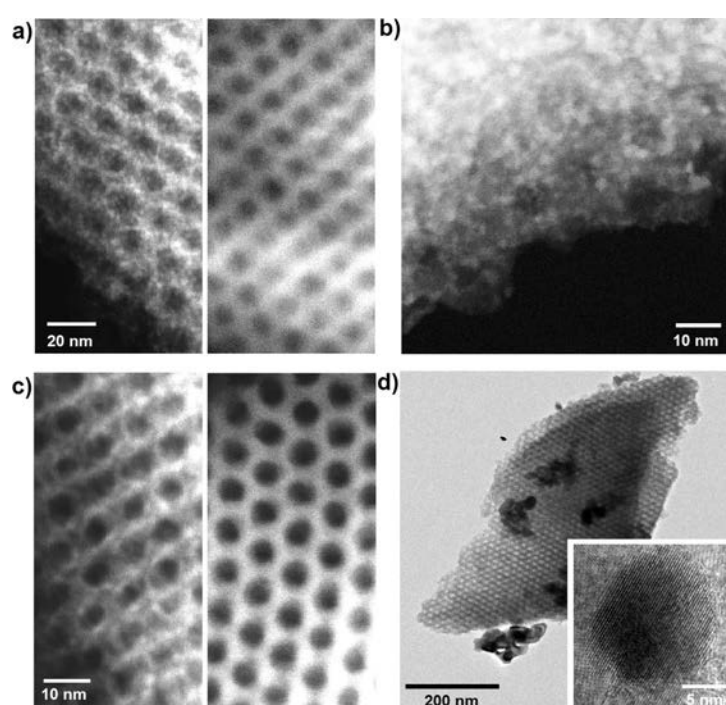


Fig. 4. (a) HAADF-STEM images of small PFO particles in FDU-12 (left-side) and void FDU-12 (right-side) for comparison; (b) HAADF-STEM image of LFO particles (brighter dots) in FDU-12 at higher magnification. (c) The covering of the pore channels in SBA-15 with PFO is presented in HAADF-STEM image (left-side) and for comparison the non-impregnated SBA-15 (right-side). (d) TEM overview of host structure FDU-12 with crystalline LFO particles (inset) outside of the porous structure (d).

structural assumptions, but is highly demanding [49]. Hence, we limit here to a qualitative study of the scattering curves, since detailed analysis goes beyond the scope of this work.

In the SAXS curves of the nanocomposites, the perovskite oxide scattering superposes the mesopores contribution. As a result, higher total intensities are observed especially at low scattering vectors (Fig. 5 and Fig. S7). The difference is less pronounced in the final part of the curve, owing to the partial pore filling. Additional proof of the successful impregnation is the shift of the host Bragg peaks toward higher q -vectors. According to the literature this effect is to be ascribed to contraction of the mesoporous network during the drying process of the metal oxide precursor

solution in the pores [45,52]. The deformation is more prominent in KIT-6 (Fig. S7a) and SBA-15 (Fig. 5a) hosts, because the Laplace pressure responsible of the strain [53] affects more such open channel-like structures than ink-bottle pore geometries. The effective impregnation of these bimodal structures is better appreciated by the clear appearance of the $Fm\bar{3}m$ lattice peaks (200), (310), (420) and (440), which indicate the filling of the small connecting mesopores (Fig. 5b). As we demonstrated in previous reports, the higher density of the filled pore walls enhances the scattering contrast between the solid matrix and the spherical voids highlighting the signals of the cubic arrangement of the pores [41,54].

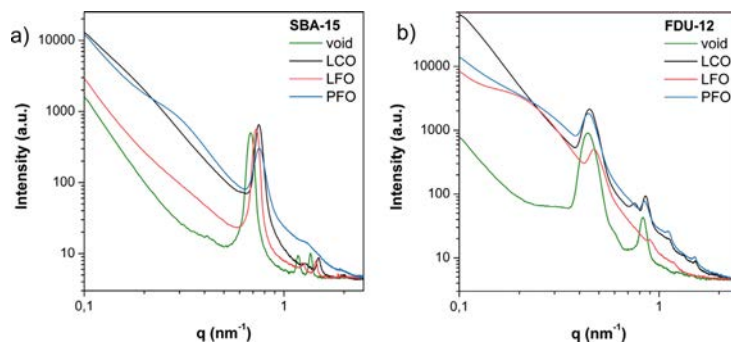


Fig. 5. SAXS patterns of the void and impregnated SBA-15 (a) and FDU-12 (b) hosts.

As interface analysis technique, SAXS is very sensitive to uniform and defined bodies, thus providing insights into the location of the perovskite nanoparticles. All the systems with highly crystalline phase denote a prominent shoulder in the first part of the SAXS curve, which represents very well the particles growing outside the pore space as shown by TEM. Further, in PFO@SBA-15 and LFO@FDU-12 patterns fewer, broader reflexes are present, which indicate that the scattering originated from the pores superpose with other contribution of the same length scale. This finding can be correlated with the remarkable growth of the metal oxide nanoparticles inside the pore space of these hosts, as already found out by nitrogen physisorption and TEM.

3.4. Formation mechanism of the supported perovskite oxides

Careful analysis of the distribution of the metal oxide species in the porous host is of prime importance for further use of the materials, but does not explain the origin of microstructural differences. As previously shown by XRD, the diverse pore geometries and oxide compositions play a fundamental role on the crystallization mechanism of the perovskite phase. Here, we want to understand such influences by following the degradation behavior of the metal nitrate precursors via thermogravimetric analyses coupled with mass spectroscopy (TG-MS). The conversion of LCO-based materials could not be investigated due to the violent exothermic degradation, which led to material loss from the thermobalance crucible, thus invalidating the analysis. Hence, only LFO-based and PFO-based systems are compared. Owing to the different nature of the perovskite A-site cation, the thermograms present very different profiles (Fig. S8). All LFO materials show a sharp mass loss between 150 °C and 170 °C, whereas for PFO the degradation occurs more smoothly and at higher temperatures, i.e. 200 °C upward. Accurate analysis of the precursor decomposition in bulk and nanocomposite materials was provided by mass spectroscopy investigations, following the evolution of several gaseous byproducts such as NO, NO₂, H₂O, CH₃, CO and CO₂ (Fig. 6 and Fig. S9). The conversion in the nanocomposites occurred at much lower temperatures and in many cases more suddenly than in bulk materials, evidencing a clear effect of nanoconfinement. Fundamental information for the understanding of the crystallization mechanism of the oxides are given by the analysis of NO, CO and H₂O release (Fig. 6) [10,14]. In KIT-6, the low pore curvature and the highly open pore framework favors the escape of the byproducts in both oxide systems, indicated by an abrupt gas evolution. As also shown by Sun et al. [15] such rapid gas development causes solidification of isolated nanoparticles in the pore channels. Hence, being mass transport inhibited, nucleation and particle growth

cannot occur properly, and quasi-amorphous materials result (Fig. 2b).

The same behavior is observed in LFO on SBA-15, but not in the PFO system (Scheme 2). Here, the degradation of praseodymium nitrate with respect to lanthanum nitrate is much more affected by the higher pore curvature and less open pore structure of the SBA-15 host. The byproducts constantly evolve for a much longer temperature range (ca. 200 °C), especially water. The slow evaporation kinetic enables to keep the metal species in liquid form, fostering mass transport in the pore channels and the formation of large domains (Scheme 2B, Fig. 4a,c) [19]. These can later migrate out of the pore space where can better crystallize (Scheme 2C, Fig. 4d). The same water evolution profile can be noticed also in the cage-like pore system KIT-5 (Fig. 6c,f), confirming the direct and strong dependency of pore curvature with degradation kinetics. However, only a hint of crystallization can be here observed. The reason of this finding can be explained as follows. In SBA-15 two conditions are realized to get crystalline nanoparticles in the pores: slow evaporation kinetics and mass transport to ensure large particles formation. Owing to the bimodal pore structure of KIT-5, the precursors are confined both in spherical and connecting pores. The thick pore walls and the ink-bottle geometry (Table 1, Fig. 1) hinder the transport between the larger cavities. Hence, the isolated particles are too small to grow, showing a similar situation as in KIT-6. As soon as the size of the cage pore is widened, i.e. in FDU-12, a different scenario is presented. The three times higher cage volume (536 nm³ and 1808 nm³ for KIT-5 and FDU-12, respectively) combined with the slow water evaporation, fosters the growth of larger particles inside the cage, thus enabling the formation of highly crystalline systems (Fig. 2e). The unusual LFO nanoparticle concentration in the pores of FDU-12 observed by SAXS and correlated with the highly inaccessible pore network (see isotherm Fig. 3b), can be better understood with closer look on the evolution of nitric oxide and carbon monoxide. The rapid release (significantly earlier than in other structures) boosts the formation of aqueous precursor phase, which can later crystallize more efficiently [15]. Finally, in L-FDU-12 systems the development of water occurs smoothly, as for the other ink-bottle pore systems KIT-5 and FDU-12. However, the mass spectra in Fig. 6c, e,f clearly evidence that the degradation of the metal oxide precursors takes place at much higher temperatures than in the other hosts. As shown elsewhere [55], higher decomposition temperatures of the precursors affect the crystallization in perovskite oxide systems. Additionally, in these nanocomposites the pore size is just few nanometers smaller than in the pristine host (Fig. S5e), indicating the presence of small guest particles in the voids. Based on these findings we suggest that, the combination

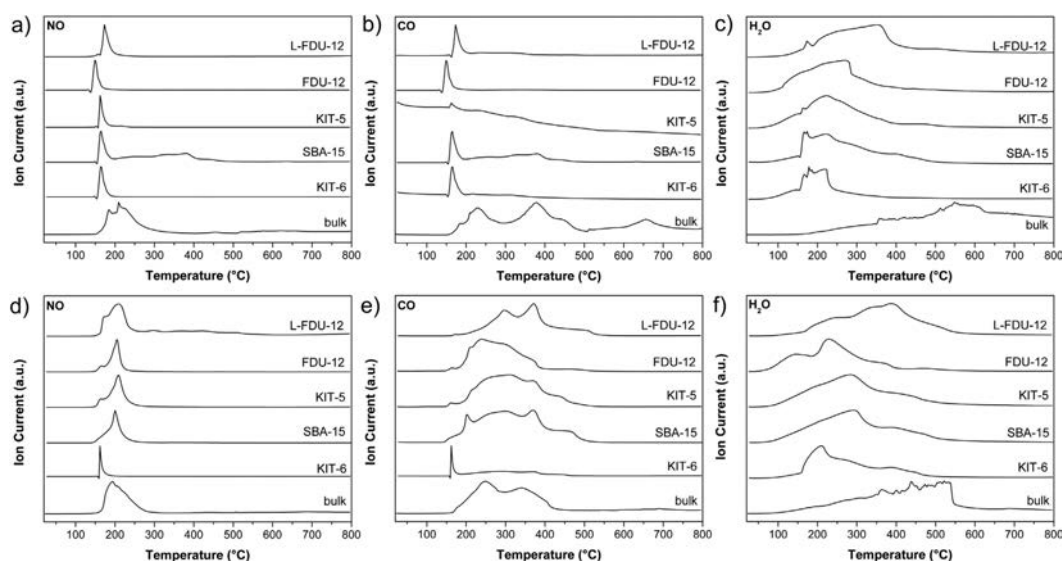
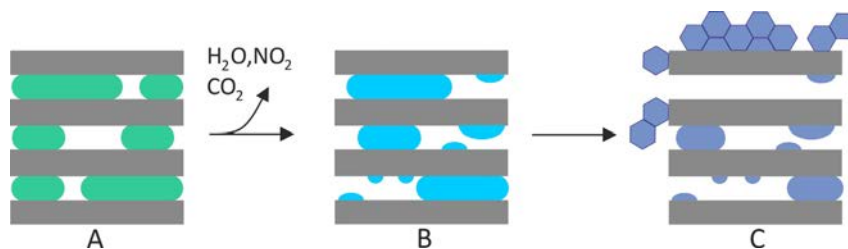


Fig. 6. Mass spectra of NO, CO and H₂O during the conversion of the precursors to LaFeO₃ (a–c) and PrFeO₃ (d–f) in the different host matrices.



Scheme 2. Sketch of the PrFeO₃ formation in SBA-15 chosen to illustrate the synthesis mechanism of the perovskite nanoparticles in porous hosts. Impregnation of the host with metal salts precursors (A), conversion to large liquid-like domains (B) and migration out of the pore followed by crystallization (C). The illustrations show an idealized scenario with higher pore filling than observed.

of higher degradation temperature along with the widespread distribution of the precursors in the large cavities of I-FDU-12 inhibit the crystallization process.

In conclusion, we can say that both ideal pore structure and favorable precursor degradation are the conditions to be fulfilled to form crystalline particles confined in porous hosts. For the metal salts conversion the key step is the water evolution which needs to take place smoothly and at sufficient low temperatures (ca. 100 °C) to build large domains of dense liquid. However the mass migration necessary at this stage is hindered if the pores are too small or badly connected. If such prerequisites are not met, isolated oxide particles are obtained, being too small to crystallize properly.

4. Conclusion

The role of the pore geometry on the synthesis of confined perovskite oxides was investigated addressing both particle distribution and their crystallization conditions. Systematic study was performed as function of pore shape (gyroidal, cylindrical, spherical) and size (7.5, 12, 17 nm). In order to perform a consistent

analysis of the pore geometry effect, the formation of three different oxide systems (LaFeO₃, PrFeO₃ and LaCoO₃) was analyzed.

We could show that the combination of pore size, connectivity and shape of the host has remarkable effect on the distribution and microstructural properties of the guest systems. In particular, the enhancement of pore curvature improves the crystallinity of the supported perovskite oxides. Mass spectroscopy investigations evidenced that the pore shape has an active role on the degradation kinetics of the impregnated precursors, especially on the evolution of water. The slow evaporation observed in curved porous systems with sufficient pore size (e.g. SBA-15 and FDU-12) induced the formation of liquid-like domains, which could later nucleate and crystallize. This mechanism was initially proposed by Stucky and Zhao [15], in describing the role of the glass container geometry for the preparation of mesoporous oxides via nanocasting. In our work we could demonstrate that the same process can be applied to the nanoscale, in which the porous silicas act as nanoreactor, directing morphology and microstructure of the guest materials. Hence, this nano-container effect can be in the future exploited to open up to a completely new approach for the synthesis of nanostructured host-guest systems using impregnation procedure.

Acknowledgments

SM thanks Prof. Dr. Michael Fröba of the University of Hamburg for the support and the fruitful discussions. Dr. Young Joo Lee, Sandra König and Isabelle Nevoigt of the University of Hamburg are gratefully acknowledged for the NMR, physisorption and x-ray diffraction measurements, respectively.

Appendix A. Supplementary material

Supplementary data associated with this article can be found, in the online version, at <http://dx.doi.org/10.1016/j.jcis.2017.05.107>.

References

- [1] P.E. De Jongh, T.M. Eggenhuisen, Melt infiltration: an emerging technique for the preparation of novel functional nanostructured materials, *Adv. Mater.* 25 (2013) 6672–6690, <http://dx.doi.org/10.1002/adma.201301912>.
- [2] L. Borchardt, W. Nickel, M. Casco, I. Senkowska, V. Bon, D. Wallacher, N. Grimm, S. Krause, J. Silvestre-Albero, Illuminating solid gas storage in confined spaces - methane hydrate formation in porous model carbons, *Phys. Chem. Chem. Phys.* 18 (2016) 20607–20614, <http://dx.doi.org/10.1039/C6CP03993F>.
- [3] P. Adelhelm, P.E. de Jongh, The impact of carbon materials on the hydrogen storage properties of light metal hydrides, *J. Mater. Chem.* 21 (2011) 2417, <http://dx.doi.org/10.1039/c0jm02593c>.
- [4] P.G. Bruce, S.A. Freunberger, L.J. Hardwick, J.M. Tarascon, Li–O₂ and Li–S batteries with high energy storage, *Nat. Mater.* 11 (2011) 172, <http://dx.doi.org/10.1038/nmat3237>.
- [5] X. Ji, K.T. Lee, L.F. Nazar, A highly ordered nanostructured carbon-sulphur cathode for lithium-sulphur batteries, *Nat. Mater.* 8 (2009) 500–506, <http://dx.doi.org/10.1038/nmat2460>.
- [6] T. Waitz, T. Wagner, T. Sauerwald, C.D. Kohl, M. Tiemann, Ordered mesoporous In₂O₃: synthesis by structure replication and application as a methane gas sensor, *Adv. Funct. Mater.* 19 (2009) 653–661, <http://dx.doi.org/10.1002/adfm.200801458>.
- [7] T. Wagner, S. Haffer, C. Weinberger, D. Klaus, M. Tiemann, Mesoporous materials as gas sensors, *Chem. Soc. Rev.* 42 (2013) 4036–4053, <http://dx.doi.org/10.1039/C2CS35379B>.
- [8] D.J. Lensveld, J. Gerbrand Mesu, A. Jos van Dillen, K.P. de Jong, Synthesis and characterisation of MCM-41 supported nickel oxide catalysts, *Microporous Mesoporous Mater.* 44 (2001) 401–407, [http://dx.doi.org/10.1016/S1387-1811\(01\)00214-1](http://dx.doi.org/10.1016/S1387-1811(01)00214-1).
- [9] M. Dreifke, D.J. Fried, F.J. Brieler, M. Fröba, Kinetic investigations of 6-phosphogluconate dehydrogenase confined in mesoporous silica, *J. Mol. Catal. B Enzym.* 132 (2016) 5–15, <http://dx.doi.org/10.1016/j.molcatb.2016.06.009>.
- [10] J.R.A. Sietsma, H. Friedrich, A. Broersma, M. Versluijs-Helder, A. Jos van Dillen, P.E. de Jongh, K.P. de Jong, How nitric oxide affects the decomposition of supported nickel nitrate to arrive at highly dispersed catalysts, *J. Catal.* 260 (2008) 227–235, <http://dx.doi.org/10.1016/j.jcat.2008.10.007>.
- [11] Y. Wang, F. Caruso, Nanoporous protein particles through templating mesoporous silica spheres, *Adv. Mater.* 18 (2006) 795–800, <http://dx.doi.org/10.1002/adma.200501901>.
- [12] V. Mamaeva, C. Sahlgren, M. Lindén, Mesoporous silica nanoparticles in medicine—recent advances, *Adv. Drug Deliv. Rev.* 65 (2013) 689–702, <http://dx.doi.org/10.1016/j.addr.2012.07.018>.
- [13] D. Gu, F. Schüth, Synthesis of non-siliceous mesoporous oxides, *Chem. Soc. Rev.* 43 (2014) 313–344, <http://dx.doi.org/10.1039/C3CS60155B>.
- [14] M. Wolters, P. Munnik, J.H. Bitter, P.E. de Jongh, K.P. de Jong, How NO affects nickel and cobalt nitrates at low temperatures to arrive at highly dispersed silica-supported nickel and cobalt catalysts, *J. Phys. Chem. C* 115 (2011) 3332–3339, <http://dx.doi.org/10.1021/jp1081406>.
- [15] X. Sun, Y. Shi, P. Zhang, C. Zheng, X. Zheng, F. Zhang, Y. Zhang, N. Guan, D. Zhao, G.D. Stucky, Container effect in nanocasting synthesis of mesoporous metal oxides, *J. Am. Chem. Soc.* 133 (2011) 14542–14545, <http://dx.doi.org/10.1021/ja2060512>.
- [16] J.-M. Ha, B.D. Hamilton, M.A. Hillmyer, M.D. Ward, Phase behavior and polymorphism of organic crystals confined within nanoscale chambers, *Cryst. Growth Des.* 9 (2009) 4766–4777, <http://dx.doi.org/10.1021/cg9006185>.
- [17] J.M. Ha, J.H. Wolf, M.A. Hillmyer, M.D. Ward, Polymorph selectivity under nanoscopic confinement, *J. Am. Chem. Soc.* 126 (2004) 3382–3383, <http://dx.doi.org/10.1021/ja049724r>.
- [18] Q. Jiang, C. Hu, M.D. Ward, Stereochemical control of polymorph transitions in nanoscale reactors, *J. Am. Chem. Soc.* 135 (2013) 2144–2147, <http://dx.doi.org/10.1021/ja312511v>.
- [19] Q. Jiang, M.D. Ward, Crystallization under nanoscale confinement, *Chem. Soc. Rev.* 43 (2014) 2066–2079, <http://dx.doi.org/10.1039/c3cs60234f>.
- [20] Y. Diao, T. Harada, A.S. Myerson, T.A. Hatton, B.L. Trout, The role of nanopore shape in surface-induced crystallization, *Nat. Mater.* 10 (2011) 867–871, <http://dx.doi.org/10.1038/nmat3117>.
- [21] H. Li, J. Zhu, P. Xiao, Y. Zhan, K. Lv, L. Wu, M. Li, On the mechanism of oxidative degradation of rhodamine B over LaFeO₃ catalysts supported on silica materials: Role of support, *Microporous Mesoporous Mater.* 221 (2016) 159–166, <http://dx.doi.org/10.1016/j.micromeso.2015.09.034>.
- [22] S. Haffer, T. Waitz, M. Tiemann, Mesoporous In₂O₃ with regular morphology by nanocasting: a simple relation between defined particle shape and growth mechanism, *J. Phys. Chem. C* 114 (2010) 2075–2081, <http://dx.doi.org/10.1021/jp910336f>.
- [23] F. Deganello, M.L. Testa, V. La Parola, A. Longo, A.C. Tavares, LaFeO₃-based nanopowders prepared by a soft-hard templating approach: The effect of silica texture, *J. Mater. Chem. A* 2 (2014) 8438–8447, <http://dx.doi.org/10.1039/c3ta15382g>.
- [24] D. Zhao, Y. Wan, W. Zhou, *Ordered Mesoporous Materials*, Wiley-VCH Verlag & Co, KGaA, 2013.
- [25] B. Smarsly, M. Groenewolt, M. Antonietti, SAXS analysis of mesoporous model materials: A validation of data evaluation techniques to characterize pore size, shape, surface area, and curvature of the interface, *Prog. Colloid Polym. Sci.* 130 (2005) 105–113, <http://dx.doi.org/10.1007/b107347>.
- [26] S. Royer, D. Duprez, F. Can, X. Courtois, C. Batio-Dupeyrat, S. Laassiri, H. Alamdari, Perovskites as substitutes of noble metals for heterogeneous catalysis: Dream or reality, *Chem. Rev.* 114 (2014) 10292–10368, <http://dx.doi.org/10.1021/cr500032a>.
- [27] B.E. Kayaalp, Y.J. Lee, A. Kornowski, S. Gross, M. D'Arienzo, S. Mascotto, Cooperative assembly synthesis of mesoporous SrTiO₃ with enhanced photocatalytic properties, *RSC Adv.* 6 (2016) 90401–90409, <http://dx.doi.org/10.1039/C6RA13800D>.
- [28] D. Zhao, J. Feng, Q. Huo, N. Melosh, G. Fredrickson, B. Chmelka, G. Stucky, Triblock copolymer syntheses of mesoporous silica with periodic 50 to 300 angstrom pores, *Science* (80-) 279 (1998) 548–552, <http://dx.doi.org/10.1126/science.279.5350.548>.
- [29] F. Kleitz, S.H. Choi, R. Ryoo, Cubic Ia3d large mesoporous silica: synthesis and replication to platinum nanowires, carbon nanorods and carbon nanotubes, *Chem. Commun.* (2003) 2136–2137, <http://dx.doi.org/10.1039/b306504a>.
- [30] F. Kleitz, D.N. Liu, G.M. Anilkumar, I.S. Park, L.A. Solovov, A.N. Shmakov, R. Ryoo, Large cage face-centered-cubic Fm3m mesoporous silica: synthesis and structure, *J. Phys. Chem. B* 107 (2003) 14296–14300, <http://dx.doi.org/10.1021/jp036136b>.
- [31] K. Morishige, K. Yoshida, Neck size of ordered cage-type mesoporous silica fdu-12 and origin of gradual desorption, *J. Phys. Chem. C* 114 (2010) 7095–7101, <http://dx.doi.org/10.1021/jp100171n>.
- [32] T. Yu, H. Zhang, X. Yan, Z. Chen, X. Zou, P. Oleynikov, D. Zhao, Pore structures of ordered large cage-type mesoporous silica FDU-12s, *J. Phys. Chem. B* 110 (2006) 21467–21472, <http://dx.doi.org/10.1021/jp064534j>.
- [33] M. Sadakane, A. Takahito Asanuma, W. Jun Kubo, Ueda, Facile procedure to prepare three-dimensionally ordered macroporous (3DOM) Perovskite-type mixed metal oxides by colloidal crystal templating method, *Chem. Mater.* 17 (2005) 3546–3551, <http://dx.doi.org/10.1021/CM050551U>.
- [34] X. Deng, K. Chen, H. Tüysüz, A Protocol for the nanocasting method: preparation of ordered mesoporous metal oxides, *Chem. Mater.* 29 (2017) 40–52, <http://dx.doi.org/10.1021/acs.chemmater.6b02645>.
- [35] G. Ashiotis, A. Deschilde, Z. Nawaz, J.P. Wright, D. Karkoulis, F.E. Picca, J. Kieffer, The fast azimuthal integration Python library: PyFAI, *J. Appl. Crystallogr.* 48 (2015) 510–519, <http://dx.doi.org/10.1107/S1600576715004306>.
- [36] D. Balzar, N. Audebrand, M.R. Daymond, A. Fitch, A. Hewat, J.I. Langford, A. Le Bail, D. Louër, O. Masson, C.N. McCowan, N.C. Popa, P.W. Stephens, B.H. Toby, Size-strain line-broadening analysis of the ceria round-robin sample, *J. Appl. Crystallogr.* 37 (2004) 911–924, <http://dx.doi.org/10.1107/S0021889804022551>.
- [37] S. Brunauer, P.H. Emmett, E. Teller, Adsorption of gases in multimolecular layers, *J. Am. Chem. Soc.* 60 (1938) 309–319, <http://dx.doi.org/10.1021/ja01269a023>.
- [38] A.V. Neimark, P.I. Ravikovitch, Capillary condensation in MMS and pore structure characterization, *Microporous Mesoporous Mater.* 44–45 (2001) 697–707, [http://dx.doi.org/10.1016/S1387-1811\(01\)00251-7](http://dx.doi.org/10.1016/S1387-1811(01)00251-7).
- [39] S. Förster, L. Apostol, W. Bras, Scatter : software for the analysis of nano- and mesoscale small-angle scattering, *J. Appl. Crystallogr.* 43 (2010) 639–646, <http://dx.doi.org/10.1107/S0021889810008289>.
- [40] S. Förster, A. Timmann, M. Konrad, A.C. Schellbach, A. Meyer, S.S. Funari, P. Mulvaney, R. Knott, Scattering curves of ordered mesoscopic materials, *J. Phys. Chem. B* 109 (2005) 1347–1360.
- [41] S. Mascotto, D. Kuzmicz, D. Wallacher, M. Siebenbürger, D. Clemens, S. Risse, J. Yuan, M. Antonietti, M. Ballauff, Poly(ionic liquid)-derived nanoporous carbon analyzed by combination of gas physisorption and small-angle neutron scattering, *Carbon* 82 (2015) 425–435, <http://dx.doi.org/10.1016/j.carbon.2014.10.086>.
- [42] Y. Wan, H. Yang, D. Zhao, Host-guest chemistry in the synthesis of ordered materials, *Acc. Chem. Res.* 39 (2006) 423–432, <http://dx.doi.org/10.1021/ar050091a>.
- [43] J.R.A. Sietsma, J.D. Meeldijk, M. Versluijs-Helder, A. Broersma, A.J. van Dillen, P. E. de Jongh, K.P. de Jong, Ordered mesoporous silica to study the preparation of Ni/SiO₂ ex Nitrate catalysts: impregnation, drying, and thermal treatments, *Chem. Mater.* 20 (2008) 2921–2931, <http://dx.doi.org/10.1021/cm702610h>.
- [44] M. Tiemann, Repeated templating, *Chem. Mater.* 20 (2008) 961–971, <http://dx.doi.org/10.1021/cm702050s>.
- [45] M. Sakeye, S. Ziller, H. Amenitsch, M. Lindén, J.-H. Smätt, Detailed Study of the nanocasting process by in situ x-ray scattering and diffraction, *J. Phys. Chem. C* 120 (2016) 1854–1862, <http://dx.doi.org/10.1021/acs.jpcc.5b07993>.

- [46] X. Deng, W.N. Schmidt, H. Tüysüz, Impacts of geometry, symmetry, and morphology of nanocast Co_3O_4 on its catalytic activity for water oxidation, *Chem. Mater.* 26 (2014) 6127–6134, <http://dx.doi.org/10.1021/cm5023163>.
- [47] Y. Shi, Y. Wan, D. Zhao, Ordered mesoporous non-oxide materials, *Chem. Soc. Rev.* 40 (2011) 3854, <http://dx.doi.org/10.1039/c0cs00186d>.
- [48] F. Meneghetti, E. Wendel, S. Mascotto, B.M. Smarsly, E. Tondello, H. Bertagnolli, S. Gross, Combined use of XAFS, XRD and TEM to unravel the microstructural evolution of nanostructured ZrO_2 - SiO_2 binary oxides: from nanometres down to the molecular domain, *CrystEngComm*. 12 (2010) 1639, <http://dx.doi.org/10.1039/b911004f>.
- [49] C.J. Gommers, G. Prieto, J. Zecevic, M. Vanhale, B. Goderis, K.P. DeJong, P.E. DeJongh, Mesoscale Characterization of nanoparticles distribution using X-ray scattering, *Angew. Chemie - Int. Ed.* 54 (2015) 11804–11808, <http://dx.doi.org/10.1002/anie.201505359>.
- [50] B.M. Smarsly, H. Kaper, S. Mascotto, C. Weidmann, Charakterisierung mesoporöser Materialien mittels Kleinwinkelstreuung (SAXS/SANS), *Chemie-Ingenieur-Technik*. 82 (2010) 823–828, <http://dx.doi.org/10.1002/cite.201000075>.
- [51] A. Petzold, A. Juhl, J. Scholz, B. Ufer, G. Goerigk, M. Fröba, M. Ballauff, S. Mascotto, Distribution of sulfur in carbon/sulfur nanocomposites analyzed by small-angle x-ray scattering, *Langmuir*. 32 (2016) 2780–2786, <http://dx.doi.org/10.1021/acs.langmuir.5b04734>.
- [52] J. Prass, D. Mütter, P. Fratzl, O. Paris, Capillarity-driven deformation of ordered nanoporous silica, *Appl. Phys. Lett.* 95 (2009) 97–100, <http://dx.doi.org/10.1063/1.3213564>.
- [53] M. Erko, D. Wallacher, O. Paris, Deformation mechanism of nanoporous materials upon water freezing and melting, *Appl. Phys. Lett.* 101 (2012), <http://dx.doi.org/10.1063/1.4764536>.
- [54] S. Mascotto, D. Wallacher, A. Brandt, T. Hauss, M. Thommes, G.A. Zickler, S.S. Funari, A. Timmann, B.M. Smarsly, Analysis of microporosity in ordered mesoporous hierarchically structured silica by combining physisorption with in situ small-angle scattering (SAXS and SANS), *Langmuir*. 25 (2009) 12670–12681, <http://dx.doi.org/10.1021/la9013619>.
- [55] U. Hasenkox, S. Hoffmann, R. Waser, Influence of precursor chemistry on the formation of MTiO_3 (M = Ba, Sr) ceramic thin films, *J. Sol-Gel Sci. Technol.* 12 (1998) 67–79, <http://dx.doi.org/10.1023/A:1026480027046>.

6.3. Functional Nanostructured Perovskite Oxides from Radical Polymer Precursors

Jonas Scholz, Alberto Garbujo, Bugra Kayaalp, Kurt Klauke, Antonella Glisenti,
and Simone Mascotto

Reproduced with permission from *Inorg. Chem.* 2019, 58, 23, 15942–15952. Copyright © 2019 American Chemical Society. To access the final edited and published work see:

<https://doi.org/10.1021/acs.inorgchem.9b02460>

This work constitutes a new approach for the low-temperature synthesis of perovskite oxides based on a polymer complex route. This publication does not directly refer to porous systems, however, the nanostructure of the present materials, i.a. the crystallite sizes, and the surface morphology were thoroughly analyzed in order to impact the ensuing functional properties.

Different acrylic molecules (acrylamide, acrylic acid, methacrylic acid) were utilized both as monomers in a radical polymerization and as chelating agents for the complexation of precursor cations. The suitability of this method was confirmed for various La-based perovskite systems (LCO, LNO, LFO) as well as SrTiO₃ and solid-solutions thereof. Nanocrystalline oxides exhibiting minimal amounts of impurity phases were obtained at calcination temperatures as low as 600 °C.

In addition, the materials prepared by this method showed significantly improved functional properties compared to oxides prepared by a conventional citrate method. In the catalytic oxidation of CO over LaCoO₃, T₅₀ was achieved 30 °C lower by the acrylamide- and acrylic acid-derived oxide than by the conventionally prepared LCO. The acrylamide sample also displayed significantly improved oxygen exchange properties compared to conventional LCO, due to a combination of nanosized crystallites and few carbonate impurities.

While the initial choice of radical starter for the polymerization did not have any

influence on material properties, the use of an UV-initiator, i.e. a gentle polymerization process, did allow for a direct adaption of this method for a spin coating procedure. Highly homogeneous, nanocrystalline LaCoO_3 thin films were obtained from acrylamide monomers.

In conclusion, the use of bifunctional acrylic molecules provides perovskite oxides with improved functional properties. The synthesis can also be easily adjusted to prepare different forms of solids.

Functional Nanostructured Perovskite Oxides from Radical Polymer Precursors

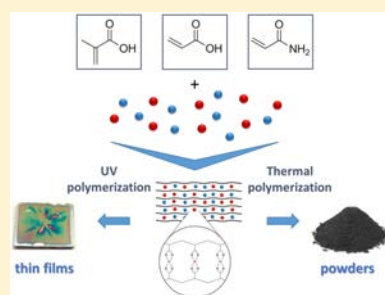
Jonas Scholz,[†] Alberto Garbujo,[‡] Buğra Kayaalp,[†] Kurt Klauke,[†] Antonella Glisenti,^{‡,§} and Simone Mascotto^{*,†,§}

[†]Institut für Anorganische und Angewandte Chemie, Universität Hamburg, Martin-Luther-King-Platz 6, 20146 Hamburg, Germany

[‡]Dipartimento di Scienze Chimiche, Università degli Studi di Padova, via Marzolo 1, 35131 Padova, Italy

Supporting Information

ABSTRACT: In the present work, nanostructured perovskite oxides with improved reactivity, tunable morphology, and different forms (powder, thin films) were prepared using acrylic molecules such as acrylamide, acrylic acid, and methacrylic acid as novel chelating agents in a straightforward fashion. The approach, developed for LaCoO_3 , was also applied to oxides of the type LaMO_3 ($M = \text{Fe}, \text{Ni}$), SrTiO_3 , and solid solutions thereof. The polymer-to-oxide evolution followed by XRD and IR showed merely a minimal amount of carbonate residuals even at temperatures as low as 600 °C. The different cross-linking degree of the polymeric compounds influenced the material crystallization leading to oxides with different grain sizes at the same calcination temperature. Among the prepared perovskites, acrylamide-derived LaCoO_3 exhibited the highest oxygen surface reactivity as demonstrated by XPS and TPD measurements. As a result, the materials showed enhanced catalytic performance, leading to complete oxidation of CO at approximately 200 °C, which was almost 100 °C lower than for citric-acid-based samples. Finally, by exploiting the UV photopolymerization of the acrylic group, homogeneous, crystalline perovskite thin films of optical quality were successfully prepared through a straightforward spin-coating approach. The findings of this work demonstrate that this novel synthesis route is a better alternative to state-of-the-art citrate-based methods for the preparation of prospective catalysis, sensing, and energy conversion materials of high purity, activity, and tunable form.



INTRODUCTION

Ternary oxides of the perovskite family are an outstanding class of materials due to their enhanced structural flexibility and ability to accommodate nonstoichiometry, which enables their use in sensing,¹ energy,² data storage,³ and in various catalytic applications.^{4–6} In order to benefit from this wide application potential, it is necessary to develop synthesis strategies which generate materials with high chemical purity, surface activity, tunable textural properties (e.g., crystallinity, porosity), and different forms (e.g., powders, thin films).^{7,8}

With respect to solid state strategies, the liquid phase synthesis based on the polymer complex method⁹ is the most suitable procedure for this purpose because it relies on a sol-gel-like chemistry.¹⁰ This approach is based on the use of bifunctional organic molecules, which act both as chelating agents for the metal cations and as monomers, thus evolving into an organic–inorganic polymeric material when heated. Subsequent to thermal degradation of the macromolecule, the oxide phase is obtained. Citric acid (CA), well-known for the Pechini¹¹ and citrate methods,¹² is the most widespread chelating agent because of its three carboxylic groups, which act both as complexing and polymerizing units via polycondensation. In order to ensure proper ion complexation, CA is used in molar excess and often with ligands of higher

denticity such as EDTA.¹³ As a consequence of the high organic content in the reaction mixture, spontaneous formation of carbonate phases occurs during the thermal conversion to oxides. The group of Caro investigated in great detail the degradation process of the CA/EDTA-based polymer to obtain complex perovskite solid solutions (e.g., $\text{Ba}_{0.5}\text{Sr}_{0.5}\text{Co}_{0.8}\text{Fe}_{0.2}\text{O}_{3-\delta}$) by TEM and related spectroscopic techniques.¹⁴ They found that the perovskite structure starts to form at 600–650 °C due to the decomposition of carbonate and spinel intermediates. Whereas spinel compounds readily decomposed at temperatures below 500 °C, alkaline-earth carbonates completely disappeared only at 750 °C after 10 h of annealing. Similar findings were confirmed by Najjar and Batis,¹⁵ who were able to demonstrate a reduction but not the complete elimination of La-based carbonate impurities in LaMnO_3 even after 24 h at 700 °C using IR spectroscopy.¹⁵ These species have serious detrimental effects especially on the (electro)catalytic properties of the perovskite as they block the oxygen surface exchange and hinder the charge carrier transport in the material.^{16–18} Such prolonged high temperature treatments required to achieve phase purity lead to an

Received: August 13, 2019

Published: November 11, 2019

inevitable collapse of the porous structure and thereby shrinkage of specific surface area.

Therefore, strategies should be developed to effectively reduce carbonate impurities at lower temperatures. One possibility is to limit the molar carbon content of the polymeric matrix by choosing chelating molecules with lower molecular weight than CA. In the present work, we show how methacrylic acid (MA), acrylic acid (AA), and acrylamide (AAM) are used as bifunctional networking and complexing agents to prepare highly pure perovskite oxides, with better oxygen surface exchange and catalytic activity than CA-based counterparts. In his comprehensive review work, Kakihana¹⁹ mentioned the use of acrylic monomers as possible complexing agents to be used in the polymer complex synthesis. In addition to the lower carbon content with respect to CA, the carboxylic/amidic functionalities are exclusively devoted to ion complexation as the polymerization proceeds through modification of the acrylic functionality.

Despite these attractive characteristics, the employment of acrylic monomers for the production of multimetal oxide systems is almost negligible in the literature. The main reason, most probably, lies in their assumed poor complexing capability, which would affect the phase purity of the oxide. This explains why, when used, they have been considered merely as networking agents and therefore were always combined with strong complexing molecules like EDTA or CA.^{20–22}

Herein, we follow accurately the acrylate-based synthesis mechanism of LaCoO₃ (LCO), chosen as a model compound, and thoroughly investigate its improved surface reactivity.

In contrast to CA-based polyesters, the thermal conversion of the radically formed polymers led to the formation of carbonate-poor perovskite structures at temperatures as low as 550–600 °C. Under such mild conditions, the materials exhibited not only moderate specific surface areas of approximately 20 m²/g but also very active surface chemistry. In particular, AAM-derived LCO showed much stronger release of oxygen up to 600 °C than all the other materials. As a result, functional assessment via catalytic CO oxidation demonstrated the enhanced conversion over acrylate-derived LCO with respect to the citrate-based counterpart.

Another advantage offered by the radical polymerization is its activation by UV light. In the context of today's environmental concerns, photopolymerization reactions have significant relevance as green technology procedures as they are characterized by low electrical power input, low temperature operation, and the absence of any volatile organic compound release. While powder materials prepared in this fashion exhibited very similar structural properties to the thermally polymerized counterparts, the UV photopolymerization showed great potential for directing the material form. In this way, crystalline, homogeneous thin films of LCO of optical quality could be prepared by spin coating in a facile and straightforward fashion.

Due to their low carbon content and flexible synthesis parameters, radical polymer complexes thus present a better alternative to standard citrate-based materials, leading to highly pure oxides with tunable morphology and enhanced catalytic activity. On the basis of these appealing material properties, this synthesis approach is therefore highly suitable for the preparation of highly performing heterogeneous catalysts and energy conversion materials.

EXPERIMENTAL PART

Chemicals. Acrylamide (98.5%, Acros Organics), acrylic acid (98.0%, Acros Organics), ammonia (25.0%, VWR Chemicals), benzoyl peroxide (97.0%, Alfa Aesar), cobalt nitrate hexahydrate (97.7%, Alfa Aesar), citric acid (99.6%, Acros Organics), dichloromethane (99.0%, BCD), dimethylformamide (99.5%, VWR Chemicals), ethanol (100%, VWR Chemicals), ethylene glycol (99.7%, VWR Chemicals), glycerol (99.0%, Alfa Aesar), hydrogen peroxide (30.0%, VWR Chemicals), 1-hydroxycyclohexyl phenyl ketone (98.0%, Alfa Aesar), iron nitrate nonahydrate (99.0%, Merck), lanthanum nitrate hexahydrate (99.9%, Alfa Aesar), methanol (100%, VWR Chemicals), methacrylic acid (99.5%, Acros Organics), nickel nitrate hexahydrate (97.0%, Sigma-Aldrich), poly(vinyl alcohol) (78.0%, Acros Organics), strontium nitrate (99.0%, Acros Organics), tetrahydrofuran (99.5%, VWR Chemicals), and titanium(IV) isopropoxide (97.0%, Alfa Aesar) were used as received without further purifications.

Acrylate-Based Synthesis of La-Based Perovskites. Perovskite oxides were prepared using a molar ratio of acrylate polymer to metal cations of 4:1. Equimolar amounts of lanthanum nitrate hexahydrate (433 mg) and either cobalt nitrate hexahydrate (298 mg), iron nitrate nonahydrate (408 mg), or nickel nitrate hexahydrate (300 mg) were dissolved in a mixture of solvent (1.0 mL) and a respective complexing agent—acrylamide (569 mg), acrylic acid (577 mg), or methacrylic acid (689 mg) within 10 min under stirring at room temperature. Various solvents could be applied for the reaction route including water (with the exception of methacrylic acid), DMF, THF, dichloromethane, methanol, and ethanol. In the case of thermal polymerization, benzoyl peroxide (10 mg) was added; the reaction mixture was stirred for 5 min at room temperature and then heated up to 80 °C for MA and AA solutions and 60 °C in the case of AAM-based solutions under stirring for 5 min to initiate the polymerization. With respect to the UV-light induced polymerization, 1-hydroxycyclohexyl phenyl ketone (10 mg) was added as radical initiator, and the solution was stirred for 5 min at room temperature. Subsequently, the reaction mixture, cast into a Petri dish, was exposed to UV radiation from a high-pressure mercury vapor lamp (Philips HPK-125 W) for 15 min at room temperature. The resulting polymer was then calcined in air using a heating rate of 2 °C/min at 400 °C for 2 h and subsequently at 600 °C for 2 h to guarantee complete removal of the organic content and the formation of the perovskite structure, respectively.

For reasons of simplicity, throughout the whole work, LaCoO₃ is referred to as LCO_X with X representing the complexing agent. Following the same principle, LaFeO₃, SrTiO₃, and LaNiO₃ are abbreviated as LFO_X, STO_X, and LNO_X, respectively.

Acrylate-Based Synthesis of SrTiO₃-Based Perovskites. In a typical MA-based chelating synthesis of SrTiO₃, methacrylic acid (9.72 g) and titanium(IV) isopropoxide (1.47 g) were respectively added to ethanol (7.0 mL) under continuous stirring. A second mixture was prepared by dissolving strontium nitrate (1.06 g) in ammonia solution (25 wt %, 3.3 mL) due to its insufficient solubility in ethanol. After stirring for 30 min, the ammonia-based solution was added dropwise to the first solution, and the resulting mixture was further stirred for 45 min. Finally, either benzoyl peroxide (40 mg) or 1-hydroxycyclohexyl phenyl ketone (50 mg) was added to the mixture as a thermal and photoinduced initiator, respectively. Thermal polymerization was undergone by heating the mixture to 90 °C under continuous stirring for 1 h. For UV-initiated polymerization, the solution was poured into a Petri dish, which was then irradiated with a high-pressure mercury vapor lamp (Philips HPK-125W) and kept at 50 °C simultaneously for solvent evaporation for 1 h. After drying overnight at ~60 °C, the polymers were ground and obtained powders were calcined under air employing a 2 °C/min heating ramp with a 2 h hold time at an intermediate temperature of 400 °C and a final temperature of 650 °C, respectively.

Citrate Method. For reasons of comparability, in this case the molar ratio of citric acid to metal cations was equally chosen as 4:1. Lanthanum nitrate hexahydrate (1.175 g), cobalt nitrate hexahydrate

(0.790 g), and citric acid (3.912 g) were dissolved in water (4.00 g) and then stirred at 70 °C for 90 min. Polycondensation of citric acid was promoted by heating up to 130 °C for 2 h. Subsequently, the gel was converted into the corresponding perovskite oxide by calcination in air at 600 °C for 2 h at a heating rate of 2 °C/min with an intermediate step of 2 h at 400 °C to ensure complete removal of the polymer.

Formation of LCO Thin Films. The synthesis of LCO thin films follows the acrylate-based synthesis of La-based perovskites with some slight modifications to adjust it to the spin coating process. Cobalt nitrate hexahydrate (433 mg), lanthanum nitrate hexahydrate (298 mg), and acrylamide (284 mg) were dissolved in methanol (0.67 mL) under stirring at room temperature within 5 min. Methanol as a solvent as well as an acrylamide to metal cation ratio of 2:1 were chosen to decrease the viscosity of the solution and enhance the wetting of the silicon substrate. 1-Hydroxycyclohexyl phenyl ketone (10 mg) was added as radical initiator, and the solution was stirred for another 5 min. In order to exclude possible impurities or residues, the solution was filtered using a PTFE syringe filter with a pore size of 0.45 μm . The silicon wafer was cleaned in a three-step process. First the wafer was placed in a solution of ammonia (25 wt %)/hydrogen peroxide (30 vol %)/demineralized water (ratios 1/1/5) for 15 min. Then, the wafer was put in an acetone bath for 15 min under ultrasonic stirring. Finally, this step was repeated using demineralized water as a solvent. Remaining water was removed using pressurized air.

Subsequently, the solution was spin coated onto a silicon wafer employing a SPIN150i infinite by Polos. For a wafer of the size 11 \times 11 mm, 50 μL of solution was dispensed dynamically while spinning at 8000 rpm for 30 s. The coated wafer was then irradiated by UV light with a high-pressure mercury vapor lamp (Philips HPK-125 W) for 15 min to guarantee complete polymerization. Finally, the coated wafer was calcined under air employing a 2 °C/min heating ramp with a 1 h hold time at 300 °C before maintaining 600 °C for 1 h to obtain the perovskite thin-film.

Characterization Methods. X-ray diffraction measurements were carried out with an X'Pert Pro diffractometer (PANalytical Corp.) with 0.15406 nm Ni-filtered Cu $K\alpha$ radiation in Bragg–Brentano geometry, operating at 45 kV and 40 mA, a step size 0.0130, and a step time 74 s per step. The crystallite size was determined using the Scherrer equation from the full width at half-maximum (fwhm) of the most intense reflection (110). The data analysis was performed using X'Pert HighScore Plus by PANalytical and the ICDD database for peak identification.

TG-DSC measurements were carried out using an STA 449 F3 Jupiter by Netzsch. The temperature profile followed the actual synthesis conditions, i.e., from RT to 400 °C with a heating rate of 2 °C/min, 2 h at 400 °C, another increase up to 600 °C with a heating rate of 2 °C/min, and a final step at 600 °C for 2 h. The measurement was performed under an oxygen/argon atmosphere (20/80) with a flow rate of 40 mL/min.

SEM images were obtained on a LEO1550 with a spatial resolution of \sim 1 nm. The powder was fixed on a standard carbon conductive tab and was investigated without further conductive coating. Energy dispersive X-ray (EDX) mapping was implemented on several analysis points on the sample, and average atomic ratios were calculated for each cation of LaCoO_3 .

^1H NMR spectra were obtained with a Bruker Avance I 500 MHz spectrometer with a 5 mm BBI sample holder with ATM and z-gradient. Before the measurement, the chemicals had been dissolved in D_2O .

The nitrogen sorption isotherms were obtained at 77 K using a Quadrasorb SI-MP by Quantachrome. Outgassing was performed with a Masterprep Degasser (Quantachrome Corp.) at 120 °C for 12 h. Specific surface areas were determined using the Brunauer–Emmett–Teller (BET) method²³ at $p/p_0 = 0.07$ – 0.3 .

IR spectroscopy was performed employing the KBr pellet technique; the mid-IR spectra from 4000 to 400 cm^{-1} were acquired with a Bruker Tensor 27. Correction of the baseline was achieved using the software OPUS 7.2 by Bruker.

X-ray photoelectron spectroscopy was carried out by means of a ParkinElmer PHI 5600ci Multi Technique System, using Al $K\alpha$ radiation (1486.6 eV) working at 250 W. The spectrometer was calibrated by assuming the binding energy (BE) of the Au 4f_{7/2} line to be 84.0 eV with respect to the Fermi level. Both extended spectra (survey –187.85 eV pass energy, 0.5 eV step⁻¹, 0.05 s step⁻¹) and detailed spectra (for La 3d, Co 2p, O 1s, and C 1s, –23.5 eV pass energy, 0.1 eV step⁻¹, 0.1 s step⁻¹) were collected. The standard deviation in the BE values of the XPS line is 0.10 eV. The atomic percentage, after a Shirley-type background subtraction,²⁴ was evaluated by using the PHI sensitivity factors.²⁵ The peak positions were corrected for the charging effects by considering the C 1s peak at 285.0 eV and evaluating the BE differences.²⁶ The fitting procedure was carried out after the Shirley-type background subtraction. The selected peak shape is a Voigt function in which the Lorentian amount and the fwhm are kept constant. These parameters have been selected taking into consideration the values obtained with the same instrument on corresponding simple oxides (lanthanum oxide, cobalt oxide).

Impedance spectroscopy was performed using a Novocontrol Alpha A impedance analyzer, a NORECs Probst sample chamber, and a Novocontrol-HT temperature controller. Measurements were recorded in the range between 10⁻² Hz and 10⁷ Hz with an amplitude of 50 mV_{rms}. Equivalent circuit fitting was performed using a Novocontrol WinFIT with an inductance representing the electrical leads and a resistor representing the sample connected in series. A flow of 20 sccm dry air and a dwelling time of 3 h at each temperature were employed. The as-prepared powders were first mixed with 3 wt % PVA as a binder and subsequently pressed into disks of 13 mm diameter and ca. 1 mm thickness at 222 MPa. Silver conductive paste (Plano GmbH) was applied to the flat sides, and the samples were subsequently heated to 600 °C for 12 h before the measurements were performed.

TG/MS and O₂-TPD measurements were performed using a QMS 403 Aëolos Quadro quadrupole mass spectrometer by Netzsch coupled with a thermal analyzer NETZSCH STA 449 F3 Jupiter. Each sample underwent two temperature cycles of heating up from room temperature to 600 °C using a heating ramp of 10 °C/min and then were maintained at 600 °C for 1 h before cooling down to room temperature at 10 °C/min. During the first cycle, an oxygen/argon atmosphere (50:50) with a flow rate of 500 mL/min was employed. During the second cycle, the measurement was performed under a pure argon atmosphere setting a flow rate of 240 mL/min.

The H₂-TPR measurements were carried out with a Chembet-3000 by Quantachrome equipped with a TCD detector. A 50 mg sample in a quartz reactor was heated from RT to 800 and 1000 °C using a heating rate of 10 °C/min under a constant flow (20 mL/min) of H₂ (5% in Ar). TPR samples were previously outgassed with Ar (20 mL/min) for 2 h at 200 °C.

The catalytic activity was determined by loading 50 mg of respective sample in a quartz reactor (6 mm i.d.). The temperature was monitored by a thermocouple inserted right upstream of the fixed bed. The conversion of CO and O₂ to CO₂ was studied using stoichiometric amounts of reactants (4% of CO and 2% of O₂) in a He atmosphere at a flow rate of 100 mL/min at atmospheric pressures. The flows were controlled by thermal mass flowmeters (Vögtlin Instruments). The temperature of the bed was raised from room temperature to 400 °C at a heating rate of 1 °C/min. The data was collected every 9 min using an Agilent 7890A gas chromatograph equipped with a TCD detector.

RESULTS AND DISCUSSION

In order to demonstrate that acrylic monomers do not solely serve networking purposes, as shown in the literature so far,²⁰ but can also be suitable complexing agents for metal ions, NMR analyses were performed. ^1H NMR spectra of an aqueous solution containing $\text{La}^{3+}/\text{Co}^{2+}$ cations and acrylic acid or acrylamide were compared to those of the acrylic monomers in water. As evidenced by Figure 1, the addition of cations

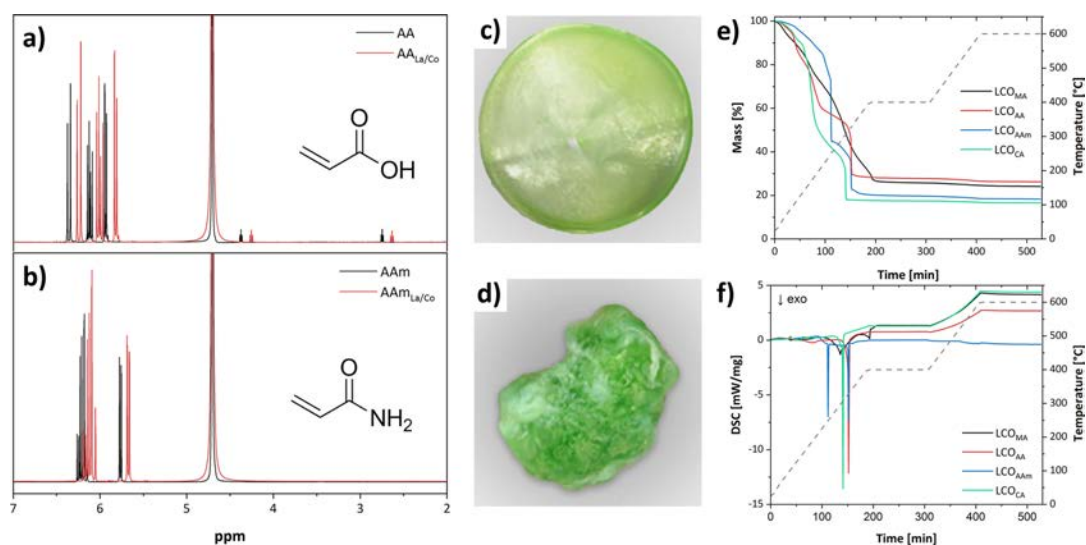


Figure 1. ¹H NMR spectra of acrylic acid dissolved in water (black) and acrylic acid and La³⁺/Co²⁺ cations dissolved in water (red, a) and of acrylamide dissolved in water (black) and acrylamide and La³⁺/Co²⁺ cations dissolved in water (red, b). Polyacrylic acid containing La and Ni cations obtained via UV initiated (c) and thermal polymerization (d) prior to calcination. Thermogravimetric analyses (e) and coupled DSC measurements (f) of LCO_{MA} (black), LCO_{AA} (red), LCO_{AAm} (blue) and LCO_{CA} (green) under synthesis conditions. The dashed gray line refers to the annealing program, whereas the associated temperature is displayed at the right y-axis.

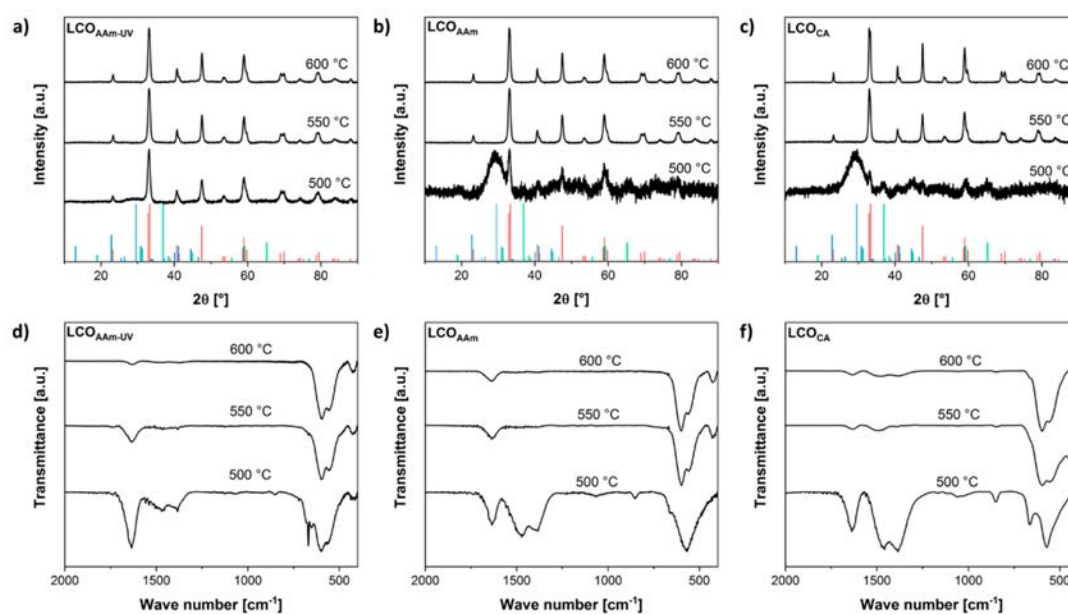


Figure 2. X-ray diffractograms of AAm-derived LCO based on UV-initiated polymerization (a) and thermal polymerization (b) as well as of LCO_{CA} (c) and the corresponding IR spectra (d, e, f). The reference diffractograms of LCO₃₃, La₂O₂CO₃³⁴ and Co₃O₄³⁵ are depicted in red, blue, and green, respectively.

promotes an upfield shift of 0.11 and 0.07 ppm for acrylic acid and acrylamide, respectively, indicating the formation of an

M–O bond (where M = La³⁺, Co²⁺) between metal and a complexing agent.^{27,28}

Thermal- and UV-activated radical polymerization of the monomers led to hybrid polymers, i.e. metal-ion-containing polymers, with different morphologies. Owing to the gentle photopolymerization reaction at room temperature, homogeneous, semitransparent membranes could be obtained (Figure 1c). On the contrary, thermal-activated reactions were very exothermic and accompanied by significant evolution of nitrous gases, thus promoting the formation of a lumpy polymer (Figure 1d), similar to the one obtained by the citrate route.

Significant understanding of the thermal evolution mechanism of the hybrid polymer was achieved by thermal analyses. In order to compare CA- and acrylate-based polymers, this study was limited to macromolecules obtained by thermal polymerization originating from LCO as a final inorganic product. The TG and DSC analyses in Figure 1 and Figure S1 follow the temperature program usually adopted for the production of perovskites via the citrate method. The decomposition of the polymeric material is triggered by the degradation of nitrates below 200 °C,²⁹ whereas the strong exothermic mass loss at higher temperatures corresponds to the oxidation of the organic matrix. After 2 h of dwell-time at 400 °C, needed to ensure the complete removal of the organic phase, an endothermic process most likely ascribed to the formation of an inorganic crystalline structure is observed. All the systems present very similar decomposition trends with the exception of MA for which the extent of the exothermic process is much lower.

Comparable thermal analyses are observed for LaFeO₃ (Figure S2), indicating that the inorganic species do not significantly influence the decomposition of the polymer.

The evolution of the amorphous precursors toward a crystalline LCO phase through heat treatment at 500–600 °C for 2 h was characterized by combining IR spectroscopy and XRD. The final products with identical nominal stoichiometry were compared on the basis of their precursors, i.e., acrylamide-based polymers (obtained by thermal and UV activation) and the standard CA-based systems (Figure 2). As reported by the group of Caro,¹⁴ the degradation of the carbonate phases is a decisive step toward the formation of the perovskite structure. To detect it, IR spectroscopy is a very suitable method complementary to XRD. The presence of carbonates is evidenced by the strong bands at 1476 and 1383 cm⁻¹. The signals at 1060 and 840 cm⁻¹ represent the stretching vibration of the carbonate and the vibration of the carbon atom out of the plane of the group, respectively.^{15,30} Carbonate phases are thus detected in all materials at 500 °C as also confirmed by the strong amorphous broad signal at 30° in the XRD pattern of Figure 2. In addition, small reflections ascribable to LaCoO₃ (00-048-0123) and Co₃O₄ (00-001-1152) are detected. Therefore, as already predicted for CA/EDTA-derived ceramics,¹⁴ the evolution of the perovskite phase in the case of acrylic polymers proceeds similarly by transformation of the metastable spinel and carbonate structures. Even though these signals vanish in the diffractograms at higher temperatures, a considerable amount of carbonates is still present in the CA-derived perovskite even at 600 °C as shown by IR. On the contrary, acrylate-derived materials exhibit a very low carbonate concentration at this temperature independent of the choice of monomer and polymerization method (Figures 2, S3, S4). This finding is most likely ascribed to the reduced carbon content (carbon

content ratio CA/MA/AA/AAm set at 1:0.67:0.5:0.5) of the acrylate matrices with respect to the CA-polyester.

The use of different polymeric precursors, however, results in significant microstructural differences. The thermal evolution of the average crystallite size obtained by the Scherrer formula (Figure 3a) displays how AA- and MA-

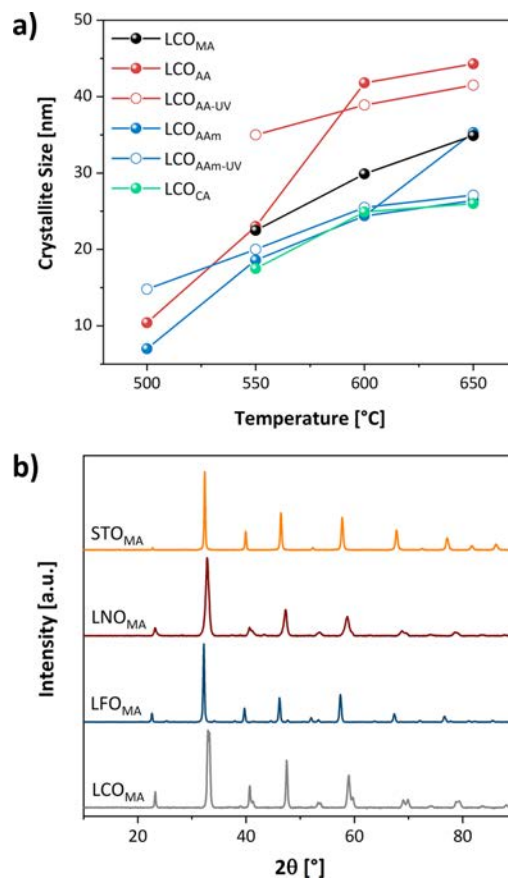


Figure 3. Crystallite sizes of LCO dependent on the calcination temperature. (a) LCO based on thermal polymerization of MA (black), AA (red), AAm (blue), and CA is displayed as bullet points. LCO based on UV initiated polymerization of MA (black), AA (red), and AAm (blue) is displayed as void bullet points. X-ray diffractograms of perovskite oxides STO_{MA} (orange), LNO_{MA} (dark red), LFO_{MA} (dark blue), and LCO_{MA} (gray) based on thermally initiated polymerization (b).

derived LCO possess significantly larger crystallites than AAm- and CA-derived materials. In order to account for the effect of strain on the peak broadening, which might affect the calculation of the crystallite size using the Scherrer method, we also determined the average crystallite size using the Williamson–Hall approach³¹ (Table 1 and Figure S5). With the MA-derived sample being the only exception, the strain component does not influence the mean grain size, which is in good agreement with the results obtained by the Scherrer method. This significant microstructural difference using

Table 1. Textural Properties of LCO: Average Crystallite Size Calculated by the Scherrer Equation (Φ_S), Average Crystallite Size Calculated by the Williamson–Hall Method (Φ_{WH}), Strain Component of the Peak Broadening from the Williamson–Hall Method (C_{WH}^E), Specific Surface Area Obtained by the BET Method (S_{BET}), Surface Ratio of the Ions Determined by EDX and XPS, and T_{50} Values of the Catalytic Conversion of CO

polymer precursor	Φ_S [nm]	Φ_{WH} [nm]	C_{WH}^E [$\times 10^{-2}$]	S_{BET} [m^2/g]	La/Co EDX	O/(La+Co) XPS	La/Co XPS	T_{50} [$^{\circ}C$]
MA	30	39	1.02	11	0.99	1.98	1.88	239
MA _{UV}	36	32	0.44	16	1.16			239
AA	42	36	0.33	18	0.93	1.77	1.80	210
AA _{UV}	39	36	0.42	22	1.00			195
AAM	24	20	0.19	17	0.99	2.42	1.98	192
AAM _{UV}	26	20	0.16	19	0.96			189
CA	25	22	0.22	23	1.04	2.27	1.76	225

diverse polymers can be likely explained by the polymerization behavior of the monomers (Figure 4a). In general, AA and MA form polymers with a linear structure.³² During the annealing step, this might lead to the formation of large amorphous domains, thus easing the grain growth. In the case of AAm and CA, the polymerization is highly cross-linked.¹⁰ Due to this entangled structure, multiple nucleation centers are formed, leading to a limited crystal growth.

In order to compare the citrate method with this novel synthesis approach, the same molar excess of complexing agent to metal cations was chosen, i.e., 4:1. The concentration limit of acrylic monomers in the synthesis of perovskites was tested additionally. A pure LCO phase could also be obtained at reduced acrylic concentrations at a 2:1 molar ratio (Figure S6).

The general applicability of the use of acrylates for the synthesis of manifold perovskite oxides is shown in Figure 3b. Along with LaFeO₃ (LFO) and LaNiO₃ (LNO), the preparation of SrTiO₃ (STO) using both thermal- and UV-activated polymerization was carried out. The high phase purity and the poor concentration of carbonates typical for this synthesis protocol are also demonstrated for the aforementioned compositions (Figures S7, S8). Moreover, we showed that the acrylate approach is highly suitable for the preparation of doped (e.g., La_{0.1}Sr_{0.9}TiO₃) and highly substituted perov-

skites (e.g., LaCo_{0.3}Fe_{0.8}O₃ and La_{0.8}Sr_{0.2}Co_{0.2}Fe_{0.8}O₃) within a very broad compositional range (Figure S7a).

The morphology of the LCO materials was investigated by means of electron microscopy (Figure 4b). Macroscopic aggregates of different shapes could be obtained based on the chelating agent employed in the initial reactions. With respect to the very large agglomerates of the CA-derived oxide, AA and AAM result in porous lamellar-like structures of approximately 2 μ m. In the case of MA, three-dimensional aggregates of slightly smaller size are formed. No particular differences are detected in the materials prepared via UV-polymerization (Figure S9, S10). However, the nanoscopic textures of the materials are almost identical, consisting of interconnected perovskite grains with interparticle porosity. As a consequence of the very low calcination temperatures, gas physisorption analyses showed specific surface areas between 10 and 20 m²/g (Table 1 and Table S2). In particular, MA derived material possesses the lowest surface area, whereas CA-based LCO exhibits the highest values. Surface area values do not follow the trend in crystal size. This could be correlated with different levels of particle agglomeration of the materials. Composition analysis performed by SEM/EDX spectroscopy pointed out the highly stoichiometric character of the LCO materials (Table 1).

Profound investigation of the surface chemistry of the materials was carried out by XPS analyses. The peak positions of La are in accordance with those of La³⁺ found in perovskite oxides.¹² The spin-orbits La 3d_{3/2} and La 3d_{5/2} are separated by 16.8 eV for all samples (Figure S11b), as usually reported for La³⁺.³⁶ Strong La³⁺ enrichment was observed for all the studied materials (Table 1), and it is correlated with the typical A-site migration phenomenon observed after high temperature treatments.^{16–18} The state of the oxygen species as well as of the cobalt ions is of particular interest for the functional assessment of the perovskites, especially in case of catalytic applications. The values of spin-orbit splitting of the Co 2p peaks varied in a narrow range from 15.0 eV (LCO_{MA}) to 15.2 eV (LCO_{AAV}, LCO_{AAM}), also agreeing well with values reported for Co³⁺ (Figure 5a).^{37,38} The asymmetry of Co 2p 3/2, as underlined by deconvolution is likely explained by a certain degree of hydroxylation of Co³⁺. The presence of Co²⁺ and of possible Co₃O₄ surface impurities can be excluded, as the typical shakeup satellite peaks at approximately 787 and 804 eV of this species are missing.^{39–42} Bulk traces of Co²⁺, not

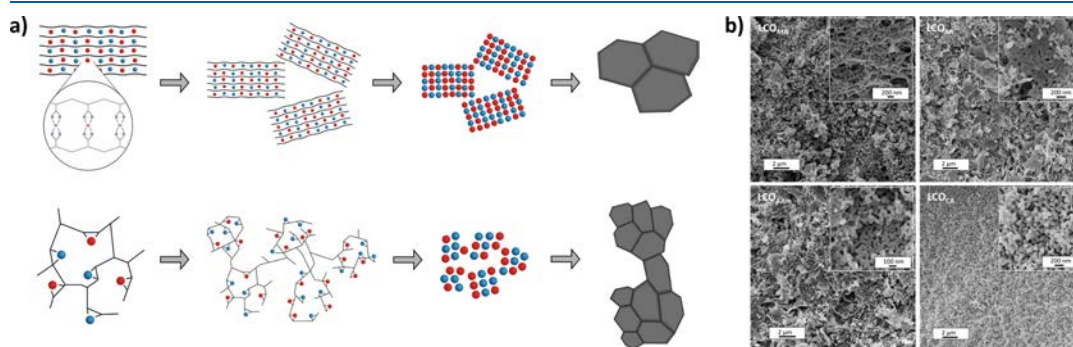


Figure 4. Proposed explanation for microstructure oxide evolution as a function of polymer structure (a). SEM images of LCO_{MAV}, LCO_{AAV}, LCO_{AAM} and LCO_{CA} showing the different morphologies of the polymer-derived perovskites (b).

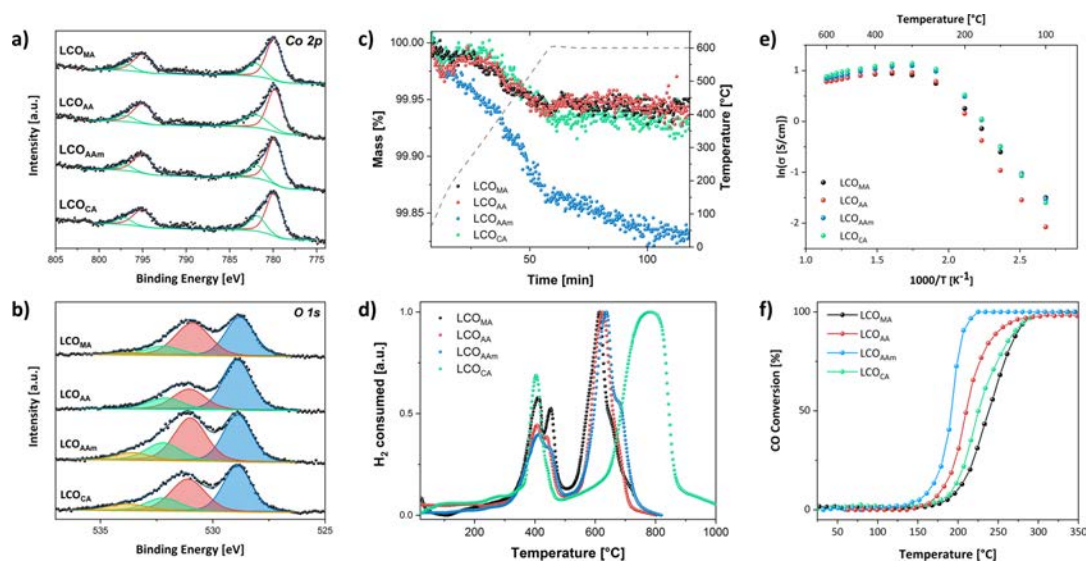


Figure 5. Co 2p (a) and O 1s (b) XPS spectra of LaCoO₃ synthesized from methacrylic acid, acrylic acid, acrylamide, and citric acid, respectively. The Co 2p spectra could each be deconvoluted into two contributions due to the coexistence of Co³⁺ lattice (red) and Co³⁺ bound to hydroxylated species (green). The O 1s spectra could be each deconvoluted into four contributions—lattice oxygen (blue), hydroxide (red), chemisorbed oxygen (green), and organic rests and water (yellow). TG analyses (c) and H₂-TPR profiles (d) of LCO produced from MA (black), AA (red), AAm (blue), and CA (green), respectively. Arrhenius plots of the conductivity of thermally polymerized LCO samples (e). Conversion rate of carbon monoxide dependent on the temperature in the presence of LaCoO₃ as a catalyst (f). LaCoO₃ based on thermal polymerization produced from MA (black), AA (red), and AAm (blue) and based on citric acid using CA (green).

detected with the methods at our disposal, could be addressed using SQUID magnetometry.

All the LaCoO₃ materials present similar profiles of the O 1s spectrum (Figure 5b). The peak at around 529 eV is ascribed to lattice oxygen, O²⁻. A second peak at 531 eV originates from hydroxyl oxygen (OH), whereas a third contribution at approximately 532 eV is assigned to chemisorbed oxygen (O⁻). Loosely bonded oxygen species such as water or organic rests are identified by a fourth peak at 533.7 eV.^{17,43,44} The presence of such latter species is also confirmed by the signal at 290 eV in the C 1s spectrum (Figure S11a). Interestingly, it can be noted that, both in O 1s and C 1s spectra, AA- and MA-derived materials exhibit the lowest concentration of organic rests. This is a sign of less defective surfaces, in agreement with their larger crystallite size. Moreover, due to the comparable surface carbon amount of AAm and CA-derived oxides, it can be postulated that the higher carbonate concentration detected by IR for the CA-derived systems represents rather a bulk than a surface condition. To properly disclose this status, quantitative characterization of the carbonate species (e.g., using the carbonate acid titration method⁴⁵) could be performed.

As it can be seen from Figure 5b and in Table S3, the concentration of the physically adsorbed oxygen species is significantly higher in LCO_{CA} and particularly in LCO_{AAM} samples, most probably as a result of the smaller crystallite size and therefore higher concentration of surface defects. More specific insights into the surface oxygen characteristics of the materials are given by the study of oxygen desorption via TGM (Figure 5c). After the removal of surface contaminations (e.g., water, carbonates) during a first oxidative cycle, pure

oxygen desorption was determined. It is evident that the AAm-derived sample exhibits much larger oxygen loss compared to the other materials. From the shape of the curve, a low temperature ($T < 400$ °C) and high temperature ($T > 400$ °C) oxygen desorption is inferred, which likely corresponds to the release of α - and β -oxygen species, respectively.^{5,46} Similar oxygen release behavior of the materials was registered in the case of TPD-MS measurements (Figure S12a). Hence, even if XPS spectra of LCO_{AAM} and LCO_{CA} suggest very similar surface oxygen chemistry, only LCO_{AAM} displays significant oxygen exchange activity, indicating that the significant carbonate contaminations in LCO_{CA} (Figure 2f) might play a role. To complete the study of the materials' surface reactivity, TPR measurements were carried out. The surface reduction profiles of the acrylate-derived LaCoO₃ are much more detailed than for the citrate-derived oxide (Figure 5d, Table S4). All the materials show a first signal around 400 °C, ascribed to the reduction of Co³⁺ to Co²⁺, in very good agreement with the temperature necessary for the oxygen desorption (Figure 5c). Interestingly, only the acrylate-derived systems present a satellite peak, which is also usually observed in LaCoO₃.^{46,47} The signal at higher temperature identifies the transition of Co²⁺ to Co.^{43,48} Notably, this reduction occurs approximately 200 °C later for LCO_{CA}. Considering that materials were treated up to 600 °C, this delayed conversion might be related to the transformation of the residual carbonate species in the material, which occur at $T > 700$ °C. The decomposition of the LaCoO₃ structure and the consequent formation of Co and La₂O₃ after the reduction process was confirmed by XRD (Figure S12b).

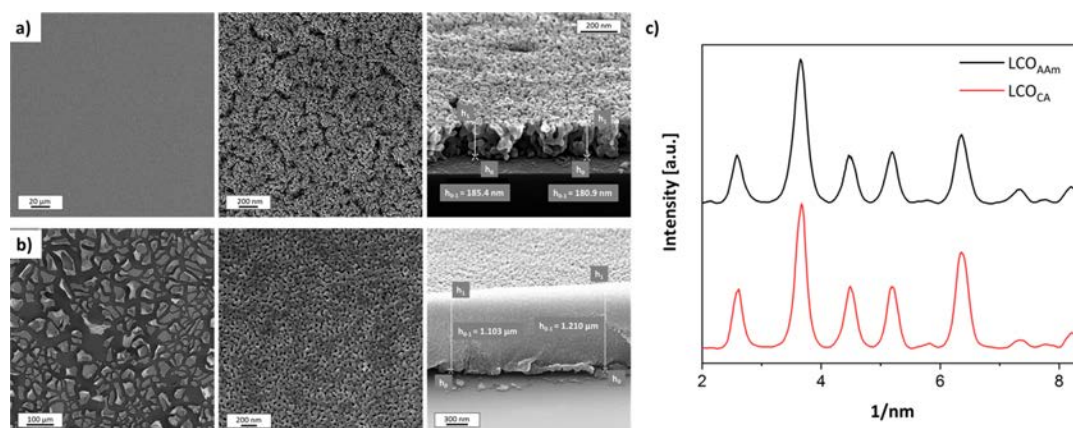


Figure 6. SEM images of LCO thin-films prepared from UV-polymerized AAm (a) and thermally polymerized CA (b) and the resulting electron diffractogram (c) of LCO_{AAm} (black) and LCO_{CA} (red).

Electrochemical impedance spectroscopy was employed to investigate the electrical properties of the LCO materials (Figure 5e). All materials display semiconducting behavior (increasing conductivity with increasing temperature) between 100 and 300 °C, whereas metallic behavior (decreasing conductivity with increasing temperature) is observed above 300 °C. This phenomenon is well-known for LCO and has been explained in terms of band-structure changes due to the transition of the Co³⁺ ions from low-spin to high-spin configuration.^{49,50} The specific conductivities were found to be roughly one order of magnitude below those determined by Petrov et al.⁴⁹ The deviation can be possibly ascribed to the poor relative density of the samples (~50%) and the significantly smaller grain size due to the low temperature consolidation at 600 °C. The most interesting part of the Arrhenius plot is the one below 300 °C. The significantly lower conductivity of the AA-derived material is probably ascribed to its larger crystallite size. The activation energies for charge migration have been found in the range of 0.27–0.34 eV between 100–200 °C for all systems, which is in line with the typical semiconducting behavior of the LaCoO₃.

Considering the high purity and significant surface reactivity, acrylate-based LaCoO₃ materials could be employed as promising catalytic converters. To test the catalytic activity of the materials, we therefore performed CO oxidation and compared it to the performance of citrate-derived perovskite. In Figure 5f, the light-off curves of the CO conversion are displayed. Aside from LCO_{MA}, the other acrylate-derived perovskites show better performance than the standard system prepared via the citrate route. In particular, LCO_{AAm} exhibited a T_{50} value 30 °C lower than LCO_{CA}, whereas the full conversion could be already reached at $T_{100} = 210$ °C (Table 1), which is almost 100 °C lower than for the CA-derived material. This enhanced performance is likely ascribed to the superior surface oxygen chemistry of this system, as evidenced by the TG-MS and XPS results and consistent with the Mars and van Krevelen mechanism for CO oxidation. Even if LCO_{CA} is structurally more similar to LCO_{AAm}, i.e., the same crystallite size and a similar surface O/(La+Co) ratio and conductivity, its catalytic performance is much lower than that of the AAm-derived material. This finding can be explained by

the negligible surface oxygen release, leading to poor oxygen vacancy concentration and thus to a less reactive surface (Figure 5c). The better catalytic properties of LCO_{AA} with respect to LCO_{CA} can be likely ascribed to its low surficial carbonate concentration, as both materials present comparable oxygen release. Catalytic tests on the perovskite oxides derived from photopolymerized polymers resemble those of thermally polymerized samples (Figure S13), indicating that the activation type of the polymerization has negligible influence on the functional properties of the materials. Also in this case, LCO_{AAm-UV} displays better performance than LCO_{AA-UV}, while LCO_{MA-UV} shows the lowest conversion.

An interesting aspect in performing the polymerization reaction via UV-curing is given by the possibility of tuning the material form by preparing thin film oxides.^{51–54} This was explored by synthesizing thin films of LCO via spin coating using an AAm-based precursor solution. In order to evaluate the effect of UV polymerization, we compared the materials with those obtained by thermal polymerization of AAm- and CA-based solutions.

In Figure 6, SEM micrographs of the AAm- and CA-based LCO films polymerized via UV irradiation and thermal treatment are shown. The acrylate-derived material displays a homogeneous and uniform oxide layer of about 180 nm thickness across the whole silicon substrate. This homogeneity is also verified by the optical quality of the thin film (Figure S15). A closer look reveals that the structure resembles the one of the powder material, which is characterized by a porous matrix of interconnected grains. In the case of thin films prepared using the citrate route, instead of homogeneous coatings, isolated plaques of approximately 50 μm width and 1 μm thickness were obtained. This phenomenon was similarly observed for the AAm-derived LCO thin films prepared by thermal polymerization (Figures S16, S17).

In order to address the microstructural properties of the thin films, a selected area electron diffraction (SAED) from TEM was performed (Figures 6, S17). The diffraction patterns of both materials obtained by UV curing of AAm solutions and by thermal polymerization of CA point out the typical rhombohedral distorted structure of LaCoO₃, demonstrating

the successful crystallization during the polymer-to-oxide transformation.

CONCLUSIONS

In this report, we demonstrated how acrylic monomers (i.e., acrylamide AAm, acrylic acid AA) are better performing than the used standard citric acid for the synthesis of LaCoO_3 for catalytic applications. As pointed out by a combination of XRD and IR spectroscopy, the lower carbon content of acrylate-based polymer complexes enabled the complete transformation of the carbonate intermediates to oxides, thus leading to perovskite materials with much higher purity than citric-acid-based counterparts at temperatures as low as 600 °C. The applicability of this approach was verified not only for LaCoO_3 but also for a large pool of perovskite structures (e.g., LaFeO_3 , LaNiO_3 , SrTiO_3) and their corresponding solid solutions. Depending on the type of monomer chosen, materials with different crystallinity were obtained without changing the synthesis conditions. Acrylate-based LaCoO_3 powders are characterized by improved surface activity and oxygen exchange properties. As a result, their enhanced performance in comparison to the standard citrate-based material were demonstrated via catalytic CO oxidation. In particular, acrylamide-derived LCO exhibited a T_{50} 30 °C lower than the citrate-based material, whereas the full conversion could be already reached at $T_{100} = 210$ °C. In addition, aside from the preparation of powder materials, polymerization via UV activation of the radical group was highly suitable for the synthesis of perovskite thin films using a facile spin coating approach. With respect to thermally polymerized AAm and CA systems, the UV curing originated highly homogeneous, nanocrystalline LaCoO_3 films of optical quality.

In conclusion, we could demonstrate that acrylic monomers are suitable precursors for the preparation of nanostructured perovskite materials with high purity, tailorable form, and more importantly improved catalytic activity. Therefore, these characteristics make this synthesis route highly attractive for the preparation of prospective energy conversion materials and a better alternative to state-of-the-art citrate-based methods. Considering the significant oxygen release at temperatures higher than 400 °C, acrylate-based perovskite oxides are specifically promising materials for high-temperature (electro)-catalysis applications such as fuel cells and electrolyzers.

ASSOCIATED CONTENT

Supporting Information

The Supporting Information is available free of charge on the ACS Publications website at DOI: 10.1021/acs.inorgchem.9b02460.

TG-DSC measurements of investigated LCO and LFO samples (Figures S1, S2); XRD patterns and IR spectra of investigated LCO samples and their intermediates (Figures S3, S4, S6); Williamson–Hall plots and derived parameters of investigated LCO samples (Figure S5, Table S1); XRD patterns of investigated LCO, STO, LNO, and LFO and solid solutions thereof (Figure S7); characterization of investigated STO and LSTO samples by means of XRD, IR, N_2 -physisorption, and SEM/EDX (Figures S8, S9, Table S2); SEM images of investigated LCO samples (Figure S10); surface characterization of investigated LCO samples by means of XPS, TPD-MS, XRD, and H_2 -TPR measurements (Figures S11, S12;

Tables S3, S4); catalytic CO oxidation over investigated LCO samples (Figure S13); N_2 -physisorption isotherms of investigated LCO samples (Figure S14); characterization of investigated LCO thin-films by means of photography, SEM, TEM, and electron diffraction (Figures S15–S17) (PDF)

AUTHOR INFORMATION

Corresponding Author

*E-mail: simone.mascotto@chemie.uni-hamburg.de.

ORCID

Antonella Glisenti: 0000-0003-4334-2150

Simone Mascotto: 0000-0002-3503-6391

Notes

The authors declare no competing financial interest.

ACKNOWLEDGMENTS

The authors thank Prof. Michael Fröba of the University of Hamburg for the support and the fruitful discussions. Kurt Klauke was financially supported by the Ph.D. fellowship of the University of Hamburg. PIER is gratefully acknowledged for funding (Project ID: PIF-2016-56).

REFERENCES

- (1) Brosha, E. L.; Mukundan, R.; Brown, D. R.; Garzon, F. H.; Visser, J. H.; Zanini, M.; Zhou, Z.; Logothetis, E. M. CO/HC Sensors Based on Thin Films of LaCoO_3 and $\text{La}_{0.8}\text{Sr}_{0.2}\text{CoO}_{3-\delta}$ Metal Oxides. *Sens. Actuators, B* **2000**, *69* (1), 171–182.
- (2) Fabbri, E.; Pergolesi, D.; Traversa, E. Materials Challenges toward Proton-Conducting Oxide Fuel Cells: A Critical Review. *Chem. Soc. Rev.* **2010**, *39* (11), 4355–4369.
- (3) Felser, C.; Fecher, G. H.; Balke, B. Spintronics: A Challenge for Materials Science and Solid-State Chemistry. *Angew. Chem., Int. Ed.* **2007**, *46* (5), 668–699.
- (4) Kayaalp, B. E.; Lee, Y. J.; Kornowski, A.; Gross, S.; D'Arienzo, M.; Mascotto, S. Cooperative Assembly Synthesis of Mesoporous SrTiO_3 with Enhanced Photocatalytic Properties. *RSC Adv.* **2016**, *6* (93), 90401–90409.
- (5) Kayaalp, B.; Lee, S.; Klauke, K.; Seo, J.; Nodari, L.; Kornowski, A.; Jung, W.; Mascotto, S. Template-Free Mesoporous $\text{La}_{0.3}\text{Sr}_{0.7}\text{Ti}_{1-x}\text{Fe}_x\text{O}_{3-\delta}$ for CH_4 and CO Oxidation Catalysis. *Appl. Catal., B* **2019**, *245*, 536–545.
- (6) Zhu, Y.; Zhou, W.; Yu, J.; Chen, Y.; Liu, M.; Shao, Z. Enhancing Electrocatalytic Activity of Perovskite Oxides by Tuning Cation Deficiency for Oxygen Reduction and Evolution Reactions. *Chem. Mater.* **2016**, *28* (6), 1691–1697.
- (7) Royer, S.; Duprez, D.; Can, F.; Courtois, X.; Batiot-Dupeyrat, C.; Laassiri, S.; Alamdari, H. Perovskites as Substitutes of Noble Metals for Heterogeneous Catalysis: Dream or Reality. *Chem. Rev.* **2014**, *114* (20), 10292–10368.
- (8) Granger, P.; Pârăulescu, V. I.; Kaliaguine, S.; Prellier, W. *Perovskites and Related Mixed Oxides: Concepts and Applications*; Wiley - VCH, 2016.
- (9) Kakihana, M.; Okubo, T.; Arima, M.; Nakamura, Y.; Yashima, M.; Yoshimura, M. Polymerized Complex Route to the Synthesis of Pure SrTiO_3 at Reduced Temperatures: Implication for Formation of Sr-Ti Heterometallic Citric Acid Complex. *J. Sol-Gel Sci. Technol.* **1998**, *12* (2), 95–109.
- (10) Danks, A. E.; Hall, S. R.; Schnepf, Z. The Evolution of “sol-Gel” Chemistry as a Technique for Materials Synthesis. *Mater. Horiz.* **2016**, *3* (2), 91–112.
- (11) Pechini, M. P. Method of Preparing Lead and Alkaline Earth Titanates and Niobates and Coating Method Using the Same to Form a Capacitor. US3330697A, 1967.

- (12) Natile, M. M.; Eger, G.; Batocchi, P.; Mauvy, F.; Glisenti, A. Strontium and Copper Doped LaCoO₃: New Cathode Materials for Solid Oxide Fuel Cells? *Int. J. Hydrogen Energy* **2017**, *42* (3), 1724–1735.
- (13) Shao, Z. Investigation of the Permeation Behavior and Stability of a Ba_{0.5}Sr_{0.5}Co_{0.8}Fe_{0.2}O_{3-δ} Oxygen Membrane. *J. Membr. Sci.* **2000**, *172* (1–2), 177–188.
- (14) Martynczuk, J.; Arnold, M.; Wang, H.; Caro, J.; Feldhoff, A. How (Ba_{0.5}Sr_{0.5})(Fe_{0.8}Zn_{0.2})O_{3-δ} and (Ba_{0.5}Sr_{0.5})(Co_{0.8}Fe_{0.2})O_{3-δ} Perovskites Form via an EDTA/Citric Acid Complexing Method. *Adv. Mater.* **2007**, *19* (16), 2134–2140.
- (15) Najjar, H.; Batis, H. La–Mn Perovskite-Type Oxide Prepared by Combustion Method: Catalytic Activity in Ethanol Oxidation. *Appl. Catal., A* **2010**, *383* (1–2), 192–201.
- (16) Koo, B.; Kim, K.; Kim, J. K.; Kwon, H.; Han, J. W.; Jung, W. Sr Segregation in Perovskite Oxides: Why It Happens and How It Exists. *Joule* **2018**, *2* (8), 1476–1499.
- (17) Kayaalp, B.; Klauke, K.; Biesuz, M.; Iannaci, A.; Sglavo, V. M.; D'Arienzo, M.; Noei, H.; Lee, S.; Jung, W.; Mascotto, S. Surface Reconstruction under the Exposure of Electric Fields Enhances the Reactivity of Donor-Doped SrTiO₃. *J. Phys. Chem. C* **2019**, *123* (27), 16883–16892.
- (18) Klauke, K.; Kayaalp, B.; Biesuz, M.; Iannaci, A.; Sglavo, V. M.; D'Arienzo, M.; Lee, S.; Seo, J.; Jung, W.; Mascotto, S. Enhancement of the SrTiO₃ Surface Reactivity by Exposure to Electric Fields. *ChemNanoMat* **2019**, *5* (7), 948–956.
- (19) Kakihana, M. Invited Review “Sol-Gel” Preparation of High Temperature Superconducting Oxides. *J. Sol-Gel Sci. Technol.* **1996**, *6* (1), 7–55.
- (20) Sin, A.; Odier, P. Gelation by Acrylamide, a Quasi-Universal Medium for the Synthesis of Fine Oxide Powders for Electroceramic Applications. *Adv. Mater.* **2000**, *12* (9), 649–652.
- (21) Galenda, A.; Natile, M. M.; Nodari, L.; Glisenti, A. La_{0.8}Sr_{0.2}Ga_{0.8}Fe_{0.2}O_{3-δ}: Influence of the Preparation Procedure on Reactivity toward Methanol and Ethanol. *Appl. Catal., B* **2010**, *97* (3–4), 307–322.
- (22) Douy, A. Polyacrylamide Gel: An Efficient Tool for Easy Synthesis of Multicomponent Oxide Precursors of Ceramics and Glasses. *Int. J. Inorg. Mater.* **2001**, *3* (7), 699–707.
- (23) Brunauer, S.; Emmett, P. H.; Teller, E. Adsorption of Gases in Multimolecular Layers. *J. Am. Chem. Soc.* **1938**, *60* (2), 309–319.
- (24) Shirley, D. A. High-Resolution X-Ray Photoemission Spectrum of the Valence Bands of Gold. *Phys. Rev. B* **1972**, *5* (12), 4709–4714.
- (25) Moulder, J. F.; Chastain, J. *Handbook of X-Ray Photoelectron Spectroscopy: A Reference Book of Standard Spectra for Identification and Interpretation of XPS Data*, Update; Physical Electronics Division, Perkin-Elmer Corp: Eden Prairie, MN, 1992.
- (26) Castle, J. E. Practical Surface Analysis by Auger and X-Ray Photoelectron Spectroscopy. D. Briggs and M. P. Seah (Editors). John Wiley and Sons Ltd, Chichester, 1983, 533 pp., £44.50. *Surf. Interface Anal.* **1984**, *6* (6), 302–302.
- (27) Xu, Z.; Baek, K.; Kim, H. N.; Cui, J.; Qian, X.; Spring, D. R.; Shin, I.; Yoon, J. Zn²⁺-Triggered Amide Tautomerization Produces a Highly Sensitive Sensor. *J. Am. Chem. Soc.* **2010**, *132*, 601–610.
- (28) Marlin, D. S.; Gonzalez Cabrera, D.; Leigh, D. A.; Slawin, A. M. Z. Complexation-Induced Translational Isomerism: Shuttling through Stepwise Competitive Binding. *Angew. Chem., Int. Ed.* **2006**, *45* (1), 77–83.
- (29) Scholz, J.; Etter, M.; Haas, D.; Meyer, A.; Kornowski, A.; Sazama, U.; Mascotto, S. Pore Geometry Effect on the Synthesis of Silica Supported Perovskite Oxides. *J. Colloid Interface Sci.* **2017**, *504*, 346–355.
- (30) Merino, N.; Barbero, B.; Grange, P.; Cadus, L. LaCaCoO Perovskite-Type Oxides: Preparation, Characterisation, Stability, and Catalytic Potentiality for the Total Oxidation of Propane. *J. Catal.* **2005**, *231* (1), 232–244.
- (31) Williamson, G.; Hall, W. X-Ray Line Broadening from Filled Aluminium and Wolfram. *Acta Metall.* **1953**, *1* (1), 22–31.
- (32) Wittenberg, N. F. G.; Preusser, C.; Kattner, H.; Stach, M.; Lacić, I.; Hutchinson, R. A.; Buback, M. Modeling Acrylic Acid Radical Polymerization in Aqueous Solution. *Macromol. React. Eng.* **2016**, *10* (2), 95–107.
- (33) Closset, N. M. L. N. P.; van Doorn, R. H. E.; Kruidhof, H.; Boeijmsma, J. About the Crystal Structure of La_{1-x}Sr_xCoO_{3-δ} (0 ≤ x ≤ 0.6). *Powder Diff.* **1996**, *11* (1), 31–34.
- (34) Sawyer, J. O.; Caro, P.; Eyring, L. Herstellung, Analyse Und Röntgenographische Identifizierung Der Dioxymonocarbonate Des Lanthans Und Der Lanthanidenelemente. *Monatsh. Chem.* **1972**, *103* (1), 333–354.
- (35) Hanawalt, J. D.; Rinn, H. W.; Frevel, L. K. Chemical Analysis by X-Ray Diffraction. *Ind. Eng. Chem., Anal. Ed.* **1938**, *10* (9), 457–512.
- (36) Lam, D. J.; Veal, B. W.; Ellis, D. E. Electronic Structure of Lanthanum Perovskites with 3d Transition Elements. *Phys. Rev. B: Condens. Matter Mater. Phys.* **1980**, *22* (12), 5730–5739.
- (37) Tabata, K.; Matsumoto, I.; Kohiki, S. Surface Characterization and Catalytic Properties of La_{1-x}Sr_xCoO₃. *J. Mater. Sci.* **1987**, *22* (5), 1882–1886.
- (38) Ichimura, K.; Inoue, Y.; Yasumori, I. Catalysis by Mixed Oxide Perovskites. I. Hydrogenolysis of Ethylene and Ethane on LaCoO₃. *Bull. Chem. Soc. Jpn.* **1980**, *53* (11), 3044–3049.
- (39) Schenck, C.V.; Dillard, J.G.; Murray, J.W. Surface Analysis and the Adsorption of Co(II) on Goethite. *J. Colloid Interface Sci.* **1983**, *95* (2), 398–409.
- (40) McIntyre, N. S.; Cook, M. G. X-Ray Photoelectron Studies on Some Oxides and Hydroxides of Cobalt, Nickel, and Copper. *Anal. Chem.* **1975**, *47* (13), 2208–2213.
- (41) Natile, M. M.; Glisenti, A. CoO_x/CeO₂ Nanocomposite Powders: Synthesis, Characterization, and Reactivity. *Chem. Mater.* **2005**, *17* (13), 3403–3414.
- (42) Tyuliev, G.; Angelov, S. The Nature of Excess Oxygen in Co₃O_{4+x}. *Appl. Surf. Sci.* **1988**, *32* (4), 381–391.
- (43) Xiao, P.; Zhu, J.; Li, H.; Jiang, W.; Wang, T.; Zhu, Y.; Zhao, Y.; Li, J. Effect of Textural Structure on the Catalytic Performance of LaCoO₃ for CO Oxidation. *ChemCatChem* **2014**, *6* (6), 1774–1781.
- (44) Zhou, W.; Zhao, M.; Liang, F.; Smith, S. C.; Zhu, Z. High Activity and Durability of Novel Perovskite Electrocatalysts for Water Oxidation. *Mater. Horiz.* **2015**, *2* (5), 495–501.
- (45) Hatsukade, T.; Schiele, A.; Hartmann, P.; Brezesinski, T.; Janek, J. Origin of Carbon Dioxide Evolved during Cycling of Nickel-Rich Layered NCM Cathodes. *ACS Appl. Mater. Interfaces* **2018**, *10* (45), 38892–38899.
- (46) Dacquin, J. P.; Lancelot, C.; Dujardin, C.; Da Costa, P.; Djega-Mariadassou, G.; Beaunier, P.; Kaliaguine, S.; Vaudreuil, S.; Royer, S.; Granger, P. Influence of Preparation Methods of LaCoO₃ on the Catalytic Performances in the Decomposition of N₂O. *Appl. Catal., B* **2009**, *91* (3–4), 596–604.
- (47) Dacquin, J.; Dujardin, C.; Granger, P. Surface Reconstruction of Supported Pd on LaCoO₃: Consequences on the Catalytic Properties in the Decomposition of N₂O. *J. Catal.* **2008**, *253* (1), 37–49.
- (48) Wang, Y.; Ren, J.; Wang, Y.; Zhang, F.; Liu, X.; Guo, Y.; Lu, G. Nanocasted Synthesis of Mesoporous LaCoO₃ Perovskite with Extremely High Surface Area and Excellent Activity in Methane Combustion. *J. Phys. Chem. C* **2008**, *112* (39), 15293–15298.
- (49) Petrov, A. N.; Kononchuk, O. F.; Andreev, A. V.; Cherepanov, V. A.; Kofstad, P. Crystal Structure, Electrical and Magnetic Properties of La_{1-x}Sr_xCoO_{3-y}. *Solid State Ionics* **1995**, *80* (3–4), 189–199.
- (50) Senaris-Rodriguez, M.A.; Goodenough, J.B. LaCoO₃ Revisited. *J. Solid State Chem.* **1995**, *116* (2), 224–231.
- (51) Armelao, L.; Eisenmenger-Sittner, C.; Groenewolt, M.; Gross, S.; Sada, C.; Schubert, U.; Tondello, E.; Zattin, A. Zirconium and Hafnium Oxoclusters as Molecular Building Blocks for Highly Dispersed ZrO₂ or HfO₂ Nanoparticles in Silica Thin Films. *J. Mater. Chem.* **2005**, *15* (18), 1838–1848.

(52) Lee, L. H.; Chen, W. C. High-Refractive-Index Thin Films Prepared from Trialkoxysilane-Capped Poly(Methylmethacrylate)-Titania Materials. *Chem. Mater.* **2001**, *13* (3), 1137–1138.

(53) Zhang, H.; Wang, R.; Zhang, G.; Yang, B. A Covalently Attached Film Based on Poly(Methacrylic Acid)-Capped Fe₃O₄ Nanoparticles. *Thin Solid Films* **2003**, *429* (1–2), 167–173.

(54) Kololuoma, T.; Johansson, L. S.; Campbell, J. M.; Tolonen, A.; Haltunen, M.; Haatainen, T.; Rantala, J. T. The Effect of UV Irradiation on Antimony-Doped Tin Dioxide Thin Films Derived from Methacrylic Acid Modified Precursors. *Chem. Mater.* **2002**, *14* (10), 4443–4447.

7. Unpublished Work

7.1. Porous Perovskite Oxides

In the previous section, a new synthesis approach for the preparation of nanocrystalline perovskite oxides was presented. The employment of acrylamide as complexing agent resulted in improved surface properties and consequently lead to an increased catalytic activity. Accordingly, further enhancement of the attainable surface area is desired for a high performance perovskite oxide catalyst.

One approach towards that aim is to establish a nanoporous architecture. However, the inadequacies of the nanocasting procedure and the employment of soft templates have been detailed in previous chapters. A suitable alternative is required.

Hereby, a multistep method based on the use of solid silica endotemplates is presented. A ladder-like polysilsesquioxane (LLPSSO) with methacryl functionality acts as template. The general concept of the perovskite oxide synthesis, which was introduced in the previous chapter, relies on the formation of a polyacrylamide matrix, which contains respective metal precursors.^[242] Addition of the functionalized template to the initial reaction mixture enables co-polymerization of acrylamide monomers and methacrylic acid moieties. Thus, direct incorporation of the silica structures into the polymer matrix can be achieved. The perovskite oxide phase then forms around the silica material during heat treatment, in which the organic polymer is burned out. The silica phase is removed in a subsequent etching step (Figure 7.1). The resulting perovskite oxide material then should incorporate pores the size of the removed LLPSSO.

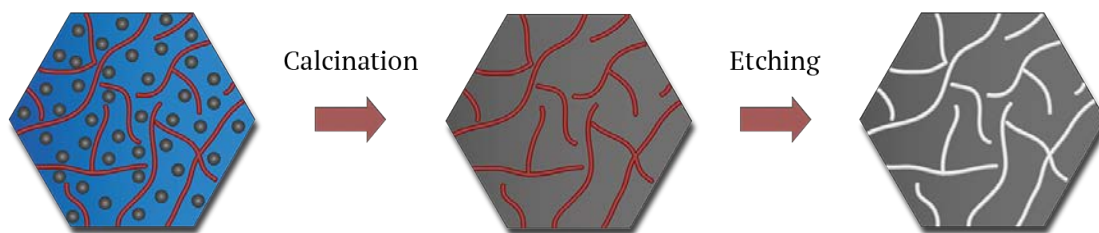


Figure 7.1.: Schematic illustration of the formation of nanoporous perovskite oxide by using LLPSSO as a solid template (blue - polyacrylamide matrix; grey - metal ion; red - LLPSSO).

In the following section, the suitability of this approach will be presented. Accordingly, features of ladder-like polysilsesquioxane, the formation of a perovskite oxide/LLPSSO composite, and the removal of the template will be emphasized.

7.1.1. Characterization of Ladder-like Polysilsesquioxane Templates

The ladder-like polysilsesquioxanes were prepared according to Choi *et al.*^[130] Different combinations of functionality were introduced (Figure 7.2). On the one hand, an acrylic component from the methacryloxypropyl moieties was provided to allow for radical polymerization with the acrylamide monomers used in the synthesis approach. This should guarantee homogeneous distribution of the silica over the material and reaction with the monomers leading to a strong incorporation into the polymer network. On the other hand, phenyl functionalities were added in order to form repulsive interactions between separate 'ladders' to prevent agglomeration. In this work, ratios of acrylic functionality to phenyl functionality of 100:0, 80:20, 70:30 and 10:90 were employed. The respective ratio of the employed LLPSSO will be denoted in the index throughout the following work.

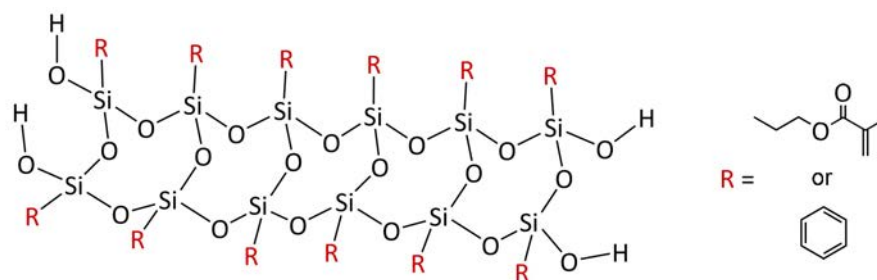


Figure 7.2.: Characteristic ladder-like structure of polysilsesquioxanes. R refers to different organic functionalities (methacryl or phenyl).^[130]

The successful completion of the syntheses was confirmed using $^1\text{H-NMR}$, $^{29}\text{Si-NMR}$ and IR spectroscopy. $^1\text{H-NMR}$ spectra are displayed in Figure 7.3. Two peaks between 6 and 5.5 ppm can be distinguished that belong to the C=C bond of methacrylic groups (marked as 'e'). The remaining peaks of the methacryloxypropyl group ('b-f') were also observed at peak values that concur with literature.^[130] As the intensity of the methacryloxypropyl signals decreases upon variation of the functional group ratio, the intensity of the broad peak at 7.4 ppm increases. Accordingly, this peak (denoted as 'a') can be attributed to the phenyl moieties. The IR spectra in Figure 7.4 all exhibit two broad absorption bands at 1107 and 1018 cm^{-1} , respectively, that are characteristic of the stretching vibration of the Si-O-Si bond in the horizontal and vertical direction of ladder-like structures.^[243] Additionally, features that are specific to the respective functional groups can be observed depending on the ratio of methacryloxypropyl to phenyl moieties. Strong absorption bands at 1714 and 1637 cm^{-1} can be ascribed to the stretching vibration of C=O and the deformation of the C=C bond of the methacrylate group. Moreover, the characteristic stretching vibration of the ester group is exhibited at 1295 cm^{-1} with a shoulder at 1320 cm^{-1} . Above 1400 cm^{-1} , =CH deformation and rocking vibrations can be observed.^[130,244]

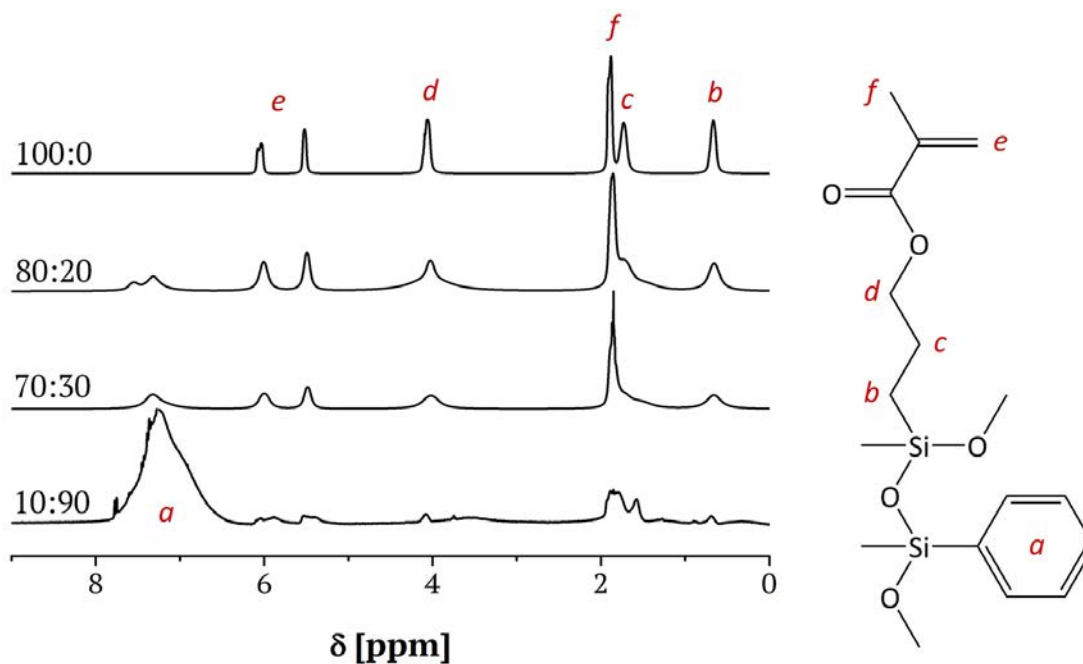


Figure 7.3.: $^1\text{H-NMR}$ spectra of ladder-like polysilsesquioxanes with different ratios of methacryloxypropyl to phenyl functional groups.

As the phenyl content increases in LLPSSO, the intensity of the IR signals of the methacryloxypropyl moiety decreases. In turn, strong absorption bands at 693 and 729 cm^{-1} due to deformation of the C-H vibrations of the monosubstituted aromatic ring become more visible. Additionally, the aromatic C=C stretching vibrations at 1594 cm^{-1} can be observed.^[244]

Thus, ladder-like polysilsesquioxane structures were successfully prepared and can function as endotemplates in the template-assisted synthesis of nanoporous perovskite oxide materials.

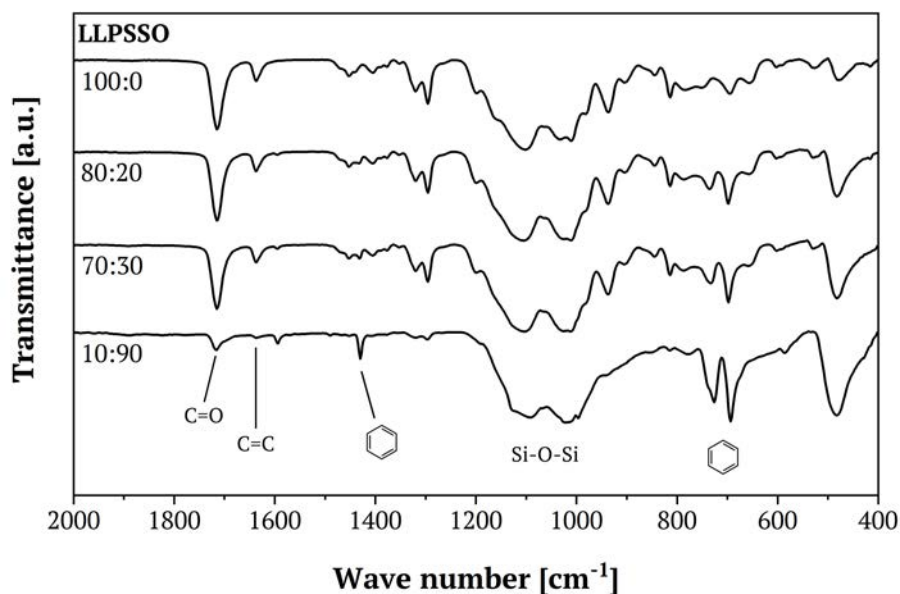


Figure 7.4.: IR spectra of ladder-like polysilsesquioxanes with different ratios of methacryloxypropyl to phenyl functional groups.

7.1.2. Preparation of Nanoporous $\text{LaCo}_{0.8}\text{Ti}_{0.2}\text{O}_3$ using Ladder-like Polysilsesquioxanes

The preparation of a nanoporous material through a hard template-assisted procedure is divided into two steps. Firstly, a composite material is formed composed of the LLPSSO template and perovskite oxide. Then, the template is removed in an etching procedure to obtain a porous perovskite oxide. LaCoO_3 has shown insufficient structural stability during the etching procedure. Partial degradation of the structure was observed due to the reduction of cobalt cations (see Appendix). Thus, reinforcement of the perovskite structure is required to stabilize the material while allowing for intensified etching conditions. The partial substitution of the cationic composition by titanium in place of cobalt presents a viable solution. Thus, the addition 20 % of titanium to the structure increases the stability while maintaining the characteristic properties of LaCoO_3 .^[245,246]

The LCTO/LLPSSO composite material and the nanoporous product after etching were thoroughly studied by means of XRD, IR spectroscopy, nitrogen physisorption and electron microscopy. Functional properties were assessed through oxygen desorption measurements using TG-MS.

With regard to the optimization of this templating approach, the ratio of the functionalities of LLPSSO, the template loading of the nanocomposite, and temperature and time of the alkaline etching procedure were varied. A general overview over these results is given in the Appendix. In the following section, the optimized synthesis approach is presented. Accordingly, LLPSSO exhibiting a methacryl to phenyl ratio of 70:30 was used as template as it accommodates high amounts of methacryl functionality, which promotes integration of the template into the polymer matrix of the starting material, and phenyl functionality to prevent agglomeration of the ladder-like structures. A template loading of 20 % with respect to the overall composite mass was favoured.

LCTO/LLPSSO Composite

The successful synthesis of the composite depends primarily on two aspects - the formation of the perovskite oxide phase and the suitable distribution of the ladder-like silica templates within the perovskite matrix. The formation of the substituted perovskite oxide was confirmed by XRD (Figure 7.5a). A distinct perovskite phase with rhombohedral structure was formed. In addition, broadening of the reflections compared to the diffractogram of pristine LCO (see Appendix) was observed, which most likely indicates the formation of smaller-sized crystallites. Accordingly Scherrer crystallite sizes of 12.3 nm were determined for the LCTO/LLPSSO composite (Table 7.1).

Moreover, a broad shoulder in the X-ray diffractogram around $28^\circ 2\theta$, ascribed to amorphous silica, was observed in the composite material. The presence of silica was further proven by a strong absorption band at 1083 nm^{-1} in the IR spectrum (Figure 7.5b). This band results from stretching vibrations of the Si-O-Si bond.

Also, a shoulder at 997 nm^{-1} is visible, indicative of silanol groups. Contrary to the IR spectrum of pure LLPSSO (Figure 7.4), organic functionalities are not detectable. The residual molecules were completely removed during the calcination step of the composite material. This thermal treatment also resulted in curing of the siliceous ladder structure. Thus, the characteristic absorption bands of the ladder structure are replaced by the vibrational modes of silica materials.^[247]

Additionally, the composite displays a strong presence of carbonates indicated by absorption bands at 1481 and 1384 nm^{-1} . Carbonate phases mostly form during calcination of carbonaceous complexing molecules.

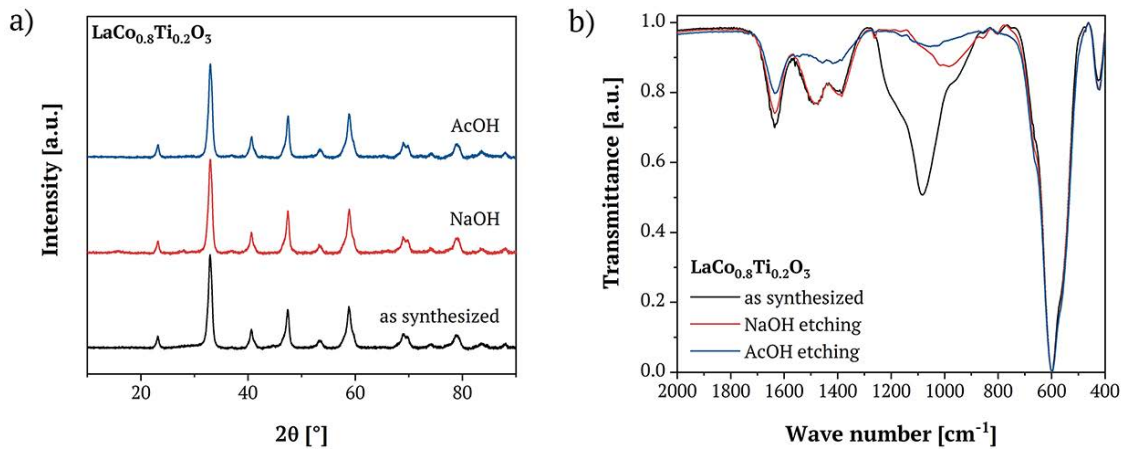


Figure 7.5.: XRD patterns (a) and IR spectra (b) of an as-synthesized LCTO/LLPSSO composite (20 wt.% of LLPSSO) (black), subsequent to a 3M NaOH etching at $80\text{ }^\circ\text{C}$ for 3 h (red) and after acetic acid treatment at room temperature for 1 h (blue).

The chemical composition of the material was determined by EDX measurements, which confirms the presence of silica (Table 7.1). In addition, slight deviation from stoichiometry of the perovskite oxide is observed, which can be ascribed to the presence of carbonates, which was shown in the IR spectrum. The addition of silica and local fluctuations can also contribute to the occurrence of non-stoichiometry.

7. Unpublished Work

Table 7.1.: Textural properties of an LCTO/LLPSSO composite throughout different etching procedures and corresponding atomic compositions determined by EDX.

	Crystallite Size [nm]	S_{BET} [m ² /g]	Atomic Composition [%]				
			La	Co	Ti	O	Si
as synthesized	12.3	34.0	20.2	13.8	2.19	57.6	6.30
NaOH	12.4	62.2	20.0	13.6	4.90	60.1	1.35
AcOH	12.8	91.9	21.5	17.1	4.27	56.1	1.12

The morphological structure of the composite was investigated by electron microscopy. In Figure 7.6a, the disordered arrangement of the silica template in the perovskite oxide matrix is displayed.

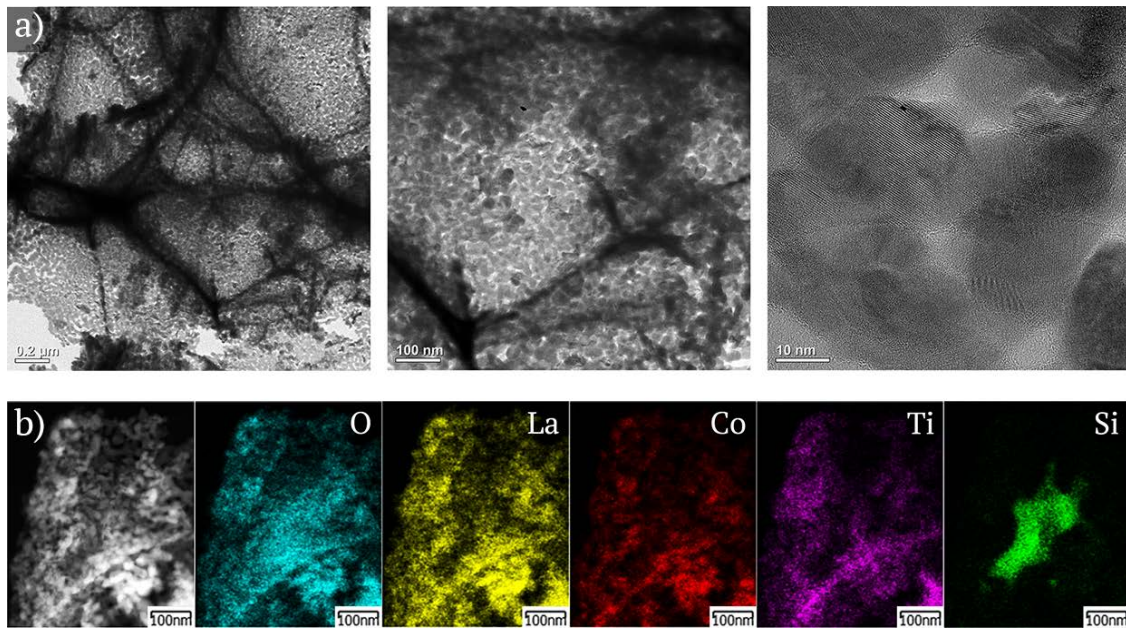


Figure 7.6.: TEM micrographs of an LCTO/LLPSSO composite (20 wt.% of LLPSSO) at different magnifications (a) and elemental mapping of the composite (b).

Several individual 'ladders' are spread over the solid. The width of these structures covers a few nanometers. However, a significant amount of the siliceous structures formed agglomerates, which partially exceed a width of 100 nm. This is further supported by elemental mapping of the silica species in Figure 7.6b. A significant presence of siliceous species is detectable only in selected regions of the perovskite oxide matrix. Accordingly, high local fluctuations of the atomic composition were deduced from EDX (7.1).

The inhomogeneous distribution of the ladder-like structures is detrimental to the templating-effect. The accumulation of LLPSSO can be considered as loss of template since their removal does not considerably contribute to a surface enhancement. Partial templating, however, was achieved.

Furthermore, the micrographs show the nanocrystalline structure of the perovskite oxide phase. The grain sizes vary between 10 and 20 nm, slightly deviating from the values calculated from XRD. Due to the interconnection of the crystallites, interparticle porosity can be observed.

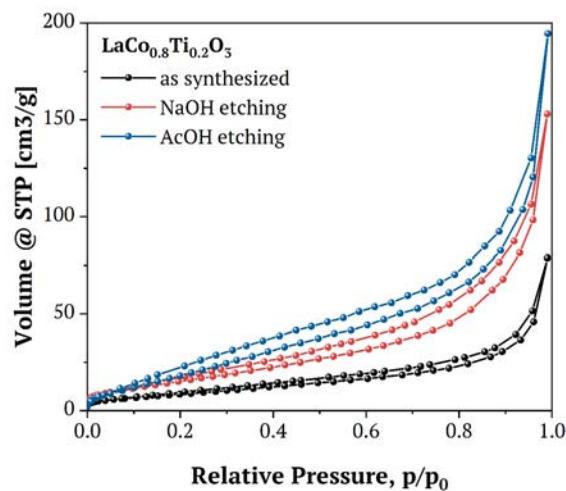


Figure 7.7.: N₂-physisorption isotherms of LCTO/Si composite as-synthesized (black), after NaOH etching (red) and after AcOH etching (blue).

The presence of interparticle porosity is also confirmed by nitrogen physisorption since the isotherm displays a typical increase at high relative pressures (Figure 7.7).^[248] Correspondingly, the isotherm exhibits a hysteresis, which is characteristic of micro-/mesoporous systems.^[249] The perovskite/silica composite has a specific surface area of $34.0 \text{ m}^2\text{g}^{-1}$.

Etching Procedure

Enhancement of the surface area necessitates the removal of the silica template through etching. The etching process comprises two distinct steps. At first, a sodium hydroxide treatment takes place in which the template is removed. Optimal conditions were defined as $80 \text{ }^\circ\text{C}$ for 3 h using a 3M NaOH solution (see Appendix). The presence of carbonate impurities necessitates an ensuing acetic acid treatment. Upon acidic etching in aqueous solution for 1 h at room temperature, contaminations detrimental to electrochemical properties of the material are removed. The compositional differences with an emphasis on the presence of carbonates as well as the change of porosity were determined throughout the process. The diffractograms in Figure 7.5a display the distinct phase of perovskite oxides, respectively. Moreover, no significant changes in the crystallite sizes were observed. A small reflection at $37 \text{ }^\circ 2\theta$, which can be ascribed to the $[3 \ 1 \ 1]$ reflection of Co_3O_4 ,^[250] appeared in the diffractogram following the sodium hydroxide etching. This phase could almost completely be removed in the subsequent acidic etching step. Correspondingly, the composition of the perovskite oxide is slightly changed (Table 7.1).

The shoulder around $28 \text{ }^\circ 2\theta$, which was also observed in the composite material is weakened in the XRD pattern of the sample after alkaline etching. The silica phase was no longer detectable following the acetic acid treatment indicating a pure perovskite oxide phase.

While the conservation of structure is a key element for successful etching, the focus lies on the removal of the template. A qualitative assessment is provided by

IR spectroscopy. Upon alkaline etching, the majority of the template was removed as the siloxane signal in the spectrum vanishes almost completely (Figure 7.5b). However, a broad band at 997 nm^{-1} is visible, indicative of silanol groups still present in the material.^[247] When subsequently treated with acetic acid, the silanol contribution disappeared and only a minimum of silica maintained in the sample. Furthermore, acetic acid etching results in a strong reduction of carbonates as the intensity of the IR bands decreases considerably.

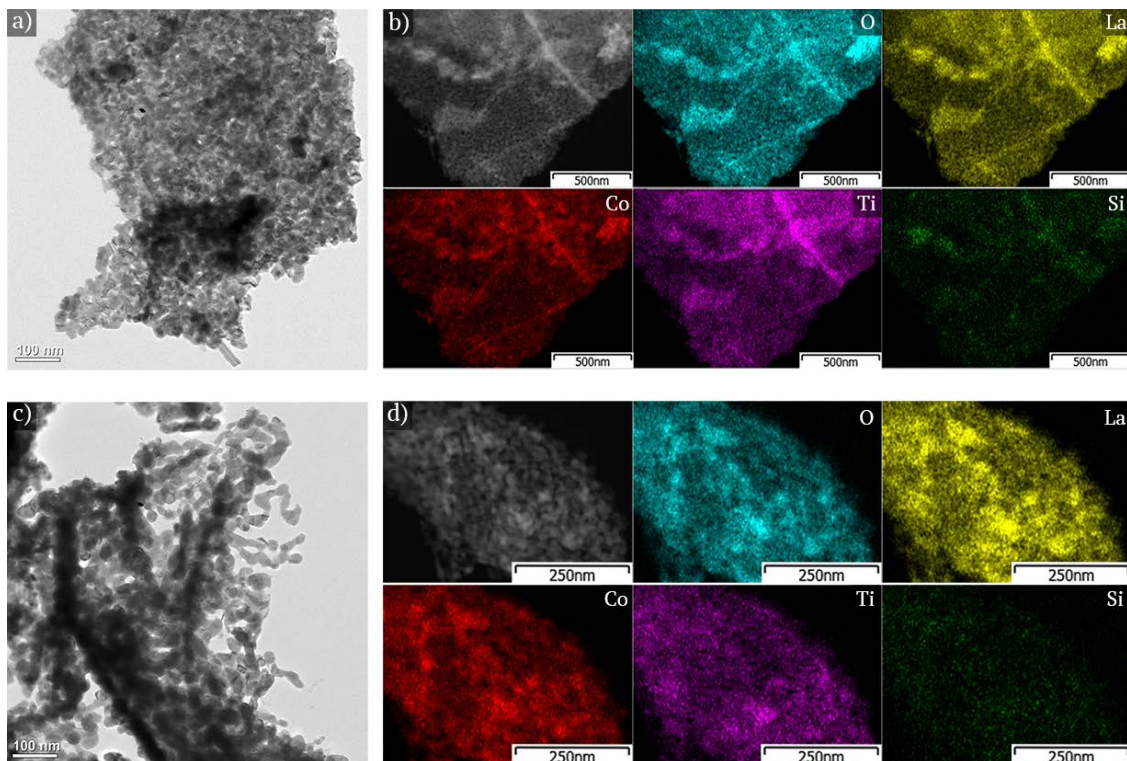


Figure 7.8.: TEM micrographs of an LCTO/LLPSSO composite (20 wt.% of LLPSSO) at different magnifications after alkaline etching (a) and subsequent to an additional acidic treatment (c) and the corresponding elemental mappings (b,d).

The assessment of the IR spectrum is corroborated by electron microscopy and EDX. While template agglomerates and distinct 'ladders' were removed, traces of silica were still detectable in the perovskite oxide matrix (Figure 7.8). However, after acetic acid treatment, the cationic composition is in good agreement with the stoichiometry of $\text{LaCo}_{0.8}\text{Ti}_{0.2}\text{O}_3$ (Table 7.1).

In addition, the removal of silica in a first etching step and both carbonates and remaining template material in the ensuing acidic etching step constituted a gradual increase in porosity as indicated by the nitrogen physisorption isotherms in Figure 7.7. Moreover, the S_{BET} values (Table 7.1) emphasize a significant increase in specific surface area. Alkaline etching resulted in an surface area increase by a factor of two. The subsequent acidic treatment further enhanced the surface area. As a result, $\text{LaCo}_{0.8}\text{Ti}_{0.2}\text{O}_3$ exhibiting a specific surface area of $91.9 \text{ m}^2\text{g}^{-1}$ was obtained.

Functional Properties of Nanoporous $\text{LaCo}_{0.8}\text{Ti}_{0.2}\text{O}_3$

In order to assess functional properties of prepared nanocomposites and the resulting porous materials to assess the impact of the increased surface area, oxygen release characteristics were investigated by means of oxygen desorption via thermogravimetric analysis coupled with mass spectrometry. The oxygen release properties correlate to the reactivity of the surface, which directly impacts the catalytic performance of a material.^[251]

In an initial oxidative cycle, surface contaminations (e.g., water, carbonates) were eliminated. Subsequently, temperature-programmed desorption of oxygen was investigated up to $600 \text{ }^\circ\text{C}$ under argon atmosphere.

Similar to measurements performed on AAm-derived LaCoO_3 ,^[242] the desorption curves in Figure 7.9 exhibit two regions, which are hard to distinguish, indicating low temperature ($T < 500 \text{ }^\circ\text{C}$) and high temperature ($T > 500 \text{ }^\circ\text{C}$) oxygen desorption. Below $500 \text{ }^\circ\text{C}$, α -oxygen is released, which refers to weakly bound oxygen species (OH , O^- and/or O_2^-) at the surface. At higher temperatures, lattice oxygen

(O^{2-}) is removed, denoted as β -oxygen.^[252]

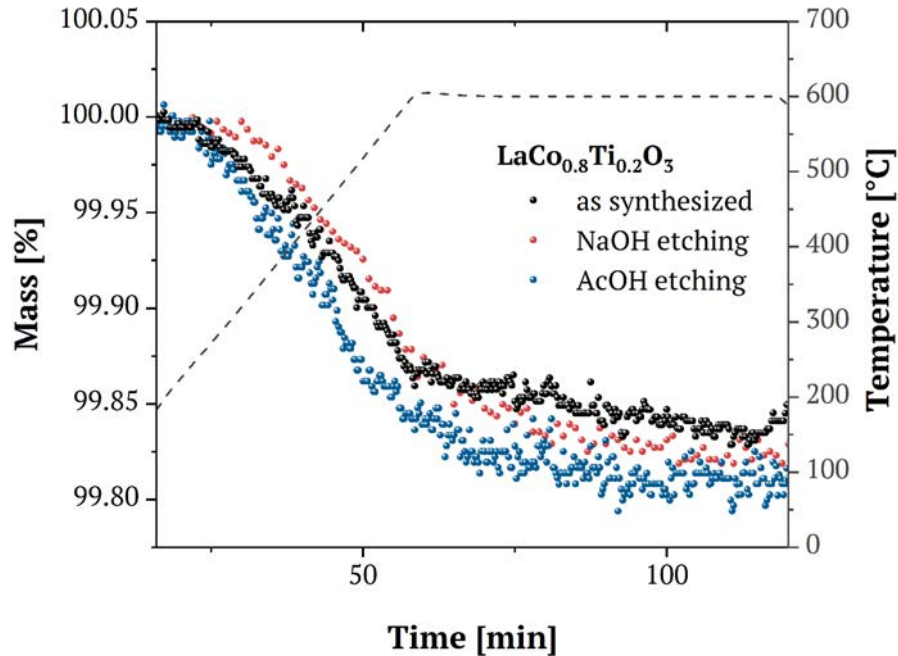


Figure 7.9.: Temperature-programmed desorption of oxygen of an LCTO nanocomposite (black), the composite after alkaline treatment (red) and after an additional AcOH etching (blue) by means of TG-MS measurements.

The thermogravimetric analysis enables a quantification of the total amount of oxygen released from a sample. The mass loss of the LCTO/LLPSSO composite material accounts for 0.16 %. The sample after alkaline treatment exhibits a mass loss of 0.18 %. The highest mass loss was observed for the material subsequent to acetic acid treatment (0.20 %). Additionally, the high-surface perovskite oxide exhibits higher oxygen release rates.

Accordingly, a correlation between the oxygen release activity and the specific surface area is observed. However, additional factors such as the presence of detrimental components (carbonates, silica) should also be taken into consideration.

Conclusion

In this section, a novel endotemplating approach for the preparation of nanoporous perovskite oxides was presented. Functionalized ladder-like polysilsesquioxanes were used as templates, the employment of which presented some challenges. On the one hand, formation of silica agglomerates prevented homogeneous distribution of the template. Accordingly, only partial templating was achieved. On the other hand, traces of silica were still present in the sample after alkaline and acidic treatment, similar to other silica-based templating methods.

Nevertheless, perovskite oxides with high surface areas above $90 \text{ m}^2\text{g}^{-1}$ were after removal of the template. These results compare well to nanostructured solids prepared through nanocasting.^[119] Accordingly, an alternative templating approach for the preparation of high surface area perovskite oxides was developed.

Moreover, the increased surface area resulted in enhanced oxygen release properties compared to pristine perovskite oxides, which were prepared through the acrylate route.^[242]

8. Discussion

The focal points of this work were the investigation of confinement effects of nanocomposite materials and the design of nanostructured perovskite oxides with improved functional properties for energy-related applications. In both cases, a clear contribution of the nanostructure to the characteristic properties of the respective materials was observed. Thus, in this section, the different results will be discussed in relation to the nanostructural characteristics.

With respect to the confinement effects, two different host-guest systems were investigated. In a first study, the confinement of sulfur within an ordered nanoporous carbon matrix in dependence of sulfur-fluid interactions was investigated. The focus was placed on the characterization of this composite material in the nano range in order to gain a better understanding of carbon-sulfur nanocomposite as Li-S battery cathode material. The employment of SANS in combination with a contrast-matching technique allowed for direct investigation of the processes taking place.

While complete filling of the pore space with sulfur was achieved, addition of a solvent with similar properties to common electrolyte fluids lead to leaching of sulfur from the pores. The interactions between sulfur and hydrophobic solvents (e.g. THF, toluene) were stronger than the adhesion forces between sulfur and carbon, and the guest species was easily removed from the host matrix. Since sulfur constitutes the active material, its loss is detrimental to the performance of the battery and presents a main issue of the capacity fading of Li-S batteries. Corresponding results have not been reported previously due to the limited availability of suitable analysis methods. Thus, sulfur-solvent interactions in the nano range have been

disregarded and loss of active material has been primarily ascribed to the well-investigated shuttle effect.^[11,23,51]

When using THF, which is used as a co-solvent in common electrolytes, sulfur maintained confined in the micropores. Thus, further design of cathode materials for Li-S batteries must take sulfur-solvent interactions into consideration by addressing both the hydrophobic character of the electrolyte and the pore properties of the carbon host. SANS in combination with contrast-matching presents a suitable characterization method for the investigation of such nanoscale processes.

The second part related to confinement effects, dealt with the impregnation behaviour and crystal formation of perovskite oxides in nanoporous silica matrices. The use of silica as a support is a promising approach to increase the surface area of perovskite oxides and correspondingly improve catalytic activity of the material. However, the perovskite formation in these nanoporous matrices does not follow the classic model, nanoconfinement effects occur. Problems such as the formation of perovskite crystals outside the pores and the lack of crystallinity of the incorporated perovskite species cannot be directly explained.^[143–145,253]

By using nanoporous silica host systems with different pore geometries, a better understanding of these processes could be obtained. A clear correlation between crystal formation and distribution of the perovskite oxides, and the nanostructure of the silica matrix was established. In this context, the decomposition of the precursor solution played a major role, which was examined by mass spectrometry. Clear differences in the decomposition kinetics of the precursors and evaporation of the solvent could be attributed to changes in the pore size and pore curvature of the respective silica matrices. The formation of perovskite crystals within the pores was particularly preferred due to a high pore curvature.

Accordingly, this study was able to provide new information on the influence of pore geometry on the crystallization processes of confined perovskite oxides. Complete understanding of the processes forms the basis for the preparation of silica supports with a suitable nanostructure.

The second main objective of this work referred to the preparation of nanostructured perovskite oxides. Both nanocrystallinity and enhancement of the specific surface area and the corresponding functional properties were addressed through a novel synthesis method based on a polymer-complex approach. The preparation of many different perovskite oxides (e.g. LCO, STO, LNO) and solid solutions thereof was achieved.

Bifunctional acrylate molecules (methacrylic acid, acrylic acid, acrylamide) were used as chelating agent and monomers. The crystallinity of the perovskite oxide correlated directly with the choice of acrylic agent. Thus, by selecting different acrylates, the grain size, i.e. the nanostructure, could be readily controlled.

Moreover, perovskite oxides with considerably higher purity were obtained by this approach compared to common citrate methods. As a consequence, the perovskite oxide powders prepared from acrylates exhibited improved functional properties as determined by O₂-TPD measurements and catalytic conversion of CO.

In order to further improve the material properties, the specific surface area was increased through the incorporation of a functionalized ladder-like polysilsesquioxane endotemplate. Even though the template approach had some shortcomings, e.g. agglomeration of the siliceous species, which resulted in inhomogeneous distribution of the template, and traces of silica due to incomplete removal of the template, the specific surface area of the perovskite oxide could be drastically increased. The nanocrystalline features of the materials were maintained. Correspondingly, oxygen exchange properties were enhanced.

The development of this synthetic method has demonstrated the big impact of the nanostructure of perovskite oxides on their functional properties. As a result, the synthesis method enables direct control over the nanostructure of the perovskite oxide and can be used to specifically improve the material properties.

In summary, a comprehensive overview over the impact of nanostructuring is presented in this work that addressed both suitable characterization methods and

functional properties of nanostructured materials. While the presence of structural features in the nanometer range necessitates special characterization methods, material properties are significantly affected by nanosize effects. Accordingly, it is shown that an improved understanding of the processes involved and the development of suitable design strategies are indispensable for the preparation of high-performance materials.

9. Experimental Section

9.1. Chemicals

Acetic acid (99.8%, VWR Chemicals), acrylamide (98.5%, Acros Organics), ammonia (25.0%, VWR Chemicals), cobalt nitrate hexahydrate (97.7%, Alfa Aesar), dichloromethane (99.0%, BCD), 1-hydroxycyclohexyl phenyl ketone (98.0%, Alfa Aesar), lanthanum nitrate hexahydrate (99.9%, Alfa Aesar), magnesium sulfate (99.0%, Grüssing GmbH), 3-methacryloxypropyltrimethoxysilane (97.0%, Alfa Aesar), phenyltrimethoxysilane (97.0%, Alfa Aesar), potassium carbonate (99.0%, Alfa Aesar), sodium hydroxide (98.5%, Acros Organics), strontium nitrate (99.0%, Acros Organics), tetrahydrofuran (99.5%, VWR Chemicals), and titanium-(IV) isopropoxide (97.0%, Alfa Aesar) were used as received without further purifications.

9.2. Synthesis of ladder-like Polysilsesquioxane

The formation of ladder-like polysilsesquioxanes was carried out according to Choi *et al.*^[130]

Prior to the synthesis, potassium carbonate was dried at 80 °C over night. THF was dried over 3 Å molecular sieves for . Potassium carbonate (K_2CO_3 , 20.0 mg, 0.145 mmol) was dissolved in water (2.40 g, 0.133 mol) and stirred for 10 min. THF (4.00 g, 56.0 mmol) was added and the solution was stirred for 30 min under N_2 -atmosphere. Subsequently, a mixture of MOPTMS and PTMS (40.0 mmol) was prepared and added dropwise. Employed mixture compositions and the corresponding amounts of respective compound are listed in Table 9.1. After 96 h of

continuous stirring, two phases were formed. The colourless phase was decanted, followed by dissolution of the cloudy, viscous product phase in DCM (30 mL) and trifold washing with water (20 mL, each). The organic phase was dried over magnesium sulfate (MgSO_4) over night, filtered and the solvent was removed *in vacuo*. Vacuum drying at 40 °C resulted in a colourless, viscous product.

Table 9.1.: Employed compositions of MOPTMS and PTMS

Ratio MOPTMS:PTMS	Amount of MOPTMS	Amount of PTMS
100:0	9.84 g (40.0 mmol)	-
90:10	8.86 g (36.0 mmol)	0.79 g (4.0 mmol)
80:20	7.87 g (32.0 mmol)	1.58 g (8.0 mmol)
70:30	6.89 g (28.0 mmol)	2.38 g (12.0 mmol)
10:90	0.98 g (4.0 mmol)	7.13 g (36.0 mmol)

9.3. Synthesis of $\text{LaCo}_{0.8}\text{Ti}_{0.2}\text{O}_3$ -LLPSSO

Composites

LCO/LLPSSO composite materials were prepared by modifying the radical polymerization approach introduced by Scholz *et al.*^[242]

The molar ratio of acrylate polymer to metal cations equaled 4:1. First, previously synthesized LLPSSO (122.8 mg, 20 wt.%) was dissolved in THF (2 mL) under rigorous stirring at room temperature. The percentage values refer to the share of LLPSSO in the final composite. Lanthanum nitrate hexahydrate (866 mg, 2.0 mmol) and cobalt nitrate hexahydrate (477 mg, 1.6 mmol) were added to the solution, which was stirred until the precursor salts were dissolved. Then, the complexing agent acrylamide (1138 mg, 8 mmol) was dissolved and titanium(IV)-isopropoxide (114 mg, 0.4 mmol) was added to the solution under stirring.

1-Hydroxycyclohexyl phenyl ketone (10 mg) as radical initiator was added. After 5 min of stirring, the solution was transferred into a petri dish and exposed to

UV radiation from a high-pressure mercury vapor lamp (Philips HPK-125 W) for 15 min at room temperature. The resulting polymer was then calcined in air at 600 °C for 2 h following 2 h at 400 °C using a heating rate of 2 °C/min for each step to obtain the perovskite oxide/LLPSSO composite.

9.4. Sodium Hydroxide Etching

The silica template was removed by sodium hydroxide etching. The perovskite oxide/LLPSSO composite (80 mg) was added to an aqueous NaOH solution (3M, 20 mL). The mixture was stirred for 3 h at 80 °C. Finally, the powder was filtrated and extensively washed with demineralized water. After drying over night at 80 °C, porous perovskite oxide was obtained.

9.5. Acetic Acid Etching

In order to remove carbonate impurities from the metal oxides, acetic acid etching was used. Glacial acetic acid was diluted with demineralized water to yield a 5 % acetic acid solution. Perovskite oxide (80 mg) was added to 25 mL of the acetic acid solution and stirred for 1 h at room temperature. The perovskite oxide was filtrated and then extensively washed with demineralized water. Lastly, the powder was dried at 80 °C over night.

9.6. Characterization Methods

X-ray diffraction measurements were carried out with an X'Pert Pro diffractometer (PANalytical Corp.) with 0.15406 nm Ni-filtered Cu K α radiation in Bragg-Brentano geometry, operating at 45 kV and 40 mA, a step size of 0.0130, and a step time of 74 s per step. The crystallite size was determined using the Scherrer equation from the full width at half-maximum (fwhm) of the most intense reflection

(110). The data analysis was performed using X'Pert HighScore Plus by PANalytical and the ICDD database for peak identification.

IR spectroscopy was performed employing the KBr pellet technique; the mid-IR spectra from 4000 to 400 cm^{-1} were acquired with a Bruker Tensor 27. Correction of the baseline was achieved using the software OPUS 7.2 by Bruker.

The nitrogen sorption isotherms were obtained at 77 K using a Quadrasorb SI-MP by Quantachrome. Outgassing was performed with a Masterprep Degasser (Quantachrome Corp.) at 120 °C for 12 h. Specific surface areas were determined using the Brunauer-Emmett-Teller (BET) method^[254] at $p/p_0 = 0.07-0.3$. Pore-size distributions were calculated using an NLDFIT equilibrium model for cylindrical silica pores.

TG-DSC measurements were carried out using an STA 449 F3 Jupiter by Netzsch. The temperature profile followed the actual synthesis conditions, i.e., from RT to 400 °C with a heating rate of 2 °C/min, 2 h at 400 °C, another increase up to 600 °C with a heating rate of 2 °C/min, and a final step at 600 °C for 2 h. The measurement was performed under an oxygen/argon atmosphere (20/80) with a flow rate of 40 mL/min.

SEM images were obtained on a LEO1550 with a spatial resolution of $\tilde{1}$ nm. The powder was fixed on a standard carbon conductive tab and was investigated without further conductive coating. Energy dispersive X-ray (EDX) mapping was implemented on several analysis points on the sample, and average atomic ratios were calculated for each cation of LaCoO_3 .

Transmission electron microscopy (TEM) and energy-dispersive X-ray spectroscopy (EDX) measurements were carried out on a JEOL JEM 2200 FS at 200 kV equipped with two CEOS Cs correctors (CETCOR, CESCOR), EDS system JED-2300 T, a Gatan 4 K UltraScan 1000 camera and a HAADF (high angle annular dark field) detector. The sample was crushed into a fine powder, which was suspended in toluene and dropped on a carbon coated 400 mesh TEM grid. The excess of solvent was removed with a filter paper and by drying the grid under air.

^1H NMR spectra were obtained with a Bruker FourierHD 300 MHz spectrometer

with a 5 mm dual sample holder with z-gradient. Before the measurement, the chemicals had been dissolved in CDCl_3 .

^{29}Si NMR spectra were obtained with a Bruker Avance III HD 400 MHz spectrometer with a 5 mm BBI sample holder with ATM and z-gradient. Before the measurement, the chemicals had been dissolved in CDCl_3 .

Bibliography

- [1] B. Scrosati, J. Garche, *Journal of Power Sources* **2010**, *195*, 2419–2430.
- [2] S. E. Hosseini, M. A. Wahid, *Renewable and Sustainable Energy Reviews* **2016**, *57*, 850–866.
- [3] IPCC, **2014**, 151.
- [4] D. Gielen, F. Boshell, D. Saygin, M. D. Bazilian, N. Wagner, R. Gorini, *Energy Strategy Reviews* **2019**, *24*, 38–50.
- [5] T. Covert, M. Greenstone, C. R. Knittel, *Journal of Economic Perspectives* **2016**, *30*, 117–138.
- [6] BP, **2019**, 1–69.
- [7] S. Royer, D. Duprez, F. Can, X. Courtois, C. Batiot-Dupeyrat, S. Laassiri, H. Alamdari, *Chemical Reviews* **2014**, *114*, 10292–10368.
- [8] S. Royer, D. Duprez, *ChemCatChem* **2011**, *3*, 24–65.
- [9] P. Granger, V. I. Parvulescu, S. Kaliaguine, W. Prellier, *Perovskites and Related Mixed Oxides: Concepts and Applications*, (Eds.: P. Granger, V. I. Parvulescu, V. I. Parvulescu, W. Prellier), Wiley-VCH Verlag GmbH & Co. KGaA, Weinheim, Germany, **2015**, pp. 1–978.
- [10] C. Mebrahtu, F. Krebs, S. Abate, S. Perathoner, G. Centi, R. Palkovits in *Studies in Surface Science and Catalysis, Vol. 178*, Elsevier B.V., **2019**, pp. 85–103.
- [11] P. G. Bruce, S. a. Freunberger, L. J. Hardwick, J.-M. Tarascon, *Nature Materials* **2012**, *11*, 19–30.

-
- [12] J. Hwang, R. R. Rao, L. Giordano, Y. Katayama, Y. Yu, Y. Shao-Horn, *Science* **2017**, *358*, 751–756.
- [13] J. Suntivich, H. A. Gasteiger, N. Yabuuchi, H. Nakanishi, J. B. Goodenough, Y. Shao-Horn, *Nature Chemistry* **2011**, *3*, 546–550.
- [14] P. Balaya, *Energy & Environmental Science* **2008**, *1*, 645.
- [15] S. Royer, D. Duprez, S. Kaliaguine, *Journal of Catalysis* **2005**, *234*, 364–375.
- [16] H. Zhu, P. Zhang, S. Dai, *ACS Catalysis* **2015**, *5*, 6370–6385.
- [17] Y.-G. Guo, J.-S. Hu, L.-J. Wan, *Advanced Materials* **2008**, *20*, 2878–2887.
- [18] J. Maier, *Nature Materials* **2005**, *4*, 805–815.
- [19] S. Royer, H. Alamdari, D. Duprez, S. Kaliaguine, *Applied Catalysis B: Environmental* **2005**, *58*, 273–288.
- [20] Q. Jiang, M. D. Ward, *Chem. Soc. Rev.* **2014**, *43*, 2066–2079.
- [21] R. J. Tilley, *Perovskites: Structure-Property Relationships*, **2016**, pp. 1–315.
- [22] J. Schuster, G. He, B. Mandlmeier, T. Yim, K. T. Lee, T. Bein, L. F. Nazar, *Angewandte Chemie International Edition* **2012**, *51*, 3591–3595.
- [23] X. Ji, L. F. Nazar, *Journal of Materials Chemistry* **2010**, *20*, 9821.
- [24] Y. V. Mikhaylik, J. R. Akridge, *Journal of The Electrochemical Society* **2004**, *151*, A1969.
- [25] A. Petzold, A. Juhl, J. Scholz, B. Ufer, G. Goerigk, M. Fröba, M. Ballauff, S. Mascotto, *Langmuir* **2016**, *32*, 2780–2786.
- [26] C. Liang, Z. Li, S. Dai, *Angewandte Chemie International Edition* **2008**, *47*, 3696–3717.
- [27] Z. Mileeva, D. Ross, D. Wilkinson, S. King, T. Ryan, H. Sharrock, *Carbon* **2012**, *50*, 5062–5075.
- [28] S. Mascotto, D. Kuzmicz, D. Wallacher, M. Siebenbürger, D. Clemens, S. Risse, J. Yuan, M. Antonietti, M. Ballauff, *Carbon* **2015**, *82*, 425–435.

- [29] M. Fernández-García, A. Martínez-Arias, J. C. Hanson, J. A. Rodriguez, *Chemical Reviews* **2004**, *104*, 4063–4104.
- [30] A.-H. Lu, F. Schüth, *Advanced Materials* **2006**, *18*, 1793–1805.
- [31] H.-E. Wang, X. Zhao, X. Li, Z. Wang, C. Liu, Z. Lu, W. Zhang, G. Cao, *Journal of Materials Chemistry A* **2017**, *5*, 25056–25063.
- [32] P. Buffat, J.-P. Borel, *Physical Review A* **1976**, *13*, 2287–2298.
- [33] M. Antonietti, G. A. Ozin, *Chemistry - A European Journal* **2004**, *10*, 28–41.
- [34] Z. Wang, L. Zhou, X. W. Lou, *Advanced Materials* **2012**, *24*, 1903–1911.
- [35] J. Yang, Y. Guo, *Chinese Chemical Letters* **2018**, *29*, 252–260.
- [36] J. Rouquerol, D. Avnir, C. W. Fairbridge, D. H. Everett, J. M. Haynes, N. Pernicone, J. D. F. Ramsay, K. S. W. Sing, K. K. Unger, *Pure and Applied Chemistry* **1994**, *66*, 1739–1758.
- [37] F. Schüth, W. Schmidt, *Advanced Engineering Materials* **2002**, *4*, 269–279.
- [38] A. Taguchi, F. Schüth, *Microporous and Mesoporous Materials* **2005**, *77*, 1–45.
- [39] J. B. Mietner, F. J. Brieler, Y. J. Lee, M. Fröba, *Angewandte Chemie International Edition* **2017**, *56*, 12348–12351.
- [40] Y. Diao, T. Harada, A. S. Myerson, T. Alan Hatton, B. L. Trout, *Nature Materials* **2011**, *10*, 867–871.
- [41] N. E. Chayen, E. Saridakis, R. El-Bahar, Y. Nemirovsky, *Journal of Molecular Biology* **2001**, *312*, 591–595.
- [42] M. D. Ward, *Chemical Reviews* **2001**, *101*, 1697–1726.
- [43] Y. Diao, A. S. Myerson, T. A. Hatton, B. L. Trout, *Langmuir* **2011**, *27*, 5324–5334.
- [44] J.-M. Ha, J. H. Wolf, M. A. Hillmyer, M. D. Ward, *Journal of the American Chemical Society* **2004**, *126*, 3382–3383.

-
- [45] J.-M. Ha, B. D. Hamilton, M. A. Hillmyer, M. D. Ward, *Crystal Growth & Design* **2009**, *9*, 4766–4777.
- [46] A. J. Page, R. P. Sear, *Journal of the American Chemical Society* **2009**, *131*, 17550–1.
- [47] P. Maheshwari, D. Dutta, S. K. Sharma, K. Sudarshan, P. K. Pujari, M. Majumder, B. Pahari, B. Bandyopadhyay, K. Ghoshray, A. Ghoshray, *The Journal of Physical Chemistry C* **2010**, *114*, 4966–4972.
- [48] B. D. Hamilton, I. Weissbuch, M. Lahav, M. A. Hillmyer, M. D. Ward, *Journal of the American Chemical Society* **2009**, *131*, 2588–2596.
- [49] H.-J. Peng, Q. Zhang, *Angewandte Chemie International Edition* **2015**, *54*, 11018–11020.
- [50] S. Xin, Y. You, H.-Q. Li, W. Zhou, Y. Li, L. Xue, H.-P. Cong, *ACS Applied Materials & Interfaces* **2016**, *8*, 33704–33711.
- [51] Y. Xu, Y. Wen, Y. Zhu, K. Gaskell, K. A. Cychosz, B. Eichhorn, K. Xu, C. Wang, *Advanced Functional Materials* **2015**, *25*, 4312–4320.
- [52] X. Sun, Y. Shi, P. Zhang, C. Zheng, X. Zheng, F. Zhang, Y. Zhang, N. Guan, D. Zhao, G. D. Stucky, *Journal of the American Chemical Society* **2011**, *133*, 14542–14545.
- [53] J. Janek, M. Martin, K. D. Becker, *Physical Chemistry Chemical Physics* **2009**, *11*, 3010.
- [54] J. Maier, *Progress in Solid State Chemistry* **1995**, *23*, 171–263.
- [55] H. Gleiter, *Acta Materialia* **2000**, *48*, 1–29.
- [56] R. Klie, Y. Ito, S. Stemmer, N. Browning, *Ultramicroscopy* **2001**, *86*, 289–302.
- [57] H. Gleiter, *Progress in Materials Science* **1989**, *33*, 223–315.
- [58] M. S. D. Read, M. Saiful Islam, G. W. Watson, F. King, F. E. Hancock, *Journal of Materials Chemistry* **2000**, *10*, 2298–2305.
-

- [59] M. S. Islam, M. Cherry, L. J. Winch, *Journal of the Chemical Society Faraday Transactions* **1996**, *92*, 479.
- [60] J. W. Fergus, *Sensors and Actuators B: Chemical* **2007**, *123*, 1169–1179.
- [61] R.-A. Eichel, *Phys. Chem. Chem. Phys.* **2011**, *13*, 368–384.
- [62] M. Ghasdi, H. Alamdari, *Sensors and Actuators B: Chemical* **2010**, *148*, 478–485.
- [63] P. Balaya, J. Jamnik, J. Fleig, J. Maier, *Applied Physics Letters* **2006**, *88*, 062109.
- [64] B. Raveau, M. M. Seikh, *Cobalt Oxides*, Wiley-VCH Verlag GmbH & Co. KGaA, Weinheim, Germany, **2012**, p. 344.
- [65] H. Tuller, *Solid State Ionics* **1997**, *94*, 63–74.
- [66] A. J. Jacobson, *Chemistry of Materials* **2010**, *22*, 660–674.
- [67] A. R. West, *Solid state chemistry and its applications by A. R. West*, Wiley-VCH Verlag GmbH & Co. KGaA, Weinheim, Germany, **2014**, p. 582.
- [68] J. Zhu, H. Li, L. Zhong, P. Xiao, X. Xu, X. Yang, Z. Zhao, J. Li, *ACS Catalysis* **2014**, *4*, 2917–2940.
- [69] R. J. H. Voorhoeve, D. W. Johnson, J. P. Remeika, P. K. Gallagher, *Science* **1977**, *195*, 827–833.
- [70] K. Momma, F. Izumi, *Journal of Applied Crystallography* **2011**, *44*, 1272–1276.
- [71] V. M. Longo, M. das Graça Sampaio Costa, A. Zirpole Simões, I. L. V. Rosa, C. O. P. Santos, J. Andrés, E. Longo, J. A. Varela, *Physical Chemistry Chemical Physics* **2010**, *12*, 7566.
- [72] A. E. Danks, S. R. Hall, Z. Schnepp, *Materials Horizons* **2016**, *3*, 91–112.
- [73] Y.-J. Lin, Y.-H. Chang, W.-D. Yang, B.-S. Tsai, *Journal of Non-Crystalline Solids* **2006**, *352*, 789–794.

-
- [74] K. J. May, C. E. Carlton, K. A. Stoerzinger, M. Risch, J. Suntivich, Y.-L. Lee, A. Grimaud, Y. Shao-Horn, *The Journal of Physical Chemistry Letters* **2012**, *3*, 3264–3270.
- [75] L. Hou, H. Zhang, L. Dong, L. Zhang, D. Duprez, S. Royer, *Catalysis Today* **2017**, *287*, 30–36.
- [76] V. M. Goldschmidt, *Die Naturwissenschaften* **1926**, *14*, 477–485.
- [77] T. Ishihara, *Perovskite Oxide for Solid Oxide Fuel Cells*, (Ed.: T. Ishihara), Springer US, Boston, MA, **2009**.
- [78] M. Kubicek, A. H. Bork, J. L. M. Rupp, *Journal of Materials Chemistry A* **2017**, *5*, 11983–12000.
- [79] R. J. D. Tilley, *Defects in Solids*, John Wiley & Sons, Inc., Hoboken, NJ, USA, **2008**.
- [80] R. A. De Souza, M. S. Islam, E. Ivers-Tiffée, *Journal of Materials Chemistry* **1999**, *9*, 1621–1627.
- [81] R. A. De Souza, J. Maier, *Physical Chemistry Chemical Physics* **2003**, *5*, 740–748.
- [82] A. Jones, M. S. Islam, *The Journal of Physical Chemistry C* **2008**, *112*, 4455–4462.
- [83] Y. Zhu, W. Zhou, J. Yu, Y. Chen, M. Liu, Z. Shao, *Chemistry of Materials* **2016**, *28*, 1691–1697.
- [84] G. Kostogloudis, C. Ftikos, *Solid State Ionics* **1999**, *126*, 143–151.
- [85] H. Seim, M. Nieminen, L. Niinistö, H. Fjellvåg, L.-S. Johansson, *Applied Surface Science* **1997**, *112*, 243–250.
- [86] M. Kumar, S. Srikanth, B. Ravikumar, T.C.Alex, S. Das, *Materials Chemistry and Physics* **2009**, *113*, 803–815.
- [87] N. Q. Minh, *Journal of the American Ceramic Society* **1993**, *76*, 563–588.

- [88] B. Seyfi, M. Baghalha, H. Kazemian, *Chemical Engineering Journal* **2009**, *148*, 306–311.
- [89] N. Orlovskaya, K. Kleveland, T. Grande, M.-a. Einarsrud, *Journal of the European Ceramic Society* **2000**, *20*, 51–56.
- [90] O. Parkash, P. Ganguly, G. Rao, C. Rao, D. Rajoria, V. Bhide, *Materials Research Bulletin* **1974**, *9*, 1173–1176.
- [91] M. Futai, C. Yonghua, Louhui, *Reaction Kinetics and Catalysis Letters* **1986**, *31*, 47–54.
- [92] H. Falcón, M. J. Martínez-Lope, J. A. Alonso, J. L. Fierro, *Solid State Ionics* **2000**, *131*, 237–248.
- [93] P. Ciambelli, S. Cimino, S. De Rossi, L. Lisi, G. Minelli, P. Porta, G. Russo, *Applied Catalysis B: Environmental* **2001**, *29*, 239–250.
- [94] J. Suntivich, K. J. May, H. A. Gasteiger, J. B. Goodenough, Y. Shao-Horn, *Science* **2011**, *334*, 1383–1385.
- [95] J. M. D. Tascón, L. González Tejuca, *Reaction Kinetics and Catalysis Letters* **1980**, *15*, 185–191.
- [96] S. Zhou, X. Miao, X. Zhao, C. Ma, Y. Qiu, Z. Hu, J. Zhao, L. Shi, J. Zeng, *Nature Communications* **2016**, *7*, 11510.
- [97] D. N. Mueller, M. L. Machala, H. Bluhm, W. C. Chueh, *Nature Communications* **2015**, *6*, 6097.
- [98] J. M. D. Tascón, J. L. G. Fierro, L. G. Tejuca, *Zeitschrift für Physikalische Chemie* **1981**, *124*, 249–257.
- [99] W. H. Weinberg, *Accounts of Chemical Research* **1996**, *29*, 479–487.
- [100] Y. Zhang-Steenwinkel, L. M. Van Der Zande, H. L. Casticum, A. Blik, *Applied Catalysis B: Environmental* **2004**, *54*, 93–103.
- [101] K. R. Barnard, K. Foger, T. W. Turney, R. D. Williams, *Journal of Catalysis* **1990**, *125*, 265–275.

- [102] J. Shu, S. Kaliaguine, *Applied Catalysis B: Environmental* **1998**, *16*, L303.
- [103] R. Doshi, C. B. Alcock, J. J. Carberry, *Catalysis Letters* **1993**, *18*, 337–343.
- [104] C. Xiulan, L. Yuan, *Chemical Engineering Journal* **2000**, *78*, 205–209.
- [105] H. Taguchi, S. Yamasaki, A. Itadani, M. Yosinaga, K. Hirota, *Catalysis Communications* **2008**, *9*, 1913–1915.
- [106] H. Taguchi, S. Yamada, M. Nagao, Y. Ichikawa, K. Tabata, *Materials Research Bulletin* **2002**, *37*, 69–76.
- [107] Y. Liu, H. Dai, J. Deng, L. Zhang, Z. Zhao, X. Li, Y. Wang, S. Xie, H. Yang, G. Guo, *Inorganic Chemistry* **2013**, *52*, 8665–8676.
- [108] S. Lee, J. Lee, Y. Park, J. Wee, K. Lee, *Catalysis Today* **2006**, *117*, 376–381.
- [109] T. Nakamura, M. Misono, Y. Yoneda, *Bulletin of the Chemical Society of Japan* **1982**, *55*, 394–399.
- [110] T. Nakamura, *Journal of Catalysis* **1983**, *83*, 151–159.
- [111] L. A. Isupova, V. A. Sadykov, S. V. Tsybulya, G. N. Kryukova, V. P. Ivanov, A. N. Petrov, O. F. Kononchuk, *Reaction Kinetics and Catalysis Letters* **1997**, *62*, 129–135.
- [112] B. Levasseur, S. Kaliaguine, *Applied Catalysis A: General* **2008**, *343*, 29–38.
- [113] H. X. Dai, H. He, W. Li, Z. Z. Gao, C. T. Au, *Catalysis Letters* **2001**, *73*, 149–156.
- [114] P. Mars, D. van Krevelen, *Chemical Engineering Science* **1954**, *3*, 41–59.
- [115] L. Lisi, G. Bagnasco, P. Ciambelli, S. De Rossi, P. Porta, G. Russo, M. Turco, *Journal of Solid State Chemistry* **1999**, *146*, 176–183.
- [116] J. Hueso, D. Martínez-Martínez, A. Caballero, A. González-Elipé, B. Mun, M. Salmerón, *Catalysis Communications* **2009**, *10*, 1898–1902.
- [117] M. Misono, *Heterogeneous Catalysis of Mixed Oxides : Perovskite and Heteropoly Catalysts*, **2013**, pp. 49–51.

- [118] M. M. Natile, E. Ugel, C. Maccato, A. Glisenti, *Applied Catalysis B: Environmental* **2007**, *72*, 351–362.
- [119] Y. Wang, J. Ren, Y. Wang, F. Zhang, X. Liu, Y. Guo, G. Lu, *Journal of Physical Chemistry C* **2008**, *112*, 15293–15298.
- [120] M. M. Nair, F. Kleitz, S. Kaliaguine, *ChemCatChem* **2012**, *4*, 387–394.
- [121] R. de Lima, M. Batista, M. Wallau, E. Sanches, Y. Mascarenhas, E. Urquieta-González, *Applied Catalysis B: Environmental* **2009**, *90*, 441–450.
- [122] U. Schubert, *Chemie in unserer Zeit* **2018**, *52*, 18–25.
- [123] C.J. Brinker, G. W. Scherer, *Sol-Gel Science: The Physics and Chemistry of Sol-Gel Processing*, Academic Press, San Diego, **1990**, p. 462.
- [124] J. Livage, M. Henry, C. Sanchez, *Progress in Solid State Chemistry* **1988**, *18*, 259–341.
- [125] U. Schubert, N. Husing, *Synthesis of Inorganic Materials*, **2012**, p. 392.
- [126] F. Dong, C.-S. Ha, *Macromolecular Research* **2012**, *20*, 335–343.
- [127] J. D. Lichtenhan, Y. A. Otonari, M. J. Carr, *Macromolecules* **1995**, *28*, 8435–8437.
- [128] T. S. Haddad, J. D. Lichtenhan, *Macromolecules* **1996**, *29*, 7302–7304.
- [129] G. Li, C. U. Pittman in *Macromolecules Containing Metal and Metal-Like Elements, Vol. 4*, 3, John Wiley & Sons, Inc., Hoboken, NJ, USA, **2005**, pp. 79–131.
- [130] S.-S. Choi, A. S. Lee, H. S. Lee, H. Y. Jeon, K.-Y. Baek, D. H. Choi, S. S. Hwang, *Journal of Polymer Science Part A: Polymer Chemistry* **2011**, *49*, 5012–5018.
- [131] Q. Gao, S. Qi, Z. Wu, D. Wu, W. Yang, *Thin Solid Films* **2011**, *519*, 6499–6507.
- [132] L. Zhang, D. Dai, R. Zhang, *Polymers for Advanced Technologies* **1997**, *8*, 662–665.

-
- [133] A. S. S. Lee, S.-S. Choi, H. S. Lee, H. Y. Jeon, K.-Y. Baek, S. S. Hwang, *Journal of Polymer Science Part A: Polymer Chemistry* **2012**, *50*, 4563–4570.
- [134] K. J. Shea, D. A. Loy, *Chemistry of Materials* **2001**, *13*, 3306–3319.
- [135] K. Shea, D. Loy, *MRS Bulletin* **2001**, *26*, 368–376.
- [136] D. Zhao, Y. Wan, W. Zhou, *Ordered Mesoporous Materials*, Wiley-VCH Verlag GmbH & Co. KGaA, Weinheim, Germany, **2013**, pp. 153–217.
- [137] D. Zhao, J. Feng, Q. Huo, N. Melosh, G. H. Fredrickson, B. F. Chmelka, G. D. Stucky, *Science* **1998**, *279*, 548–552.
- [138] D. Zhao, Q. Huo, J. Feng, B. F. Chmelka, G. D. Stucky, *Journal of the American Chemical Society* **1998**, *120*, 6024–6036.
- [139] F. Kleitz, S. H. Choi, R. Ryoo, *Chemical communications (Cambridge England)* **2003**, 2136–2137.
- [140] J. Fan, C. Yu, F. Gao, J. Lei, B. Tian, L. Wang, Q. Luo, B. Tu, W. Zhou, D. Zhao, *Angewandte Chemie International Edition* **2003**, *42*, 3146–3150.
- [141] M.-J. Suh, Y.-K. Park, S.-K. Ihm, *Catalysis Today* **2016**, *265*, 210–217.
- [142] T. Valdés-Solís, G. Marbán, A. B. Fuertes, *Chemistry of Materials* **2005**, *17*, 1919–1922.
- [143] W.-H. Zhang, J.-L. Shi, H.-R. Chen, Z.-L. Hua, D.-S. Yan, *Chemistry of Materials* **2001**, *13*, 648–654.
- [144] J. R. Sietsma, H. Friedrich, A. Broersma, M. Versluijs-Helder, A. Jos van Dillen, P. E. de Jongh, K. P. de Jong, *Journal of Catalysis* **2008**, *260*, 227–235.
- [145] M. Wolters, P. Munnik, J. H. Bitter, P. E. de Jongh, K. P. de Jong, *The Journal of Physical Chemistry C* **2011**, *115*, 3332–3339.
- [146] N. Yi, Y. Cao, Y. Su, W. L. Dai, H. Y. He, K. N. Fan, *Journal of Catalysis* **2005**, *230*, 249–253.

- [147] S. Nguyen, V. Szabo, D. Trong On, S. Kaliaguine, *Microporous and Mesoporous Materials* **2002**, *54*, 51–61.
- [148] Y.-S. Chi, H.-P. Lin, C.-Y. Mou, *Applied Catalysis A: General* **2005**, *284*, 199–206.
- [149] E. Riedel, C. Janiak in *Anorganische Chemie*, DE GRUYTER, Berlin, München, Boston, **2015**, p. 974.
- [150] A. F. Hollemann, N. Wiberg, *Holleman-Wiberg, Lehrbuch der Anorganischen Chemie, 102. Aufl*, 102th, Walter de Gruyter, Berlin, **2007**, p. 2149.
- [151] S. J. Tans, M. H. Devoret, H. Dai, A. Thess, R. E. Smalley, L. J. Geerligs, C. Dekker, *Nature* **1997**, *386*, 474–477.
- [152] E. Fitzer, K.-H. Kochling, H. P. Boehm, H. Marsh, *Pure and Applied Chemistry* **1995**, *67*, 473–506.
- [153] R. E. Franklin, *Proceedings of the Royal Society of London. Series A. Mathematical and Physical Sciences* **1951**, *209*, 196–218.
- [154] J. S. McDonald-Wharry, M. Manley-Harris, K. L. Pickering, *Energy & Fuels* **2016**, *30*, 7811–7826.
- [155] H. Marsh, *Carbon* **1991**, *29*, 703–704.
- [156] Y.-R. Rhim, D. Zhang, M. Rooney, D. C. Nagle, D. H. Fairbrother, C. Herman, D. G. Drewry, *Carbon* **2010**, *48*, 31–40.
- [157] J. Lee, J. Kim, T. Hyeon, *Advanced Materials* **2006**, *18*, 2073–2094.
- [158] S. Jun, S. H. Joo, R. Ryoo, M. Kruk, M. Jaroniec, Z. Liu, T. Ohsuna, O. Terasaki, *Journal of the American Chemical Society* **2000**, *122*, 10712–10713.
- [159] X. Ji, K. T. Lee, L. F. Nazar, *Nature Materials* **2009**, *8*, 500–506.
- [160] J. Tang, J. Liu, N. L. Torad, T. Kimura, Y. Yamauchi, *Nano Today* **2014**, *9*, 305–323.
- [161] M. Kim, S. Hwang, J.-S. Yu, *J. Mater. Chem.* **2007**, *17*, 1656–1659.

- [162] J. Huang, B. G. Sumpter, V. Meunier, *Angewandte Chemie International Edition* **2008**, *47*, 520–524.
- [163] T. E. Rufford, D. Hulicova-Jurcakova, Z. Zhu, G. Q. Lu, *Electrochemistry Communications* **2008**, *10*, 1594–1597.
- [164] S. Sircar, T. Golden, M. Rao, *Carbon* **1996**, *34*, 1–12.
- [165] M. Oschatz, E. Kockrick, M. Rose, L. Borchardt, N. Klein, I. Senkovska, T. Freudenberg, Y. Korenblit, G. Yushin, S. Kaskel, *Carbon* **2010**, *48*, 3987–3992.
- [166] H. Suda, K. Haraya, *Chemical Communications* **1997**, *3*, 93–94.
- [167] H. Suda, K. Haraya, *The Journal of Physical Chemistry B* **1997**, *101*, 3988–3994.
- [168] S. H. Joo, S. J. Choi, I. Oh, J. Kwak, Z. Liu, O. Terasaki, R. Ryoo, *Nature* **2001**, *412*, 169–172.
- [169] J.-H. Nam, Y.-Y. Jang, Y.-U. Kwon, J.-D. Nam, *Electrochemistry Communications* **2004**, *6*, 737–741.
- [170] D. Herbert, J. Ulam, Electric dry cells and storage batteries, **1962**.
- [171] J. He, A. Manthiram, *Energy Storage Materials* **2019**, *20*, 55–70.
- [172] A. Manthiram, Y. Fu, S.-H. Chung, C. Zu, Y.-S. Su, *Chemical Reviews* **2014**, *114*, 11751–11787.
- [173] L. Borchardt, M. Oschatz, S. Kaskel, *Chemistry - A European Journal* **2016**, *22*, 7324–7351.
- [174] J. Scholz, B. Kayaalp, A. C. Juhl, D. Clemens, M. Fröba, S. Mascotto, *ACS Energy Letters* **2018**, *3*, 387–392.
- [175] Q. Jiang, C. Hu, M. D. Ward, *Journal of the American Chemical Society* **2013**, *135*, 2144–2147.
- [176] S. Polarz, B. Smarsly, *Journal of Nanoscience and Nanotechnology* **2002**, *2*, 581–612.

- [177] S. Ho Lee, H.-J. Kim, J. Woo Nam, H. Jung, S. Kyu Kang, K.-Y. Lee, *Studies in Surface Science and Catalysis* **2004**, *147*, 463–468.
- [178] H.-M. Zhang, Y. Teraoka, N. Yamazoe, *Chemistry Letters* **1987**, *16*, 665–668.
- [179] B. E. Kayaalp, Y. J. Lee, A. Kornowski, S. Gross, M. D'Arienzo, S. Mascotto, *RSC Advances* **2016**, *6*, 90401–90409.
- [180] M. Veith, S. Mathur, N. Lecerf, V. Huch, T. Decker, H. P. Beck, W. Eiser, R. Haberkorn, *Journal of Sol-Gel Science and Technology* **2000**, *17*, 145–158.
- [181] M. P. Pechini, Method of preparing lead and alkaline earth titanates and niobates and coating method using the same to form a capacitor, **1967**.
- [182] J. Martynczuk, M. Arnold, H. Wang, J. Caro, A. Feldhoff, *Advanced Materials* **2007**, *19*, 2134–2140.
- [183] T. Razpotnik, J. Maček, *Journal of the European Ceramic Society* **2007**, *27*, 1405–1410.
- [184] M. Gaudon, C. Laberty-Robert, F. Ansart, P. Stevens, A. Rousset, *Solid State Sciences* **2002**, *4*, 125–133.
- [185] J. D. Atwood, *Inorganic Reactions and Methods*, (Eds.: J. J. Zuckerman, J. D. Atwood), John Wiley & Sons, Inc., Hoboken, NJ, USA, **1999**, pp. 347–348.
- [186] A. Kareiva, M. Karppinen, L. Niinistö, *J. Mater. Chem.* **1994**, *4*, 1267–1270.
- [187] S. H. Park, Y.-K. Sun, *Journal of Power Sources* **2003**, *119-121*, 161–165.
- [188] R. Thirunakaran, K.-T. Kim, Y.-M. Kang, J. Young-Lee, *Materials Research Bulletin* **2005**, *40*, 177–186.
- [189] X. Ding, Y. Liu, L. Gao, L. Guo, *Journal of Alloys and Compounds* **2008**, *458*, 346–350.
- [190] Z. Shao, S. M. Haile, *Nature* **2004**, *431*, 170–173.

-
- [191] W.-C. Wu, J.-T. Huang, A. Chiba, *Journal of Power Sources* **2010**, *195*, 5868–5874.
- [192] H. Taguchi, D. Matsuda, M. Nagao, K. Tanihata, Y. Miyamoto, *Journal of the American Ceramic Society* **1992**, *75*, 201–202.
- [193] H. Najjar, H. Batis, *Applied Catalysis A: General* **2010**, *383*, 192–201.
- [194] B. Kayaalp, K. Klauke, M. Biesuz, A. Iannaci, V. M. Sglavo, M. D'Arienzo, H. Noei, S. Lee, W. Jung, S. Mascotto, *The Journal of Physical Chemistry C* **2019**, *123*, 16883–16892.
- [195] K. Klauke, B. Kayaalp, M. Biesuz, A. Iannaci, V. M. Sglavo, M. D'Arienzo, S. Lee, J. Seo, W. Jung, S. Mascotto, *ChemNanoMat* **2019**, *5*, 948–956.
- [196] C. T. Kresge, M. E. Leonowicz, W. J. Roth, J. C. Vartuli, J. S. Beck, *Nature* **1992**, *359*, 710–712.
- [197] A. Ries, A. Simões, M. Cilense, M. Zaghete, J. Varela, *Materials Characterization* **2003**, *50*, 217–221.
- [198] Q. Yang, D. Wang, C. Wang, X. Li, K. Li, Y. Peng, J. Li, *Catalysis Science and Technology* **2018**, *8*, 3166–3173.
- [199] E. Campagnoli, A. Tavares, L. Fabbrini, I. Rossetti, Y. A. Dubitsky, A. Zaopo, L. Forni, *Applied Catalysis B: Environmental* **2005**, *55*, 133–139.
- [200] F. Schüth, *Angewandte Chemie International Edition* **2003**, *42*, 3604–3622.
- [201] F. Deganello, M. L. Testa, V. La Parola, A. Longo, A. C. Tavares, *Journal of Materials Chemistry A* **2014**, *2*, 8438–8447.
- [202] C. T. Kresge, M. E. Leonowicz, W. J. Roth, J. C. Vartuli, J. S. Beck, *Nature* **1992**, *359*, 710–712.
- [203] D. Zhao, Q. Huo, J. Feng, B. F. Chmelka, G. D. Stucky, *Journal of the American Chemical Society* **1998**, *120*, 6024–6036.
- [204] D. M. Antonelli, J. Y. Ying, *Angewandte Chemie International Edition in English* **1995**, *34*, 2014–2017.
-

- [205] D. M. Antonelli, J. Y. Ying, *Angewandte Chemie International Edition in English* **1996**, *35*, 426–430.
- [206] U. Ciesla, S. Schacht, G. D. Stucky, K. K. Unger, F. Schüth, *Angewandte Chemie International Edition in English* **1996**, *35*, 541–543.
- [207] R. F. Lobo, S. I. Zones, M. E. Davis, *Journal of Inclusion Phenomena and Molecular Recognition in Chemistry* **1995**, *21*, 47–78.
- [208] E. G. Derouane, S. Determmerie, Z. Gabelica, N. Blom, *Applied Catalysis* **1981**, *1*, 201–224.
- [209] R. Ryoo, S. H. Joo, M. Kruk, M. Jaroniec, *Advanced Materials* **2001**, *13*, 677–681.
- [210] T.-W. Kim, I.-S. Park, R. Ryoo, *Angewandte Chemie International Edition* **2003**, *42*, 4375–4379.
- [211] Y. D. Xia, R. Mokaya, *Advanced Materials* **2004**, *16*, 886–891.
- [212] J. Roggenbuck, H. Schäfer, T. Tsoncheva, C. Minchev, J. Hanss, M. Tiemann, *Microporous and Mesoporous Materials* **2007**, *101*, 335–341.
- [213] J.-H. Smått, N. Schüwer, M. Järn, W. Lindner, M. Lindén, *Microporous and Mesoporous Materials* **2008**, *112*, 308–318.
- [214] Y. Xia, R. Mokaya, *Journal of Materials Chemistry* **2005**, *15*, 3126.
- [215] T. Valdés-Solís, A. Fuertes, *Materials Research Bulletin* **2006**, *41*, 2187–2197.
- [216] W. Li, J. Liu, D. Zhao, *Nature Reviews Materials* **2016**, *1*, 16023.
- [217] F. Hoffmann, M. Fröba, *Chem. Soc. Rev.* **2011**, *40*, 608–620.
- [218] D. Gu, F. Schüth, *Chem. Soc. Rev.* **2014**, *43*, 313–344.
- [219] S. Förster, T. Plantenberg, *Angewandte Chemie International Edition* **2002**, *41*, 688.
- [220] P. Zhao, N. Feng, F. Fang, G. Liu, L. Chen, J. Meng, C. Chen, L. Wang, H. Wan, G. Guan, *Catalysis Science & Technology* **2018**, *8*, 5462–5472.

- [221] J. Zhao, Y. Liu, X. Li, G. Lu, L. You, X. Liang, F. Liu, T. Zhang, Y. Du, *Sensors and Actuators B: Chemical* **2013**, *181*, 802–809.
- [222] X. Deng, K. Chen, H. Tüysüz, *Chemistry of Materials* **2017**, *29*, 40–52.
- [223] H. Yang, D. Zhao, *Journal of Materials Chemistry* **2005**, *15*, 1217–1231.
- [224] Z. Sarshar, F. Kleitz, S. Kaliaguine, *Energy & Environmental Science* **2011**, *4*, 4258.
- [225] S. A. Johnson, P. J. Ollivier, T. E. Mallouk, *Science* **1999**, *283*, 963–965.
- [226] J. Weber, M. Antonietti, A. Thomas, *Macromolecules* **2007**, *40*, 1299–1304.
- [227] A. Thomas, F. Goettmann, M. Antonietti, *Chemistry of Materials* **2008**, *20*, 738–755.
- [228] P. K. Sudeep, T. Emrick, *Polymer Reviews* **2007**, *47*, 155–163.
- [229] H. Marsh, F. Rodriguez-Reinoso, *Activated Carbon*, Elsevier Science & Technology Books, **2006**, p. 554.
- [230] Y. Zhai, Y. Dou, D. Zhao, P. F. Fulvio, R. T. Mayes, S. Dai, *Advanced Materials* **2011**, *23*, 4828–4850.
- [231] Y. Meng, D. Gu, F. Zhang, Y. Shi, H. Yang, Z. Li, C. Yu, B. Tu, D. Zhao, *Angewandte Chemie International Edition* **2005**, *44*, 7053–7059.
- [232] R. Ryoo, S. H. Joo, S. Jun, *The Journal of Physical Chemistry B* **1999**, *103*, 7743–7746.
- [233] M. Kruk, M. Jaroniec, R. Ryoo, S. H. Joo, *The Journal of Physical Chemistry B* **2000**, *104*, 7960–7968.
- [234] D. Saikia, T.-H. Wang, C.-J. Chou, J. Fang, L.-D. Tsai, H.-M. Kao, *RSC Advances* **2015**, *5*, 42922–42930.
- [235] N. Stribeck, B. Smarsly, *Progress in Colloid & Polymer Science*, (Eds.: F. Kremer, W. Richtering), Springer Berlin Heidelberg, Heidelberg, **2005**, p. 176.

- [236] H. Schnablegger, Y. Singh, *The Saxes Guide*, 4th, Anton Paar GmbH, Austria, **2017**, p. 164.
- [237] L. A. Feigin, D. I. Svergun, *Structure Analysis by Small-Angle X-Ray and Neutron Scattering*, (Ed.: G. W. Taylor), Springer US, Boston, MA, **1987**.
- [238] S. Risse, E. Härk, B. Kent, M. Ballauff, *ACS Nano* **2019**, *13*, 10233–10241.
- [239] B. M. Smarsly, S. Mascotto, C. Weidmann, H. Kaper, *Chemie Ingenieur Technik* **2010**, *82*, 823–828.
- [240] K. L. Stefanopoulos, G. E. Romanos, O. C. Vangeli, K. Mergia, N. K. Kanellopoulos, A. Koutsioubas, D. Lairez, *Langmuir* **2011**, *27*, 7980–7985.
- [241] E. Hoinkis, E. B. F. Lima, P. Schubert-Bischoff, *Langmuir* **2004**, *20*, 8823–8830.
- [242] J. Scholz, A. Garbujo, B. Kayaalp, K. Klauke, A. Glisenti, S. Mascotto, *Inorganic Chemistry* **2019**, *58*, 15942–15952.
- [243] S. Chang, T. Matsumoto, H. Matsumoto, M. Unno, *Applied Organometallic Chemistry* **2010**, *24*, 241–246.
- [244] D. A. Long, *Journal of Raman Spectroscopy* **2004**, *35*, 905–905.
- [245] B. He, Z. Wang, L. Zhao, X. Pan, X. Wu, C. Xia, *Journal of Power Sources* **2013**, *241*, 627–633.
- [246] J. Tong, W. Yang, R. Cai, B. Zhu, G. Xiong, L. Lin, *Separation and Purification Technology* **2003**, *32*, 289–299.
- [247] M. S. P. Francisco, Y. Gushikem, *J. Mater. Chem.* **2002**, *12*, 2552–2558.
- [248] M. M. Nair, S. Kaliaguine, F. Kleitz, *ACS Catalysis* **2014**, *4*, 3837–3846.
- [249] M. Thommes, *Chemie Ingenieur Technik* **2010**, *82*, 1059–1073.
- [250] G. Will, N. Masciocchi, W. Parrish, M. Hart, *Journal of Applied Crystallography* **1987**, *20*, 394–401.
- [251] J. Zhu, D. Xiao, J. Li, X. Yang, *Catalysis Letters* **2009**, *129*, 240–246.

- [252] J. Dacquin, C. Lancelot, C. Dujardin, P. Da Costa, G. Djega-Mariadassou, P. Beaunier, S. Kaliaguine, S. Vaudreuil, S. Royer, P. Granger, *Applied Catalysis B: Environmental* **2009**, *91*, 596–604.
- [253] N. Wang, X. Yu, Y. Wang, W. Chu, M. Liu, *Catalysis Today* **2013**, *212*, 98–107.
- [254] S. Brunauer, P. H. Emmett, E. Teller, *Journal of the American Chemical Society* **1938**, *60*, 309–319.
- [255] R. Zsigmondy, P. Scherrer, *Kolloidchemie Ein Lehrbuch* **1912**, *1918*, 387–409.
- [256] N. M. L. N. P. Closset, R. H. E. van Doorn, H. Kruidhof, J. Boeijsma, *Powder Diffraction* **1996**, *11*, 31–34.

11. Appendix

11.1. Supporting Information: Distribution of Sulfur in Carbon/Sulfur Nanocomposites Analyzed by Small-Angle X-ray Scattering

*Jonas Scholz¹, Buğra Kayaalp¹, Anika C. Juhl¹, Daniel Clemens², Michael Fröba¹
and Simone Mascotto¹*

¹Institut für Anorganische und Angewandte Chemie, Universität Hamburg,
Martin-Luther-King Platz 6, 20146 Hamburg, Germany

²Helmholtz-Zentrum für Materialien und Energie GmbH, Hahn-Meitner-Platz 1,
14109 Berlin, Germany

Experimental part*Chemicals*

Toluene-d8 (99.5 atom% D, C₇D₈) was purchased from Deutero GmbH. Tetrahydrofuran-d8 (99.5 atom% D, C₄D₈O) was purchased from ABCR. Deuterium oxide (99.8 atom% D, D₂O) was purchased from Ega-Chemie. All chemicals were used as received without further purification.

Materials

The ordered nanoporous carbon matrices were obtained via nanocasting. KIT-6 silica was used as the exotemplate and prepared via block copolymer templating according to ref. ¹. Mesoporous carbon CMK-8 was synthesized by impregnation of the KIT-6 silica with a resol precursor, which was prepared from phenol and formaldehyde.² An excess of resol solution in ethanol (20 wt %) was added to KIT-6 powder and centrifuged into the pores for 20 min at 4000 rpm. After decantation, the powder was dried at room temperature. The procedure was repeated 3 times. Subsequently, polymerization of resol was carried out at 120 °C for 24 h. The silica-polymer composite was carbonized in an argon atmosphere at 350 °C for 5 h (ramp of 1 °C/min) and, in a second step, at 900 °C for 2 h (ramp of 5 °C/min). Etching of silica with hydrofluoric acid (10 vol %) yielded the porous carbon. The carbon-sulfur nanocomposites were prepared via sulfur impregnation following the approach described by Ji et al.³ To a fixed amount of CMK-8, specific quantities of sulfur were added and homogeneously mixed. The samples were heated in closed vessels at 155 °C for 12 h.

SANS experiments

The SANS experiments were performed at the small-angle scattering instrument V16, which is placed in the cold neutron guide of the Helmholtz-Zentrum Berlin. Using Au-foil activation

11. Appendix

measurements, an average neutron flux of $(3.6 \pm 0.1) \cdot 10^8 \text{ cm}^{-2}\text{s}^{-1}$ was determined with deactivated choppers at the entrance of the collimation section. Measuring at two sample-detector distances, i.e. 1.7 m and 6 m, the scattering intensity was acquired in the range of $0.1 \text{ nm}^{-1} < q < 7 \text{ nm}^{-1}$. The scattering vector q is defined as $q = (4\pi/\lambda)(\sin\theta)$ with λ being the wavelength and 2θ the scattering angle. As the instrument was operated in time-of-flight (TOF) mode, at 1.7 m the choppers were run at 3000 r min^{-1} with opening apertures $\varphi_1 = 0^\circ$, $\varphi_2 = -5^\circ$, $\varphi_3 = -100^\circ$. This configuration corresponds to a neutron wavelength of $2.1 \text{ \AA} < \lambda < 3.4 \text{ \AA}$. At 6 m the configuration was: 1200 r min^{-1} , $\varphi_1 = 0^\circ$, $\varphi_2 = -5^\circ$, $\varphi_3 = -65^\circ$, resulting in $2.7 \text{ \AA} < \lambda < 7.1 \text{ \AA}$. The software MANTID has been used to reduce the data. Further information on beamline description and data acquisition can be found in ref.⁴.

Coin shaped sample holders were completely filled with 0.35 cm^3 of material, corresponding to 50 mg for the void CMK-8, 60 mg and 90 mg for the nanocomposites impregnated with 20wt.% and 50wt.% of sulfur, respectively. Each contrast matching fluid was added dropwise using an Eppendorf pipette until the materials were completely soaked but without forming a suspension of the solid in the solvent. By increasing sulfur loading the fluid amount decreased from 0.2 mL for the void system to 0.15 mL and 0.11 mL. Sealing of the cells was achieved via Viton O-rings and backing rings over stainless steel endcaps.

Evaluation of the SANS data

The efficacy of the presented analysis method is related to the goodness of the matching between the SLD of carbon and the fluid considered. In this work, assuming an average mass density of 1.8 g/cm^3 for the non-graphitic material ($\text{SLD} = 6 \cdot 10^{-6} \text{ \AA}^{-2}$), a matching of about 95% is obtained using D_2O ($\text{SLD} = 6.39 \cdot 10^{-6} \text{ \AA}^{-2}$), deuterated toluene ($\text{SLD} = 5.66 \cdot 10^{-6} \text{ \AA}^{-2}$) and deuterated THF ($\text{SLD} = 6.35 \cdot 10^{-6} \text{ \AA}^{-2}$) as contrast liquids.

Chord-length distribution

The CLD is defined as the second derivative of the scattering intensity autocorrelation function $\gamma(r)$:

$$g(r) = l_p \gamma''(r)$$

where l_p is the Porod length, the average chord length of the system and, in turn, the first momentum of $g(r)$:

$$l_p = \int_0^{\infty} r g(r) dr$$

The chord-length distribution delivers a statistical description of the distances connecting phase boundaries in a pure two-phase system with sharp interface. Therefore, at large q the curves must exhibit a Porod behavior, i.e. q^{-4} dependence:

$$I(q)_{q \rightarrow \infty} = \frac{2\pi\Delta\rho^2 S}{q^4 V} = \frac{Q}{2\pi^3 l_p q^4}$$

where $\Delta\rho$ denotes the scattering contrast between two phases and Q is the Porod invariant, which is related to the interface area (S/V) of the system:

$$Q = \frac{1}{2\pi} \int_0^{\infty} q^2 I(q) dq$$

The CLD analysis was carried out here using a parametrization method.⁵ This approach, comprehensively devised in ref. 5, does not smooth the data and leads to a more precise assessment of the morphological parameters of the carbon porous network. The CLD function $g(r)$ in this form is calculated using the software GNU PLOT and OCTAVE.

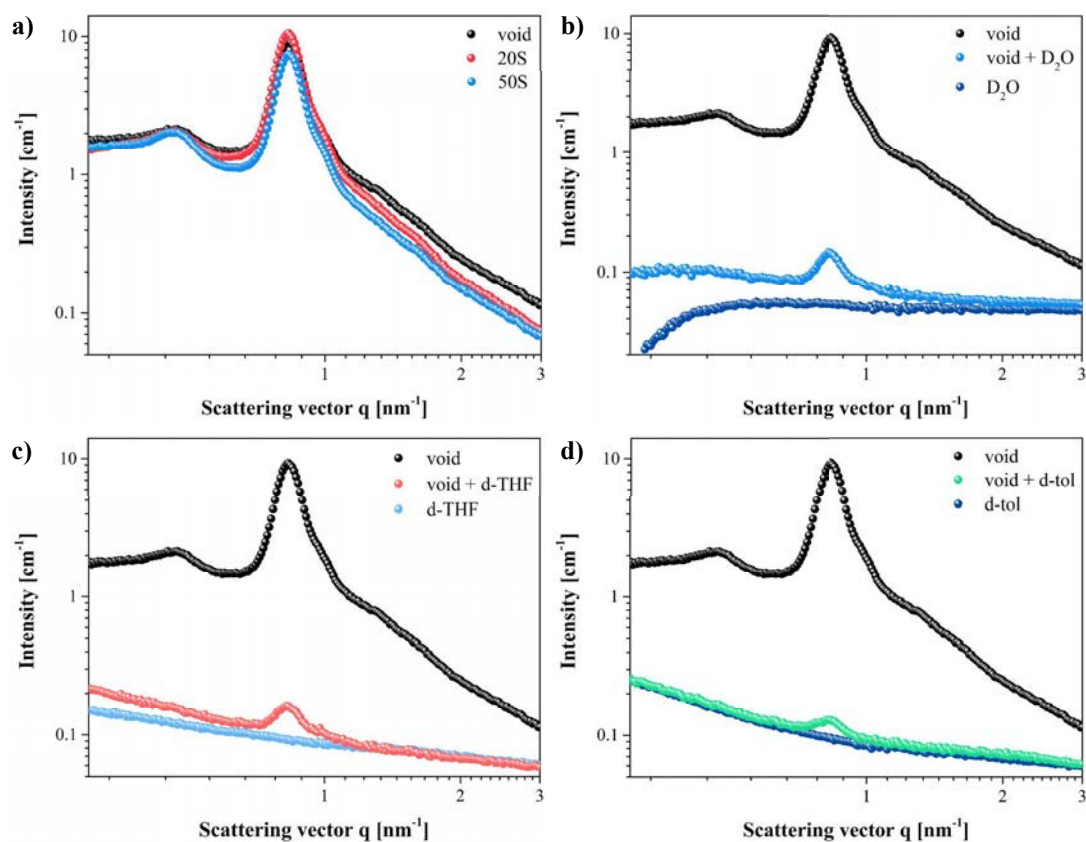
Additional SANS experiments

Fig. S1: Scattering curves of void CMK-8 (black) and CMK-8 filled with 20 wt.% (red) and 50 wt.% of sulfur (blue) (a). Scattering curves of void CMK-8 (black), void CMK-8 matched with D₂O (light blue) and bulk D₂O (dark blue) (b). Scattering curves of void CMK-8 (black), void CMK-8 matched with d-THF (red) and bulk d-THF (light blue) (c). Scattering curves of void CMK-8 (black), void CMK-8 matched with d-toluene (green) and bulk d-toluene (dark blue) (d).

The SANS curves of the analyzed materials at the dry state are depicted in Fig. S1a. In the case of the nanocomposites, when the carbon host is not completely filled with sulfur, the scattering pattern can be described as a three-phase system consisting of carbon, voids and sulfur (see Eq. 2 of the manuscript). The filling of the carbon matrix can be perceived by the slight and continuous

intensity decrease, although no precise analysis of the sulfur distribution can be performed in such conditions.

In Fig. S1b-d the matching of the CMK-8 matrix along with the scattering of the contrast matching fluids is shown. The higher intensity for the matched curves at $q < 1 \text{ nm}^{-1}$ is attributed at the slight mismatch between the scattering length density of carbon and solvent.

Analysis of sulfur content in the CMK-8 framework

The thermogravimetry analyses (Fig. S2 and Table S1) of the investigated materials, taken from our previous work⁶, shows the amount of sulfur loaded in the nanoporous carbon matrix.

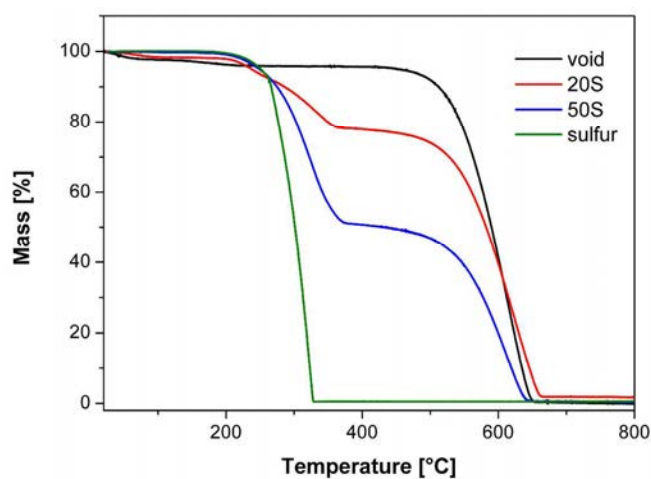


Fig. S2: Thermograms of void CMK-8 (black), CMK-8 filled with 20 wt.% (red) and 50 wt.% (blue) of sulfur, and bulk sulfur (green).

11. Appendix

Table S1: Onset temperatures of decomposition and sulfur content of void CMK-8, CMK-8 filled with 20 wt.% and 50 wt.% of sulfur, and bulk sulfur.

Sample	T _{onset} sulfur decomposition [°C]	T _{onset} carbon decomposition [°C]	Sulfur content [% wt.]
void	-	539	-
20S	220	545	20
50S	270	561	49
sulfur	282	-	100

References

- (1) Kleitz, F.; Choi, S. H.; Ryoo, R. Cubic Ia3d Large Mesoporous Silica: Synthesis and Replication to Platinum Nanowires, Carbon Nanorods and Carbon Nanotubes. *Chem. Commun.* **2003**, 2136–2137.
- (2) Huang, Y.; Cai, H.; Yu, T.; Zhang, F.; Zhang, F.; Meng, Y.; Gu, D.; Wan, Y.; Sun, X.; Tu, B.; *et al.* Formation of Mesoporous Carbon with a Face-Centered-Cubic Fd3m Structure and Bimodal Architectural Pores from the Reverse Amphiphilic Triblock Copolymer PPO-PEO-PPO. *Angew. Chemie - Int. Ed.* **2007**, *46*, 1089–1093.
- (3) Ji, X.; Lee, K. T.; Nazar, L. F. A Highly Ordered Nanostructured Carbon–sulphur Cathode for Lithium–sulphur Batteries. *Nat. Mater.* **2009**, *8*, 500–506.
- (4) Vogtt, K.; Siebenbürger, M.; Clemens, D.; Rabe, C.; Lindner, P.; Russina, M.; Fromme, M.; Mezei, F.; Ballauff, M.; IUCr. A New Time-of-Flight Small-Angle Scattering Instrument at the Helmholtz-Zentrum Berlin: V16/VSANS. *J. Appl. Crystallogr.* **2014**, *47*, 237–244.

- (5) Smarsly, B.; Antonietti, M.; Wolff, T. Evaluation of the Small-Angle X-Ray Scattering of Carbons Using Parametrization Methods. *J. Chem. Phys.* **2002**, *116*, 2618.
- (6) Petzold, A.; Juhl, A.; Scholz, J.; Ufer, B.; Goerigk, G.; Fröba, M.; Ballauff, M.; Mascotto, S. Distribution of Sulfur in Carbon/Sulfur Nanocomposites Analyzed by Small-Angle X-Ray Scattering. *Langmuir* **2016**, *32*, 2780–2786.

11.2. Supporting Information: Pore geometry effect on the synthesis of silica supported perovskite oxides

Jonas Scholz¹, Diana Haas², Martin Etter², Andreas Meyer³, Andreas Kornowski³, Uta Sazama¹ and Simone Mascotto¹

¹Institut für Anorganische und Angewandte Chemie, Universität Hamburg, Martin-Luther-King Platz 6, 20146 Hamburg, Germany

²Deutsches Elektronen-Synchrotron (DESY), Notkestraße 85, D-22607 Hamburg, Germany

³Institut für Physikalische Chemie, Universität Hamburg, Grindelallee 117, D-20146 Hamburg, Germany

Fitting of SAXS data of the void hosts

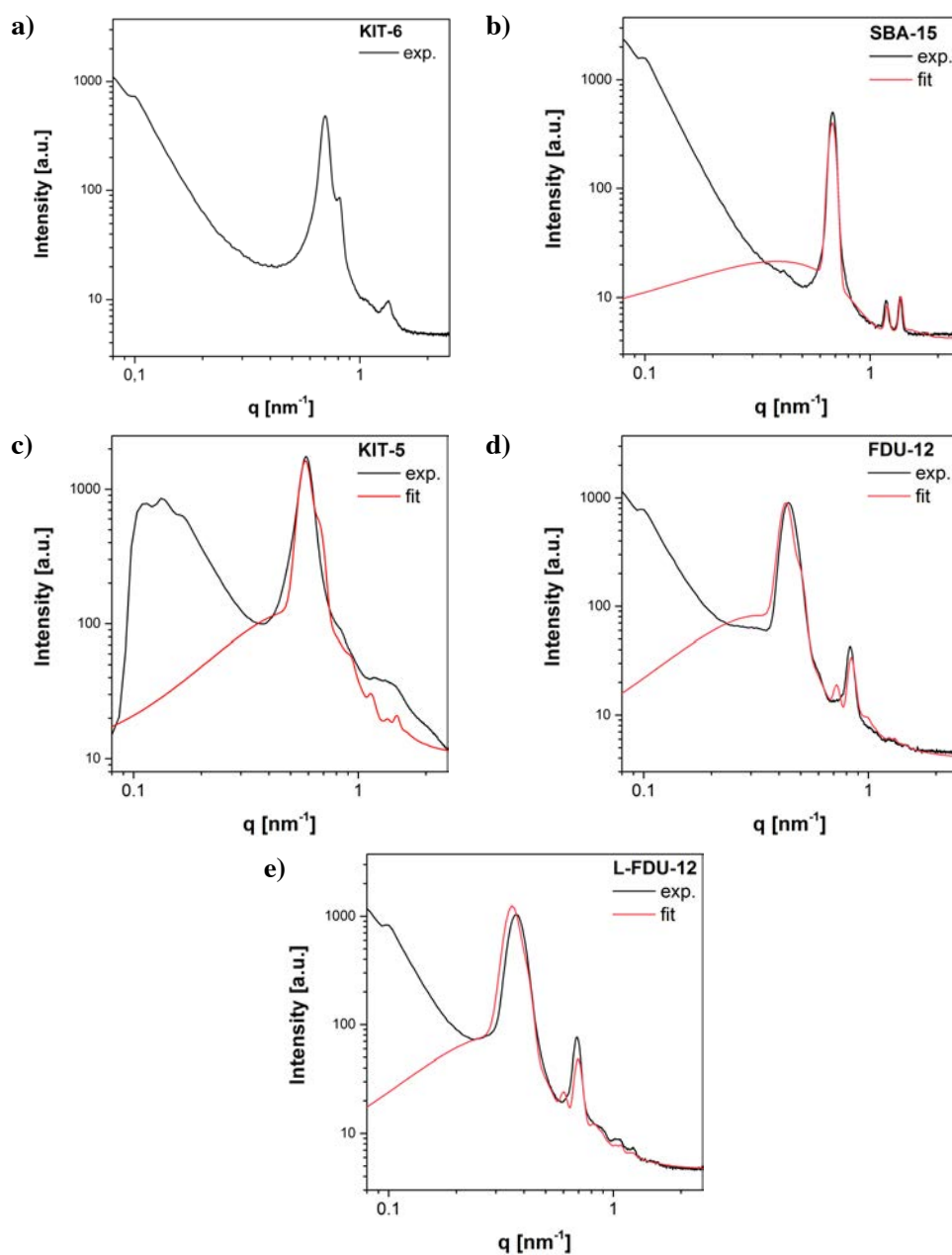
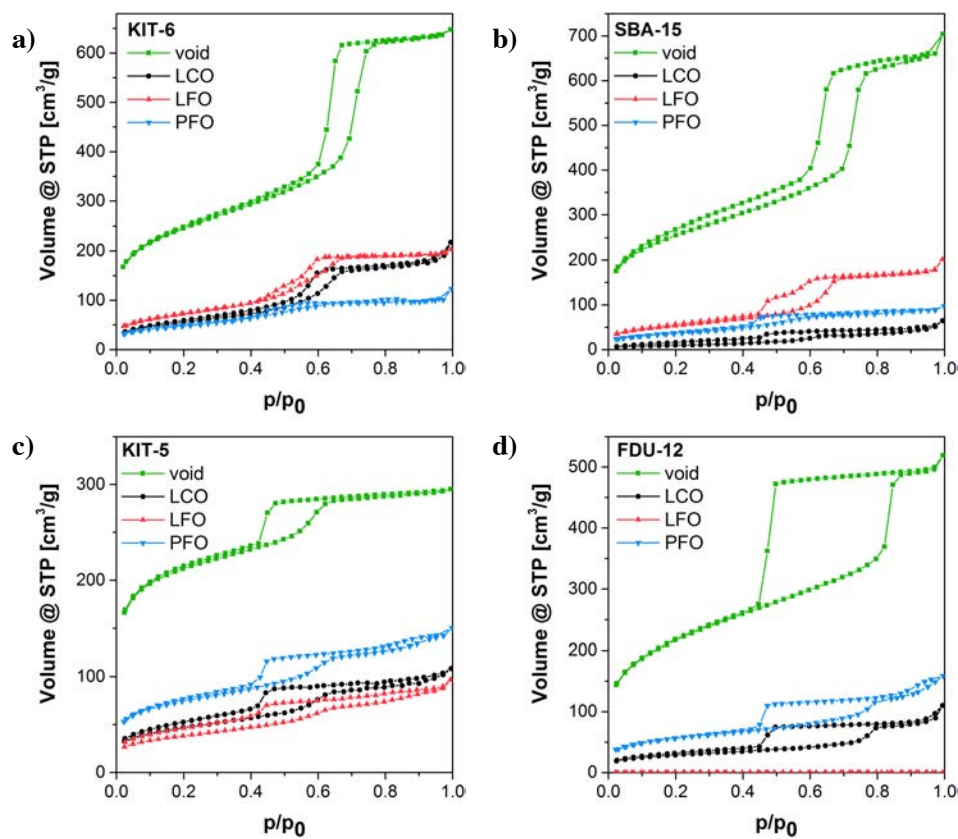


Figure S1: SAXS patterns of void KIT-6 (a), SBA-15 (b), KIT-5 (c), FDU-12 (d) and L-FDU-12 (e) with the respective fits (red curves) obtained using the software Scatter.

The SAXS curves of the host systems indicate highly mesostructural order of the pores. The curves could be fitted with suitable form and structure factor models using the software *Scatter* to calculate structural properties such as size of pore, pore-walls and lattice parameter.

The only exception was given by the KIT-6 system, for which no suitable expression of the gyroidal form and structure factor could be provided.

Nitrogen Physisorption



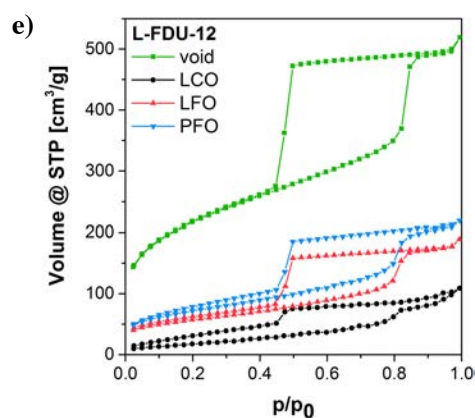
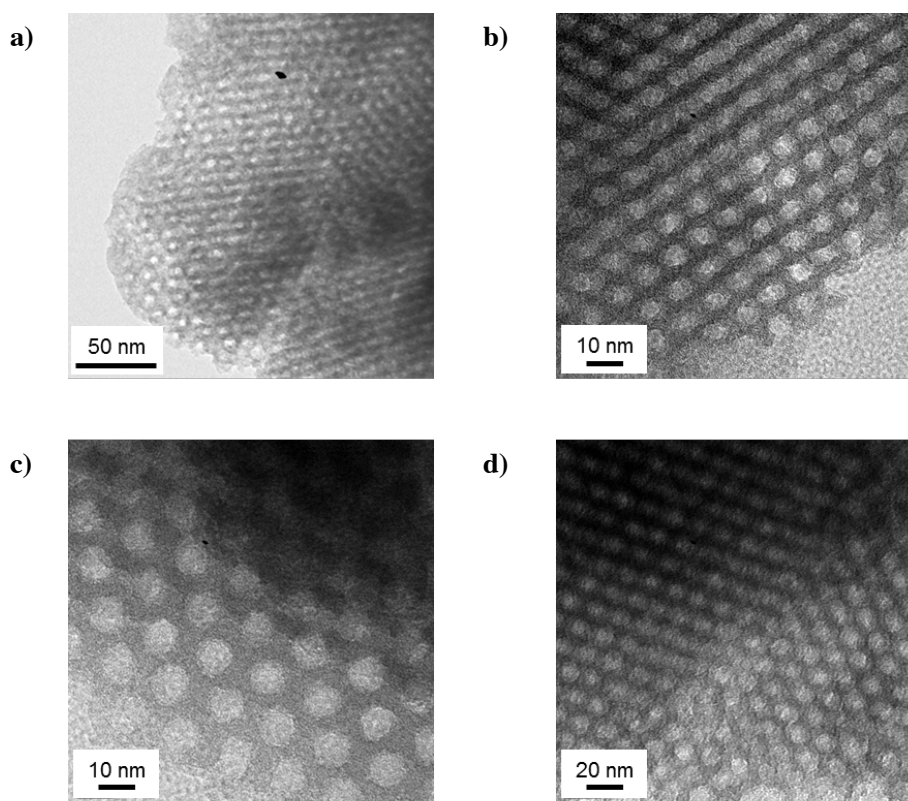


Figure S2: Nitrogen Physisorption isotherms of KIT-6 (a), SBA-15 (b), KIT-5 (c), FDU-12 (d) and L-FDU-12 (e) filled with LaCoO_3 (black), LaFeO_3 (red) and PrFeO_3 (blue), respectively. The isotherms of void silica are represented in green.

TEM Analyses of the hosts



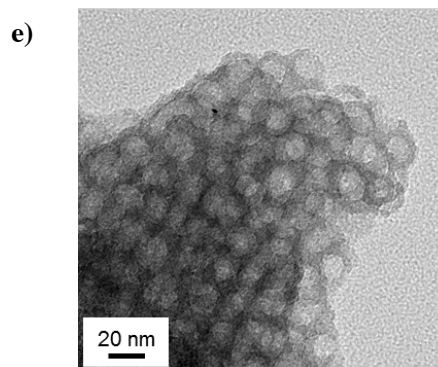


Figure S3: TEM images of the void KIT-6 (a), SBA-15 (b), KIT-5 (c), FDU-12 (d) and L-FDU-12 (e).

²⁹Si-NMR spectroscopy

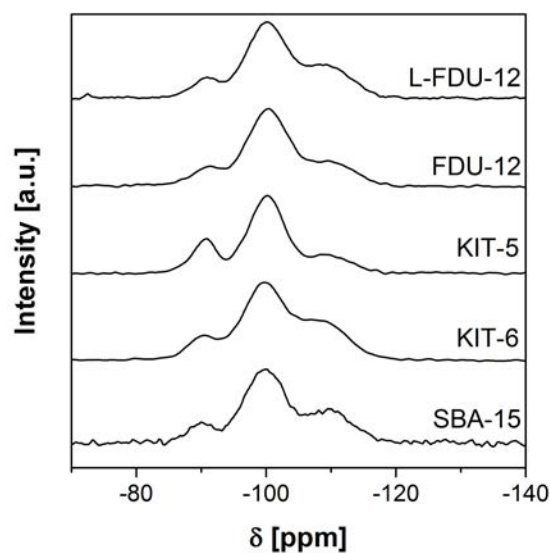


Figure S4: ²⁹Si CP-MAS solid-state NMR spectra of the void silica hosts

Analysis of the chemical environment of the silica matrices indicates a homogeneous surface chemistry in all the hosts. The materials present a majority of mono-silanol groups (Q3), whereas

fully condensed silica (Q4 signals at -110 ppm) and germinal silanols (Q2 band at -90 ppm) are equally distributed in the systems.

Rietveld refinement Analysis

Host	GOF	Cry. size [nm]	Cry. size error [nm]	Strain	Lattice parameters			Radius of mean cry. size[nm]
					<i>a</i> [Å]	<i>b</i> [Å]	<i>c</i> [Å]	
LFO								
Bulk	4.879	30.619	0.644	0.16847 +/- 0.00297	5.56201	7.85006	5.56093	11.813
FDU-12	2.586	26.820	0.457	0.15461 +/- 0.00259	5.56115	7.84674	5.55759	10.347
PFO								
Bulk	7.372	27.409	1.604	0.15151 +/- 0.00631	5.55382	7.78006	5.47774	10.575
SBA-15	1.952	26.850	78.193	0.17636 +/- 0.00695	5.55601	7.78105	5.48354	10.359
FDU-12	1.216	22.074	31.428	0.18900 +/- 0.01023	5.54886	7.78569	5.48055	8.516
LCO								
Bulk	4.432	30.670	0.740	0.13665 +/- - 0.00302	5.43576		13.12058	11.832
KIT-5	1.618	17.470	7.066	0.19140 +/- 344.12464	5.43608		13.19121	6.740
SBA-15	2.175	16.693	4.881	0.12393 +/- 4.49938	5.43566		13.13217	6.440
FDU-12	2.739	30.648	1.995	0.12180 +/- 0.00815	5.43773		13.12003	11.824
L-FDU-12	1.540	23.245	67.790	0.32107 +/- 3.62941	5.44797		13.18319	8.968

Table S1: Microstructural parameter of the perovskite crystal structures obtained by the Rietveld refinement of the XRD measurements: Goodness of fit (GOF), volume-weighted mean crystallite size and corresponding estimated standard deviation (Cry. size, Cry. size error), empirical micro-strain of the unit cell (Strain), lattice parameters of the unit cells (a , b , c), radial mean crystallite size obtained by an empirical formula of ref. 33 assuming a log-normal distribution for the distribution of crystallite sizes (Radius of mean cry. size).

Rietveld analysis of the XRD data could provide structural information of the bulk perovskite and of the crystalline nanocomposite systems. In table S1 the main features resulting from the refinements are shown. Although the GOF for the bulk systems is much higher than for the composite systems, the difference curve is flat. In contrast to that, the GOF for the composite systems is unusually low, which is due to a high expected residual value, which originates from a high background originating from the host matrix. The volume-weighted mean size of the crystallites is ca. 30 nm for all three oxide systems. The crystallite size of the impregnated oxides is always lower than for the bulk systems, probably because these guests are also grown inside the pore space. A trend can be clearly observed, however more precise assessment of the particle size cannot be done, owing to the insufficient quality of the diffraction data.

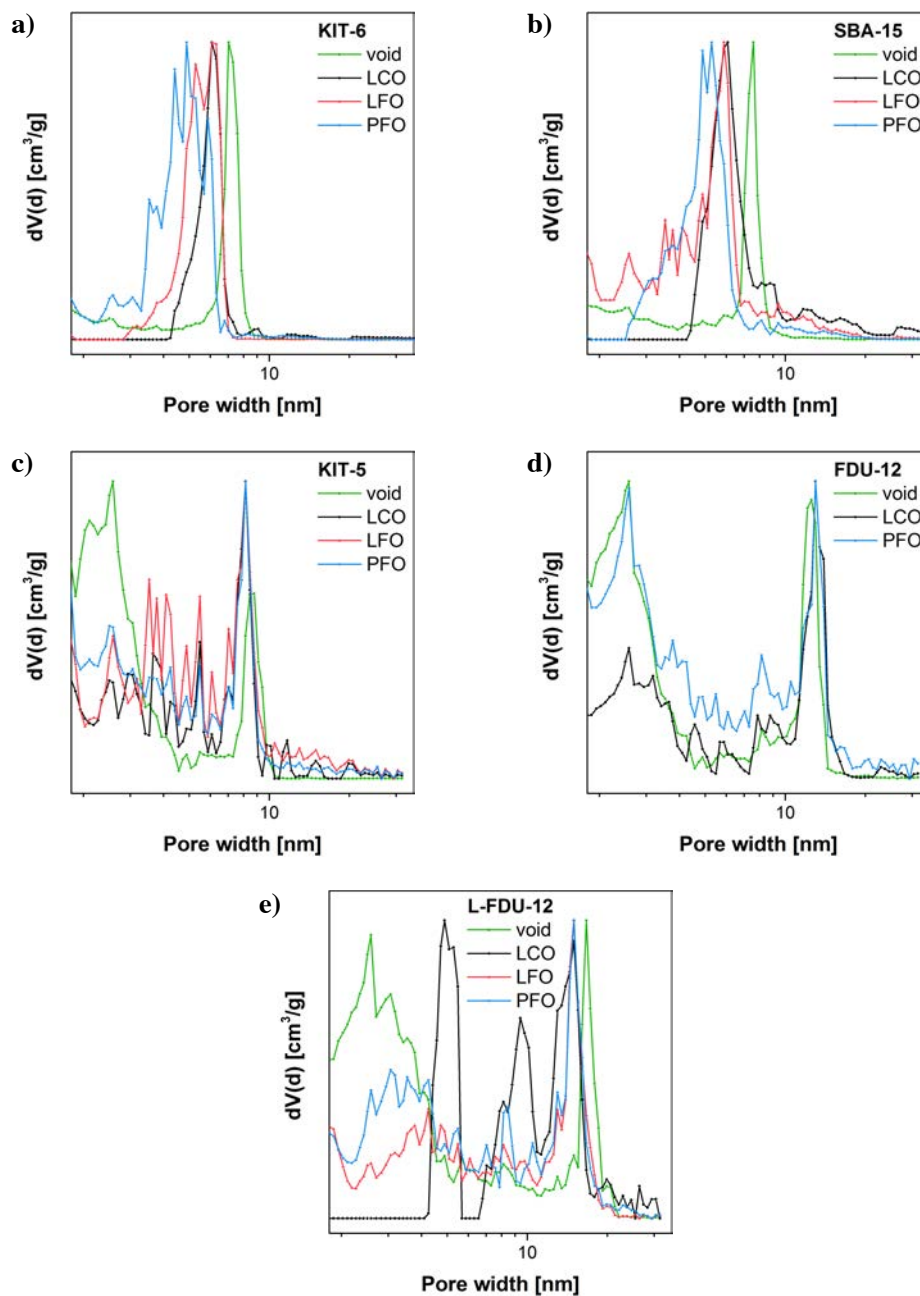
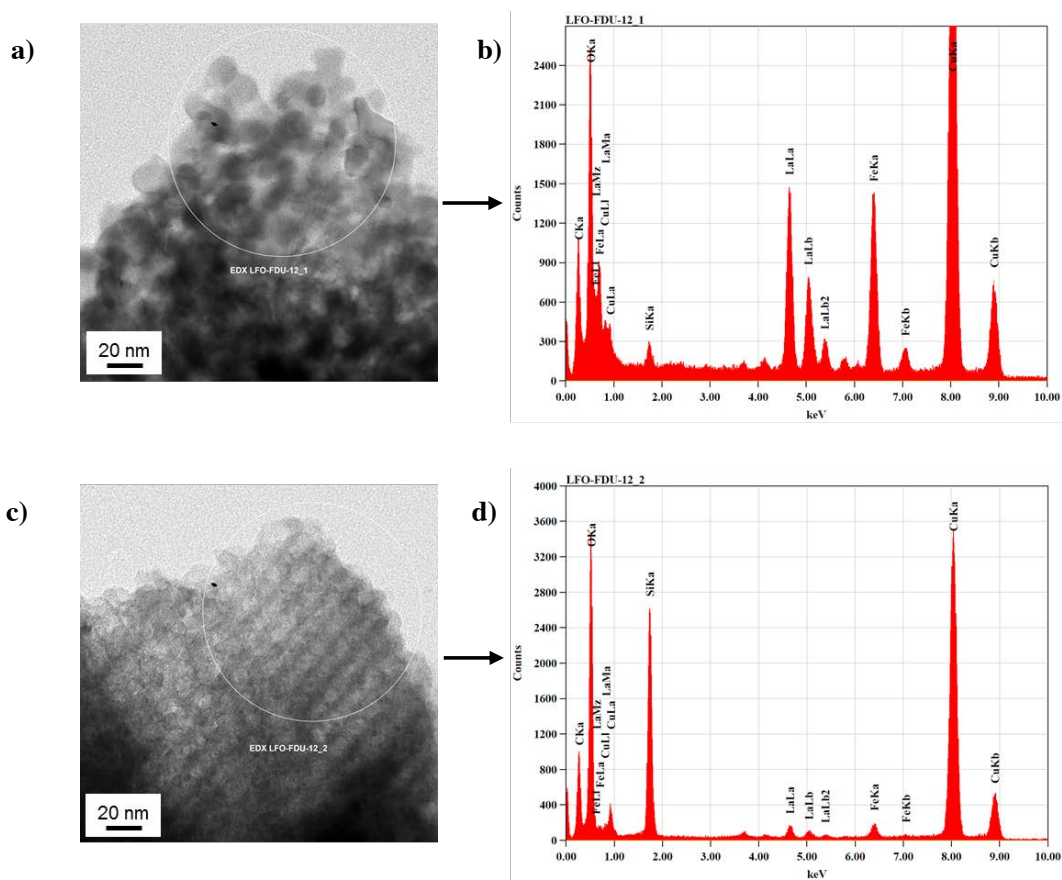
Pore size distribution of the nanocomposites

Figure S5: Pore size distribution (PSD) in semilogarithmic scale of KIT-6 (a), SBA-15 (b), KIT-5 (c), FDU-12 (d) and L-FDU-12 (e) filled with LaCoO_3 (LCO black), LaFeO_3 (LFO, red) and

11. Appendix

PrFeO_3 (PFO, blue), respectively. The void silica structures are represented in green. For FDU-12 impregnated with LFO, the PSD was not determined since nitrogen isotherm could not be measured.

TEM and EDX analyses of the nanocomposites



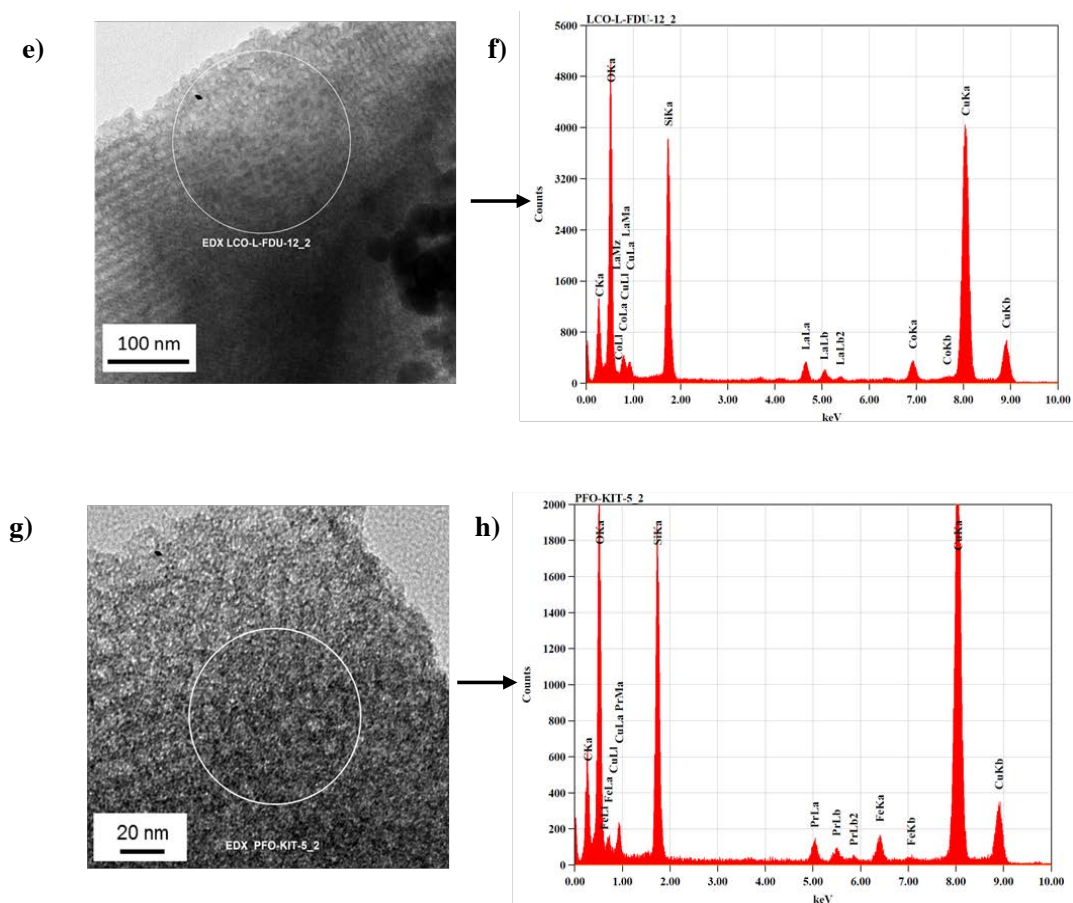


Figure S6: TEM images of LaFeO₃@ FDU-12 (a, c), LaCoO₃@L-FDU-12 (e), PrFeO₃@KIT-5 (g) and the corresponding EDX analysis (b, d, f, h) acquired in the selected areas.

Figure S6a displays LaFeO₃ crystallites formed on the outside of the pores of the silica host. Accordingly, the EDX spectrum indicates a high amount of La and Fe in equimolar proportion compared to the low Si content (b). In Fig S6c,e,g different silica host structures are depicted, with apparently no traces of perovskite oxide. However, the corresponding cations are detected in the EDX spectra (Fig. S6d,f,h) indicating the homogeneous impregnation and the oxide formation

11. Appendix

inside the pores of silica. From these composition analyses the filling grade (FG) of the hosts (Table S2) can be additionally determined.

This value was obtained by the ratio:

$$FG = \frac{\phi_{TM}}{\phi_{pore}}$$

Assuming that the volume fraction of the transition metal (ϕ_{TM}) is comparable to its atomic concentration (%TM):

$$\phi_{TM} \approx \frac{\%TM}{\%Si} \phi_{SiO_2} = \frac{\%TM}{\%Si} (1 - \phi_{pore})$$

Considering the well reproducibility of the data for the hosts with spherical pores, fillings between 5% and 7% are expected also for KIT-6 and SBA-15 silica matrices.

Host	V_P [cm ³ /g]	ϕ_{pore}	Si [% at.]	Fe [% at.]	Co [% at.]	La [% at.]	Pr [% at.]	^{a)} ϕ_{TM}	FG
FDU-12	0.51	0.53	^{b)} 20.6	^{b)} 1.3	-	^{b)} 1.2	-	0.029	0.056
KIT-5	0.58	0.56	22.9	2.03	-	-	1.6	0.039	0.07
LFDU-12	0.80	0.64	20.5	-	2.0	1.7	-	0.035	0.054

Table S2: Porosity and composition of nanocomposites in three different ink-bottle pore hosts. V_P , pore volume of the void hosts; ϕ_{pore} , volume fraction of the pores in the void host, obtained by $\phi_{pore} = V_P / (V_P + V_{SiO_2})$, where $V_{SiO_2} = \rho_{SiO_2}^{-1} = (2.2 \text{ g/cm}^3)^{-1} = 0.454 \text{ cm}^3/\text{g}$; Si, Fe, Co, La, Pr, atomic abundance of the elements obtained from the EDX spectra; ϕ_{TM} volume fraction of the transition metals; FG, filling grade of the silica matrix. ^{a)} The obtained values of ϕ_{TM} are referred to the most abundant cation. ^{b)} The values refer to the EDX spectrum in Fig. S6d.

SAXS of the nanocomposites

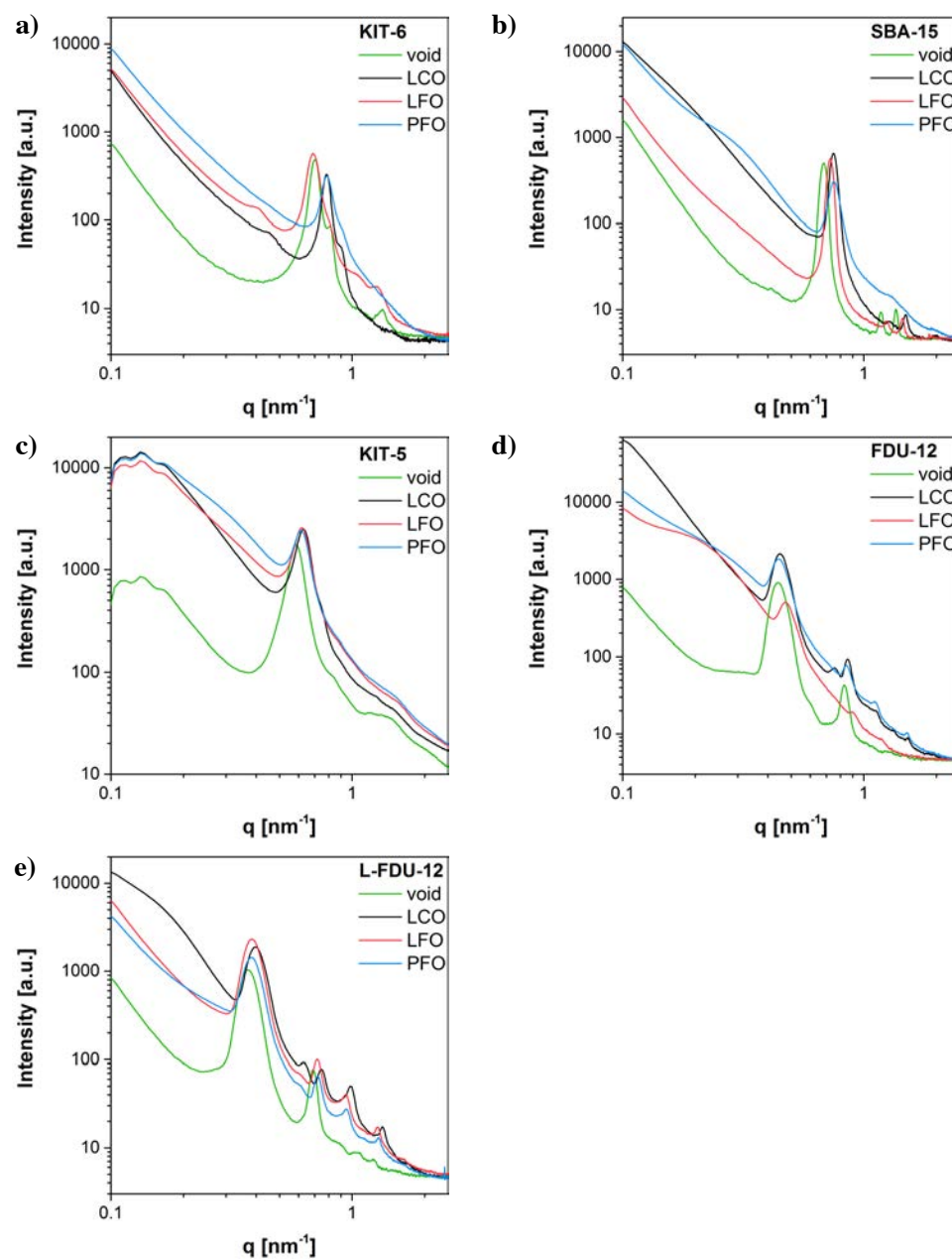
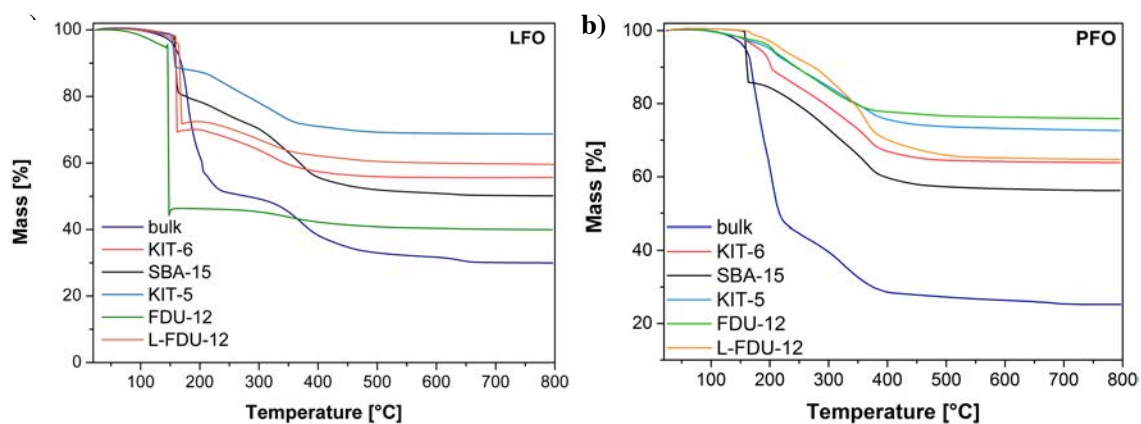
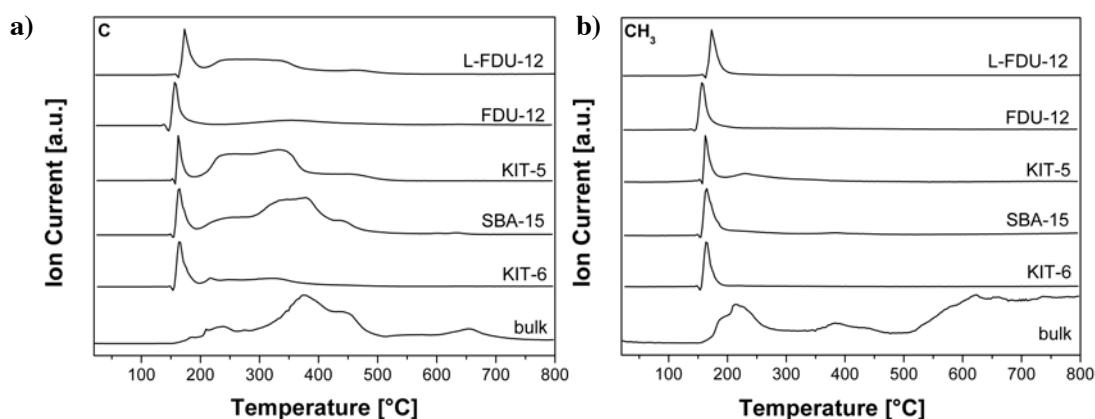


Figure S7: SAXS patterns of KIT-6 (a), SBA-15 (b), KIT-5 (c), FDU-12 (d) and L-FDU-12 (e), void (green) and filled with LaCoO_3 (black), LaFeO_3 (red) and PrFeO_3 (blue), respectively.

Thermogravimetric Measurements**Figure S8:** Thermograms of bulk and silica-impregnated LaFeO_3 (a) and PrFeO_3 (b) materials

In Fig. S8 the thermogravimetric analysis of LaFeO_3 and PrFeO_3 systems are depicted. The diverse pore volume of the silica matrices allows the incorporation of various amounts of perovskite precursors, resulting in different final rest masses.

TG-MS measurements

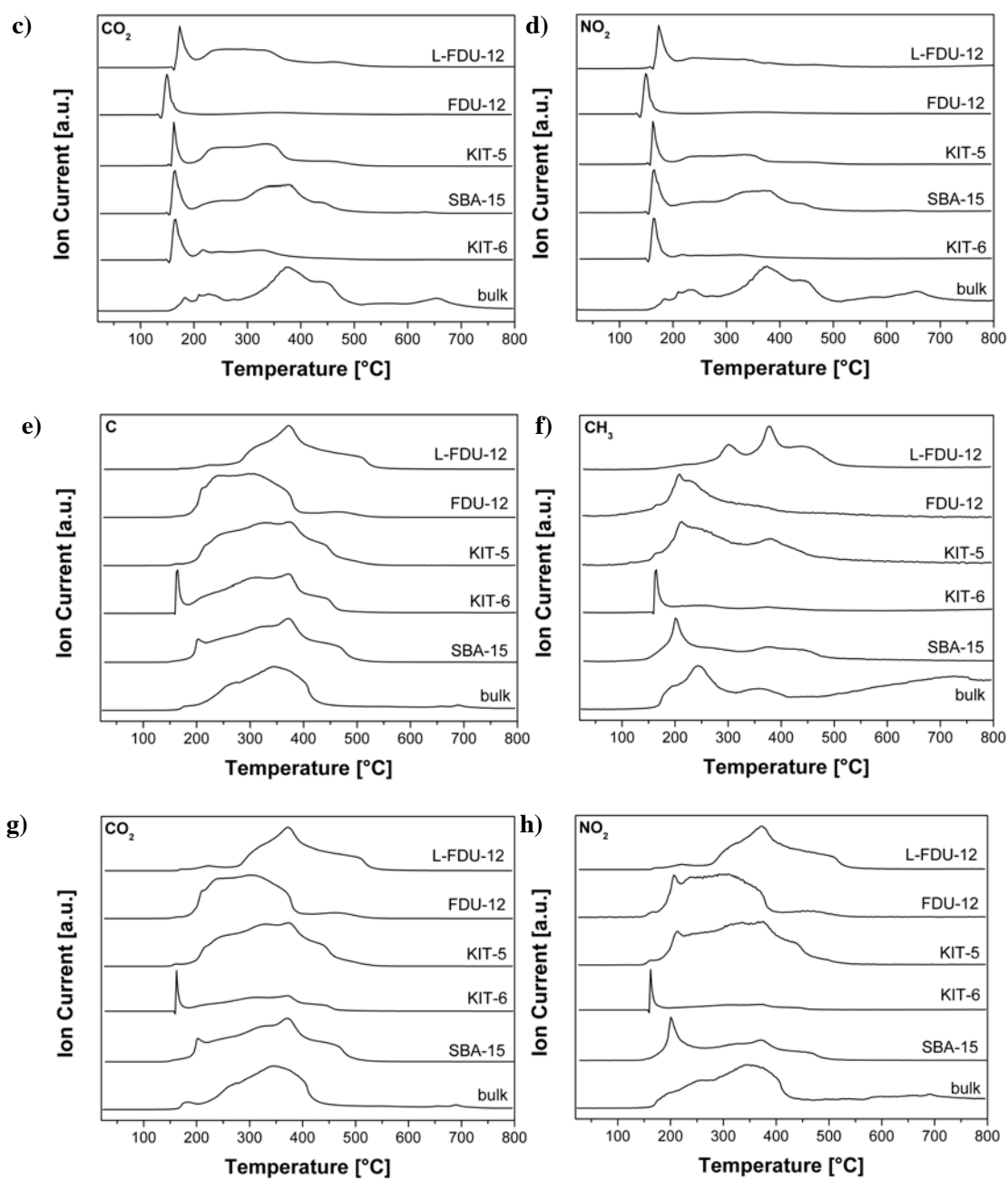


Figure S9: Temperature dependent mass spectra of LaFeO₃-impregnated KIT-6, SBA-15, KIT-5, FDU-12 and L-FDU-12 silica hosts and bulk LaFeO₃ for C (a), CH₃ (b), CO₂ (c) and NO₂ (d);

11. Appendix

Temperature dependent mass spectra of PrFeO₃-impregnated KIT-6, SBA-15, KIT-5, FDU-12 and L-FDU-12 silica hosts and bulk LaFeO₃ for C (e), CH₃ (f), CO₂ (g) and NO₂ (h).

11.3. Supporting Information: Functional Nanostructured Perovskite Oxides from Radical Polymer Precursors

*Jonas Scholz¹, Alberto Garbujó², Buğra Kayaalp¹, Kurt Klauke¹, Antonella
Glisenti² and Simone Mascotto¹*

¹Institut für Anorganische und Angewandte Chemie, Universität Hamburg,
Martin-Luther-King Platz 6, 20146 Hamburg, Germany

²Dipartimento di Scienze Chimiche, Università degli Studi di Padova, Via
Marzolo, 1, 35123 Padova, Italy

11. Appendix

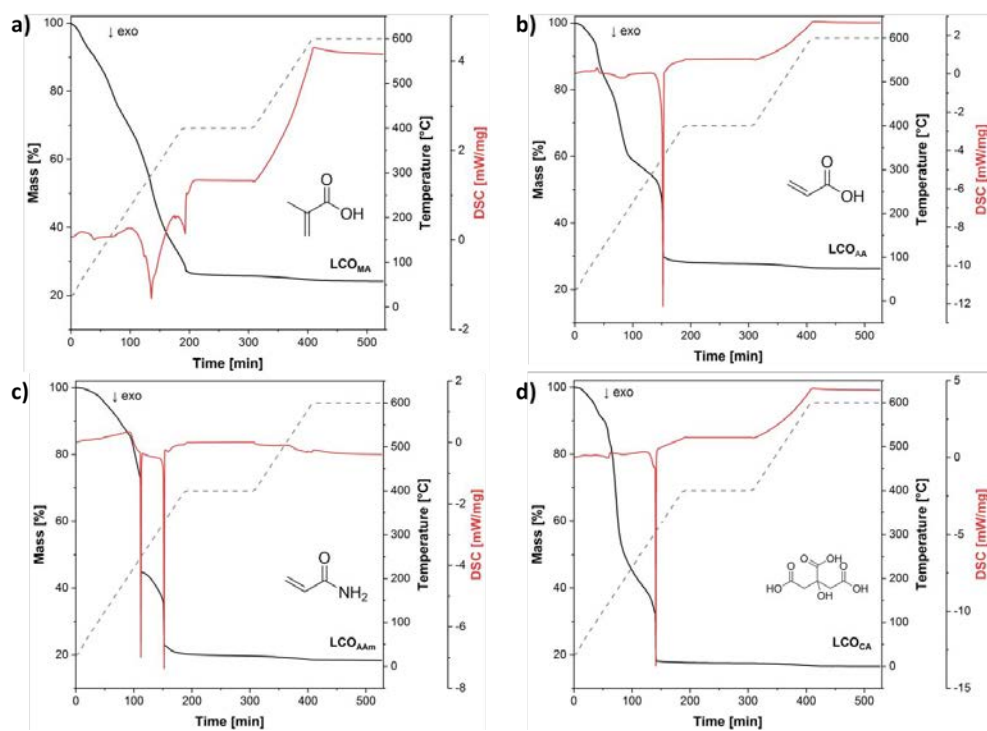


Fig. S1: Thermogravimetric analyses and coupled DSC measurements of LCO_{MA} (a), LCO_{AA} (b) LCO_{AAm} (c) and LCO_{CA} (d) during the thermal annealing used for the materials synthesis.

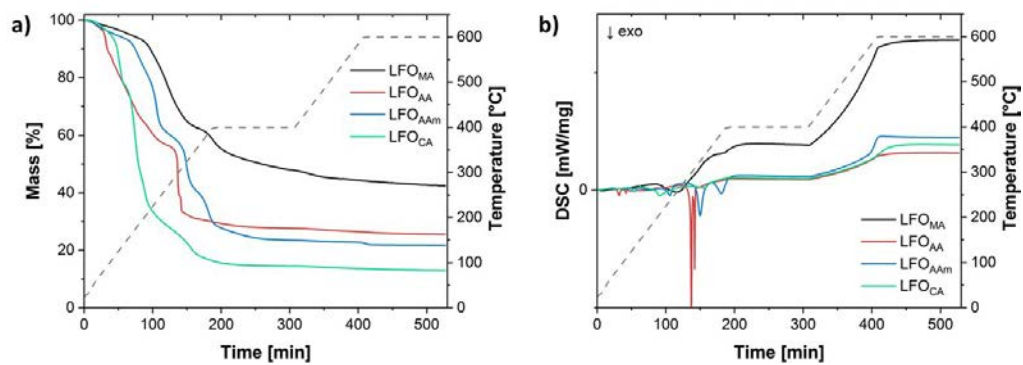


Fig. S2: Thermogravimetric analyses (a) and coupled DSC measurements (b) of LFO_{MA} (black), LFO_{AA} (red), LFO_{AAm} (blue) and LFO_{CA} (green) during the thermal annealing used for the materials synthesis.

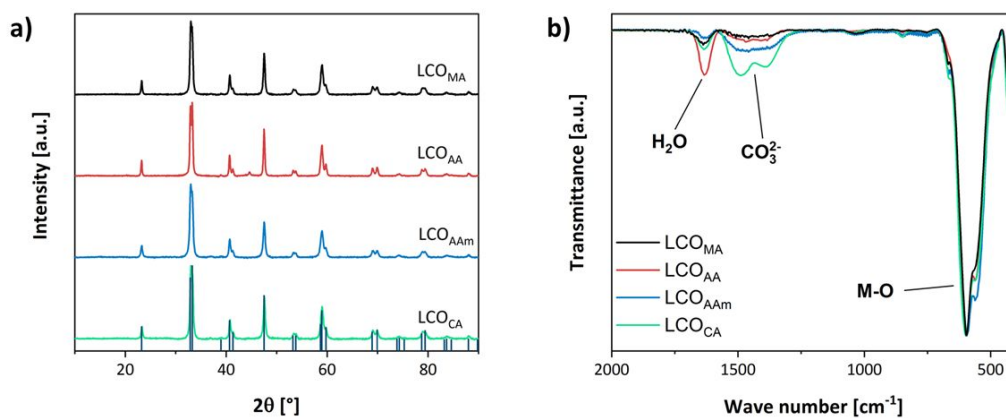


Fig. S3: X-Ray diffractograms (a) and IR spectra (b) of LaCoO₃ calcined at 600 °C derived from thermally polymerized MA (black), AA (red), AAm (blue) and CA (green). The reference diffractogram of LCO^I is depicted in dark blue.

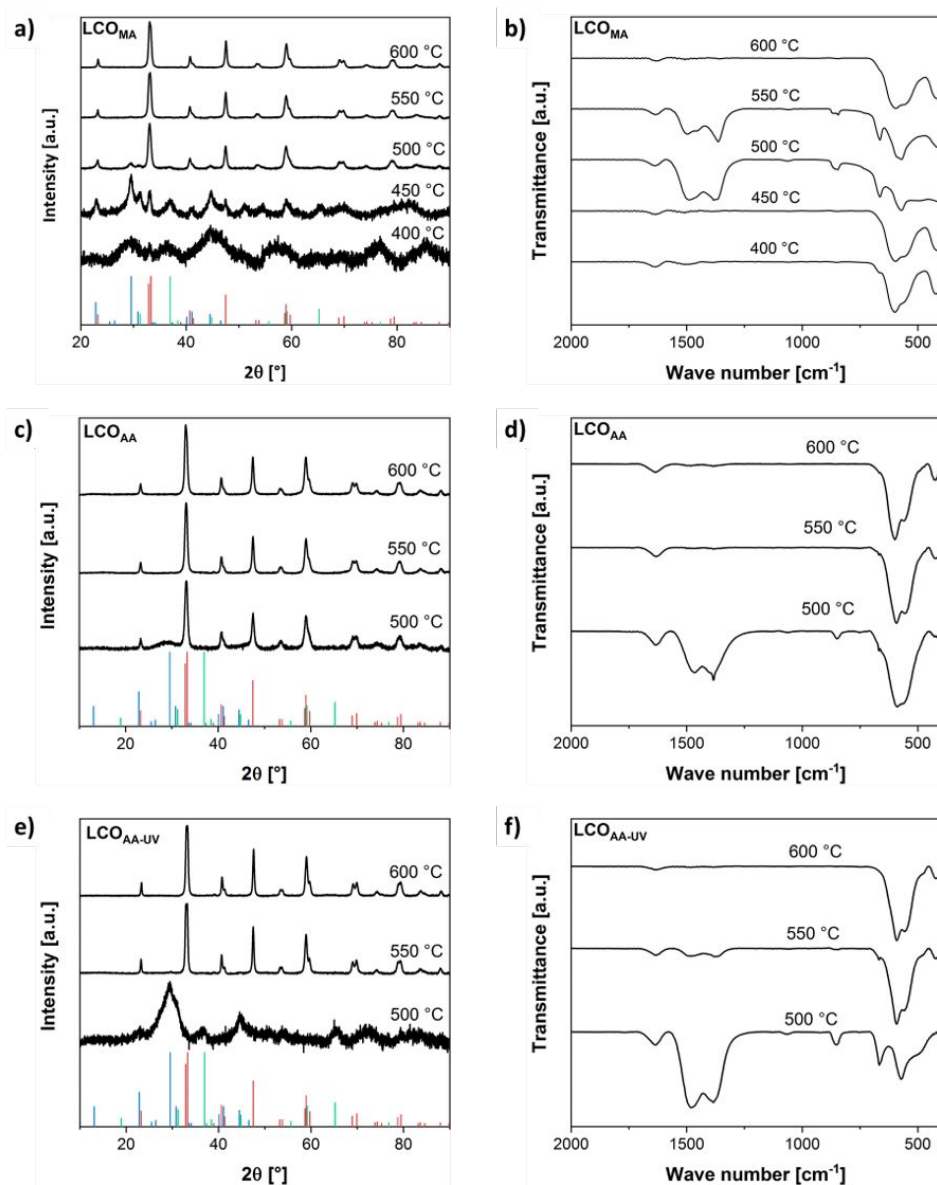


Fig. S4: X-ray diffractograms of LCO_{MA} (a) LCO_{AA} (c) and $\text{LCO}_{\text{AA-UV}}$ (e) and IR spectra of LCO_{MA} (b), LCO_{AA} (d) and $\text{LCO}_{\text{AA-UV}}$ (f) calcined in air for 2 h at different temperatures. The reference diffractograms of LCO^1 , $\text{La}_2\text{O}_2\text{CO}_3^2$ and $\text{CoCo}_2\text{O}_4^3$ are depicted in red, blue and green, respectively.

Williamson-Hall plot

A contribution of the microstrain in the peak broadening cannot be excluded. We calculated the Williamson-Hall (WH) plot⁴ for the determination of the strain and crystallite sizes from the XRD data of LCO prepared with MA, AA, AAm, CA, MA_{UV}, AA_{UV} and AAm_{UV}.

This approach associates the total broadening of the peak (β_{TOT}) with a mixed contribution of strain (β_e) and crystallite size (β_L) through the equation:

$$\beta_{TOT} = \beta_e + \beta_L = C\varepsilon \tan\theta + \frac{K\lambda}{L \cos\theta}$$

Which can be rewritten as:

$$\beta_{TOT} \cos\theta = C\varepsilon \sin\theta + \frac{K\lambda}{L}$$

The slope of the curve represents the strain (β_e), whereas the intercept gives the values of the crystallite sizes (β_L). The plots for the single materials are displayed in Fig S5 and the associated values are listed in Table S1.

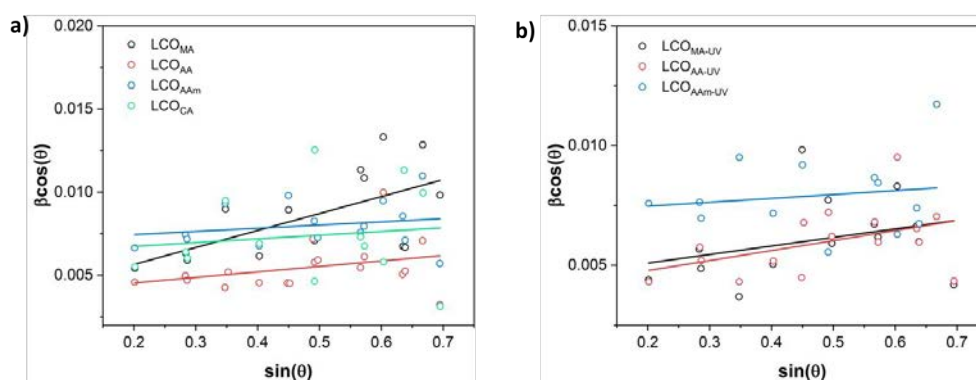


Fig. S5: Williamson-Hall plot for the LCO materials prepared under thermal (a) and UV polymerization (b)

11. Appendix

Table S1: Williamson-Hall parameters and average crystallite size (L) of the LCO materials prepared in this work. The parameters K and λ were accounted for 0.9 and 1.5406 nm, respectively

Sample	$C\varepsilon$	$K\lambda/L$	L [nm]
MA	0.0102	0.0036	39
MA-UV	0.0036	0.0044	32
AA	0.0033	0.0039	36
AA-UV	0.0042	0.0039	36
AAm	0.0019	0.0071	20
AAm-UV	0.0016	0.0071	20
CA	0.0022	0.0063	22

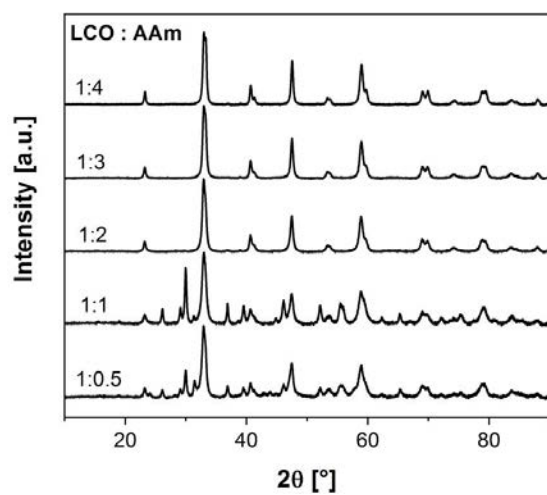


Fig. S6: LCO_{AAm} prepared from different molar ratios of metal precursor to acrylamide, calcined at 600 °C.

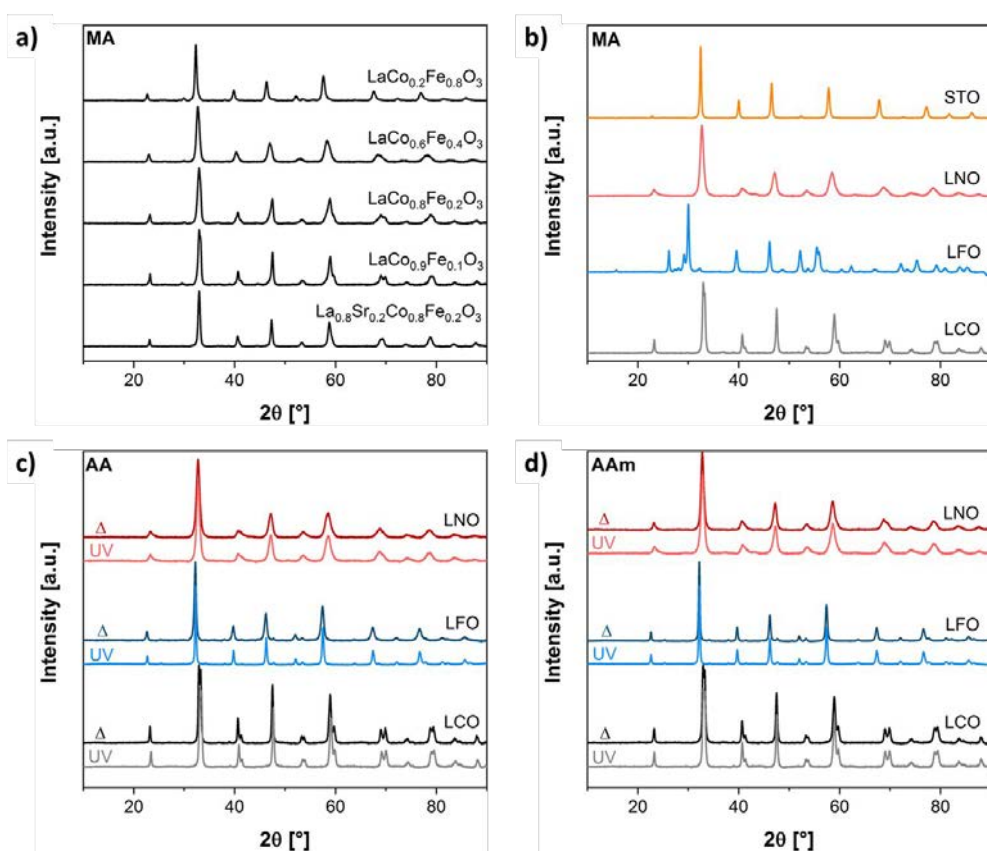


Fig. S7: X-Ray diffractograms of Fe- and Sr-doped LaCoO_3 species based on a thermal polymerization of MA (a). X-Ray diffractograms of LaCoO_3 (black), LaFeO_3 (blue), SrTiO_3 (orange, MA only) and LaNiO_3 (red) based on a thermal polymerization (Δ) or UV initiated polymerization of MA (b), AA (c) and AAm (d).

In the radical polymerization route for SrTiO_3 , the methacrylic acid to SrTiO_3 product ratio (MA : STO) was set at 11.3 : 1, whereas in a typical Pechini synthesis the organics (glycerol, citric acid) to SrTiO_3 product ratio (Gly + CA : STO) was defined at 17 : 1.

In accordance with the La-based perovskite oxides, the X-ray diffractograms of the as-prepared SrTiO_3 and $\text{La}_{0.1}\text{Sr}_{0.9}\text{TiO}_{3+\delta}$ aggregates prepared with MA show substantially high crystallinity and phase-purity without the presence of any carbonate phases (Fig. S8a).

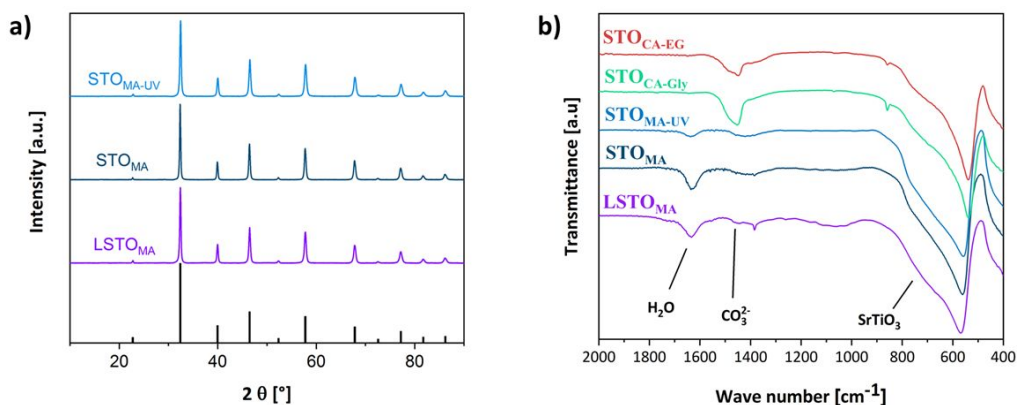


Fig. S8: X-ray diffractograms of STO_{MA} (dark blue), STO_{MA-UV} (light blue) and LSTO_{MA} (purple). A reference diffractogram of STO⁵ is displayed in black (a). IR spectra of STO prepared applying the Pechini method with ethylene glycol (red), with glycerine (green), STO based on MA obtained via UV-polymerization (light blue) and thermal polymerization (dark blue) and LSTO obtained in a thermal polymerization process of MA (violet) (b).

These results are further supported by the IR spectra shown in Fig. S8b. The infrared spectra of the perovskite oxides prepared by the radical polymerization route also indicate superior purity in comparison to SrTiO₃ prepared by the standard polymer complex (Pechini) synthesis as significant amounts of carbonate impurities are present.

Elemental ratios of the cations in the prepared samples determined by EDX spectroscopy were in good agreement with the nominal values, whereas SEM images displayed uniformly bulk aggregates of several micrometers with only textural porosity for all investigated samples independent of the polymerization route and composition (Fig. S9). It can be observed that the pores formed in the UV-based SrTiO₃ are larger than those present in the SrTiO₃ sample prepared through thermal polymerization. In accordance with the textural features observed by SEM, specific surface areas were determined by N₂ physisorption analysis to be between 13 and 19 m²/g.

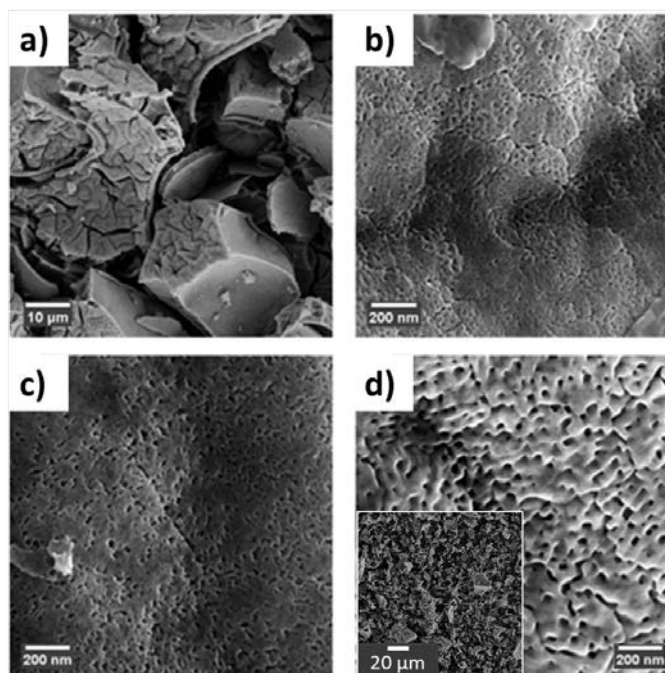


Fig. S9: SEM images of investigated samples prepared by MA radical polymerization route: Thermally prepared STO (a-b), thermally prepared LSTO (c) and UV based STO (d).

Table S2: Textural properties of $\text{La}_{0.1}\text{Sr}_{0.9}\text{TiO}_3$, i.e. crystallite size, S_{BET} and surface ratio of cations determined by EDX.

Perovskite	Polymer used	Crystallite Size	S_{BET}	Sr/Ti	La/Ti
		[nm]	[m^2/g]	EDX	EDX
SrTiO_3	MA	51	13	0.88	-
	MA_{UV}	37	16	0.82	-
$\text{La}_{0.1}\text{Sr}_{0.9}\text{TiO}_3$	MA	43	19	0.93	0.11

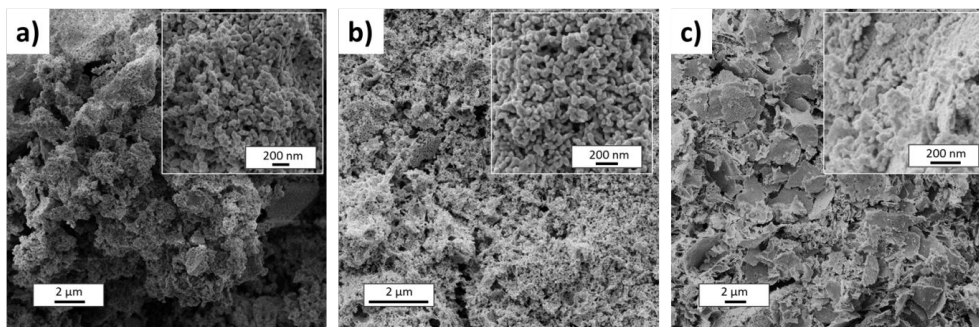


Fig. S10: SEM images of LCO_{MA-UV} (a) LCO_{AA-UV} (b) and LCO_{AAm-UV} (c).

Fig. S10 displays the SEM analysis of the LCO materials prepared by MA, AA and AAm using photopolymerization. As for the thermally polymerized systems shown in the manuscript, AA and AAm derived ceramics present porous, voluminous aggregates with the tendency to form lamellar structures. Similarly, the MA derived LCO obtained via UV polymerization has the same globular morphology as the one prepared by thermal polymerization. On the nanometric scale, all the investigated systems present aggregated nanoparticles with interparticle porosity. No significant differences among these systems were noted.

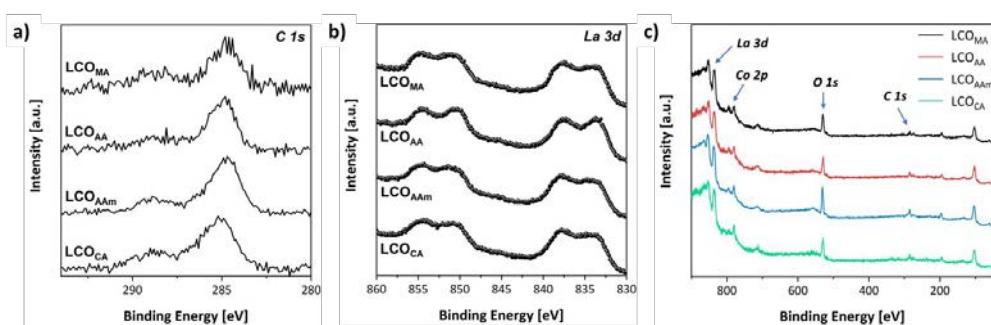


Fig. S11: C 1s (a) La 3d (b) and survey (c) XPS spectra of LaCoO₃ synthesized from methacrylic acid, acrylic acid, acrylamide and citric acid.

Table S3: Peak positions and relative concentrations of different oxygen species of LaCoO_3 obtained from the relative subpeak area of the O 1s XPS spectra.

Polymer used	O^{2-}		OH		chemisorbed O_2		physisorbed H_2O	
	Peak (eV)	Concentration (%)	Peak (eV)	Concentration (%)	Peak (eV)	Concentration (%)	Peak (eV)	Concentration (%)
MA	528.8 eV	43.1%	530.9 eV	42.8 %	532.2 eV	11.4%	533.7 eV	2.7%
AA	528.9 eV	58.5%	531.0 eV	25.2%	532.0 eV	16.3%	-	-
AAm	528.9 eV	37.8%	531.0 eV	38.6%	532.2 eV	16.6%	533.6 eV	7.0%
CA	528.9 eV	42.7%	531.3 eV	35.6%	533.2 eV	14.0%	533.8 eV	7.7%

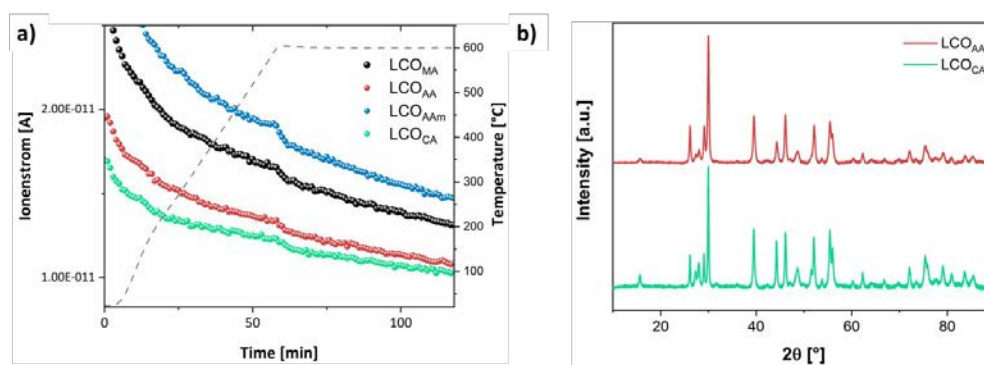


Fig. S12: TPD-MS spectra of LCO_{MA} (black), LCO_{AA} (red), LCO_{AAm} (blue) and LCO_{CA} (green) (a) and X-ray diffractograms of LaCoO_3 samples obtained from acrylic acid (red) and citric acid (green) after reduction during the H_2 -TPR measurement (b).

11. Appendix

Table S4: Reduction steps and respective temperatures of H₂-TPR measurements on LaCoO₃.

Polymer used	Co ³⁺ to Co ²⁺ [°C]	Co ^{+3.4+} to Co ²⁺ [°C]	Co ²⁺ to Co ⁰ [°C]
MA	409	453	615
AA	407	438	623
AAm	413	449	638
CA	404	-	780

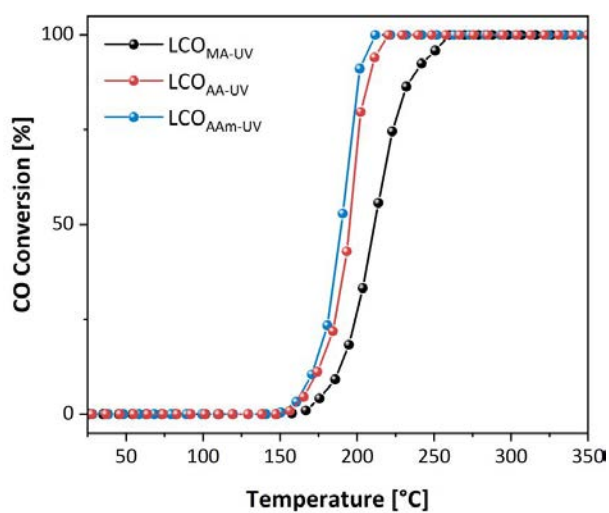


Fig. S13: Light-off curves of CO oxidation over different LaCoO₃ derived from UV-initiated polymerization.

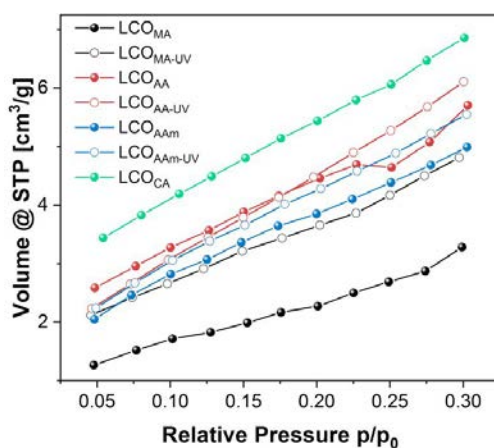


Fig. S14: Nitrogen adsorption isotherms of LCO_{MA} (black bullet points), LCO_{MA-UV} (black empty bullet points), LCO_{AA} (red bullet points), LCO_{AA-UV} (red empty bullet points), LCO_{AAm} (blue bullet points), LCO_{AAm-UV} (blue empty bullet points) and LCO_{CA} (green bullet points), up to relative pressure p/p_0 of 0.3 to determine the BET surface area.

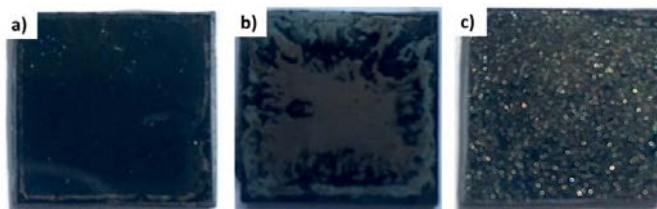


Fig. S15: Photographic images of LCO thin-films prepared from UV-polymerized AAm (a), thermally polymerized AAm (b) and thermally polymerized CA (c).

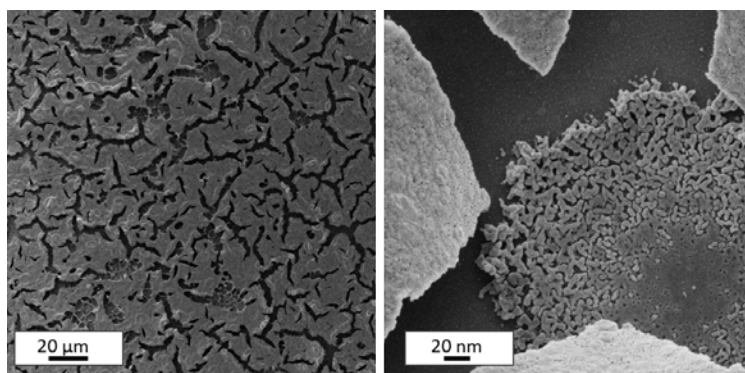


Fig. S16: SEM images of LCO thin-films prepared from thermally polymerized AAm.

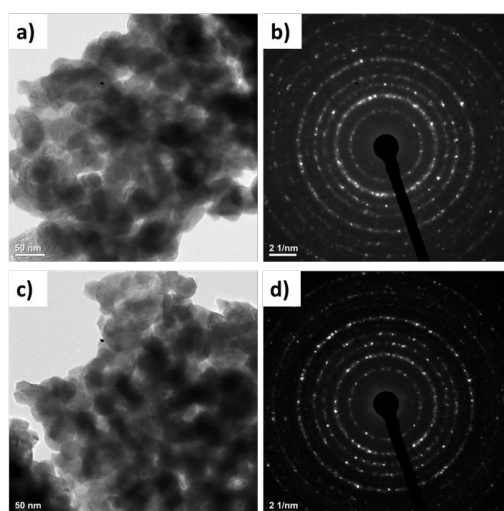


Fig. S17: TEM images of LCO_{AAm} (a) and LCO_{CA} (c) after removing the calcined perovskite oxide thin film from the silicon wafer. Electron diffraction pattern of the respective powders (b,d).

Bibliography

- (1) Closset, N. M. L. N. P.; van Doorn, R. H. E.; Kruidhof, H.; Boeijmsma, J. About the Crystal Structure of $\text{La}_{1-x}\text{Sr}_x\text{CoO}_{3-\delta}$ ($0 \leq x \leq 0.6$). *Powder Diffr.* **1996**, *11* (1), 31–34.
- (2) Sawyer, J. O.; Caro, P.; Eyring, L. Herstellung, Analyse Und Röntgenographische Identifizierung Der Dioxymonocarbonate Des Lanthans Und Der Lanthanidenelemente. *Monatshefte für Chemie* **1972**, *103* (1), 333–354.
- (3) Hanawalt, J. D.; Rinn, H. W.; Frevel, L. K. Chemical Analysis by X-Ray Diffraction. *Ind. Eng. Chem. Anal. Ed.* **1938**, *10* (9), 457–512.
- (4) Williamson, G.; Hall, W. X-Ray Line Broadening from Filled Aluminium and Wolfram. *Acta Metall.* **1953**, *1* (1), 22–31.
- (5) Nelmes, R. J.; Meyer, G. M.; Hutton, J. Thermal Motion in SrTiO_3 at Room Temperature: Anharmonic or Disordered? *Ferroelectrics* **1978**, *21* (1), 461–462.

11.4. Preparation of Nanoporous LaCoO₃ using Ladder-like Polysilsesquioxanes

In this section, the template-assisted synthesis of nanoporous LaCoO₃ utilizing LLPSSO as template is demonstrated. The following description does not represent an optimized method with regard to synthesis parameters (functionality composition of LLPSSO, template loading of the composite, etching conditions). It is rather meant to convey the concept and the challenges of this approach.

With regard to the composition of the ladder-like polysilsesquioxane, a methacryl-to-phenyl ratio of 80:20 was used as it accommodates high amounts of methacryl functionality, which promotes integration of the template into the polymer matrix of the starting material, and phenyl functionality to prevent agglomeration of the ladder-structures. A relatively low template loading of 15 wt% was chosen to further impede agglomeration of LLPSSO.

The composite was composed of LCO and LLPSSO. The formation of perovskite oxide was confirmed by X-ray diffractometry. The characteristic rhombohedral structure of LaCoO₃ is displayed in Figure 11.1a. Determination of the crystallite size by Scherrer equation^[255] resulted in an average grain size of 30 nm (Table 11.2), which is in good agreement with the values of pristine LCO..^[242] These values also concur with the display of the morphology in Figure 11.2a. TEM micrographs show agglomerates of interconnected crystalline grains.

The IR spectrum reveals the presence of silica in the composite material (Figure 11.1b). A strong absorption band at around 1050 cm⁻¹ refers to the asymmetric stretching vibrations of the Si-O-Si bond.^[244]

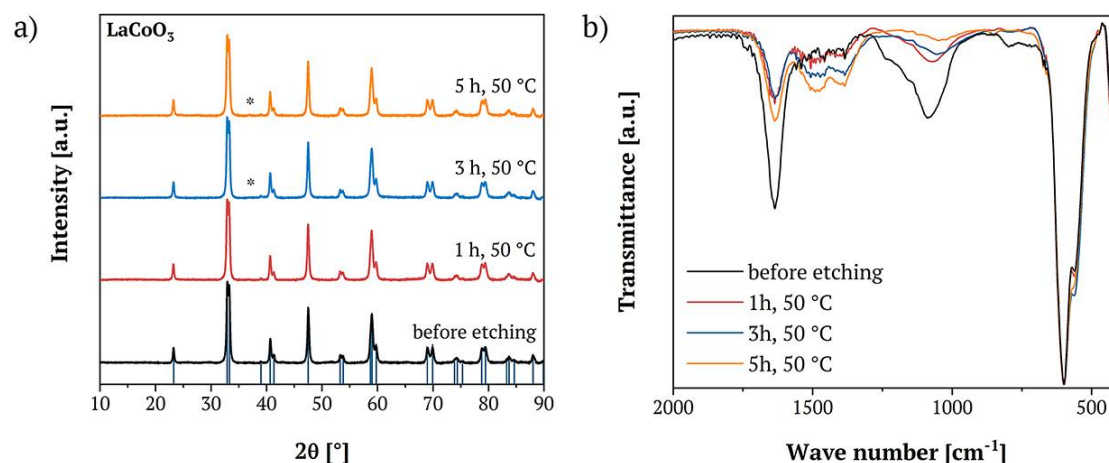


Figure 11.1.: XRD patterns (a) and IR spectra (b) of a LCO/LLPSSO composite following a 3M NaOH etching at 50 °C after 1 h (red), 3 h (blue) and 5 h (orange). The data from the initial composite is added in black. A reference diffractogram of LaCoO_3 ^[256] is depicted in dark blue.

A more discerned assessment of the template distribution in the composite was provided by electron microscopy. TEM images in Figure 11.2a show the distinct silica 'ladders'. However, only few regions are pervaded by the template. Mostly, silica agglomerates were formed. This is further supported by elemental mapping of the silica species in Figure 11.2b. A significant intensity is detectable only in selected regions of the perovskite oxide matrix. Accordingly, high local fluctuations of the atomic composition were deduced from EDX (??). The inhomogeneous distribution of the ladder-like structures is detrimental to the templating-effect. Thus, only partial templating was achieved.

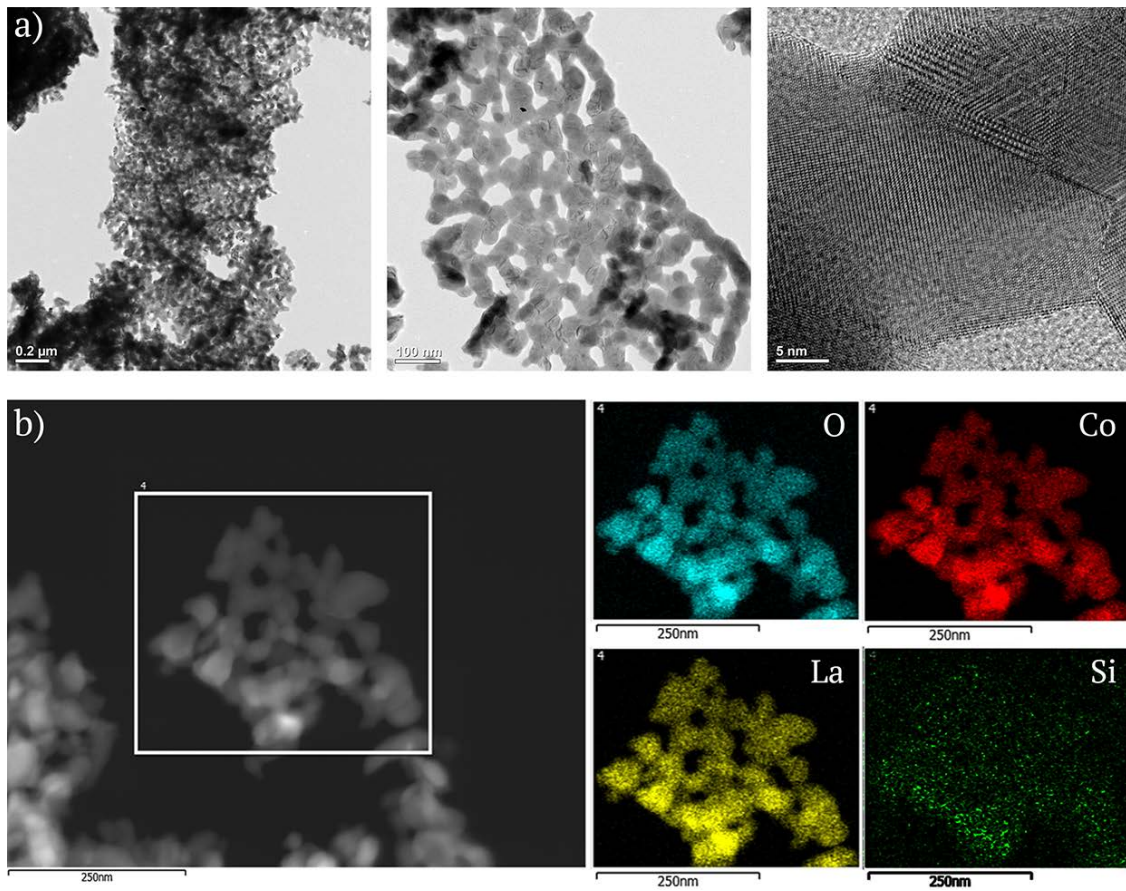


Figure 11.2.: TEM micrographs of an LCO/LLPSSO composite (15 wt.% of LLPSSO) at different magnifications (a). Corresponding element mappings of oxygen (blue), cobalt (red), lanthanum (yellow) and silicon (green) (b).

Table 11.1.: Atomic composition of an LCTO/LLPSSO composite determined by EDX.

Atomic Composition [%]			
La	Co	O	Si
19.5	16.4	62.2	2.0

Etching of the composite material presents the second step of the synthesis procedure. Complete removal of the silica network is necessary to form porosity and eliminate 'inactive' silica species, while maintaining structural integrity and stability of the perovskite phase. Sodium hydroxide solution constitutes a typical etching medium to eliminate the silica structures. XRD was employed to monitor structural changes of the perovskite structure, whereas IR spectroscopy could provide information about the amount and type of silicon species remaining in the material. Porosity was determined by means of N₂-physisorption.

The composite was treated to 3M aqueous alkaline solution for 1 h, 3 h and 5 h at 50 °C, respectively. Variation of the etching time was performed to determine suitable conditions with regard to both the removal of silica template and the stability of the perovskite oxide. The IR spectra displayed in Figure 11.1b indicate a correlation between etching time and silica content. Extended exposure to alkaline solution resulted in the gradual decrease of siliceous content as evidenced by the decrease of the absorption band at 1050 cm⁻¹. After 5 h of alkaline treatment, almost complete removal of silica was achieved.

Additionally, the etching procedure was accompanied by an accumulation of carbonate species in the material, the amount of which increased gradually with etching time. The carbonate content is demonstrated by two overlapping bands at 1489 and 1396 nm⁻¹. The occurrence of carbonates is commonly observed in literature and can be remedied by a subsequent acetic acid treatment.^[179]

The structural modifications subsequent to NaOH exposure are additionally described by determination of the specific surface area (S_{BET}). As listed in Table 11.2, a steady increase in etching time constitutes a gradually enhanced surface area by removal of silica. After 5 h of NaOH treatment, LCO with a specific surface area of 46.5 m²/g was obtained.

The overall moderate enhancement of the porosity (Figure 11.3) can be ascribed to the formation of template agglomerates, the removal of which does not contribute to a significantly increased surface area.

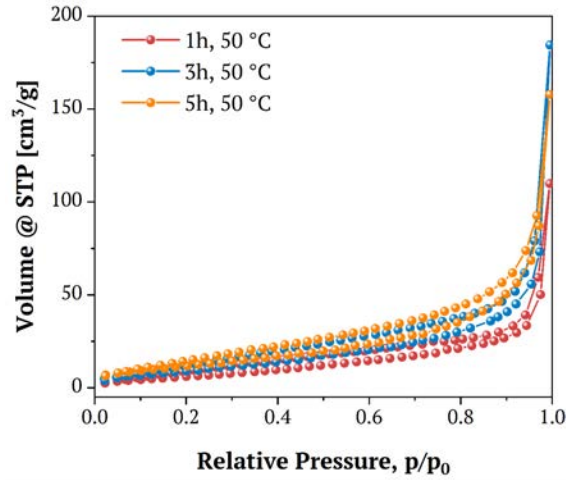


Figure 11.3.: Nitrogen physisorption isotherms of a LCO/LLPSSO composite following a 3M NaOH etching at 50 °C after 1 h (red), 3 h (blue) and 5 h (orange).

With respect to the perovskite oxide phase, compositional changes were observed. The X-ray diffractograms in Figure 11.1a indicate the formation of a secondary phase. As etching time is extended, a reflection at $37^\circ 2\theta$ is increasingly observed, which can be ascribed to the $[3\ 1\ 1]$ reflection of Co_3O_4 .^[250] Thus, partial degradation of the perovskite oxide takes place.

However, the crystallite size calculated by the *Scherrer* equation, remains constant within a small margin of error (11.2).

Table 11.2.: Textural properties of an LCO/LLPSSO composite as a function of time for NaOH etching at 50 °C.

Time [h]	Crystallite Size [nm]	S_{BET} [m ² /g]
1	30.1	26.8
3	30.9	39.0
5	31.2	46.5

Further increase of the etching temperature and/or time promoted deterioration of the perovskite structure due to reduction of the cobalt cations. Consequently, stabilization of the LCO structure was necessary as the perovskite structure did not maintain integrity throughout the alkaline treatment.

11.5. Preparation of Nanoporous $\text{LaCo}_{0.8}\text{Ti}_{0.2}\text{O}_3$ using Ladder-like Polysilsesquioxanes

In the following section, some representative sets of data are shown with respect to the optimization of the template-assisted preparation of nanoporous $\text{LaCo}_{0.8}\text{Ti}_{0.2}\text{O}_3$. Emphasized parameters for the optimization comprise the compositional variation of LLPSSO functionalities, amount of template loading, and temperature of alkaline etching.

In order to optimize the porous structure of LCTO, the amount of template loading was varied. To that effect, $\text{LaCo}_{0.8}\text{Ti}_{0.2}\text{O}_3$ composites with 15 wt%, 20 wt%, 25 wt%, and 30 wt% of LLPSSO were prepared. The compositional methacryl-to-phenyl ratio of the LLPSSO template was varied, ratios of 70:30 and 100:0 are presented in this work. The nanocomposites were etched with alkaline solution for 3 h at 60, 80 and 90 °C, respectively. Subsequently, each solid was exposed to aqueous acetic acid solution (5 %) for 1 h at room temperature. The respective diffractograms, IR spectra and N_2 -isotherms are not provided in this section as they correspond to the patterns shown in the Chapter 'Unpublished Work'. In order to prevent redundancy, the essence of these results is given in Table 11.3. Some general conclusions and some particular results are highlighted in the following section. X-ray diffractograms of LCTO-LLPSSO composites were measured at each step of the synthesis to assess the formation and stability of the perovskite structure. Generally, highly crystalline materials were obtained without impurities were observed. Crystallite sizes were calculated by applying the Scherrer equation. The sizes of different nanocomposites range from 12.2 to 15.5 nm showing no distinct template-loading dependence. A structural change, however, was observed, after

alkaline etching at 90 °C. The corresponding diffractograms indicated the presence of cobalt spinel phases due to the disintegration of the perovskite oxide structure.

Table 11.3.: Textural properties of LCTO-LLPSSO nanocomposites in dependence of template composition, template loadings, and subsequent etching conditions.

Ratio LLPSSO	Template Loading	$T_{NaOHe tching}$	Synthesis Step	Crystallite Size [nm]	S_{BET} [m ² /g]
70:30	15 wt%	-	composite	13.8	90.6
		60 °C	NaOH	15.1	88.5
			AcOH	14.1	68.9
		80 °C	NaOH	15.0	53.0
			AcOH	15.5	71.8
	20 wt%	-	composite	12.3	34.0
		60 °C	NaOH	10.7	49.7
			AcOH	12.7	61.4
		80 °C	NaOH	12.4	62.2
			AcOH	12.8	91.9
		90 °C	NaOH	14.7*	92.3
	25 wt%	-	composite	12.2	34.7
		80 °C	NaOH	13.5	54.2
			AcOH	12.2	62.8
	30 wt%	-	composite	13.6	32.0
80 °C		NaOH	13.1	58.3	
		AcOH	13.2	61.6	
100:0	20 wt%	-	composite	15.4	34.0
		90 °C	NaOH	16.7*	68.8

* Broadening of the reflections due to formation of secondary phases, which corresponds to the degradation of the structure. Accordingly, not subsequent acidic treatment was performed.

IR spectra of different composites all exhibit the characteristic silanol contribution in addition to the vibrational mode of siloxane groups. Only differences in intensity can be observed, which can be ascribed to the amount of template added to the initial reaction mixture. Upon alkaline etching, removal of the silica can be confirmed as the silica absorption band disappears almost completely as the silica agglomerates are mostly eliminated. Only small amounts of silanol compounds remain in the material. Comparable intensities indicate similar amounts of template residue independent of template loading or etching temperature.

Moreover, all composite materials exhibit a considerable carbonate absorption band. The enhanced presence of carbonates compared to the synthesis of non-templated perovskite oxide materials using the acrylate-supported complex route^[242] can be ascribed to an increased content of organic moieties in the initial hybrid polymer. This extent of organic molecules stems from the organic moieties of the LLPSSO templates.

In the context of porosity, nitrogen physisorption measurements were performed to determine the evolution of the porous properties of the different composite materials. Similar isotherms, which exhibit hysteresis and the presence of interparticle porosity, were observed for all etched samples. However, small deviations in porosity and BET surface area were determined. Considering the formation of agglomerates, partial templating is favoured under certain conditions. Accordingly, a LLPSSO_{70:30} loading of 20 wt% and an alkaline treatment of 80 °C was most beneficial for the enhancement of the specific surface area.

11.6. List of Chemicals and corresponding Safety Information

Compound	GHS hazard pictograms	H-statements	P-statements
Acetic acid, glacial		226, 314	301+330+331, 305+351+338
Acrylamide*		301, 312+332, 315, 317, 319, 340, 350, 361f, 372	302+352
Acrylic acid		226, 302+312+332, 314, 335, 400	301, 330+331, 302+350, 305+351+338
Ammonia		314, 335, 410	273, 280i, 301+330+331, 305+351+338
Benzoyl peroxide		242, 317, 319, 410	302+352
1-Butanol		226, 302, 315, 318, 335, 336	210, 280, 301+312+330, 302+352, 305+351+338+310

Citric acid		319	305+351+338
Cobalt nitrate hexahydrate*		272, 302+332, 317, 318, 334, 341, 350i, 360F, 410	221, 301+330+331, 302+352, 305+351+338, 371+380+375
Deuterium oxide	-	-	-
Dimethylformamide*		226, 312+332, 319, 360D	201, 280, 305+351+338, 308+313
Dichloromethane		315, 319, 336, 351	302+352
Ethanol		225, 319	210, 280, 305+351+338
Ethylene glycol		302, 373	301+312+330, 314
Glycerol	-	-	-
Hydrochloric acid		290, 314, 335	261, 280, 301+330+331, 303+361+353, 304+340+310, 305+351+338+310

11. Appendix

Hydrogen peroxide		302, 318, 412	264, 270, 273, 280, 305+351+338, 310, 501
1-Hydroxycyclohexyl phenyl ketone	-	-	-
Iron(III) nitrate nonahydrate		272, 315, 319	302+352, 305+351+338
Lanthanum nitrate hexahydrate		272, 315, 319, 335	302+352, 305+351+338
Magnesium sulfate	-	-	-
Mesitylene		226, 304, 315, 332, 335, 411	210, 273, 301+310+331, 302+352, 304+340+312
Methacrylic acid		227, 302+332, 311, 314, 335	301+330+331, 305+351+338
3-Methacryloxypropyltrimethoxysilane	-	-	-

Methanol		225, 301+311+331, 370	210, 280, 301+310+330, 302+352+312, 304+340+311
Nickel(II) nitrate hexahydrate*		272, 302+332, 315, 317, 318, 334, 341, 350i, 360D, 372, 410	201, 273, 281, 405
Phenyl- trimethoxysilane		226, 302, 373c	260, 264b, 301+330+331
Pluronic F127	-	-	-
Pluronic P123	-	-	-
Poly(vinyl alcohol)	-	-	-
Potassium carbonate		315, 319, 335	305+351+338
Potassium chloride	-	-	-
Praseodymium(III) nitrate hexahydrate		272, 315, 319, 335	221, 302+352, 371+380+375
Sodium hydroxide		314	301+330+331, 305+351+338

11. Appendix

Strontium nitrate		272, 318	221, 305+351+338, 371+380+375
Sulfur		228, 315	210, 302+352
Tetraethyl orthosilicate		226, 319, 332, 335	305+351+338
Tetrahydrofuran		225, 302, 319, 335, 351	201, 210, 301+312+330, 305+351+338, 308+313
Tetrahydrofuran- d ₈		225, 315, 319, 351	210, 281, 305+351+338
Titanium(IV) isopropoxide		226, 319, 331, 336	305+351+338
Toluene-d ₈		225, 304, 315, 336, 361d, 373b, 412	201, 210, 301+310+331, 302+352, 308+313

* refers to a CMR substance (cat. GHS 1A or 1B)

11.7. Posters and Presentations

11.7.1. Oral Presentations

- Jonas Scholz, Alberto Garbujo, Antonella Glisenti, Simone Mascotto, Radical polymerization as a tool to prepare mesostructured perovskite oxides with improved catalytic activity. **MC 14**, 14th International Conference on Materials Chemistry, 2019, Birmingham, United Kingdom.
- Jonas Scholz, Buğra Kayaalp, Anika Juhl, Michael Fröba, Simone Mascotto, Investigation of Li-S battery cathode materials via small-angle scattering. **Nanotage 2019**, Aachen, Germany.

11.7.2. Poster Presentations

- Jonas Scholz, Andreas Meyer, Simone Mascotto, Structural modifications of host and guest species in supported metal oxide systems, **DZT 2017**, 29. Deutsche Zeolith-Tagung, Frankfurt, Germany.
- Jonas Scholz, Buğra Kayaalp, Anika Juhl, Michael Fröba, Simone Mascotto, Solvent effect on sulfur confined in nanoporous carbon probed by small-angle neutron scattering. **DZT 2018**, 30. Deutsche Zeolith-Tagung, Kiel, Germany.
- Jonas Scholz, Alberto Garbujo, Antonella Glisenti, Simone Mascotto, Mesostructured LaCoO_3 prepared by acrylic polymers for heterogeneous catalysis. **Workshop** Advanced inorganic materials: green and unconventional synthesis approaches and functional assessment, 2018, Padova, Italy.

12. Acknowledgements

First and foremost, I would like to thank my supervisor Prof. Simone Mascotto for accepting me in his group and providing me with inspiring and original topics for my PhD studies, and introducing me to the big world of small-angle scattering. I am thankful for his encouragement during challenging times, and his guidance and support in the development of this work.

Furthermore I am grateful for Prof. Michael Steiger for taking over the second supervision of this work.

In addition, I am thankful for getting to know Buğra and Kurt. Their friendship over the years has meant a lot to me and I am glad that we could spend this time together.

I am also very grateful for Isabelle, Sandra, and Uta. Their contribution goes beyond the characterization of my samples. They always provided help and support, as well as the occasional chocolate bar.

Moreover, I would like to thank my intern students Christin, Ekaterina, Michael, Stefan, Tobias, and Wladi for their valuable contributions to my work.

I also want to thank current and former members of the work group, Janina, Malte, Benedikt, Dominik, Benjamin, and Julius who contributed to the familiar atmosphere in our work group.

In addition, I am appreciative of the members of the Fröba group for welcoming me and the rest of the Mascotto group, and for the fun times in Denmark.

Furthermore, I am grateful for my friends and my wonderful family, who always had my back and provided motivation and encouragement.

Most of all, I want to thank Michelle. She gave me the necessary strength during this challenging time and I could not imagine having done this without her.

13. Eidesstattliche Versicherung

Hiermit versichere ich an Eides statt, die vorliegende Dissertation selbst verfasst und keine anderen als die angegebenen Hilfsmittel benutzt zu haben. Die eingereichte schriftliche Fassung entspricht der auf dem elektronischen Speichermedium. Ich versichere, dass diese Dissertation nicht in einem früheren Promotionsverfahren eingereicht wurde.

Hamburg, den 29.02.2020